Large eddy simulation of reactive solid fuel systems using advanced flamelet approaches

Von der Fakultät für Ingenieurwissenschaften, Abteilung Maschinenbau und Verfahrenstechnik

der

Universität Duisburg-Essen

zur Erlangung des akademischen Grades

eines

Doktors der Ingenieurwissenschaften

Dr.-Ing.

genehmigte Dissertation

von

Dominik Meller
aus
Moers

Gutachter: Univ.-Prof. Dr.-Ing. Andreas M. Kempf
Prof. Dr. Oliver T. Stein
Tag der mündlichen Prüfung: 12.01.2024

Zusammenfassung

Der weltweit steigende Energiebedarf stellt eine bedeutende Herausforderung für die Erreichung der CO_2-Reduktionsziele zur Eindämmung der Erderwärmung dar. Trotz bedeutender technologischer Fortschritte im Bereich erneuerbarer Energien wie Wasserstoff sowie Eisenoxidation und -reduktion bleibt der globale Energiemix weiterhin von fossilen Brennstoffen, insbesondere Kohle, dominiert. Eine Transformation hin zu saubereren Energiequellen wird voraussichtlich auch zu einer Verringerung der Nachfrage nach Kohle führen. Dennoch ist es unwahrscheinlich, dass die Nutzung von Kohle in naher Zukunft vollständig eingestellt wird. Infolgedessen kommt der Erforschung der Kohleverbrennung und der Umsetzung effektiver Maßnahmen zur Emissionsreduktion entscheidende Bedeutung zu. Im Kontext der kohlenstoffneutralen Stromerzeugung spielt die Kohlenstoffabscheidung, -nutzung und -speicherung (CCUS) eine zentrale Rolle. Zusätzlich verspricht die Kofeuerung von Kohle mit Additiven wie Ammoniak oder Biomasse eine erhebliche Reduktion der CO_2-Emissionen.

Das Ziel dieser Arbeit besteht darin, das Verständnis und die Optimierung der Verbrennung von Kohle sowohl einzeln als auch in Kofeuerung mit anderen Brennstoffen durch den Einsatz fortschrittlicher Large-Eddy-Simulationen (LES) und moderner Modelle für die Kohleverbrennung zu verbessern. Das Simulationstool kombiniert Flamelet-basierte Tabellierungsstrategien mit einem Euler-Lagrange-Ansatz und bietet eine breitere Anwendbarkeit, die zukünftig auch andere feste Brennstoffe wie Biomasse oder Eisen einschließen kann. Die Studien umfassen verschiedene Konfigurationen von Kohlestaubflammen, beginnend von Laborexperimenten bis hin zu halbindustriellen Brenneröfen. Detaillierte LES und Vergleiche mit experimentellen Daten zeigen verbesserte Vorhersagen von Verbrennungseigenschaften wie Temperaturprofilen und Spezieskonzentrationen.

Die Untersuchungen an einer Kohlestaubflamme im Labormaßstab unterstreichen die Bedeutung der Berücksichtigung experimenteller Artefakte, insbesondere Probeneffekte bei der Speziesmessung. Die Simulationsergebnisse zeigen signifikante Abweichungen von bis zu 50 % in den Spezieskonzentrationen, hauptsächlich aufgrund des Probeneffekts. In einer weiteren Studie, die als Pionierarbeit auf diesem Gebiet gilt, wird die Kofeuerung von Kohle und Ammoniak untersucht. Es wird ein innovativer Reaktionsmechanismus entwickelt, der als Grundlage für die Generierung der Flamelet-Tabelle dient. Die durchgeführten Simulationen zeigen eine gute Übereinstimmung mit den experimentellen Daten und führen zu einer substantiellen Verbesserung der Vorhersagegenauigkeit hinsichtlich der OH- und NH-Reaktionszonen. Dieser Fortschritt resultiert aus der Anwendung des neu entwickelten Reaktionsmechanismus.

Eine weitere Studie untersucht einen halbindustriellen Kohleofen mit einem low-NO_x-Brenner, um Verbrennungseigenschaften und NO_x-Bildungsprozesse zu analysieren. Es zeigt sich eine insgesamt gute Übereinstimmung mit den experimentellen Daten, wobei die Integration einer zusätzlichen Transportgleichung für NO die Vorhersagegenauigkeit erheblich verbessert. Diese Verbesserung resultiert aus der Berücksichtigung von NO-Produktions- und -Verbrauchsprozessen, indem der NO-Quellterm in Bildungs- und Verbrauchsteile aufgespalten wird.

Das entwickelte Simulationstool zeigt vielversprechende Aussichten für die Untersuchung umweltfreundlicherer Verbrennungsprozesse, einschließlich der Kofeuerung von Kohle mit Ammoniak oder Biomasse. Es birgt daher auch Potenzial für künftige Anwendungen in Technologien wie der Eisenoxidation und -reduktion.

Abstract

The rising global energy demand poses a significant challenge in achieving CO_2 reduction targets to mitigate global warming. Despite the ongoing progress in renewable energy technologies, such as hydrogen and iron oxidation/reduction, fossil fuels, particularly coal, continue to dominate the global energy mix. While efforts to transition to cleaner energy sources are expected to reduce coal demand, it is unlikely that coal usage will cease in the near future. Thus, the study of coal combustion and the implementation of effective emission reduction measures remain crucial. In the context of carbon-neutral power generation, carbon capture, utilization, and storage (CCUS) has become a pivotal technology. Additionally, the co-firing of coal with secondary fuel sources like ammonia or biomass shows promise for substantial CO_2 emissions reduction.

The primary objective of this work is to advance the comprehension and optimization of single and co-fired coal combustion through the application of sophisticated large eddy simulations (LES) using advanced models for coal combustion. This approach incorporates flamelet-based tabulation strategies within an Euler-Lagrange framework, offering broader applicability beyond coal to encompass also other solid fuels, such as biomass or iron. Studies are conducted on several pulverized coal flame configurations, ranging from laboratory-scale experiments to semi-industrial burner furnaces. Detailed LES and comparisons with experimental data demonstrate improved predictions of combustion characteristics, including temperature distributions and species concentrations.

The investigations on a laboratory-scale coal jet flame highlight the significance of considering experimental artifacts and probing effects during simulation. Substantial deviations of up to 50 % are found in the species concentration results, primarily attributed to the probing effect. In a separate study on the laboratory-scale coal jet flame, an investigation is conducted on the co-firing of coal and ammonia. This study represents one of the pioneering LES carried out on this topic. Initially, a novel reaction mechanism is generated, serving as the foundation for the subsequent flamelet table generation. The simulations show reasonable agreement with experimental data, improving predictions of OH and NH reaction zones when using the novel reaction mechanism.

Another study examines a semi-industrial scale coal furnace equipped with a low-NO_x burner, aiming to investigate the combustion characteristics and the processes of NO_x formation. The results show an overall good agreement with experimental data. The incorporation of an additional transport equation for NO yields a substantial enhancement in the predictive accuracy of NO concentrations. This is achieved through the comprehensive consideration of NO production and destruction processes by splitting the NO source term into a formation and a rescaled consumption part.

The developed simulation framework shows great promise in investigating cleaner combustion processes, including coal and ammonia or coal and biomass co-firing, and holds potential for future applications in technologies such as iron oxidation and reduction.

Preface

This thesis represents a compilation of journal papers that were published during my time as a PhD student at the Chair of Fluid Dynamics at the University of Duisburg-Essen.

I would like to gratefully acknowledge the head of the department, Prof. Dr.-Ing. Andreas Markus Kempf, who gave me the opportunity to complete the PhD under his guidance, supported me all the way, gave me the chance to freely evolve and to present our works at leading international conferences and workshops, allowing me to travel all over the world and meet many interesting scientists.

I would like to give deep gratitude to Prof. Dr. Oliver Thomas Stein from the Engler-Bunte-Institute at the Karlsruhe Institute of Technology, who always dedicated his time to me and supported me with his scientific advice, leading to fruitful and innovative discussions, which finally resulted in the publications of this thesis. Furthermore, I would like to thank him for his willingness to report on this work.

I would like to deeply thank Dr. Lilliana Abarca-Guerrero, who, after a short first meeting in Guatemala City, welcomed me so warmly and gave me the opportunity to gain new perspectives during a research stay at the Costa Rican Institute of Technology (ITCR) — TEC in Cartago.

I am indebted to many of my colleagues from the Chair of Fluid Dynamics who have supported me during my PhD time. I would like to name Linus and Timo, not only for having helped me to understand this strange world of computational fluid dynamics, but also for being the best office mates. Among them, Sylvia, Monika, Khadijeh, Seung-Jin, Max, Johannes, Pascal, Andi, Marvin, Amir, Piotr, Parsa, Luis, Patrick, Jonas, Irenäus, and Robert should be mentioned, who not only have generously contributed to my work with much appreciated input, but making the past few years so much nicer.

Finally, I would like to show my gratitude to my family and friends who unconditionally supported me and believed in me.

"*If we knew what it was we were doing, it would not be called research, would it?*"
- Albert Einstein

Contents

List of Figures

List of Tables

Nomenclature

Abbreviations

0D	Zero-dimensional
1D	One-dimensional
2D	Two-dimensional
3D	Three-dimensional
4D	Four-dimensional
5D	Five-dimensional
ACS	American Chemical Society
BFR	Burner flow reactor
BYU	Brigham Young University
C120	Reaction mechanism (for coal combustion) including 120 species
C129	Reaction mechanism (for coal and ammonia combustion) including 129 species
CBC	Workshop on measurement and simulation of coal and biomass conversion
CDS	Central differencing scheme
CFD	Computational fluid dynamics
CMC	Conditional moment closure
CNH_3	Reaction mechanism (for ammonia combustion) including 31 species
CPD	Chemical percolation devolatilization
CPU	Central processing unit
CRECK	Chemical Reaction Engineering and Chemical Kinetics Lab
CRIEPI	Central Research Institute of Electric Power Industry
DAE	Distributed activation energy
daf	Dry and ash-free
DFG	Deutsche Forschungsgemeinschaft (German Research Foundation)
DNS	Direct numerical simulation
DOM	Discrete ordinates method
DRG	Directed relation graph
EBU	Eddy break up
EDC	Eddy dissipation concept
ERZ	External recirculation zone
FC	Fixed carbon
FDF	Filtered density function
FDM	Finite difference method
FEM	Finite element method
FG-DVC	Functional group-depolymerization, vaporization and crosslinking
FGM	Flamelet-generated manifolds
FLASHCHAIN	Flash-distillation chain-statistics
FLUT	Flamelet look-up table
FPI	Flame-prolongation of ILDM
FPV	Flamelet/progress variable
FRC	Finite rate chemistry
FVM	Finite volume method
GCV	Gross calorific value
GWSGG	Grey weighted sum of grey gases
HHV	Higher heating value

IEA	International Energy Agency
IFRF	International Flame Research Foundation
ILDM	Intrinsic low-dimensional manifolds
IPCC	Intergovernmental Panel on Climate Change
IRZ	Internal recirculation zone
LES	Large eddy simulation
LHS	Left-hand side
LHV	Lower heating value
LIF	Laser-induced fluorescence
MPI	Message passing interface
NCV	Net calorific value
NO_x	Nitrogen oxides
PA	Proximate analysis
PCC	Pulverized coal combustion
PDF	Probability density function
PFA	Path flux analysis
PFGM	Premixed flamelet-generated manifolds
PIV	Particle image velocimetry
PKP	Particle kinetics preprocessor
PLIF	Planar laser-induced fluorescence
QUICK	Quadratic upstream interpolation for convective kinematics
RANS	Reynolds-averaged Navier-Stokes
RHS	Right-hand side
RTE	Radiative transfer equation
SES	Sensor-enhanced Smagorinsky
SFOR	Single first order
SGS	Subgrid scale
TCI	Turbulence-chemistry interaction
TCM	Two-competing model
TVD	Total variation diminishing
UA	Ultimate analysis
UDS	Upwind differencing scheme
URANS	Unsteady Reynolds-averaged Navier-Stokes
VM	Volatile matter
VM,prox	Volatile matter of the proximate analysis

Lower case Latin letters

$a_{\alpha j}$	Number of all elements j in a molecule of species α	-
a_m	Runge-Kutta coefficient for the sub-step m	-
a_p	Particle acceleration	$\mathrm{m/(s^2)}$
b_α	Weighting factor for species α	-
b_char	Char burnout	-
b_m	Runge-Kutta coefficient for the sub-step m	-
c	Normalized combustion progress variable	-
c	Speed of sound	m/s
c_α	Molar concentration of species α	$\mathrm{mol/(m^3)}$
c_D	Drag coefficient	-
c_p	Heat capacity at constant pressure	$\mathrm{J/(kg \cdot K)}$
$c_{p,\mathrm{p}}$	Particle's specific heat capacity at constant pressure	$\mathrm{J/(kg \cdot K)}$
d_p	Particle diameter	m

d_{pc}	Probe correction diameter	m
f	Correction factor for interpolation from Eulerian to Langrangian phase and vice versa close to walls	-
g_i	(Components) of the gravitational acceleration vector	$\mathrm{m/(s^2)}$
g_{ij}	Velocity gradient tensor	$\mathrm{1/s}$
g_j^{SGS}	Subgrid scale species fluxes into direction j	$\mathrm{1/(m^2 \cdot s)}$
h	Specific enthalpy	$\mathrm{J/kg}$
h_{c}	Body force components acting on species α	$\mathrm{m \cdot kg/(s^2)}$
h_{c}	Specific standard enthalpy of formation	$\mathrm{J/kg}$
h_{s}	Specific sensible enthalpy of the mixture	$\mathrm{J/kg}$
k	Turbulent kinetic energy	$\mathrm{m^2/s}$
k	Wave number	$\mathrm{1/m}$
$k_{\mathrm{b},\gamma}$	Backward rate constants of reaction γ	$\mathrm{1/s}$
k_γ	Specific rate constant of reaction γ	$\mathrm{1/s}$
k_{devol}	Devolatilization rate	$\mathrm{1/s}$
$k_{\mathrm{f},\gamma}$	Forward rate constants of reaction γ	$\mathrm{1/s}$
k_i	Intrinsic reactivity for char burnout	$\mathrm{kg/(m^2 \cdot s \cdot Pa)}$
k_{SGS}	Subgrid scale kinetic energy	$\mathrm{m^2/s}$
l	Characteristic length scale	m
l_s	Characteristic system length scale	m
m	Mass	kg
$m_{e,\alpha}$	Particle's elemental coefficient	$\mathrm{m^3/kg}$
m_{p}	Particle mass	kg
$\dot{m}_{\mathrm{p}}$	Particle mass flow	$\mathrm{kg/s}$
m_{t}	Total mass	kg
n_γ	Temperature exponent of reaction γ	-
p	Pressure	Pa
$\overline{p}_{\mathrm{mod}}$	Filtered pseudo-pressure	Pa
$\dot{q}$	Heat flux	$\mathrm{W/kg}$
q_γ	Reaction rate of reaction γ	$\mathrm{mol/(m^3 \cdot s)}$
q_j	Enthalpy flux into direction j	$\mathrm{J/(m^2 \cdot s)}$
q_j^{SGS}	Subgrid scale enthalpy fluxes into direction j	$\mathrm{J/(m^2 \cdot s)}$
r	Radius	m
$\overline{r}_{\mathrm{pore}}$	Mean pore radius	m
$\hat{s}$	Ray direction	m
s_{l}	Laminar burning velocity or flame speed	$\mathrm{m/s}$
u_i	(Components) of the velocity vector	$\mathrm{m/s}$
$v'_{\alpha\gamma}$	Forward molar stoichiometric coefficients for species α within reaction γ	-
$v''_{\alpha\gamma}$	Backward molar stoichiometric coefficients for species α within reaction γ	-
v_{K}	Kolmogorov velocity scale	$\mathrm{m/s}$
w	Weighting factor for interpolation from Eulerian to Langrangian phase and vice versa	-
w_j	Quadrature weight	-
w_m	Runge-Kutta coefficient for the sub-step m	-
x_i	(Components) of the spatial coordinate vector	m
x_{p}	Particle position	m

Upper case Latin letters

A	Mixture fraction parameter	-
A	Pre-exponential factor for Arrhenius expression of SFOR model	$1/\mathrm{s}$
A_γ	Pre-exponential factor of reaction γ	-
A_i	Pre-exponential factor for Arrhenius expression of char burnout model	$\mathrm{kg}/(\mathrm{m}^2 \cdot \mathrm{s} \cdot \mathrm{Pa})$
A_p	Projected particle area	m^2
$A_{w,\alpha}$	Atomic weights of the respective particle elements	Da
B	Blowing correction	-
B	Mixture fraction parameter	-
C	Reactive scalar describing the flame progress	-
C_0	Dispersion constant	-
C_diff	Mass diffusion-limited rate constant	$\mathrm{s}/(\mathrm{K}^{0.75})$
C_{Kn}	Dimensional constant	$\mathrm{kg}^{0.5}/(\mathrm{K}^{0.5} \cdot \mathrm{kmol}^{0.5} \cdot \mathrm{s})$
C_m	Model constant in Sigma/(Sensor-enhanced) Smagorinsky model	-
C_p	Model constant	-
C_sensor	Model constant in Sensor-enhanced Smagorinsky model	-
C_χ	Subgrid dissipation rate constant	-
$\mathcal{D}$	Sample space of the particle diameter d_p	m
$\dot{\mathcal{D}}$	Conditional rate of change of the particle diameter d_p	m/s
D	Domain	-
D_0	Binary diffusion coefficient for O_2 in N_2	m^2/s
D_α	Species diffusion coefficient α	m^2/s
D_e	Effective diffusion coefficient in the particle pores	m^2/s
D_{Kn}	Knudsen diffusion coefficient	m^2/s
D_ox	Oxygen diffusion coefficient	m^2/s
D_S	Differential operator in Smagorinsky model	$1/\mathrm{s}$
D_σ	Differential operator in Sigma model	$1/\mathrm{s}$
D_{th}	Thermal diffusion coefficient	m^2/s
D_Z	Molecular diffusivity of the mixture fraction Z	m^2/s
E	Turbulent kinetic energy	m^2/s
E_A	Activation energy for Arrhenius expression of SFOR model	$\mathrm{J}/(\mathrm{kmol} \cdot \mathrm{K})$
$E_{\mathrm{A},\gamma}$	Activation energy of reaction γ	$\mathrm{J}/(\mathrm{kmol} \cdot \mathrm{K})$
E_i	Activation energy for Arrhenius expression of char burnout model	$\mathrm{J}/(\mathrm{kmol} \cdot \mathrm{K})$
F_CS	Coherent structure function	-
F_D	Drag force	$\mathrm{m} \cdot \mathrm{kg}/(\mathrm{s}^2)$
F_G	Gravitational force	$\mathrm{m} \cdot \mathrm{kg}/(\mathrm{s}^2)$
G	Filter operator	-
G	Incident radiation	$\mathrm{W}/(\mathrm{m}^2)$
G_{ij}	Square of velocity gradient tensor	$1/(\mathrm{s}^2)$
I	Radiative energy intensity	$\mathrm{W}/(\mathrm{m}^2)$
I_1, I_2, I_3	Invariants of matrix G_{ij}	-
I_b	Black body intensity	$\mathrm{W}/(\mathrm{m}^2)$
$I_\mathrm{b,p}$	Black body particle intensity	$\mathrm{W}/(\mathrm{m}^2)$
K_γ	Equilibrium constant	-
L	Characteristic length scale	m
$\dot{\mathcal{N}}$	Conditional rate of change of the particle number due	

	to coalescence and particle break-up	1/s
N_i	Number of cells in each direction i	-
N_p	Number of particles within a cell volume	-
N_r	Number of reactions	-
N_s	Number of species	-
$\widetilde{P}$	Favre-filtered subgrid PDF	-
P_BO	Particle burnout	-
Q	Q-factor	-
Q	Volume flow	$\mathrm{m^3/s}$
$\dot{Q}_\mathrm{rad}$	Radiative source term	$\mathrm{J/(m^3 \cdot s)}$
R_char	Bulk molecular mass diffusion rate of char	s/m
R_ox	Bulk molecular mass diffusion rate of oxygen	s/m
S_a	Specific internal surface area	$\mathrm{m^2/kg}$
$\dot{S}_\mathrm{h}$	Interphase radiative source term	$\mathrm{J/(m^3 \cdot s)}$
S_{ij}	Strain rate tensor	1/s
S_L	Laminar burning velocity or flame speed	m/s
$\dot{S}_\mathrm{mass}$	Mass source term	kg/s
$\dot{S}_\mathrm{mom}$	Momentum equation source term	$\mathrm{kg/(m^2 \cdot s^2)}$
$\overline{\dot{S}}_\mathrm{p}$	Filtered source term due to the subgrid effect of the particles on $\widetilde{Z''^2}$	$\mathrm{kg/(m^3 \cdot s)}$
$\overline{\dot{S}}_{\chi Z}$	Filtered source term due to unresolved scalar dissipation rate	$\mathrm{kg/(m^3 \cdot s)}$
$\dot{S}_{Y_\alpha}$	Interphase species source term	kg/s
$\mathcal{T}$	Sample space of the particle temperature T	K
$\dot{\mathcal{T}}$	Conditional rate of change of the particle temperature T	K/s
T	Temperature	K
T_0	Reference temperature	K
T_p	Particle temperature	K
V	General control volume	$\mathrm{m^3}$
$V_{\alpha,i}$	(Components) of the diffusion velocity of species alpha	m/s
V_i^c	(Components) of the diffusion correction velocity	m/s
W	Molecular weight	kg/kmol
W	Wiener term	-
X	Mixture fraction parameter	-
X_α	Mole fraction of species α	-
Y	Mixture fraction parameter	-
Y_α	Mass fraction of species α	-
Y_p	Combustion progress variable	-
$Y_{\mathrm{p},\alpha}$	Particle's mass fraction of element α (from ultimate analysis)	-
$Y_\mathrm{p,norm}$	Normalized combustion progress variable	-
Y_PV	Combustion progress variable	-
Z	Mixture fraction	-
Z	Mixture fraction parameter (sum of all mixture fractions)	-
$\widetilde{Z''^2}$	Subgrid variance of mixture fraction Z	-
Z_j	Elemental mass fraction	-

Lower case Greek letters

α_1, α_2, α_3	Angles from the invariants of g_{ij}	-
δ	Dirac delta function	-
δ_{ij}	Kronecker delta	-

δ_l	Laminar flame thickness	m
δ_th	Thermal flame thickness	m
ϵ	Dissipation rate	$\mathrm{m^2/(s^3)}$
ϵ_ash	Emissivity of the ash particle	-
ϵ_coal	Emissivity of the unreacted coal particle	-
ϵ_p	Particle emissivity	-
η	Effectiveness factor	-
η_K	Kolmogorov length scale	m
θ_p	Coal porosity	-
κ	Absorption coefficient	-
λ	Thermal conductivity	$\mathrm{W/(m \cdot K)}$
λ_m	Mean free path length	m
μ	Dynamic viscosity	$\mathrm{Pa \cdot s}$
μ_t	Turbulent eddy viscosity	$\mathrm{Pa \cdot s}$
ν_i	Elemental mole fraction	-
ν_t	Turbulent eddy viscosity	$\mathrm{m^2 \cdot s}$
ξ	Splitting factor	-
ρ	Density	$\mathrm{kg/(m^3)}$
$\rho_\mathrm{p,bulk}$	Bulk particle density (considering pores)	$\mathrm{kg/(m^3)}$
$\rho_\mathrm{p,true}$	True particle density	$\mathrm{kg/(m^3)}$
σ_1, σ_2, σ_3	Singular values of g_{ij}	-
σ_sc	Scattering coefficient	-
τ	Pore tortuosity	-
τ_c	Chemical time scale	s
τ_con	Convective time scale	s
τ_{ij}	Viscous stress tensor	$\mathrm{N/(m^2)}$
τ_{ij}^SGS	Subgrid stress tensor	$\mathrm{N/(m^2)}$
$\tau_{ij}^\mathrm{SGS,D}$	Deviatoric part of the subgrid stress tensor	$\mathrm{N/(m^2)}$
τ_K	Kolmogorov time scale	s
τ_p	Particle relaxation time	s
$\tau_\mathrm{p,t}$	Turbulent particle relaxation time	s
τ_t	Turbulent time scale	s
ϕ	Thiele modulus	-
χ	Scalar dissipation rate	1/s
$\underset{\sim}{\chi}_\alpha$	Chemical symbol of species α	-
ψ	Favre-filtered scalar-dependent quantity	-
$\dot{\omega}_\alpha$	Chemical species source term	$\mathrm{kg/(m^3 \cdot s)}$
$\dot{\omega}_{\gamma,\alpha}$	Chemical species source term of reaction γ	$\mathrm{kg/(m^3 \cdot s)}$

Upper case Greek letters

Γ	Gamma function for beta PDF	-
Δ	Filter size	m
$\Delta h_{\mathrm{f},\alpha}^\circ$	Enthalpy of formation of species α at reference temperature T_0	J/kg
Δt	Time step width	s
Δ_x	Cell size	m
Φ	Equivalence ratio	-
Ω	Unit angle	$\mathrm{m^2}$
Ω_{ij}	Rotation rate tensor	1/s

Subscripts to an arbitrary quantity ϕ

ϕ_0	Reference condition/initial state at $t = 0$/state of the largest eddies
ϕ_α	Value for a species α
ϕ_b	Burned
ϕ_b	Value at the bottom cell surface
ϕ_char	Char burnout/char off-gases
ϕ_crit	Critical condition
ϕ_C	Value at the cell center
ϕ_γ	Value for a reaction γ
ϕ_evap	Evaporation
ϕ_Exp	Experimental quantity
ϕ_E	Value at the cell center of the eastern adjacent cell
ϕ_e	Value at the eastern cell surface
ϕ_F	Fuel
ϕ_f	Value at the cell surface f
ϕ_g	Gas phase quantity
ϕ_IB	Immersed boundary
ϕ_max	Maximum value
ϕ_min	Minimum value
ϕ_norm	Normalized
ϕ_N	Value at the cell center of the northern adjacent cell
ϕ_n	Value at the northern cell surface
ϕ_ox	Oxidizer
ϕ_pc	Probe-corrected
ϕ_pil	Pilot
ϕ_p	Particle
ϕ_ref	Reference condition
ϕ_smago	Smagorinsky
ϕ_st	Stoichiometric condition
ϕ_S	Value at the cell center of the southern adjacent cell
ϕ_s	Value at the southern cell surface
ϕ_TAB	Quantity taken from the flamelet library
ϕ_t	Value at the top cell surface
ϕ_u	Unburned
ϕ_vol	Volatiles
ϕ_W	Value at the cell center of the western adjacent cell
ϕ_w	Value at the western cell surface

Superscripts to an arbitrary quantity ϕ

ϕ'	Fluctuation
ϕ^SGS	Subgrid scale

Mathematical symbols and operators to an arbitrary quantity ϕ

$d\phi$	Total derivative
$\partial\phi$	Partial derivative
$\overline{\phi}$	Filtering in LES
$\overline{\phi}$	Temporal averaging in RANS
$\widehat{\phi}$	Test-filtering for dynamic models
$\widetilde{\phi}$	Mass weighted Favre-filtering in LES

Dimensionless numbers

CFL	Courant Friedrichs Lewy number
Da	Damköhler number
Fr	Froude number
Kn	Knudsen number
Le	Lewis number
Ma	Mach number
Nu	Nusselt number
Pr	Prandtl number
Pr_t	Turbulent Prandtl number
Re	Reynolds number
Re_p	Particle Reynolds number
Sc	Schmidt number
Sc_t	Turbulent Schmidt number
St	Stokes number

Physio-chemical constants

R_u	Universal gas constant	$8.314\mathrm{J}/(\mathrm{mol} \cdot \mathrm{K})$
σ	Stefan-Boltzmann constant	$5.6704 \cdot 10^{8}\ \mathrm{W}/(\mathrm{m}^2 \cdot \mathrm{K}^4)$

Chapter 1

Introduction

This thesis focuses on the modeling and simulation of pulverized solid fuel combustion, with a particular emphasis on coal as the primary fuel source investigated. The subsequent sections provide a comprehensive background on the global context, highlighting the factors that motivated this research. Furthermore, a concise review of the existing research on numerical simulation of solid fuels (and, in particular, coal) is presented. After providing a detailed background discussion, this thesis proceeds to outline its specific aims and contributions, giving a brief summary of the conducted research and its relevance to the field.

1.1 Motivation

Despite global efforts towards green initiatives over the past decades, the predominant use of energy of modern society continues to rely heavily on fossil fuels. In 2021, coal, oil, and gas collectively constituted 83 % of the global primary energy consumption. Coal specifically held the second-largest share, accounting for 27 % of the energy mix, following oil (31 %) [14].

The invasion of Ukraine by Russia has resulted in bans and sanctions that have reshuffled global coal trade flows. According to the International Energy Agency (IEA) [57], Europe experienced increased coal usage for electricity generation in 2022 due to high natural gas prices. Despite a decline in the United States, coal power generation reached a new record in 2022, primarily driven by India and the European Union, with a smaller contribution from China. The heavy reliance on Russian gas compelled the European Union, particularly Germany, to reopen coal power plants to meet the electricity demand. However, efforts to enhance efficiency and expand renewables are expected to lead to a decrease in coal generation and demand by 2024.

The IEA predicts that global coal demand will stabilize at around 8 billion tons through 2025, with uncertainties influencing future growth [57]. China and India play significant roles in the global demand, with China's power sector alone accounting for one-third of the global coal consumption. While the United States and the European Union are projected to witness declines in coal consumption, the transition to a cleaner energy mix will heavily depend on countries like China and India, which together accounted for approximately 66 % of the global coal consumption in 2021 [14]. China and India are not only the largest consumers but also producers of coal, increasing domestic production to address price hikes and supply shortages. The IEA indicates that global coal production reached its highest level ever in 2022, driven by increased production in these countries [57]. Without scalable low-emissions alternatives, global coal demand is expected to remain stagnant. Therefore, a complete global ban on coal firing in the coming years appears highly unlikely.

However, it is crucial to acknowledge that the extraction of coal and its combustion for power generation not only impacts the environment and health due to the emission of strong pollutants such as carbon monoxide (CO), nitrogen oxides (NO_x), sulphur dioxide (SO_2), mercury (Hg), arsenic (As), but it is also a significant contributor to the anthropogenic climate change [206], still accounting for about $42 - 44$ % of human-made carbon dioxide (CO_2) emissions (2020) [56].

In response to the challenge posed by climate change, the Paris Agreement was established as a comprehensive international accord, with the primary objective of limiting global warming to a maximum of 1.5 °C above pre-industrial levels [174]. To attain this ambitious target, the Intergovernmental Panel on Climate Change (IPCC) has emphasized the urgent need for a substantial reduction in global CO_2 emissions [62]. Specifically, the IPCC has recommended a decrease in annual CO_2 emissions from 42 Gt in 2017 to approximately 20 Gt by 2030, ultimately striving for a net-zero emission status by 2050. This objective stands in stark contrast to the prevailing trajectory of coal consumption and overall primary energy demand, as previously highlighted by the IEA [57].

Hence, the IPCC has outlined four primary objectives to effectively mitigate CO_2 emissions. These objectives involve decreasing the use of energy, transitioning to electrified energy services, achieving decarbonization of the power sector, and attaining the decarbonization of non-electric fuel usage across diverse energy end-use sectors [62].

The decarbonization of the power sector is a significant research area within the numerical combustion community, and the current thesis is dedicated to addressing this objective. To target this issue, extensive efforts are being made to improve combustion efficiency and energy conversion and minimize emissions during coal conversion.

To obtain further insight into the combustion process of solid fuels, both, experimental and numerical investigations can be conducted. Conducting experimental investigations of coal combustion is challenging due to the harsh operating conditions, safety concerns, and high costs involved. Experimental measurements often provide limited spatial and temporal resolution, making it difficult to capture the detailed phenomena occurring within the combustion process. Numerical simulations overcome these limitations by offering a cost-effective and flexible approach to study coal combustion. Through computational models, a wide range of operating conditions can be simulated and analyzed, providing detailed insights into the combustion process that would be otherwise challenging or impossible to obtain experimentally. The experimental data thereby plays a vital role in validating these numerical models. Consequently, computational fluid dynamics (CFD) has gained significant importance in recent years for conducting comprehensive investigations of combustion processes in general.

Numerical simulations allow us to analyze the fundamental processes involved in coal combustion, such as fuel-air mixing, flame propagation, and heat transfer, to optimize combustion conditions and enhance energy conversion efficiency. By understanding the complex interactions between turbulence, chemistry, and radiative heat transfer, we can design and optimize combustion systems to achieve higher efficiencies and reduced environmental impact.

These efforts to decarbonize the power sector encompass not only the combustion process itself, but also the investigation of complex burner designs aimed at reducing emissions, such as low-NO_x burners. Through simulations, the effects of various operational parameters, fuel properties, and burner configurations on combustion efficiency, emissions, and overall system performance can be evaluated. This knowledge can guide the design and optimization of combustion systems, enabling the development of cleaner, more efficient, and sustainable energy solutions.

Furthermore, current research efforts are directed towards the co-firing of coal with diverse secondary fuel sources, such as the co-firing of coal and biomass or coal and ammonia. These measures allow for the continued operation of existing coal-fired power plants at markedly reduced CO_2 emissions. As the world transitions towards cleaner and renewable energy sources, it is crucial to understand the combustion characteristics of alternative fuels and their interactions with coal. Numerical simulations provide a platform to study co-firing scenarios, where coal is combusted together with biomass, natural gas, or other renewable fuels like ammonia. By investigating the complex combustion dynamics of such fuel mixtures, we can optimize co-firing strategies and facilitate fuel flexibility. In this work, both, the investigations of a low-NO_x burner and the co-firing of coal and ammonia are addressed.

In conclusion, the numerical study of coal combustion is motivated by the pressing need to address environmental concerns, improve combustion efficiency, optimize system design, and facilitate the transition towards cleaner energy sources. By leveraging computational models, in-depth insights into the complex phenomena occurring during coal combustion are gained, and innovative solutions to mitigate environmental impacts can be developed, enhancing energy conversion efficiency, and paving the way for a sustainable energy future. The developed models, thereby, exhibit potential for transferability and applicability to other solid fuels, such as biomass, as well as emerging research areas, like metal fuels.

In the subsequent section, a concise overview of the current state-of-the-art research and key numerical advancements in the field of solid fuel combustion, and in particular, coal combustion, shall be given.

1.2 State-of-the-art

Turbulent combustion processes can be studied using different simulation methods, each offering varying levels of detail. These methods fall into three distinct paradigms: direct numerical simulation (DNS), large eddy simulation (LES), and Reynolds-averaged Navier-Stokes (RANS) simulation. DNS offers the highest precision in describing turbulent flows by resolving all relevant scales. However, it is crucial to acknowledge that the computational expenses associated with DNS are substantially elevated. Consequently, the current generation of computers can effectively handle only small computational domains with flows at moderate Reynolds numbers. Thus, when dealing with industrial burners or larger-scale simulations, alternative methodologies become indispensable. For example, LES decomposes the turbulent flow field into a filtered and unresolved contribution, thus resolving larger scales of the filtered fields and modeling unresolved smaller scales. On the other hand, RANS simulations solely compute time-averaged flow fields, resulting in the least computational burden. The following section will review numerical efforts across all three paradigms in the field of pulverized coal combustion.

The earliest CFD investigations of pulverized coal flames can be traced back to the 1980s [85, 113, 151, 153, 154, 169, 185]. During that era, the computational cost of LES and DNS was prohibitively high, leaving RANS simulations as the only option. Smith et al. [153] and Smoot [154] conducted RANS simulations of the experimental facilities at Brigham Young University. Truelove and Williams [169] performed RANS simulations of a 300 kW combustor and a full-scale 40 MW burner, matching their simulations to experimental data. Lockwood and Salooja [85] focused on simulating the 2.5 MW International Flame Research Foundation (IFRF) No. 1 furnace using RANS, achieving satisfactory results in terms of temperature and species mass fractions. Furthermore, Peters and Weber [113], Smart et al. [151] and Weber et al. [185] conducted RANS simulations of the IFRF No. 1 furnace, comparing their results to more detailed velocity and $\mathrm{NO_x}$ measurements.

The practical application of DNS is limited to highly simplified test cases, and when both, turbulent length scales and solid particles are resolved, investigations are typically restricted to single particles or small static groups of particles. For example, Vascellari et al. [179] conducted a study on single coal particle ignition in a laminar entrained-flow reactor using DNS to evaluate a non-premixed flamelet approach, showing accurate prediction of ignition by incorporating DNS data for scalar dissipation rate profiles and good agreement with experimental results. Similarly, Tufano et al. [171, 172] utilized DNS to study volatile combustion of isolated coal particles and particle ensembles in laminar and turbulent flow. The investigations highlight the impact of group effects in laminar flows, as well as particle Reynolds number and turbulence on devolatilization and burning behavior, emphasizing the challenges in applying standard models for flamelet approaches at high Reynolds numbers.

In contrast to fully resolved DNS, where both, all turbulent length scales and the solid particles are resolved, the concept of carrier-phase (CP)-DNS has become increasingly prevalent in studying particle groups in pulverized coal flames. Originally developed for spray combustion [112], CP-DNS resolves all scales of turbulence, while particles are treated within a point-particle framework. Luo et al. [87] and Hara et al. [44] were among the first to apply CP-DNS to simplified pulverized coal flame configurations, utilizing reduced chemistry descriptions. Subsequently, Rieth et al. [140] conducted a more elaborate CP-DNS study, exploring coal particle ignition in a turbulent mixing layer with detailed kinetics. The study provides insights into solid particle ignition and burning mechanisms, flame structure, and combustion modes, revealing ignition at very lean conditions with subsequent volatile combustion occurring in non-premixed and premixed modes, leading to complex flame structures. The DNS database and initial analysis served as fundamental input for a series of subsequent studies aimed at assessing the applicability of flamelet modeling for coal combustion [141, 193, 194]. Wen et al. [195] performed CP-DNS of pulverized coal combustion in a mixing layer to investigate NO_x formation, focusing on early devolatilization stages and revealing differences in NO_x production pathways compared to fuel-nitrogen-free flames, confirming the suitability of flamelet models, but noting discrepancies in NO_x species prediction by the flamelet model. Shamooni et al. [145] further examined NO_x formation in the same mixing layer setup, adopting a comprehensive homogeneous mechanism including all standard pathways of NO_x and pyridine oxidation. The results reveal distinct branches of NO formation, highlighting the significant contributions of fuel-bound nitrogen species, such as ammonia, hydrogen cyanide, and pyridine to NO production and destruction mechanisms. Despite advancements in computational capabilities in recent years, the high computational costs associated with DNS remain unsustainable for broader and more complex applications.

In recent years, LES has emerged as a potent tool for simulating PCC, following its initial applications by Kurose and Makino [78]. LES offers a favorable compromise between enhanced predictive accuracy and a moderate increase in computational requirements over RANS. Subsequent to the pioneering LES study on PCC flames, several other research groups have adopted this technique to conduct numerous investigations on different PCC flame configurations [34, 111, 130, 137, 162, 184]. Franchetti et al. [34] successfully applied LES to a pulverized coal jet flame, using a set of models representing coal combustion, particle transport, and radiative heat transfer. The simulation results demonstrated good agreement with experimental data, highlighting the potential of LES for simulations of pulverized coal combustion and paving the way for future developments in coal combustion models and applications to more complex burners. Stein et al. [162] conducted a study comparing simulation results of pulverized coal combustion from three research groups using different CFD codes and particle transport approaches, showing that both, numerical methods and model choices significantly influence the LES results. While they achieved good agreement with experimental data for the non-reacting case, notable differences arose for the PCC case, emphasizing the necessity for further research and development in comprehensive PCC-LES modeling. In the literature, LES studies of PCC flames covering a thermal power range spanning from several kilowatts (kW) up to several megawatts (MW) already exist, with predominant emphasis on air-fired systems. For example, Rabaçal et al. [130] investigated a 100 kW coal flame co-fired with natural gas using phenomenological network models to optimize devolatilization kinetic data. The simulation results showed good agreement with experimental measurements, revealing distinct CO_2 production zones from gaseous and char combustion and variations in particle properties across different regions of the combustion process. Olenik et al. [111] conducted a pioneering study utilizing LES to investigate turbulent PCC within the 2.5 MW IFRF No. 1 furnace. The simulations showed a good predictive accuracy for velocity statistics and mean species profiles; however, temperature underprediction was observed, possibly attributed to the simplified turbulence-chemistry interaction model used in the simulations. Rieth et al. [137] conducted a comprehensive study employing a flamelet model in LES of the same semi-industrial furnace configuration, yielding favorable agreement with experimental data and providing valuable insights into the coal conversion process through detailed analysis of instantaneous particle and gas phase data.

While numerous test flames have been employed (see e.g. the target flames of the workshop on measurement and simulation of coal and biomass conversion (CBC) [161]) and extensive numerical studies have been conducted on pulverized coal flames, there is a notable gap in research addressing the optimization and enhancement of current coal-fired power plants, especially concerning the reduction of carbon dioxide emissions. This optimization endeavor encompasses various strategies, such as oxy-fuel combustion, pure biomass combustion, and co-firing approaches, in which coal is fired together with secondary fuels like biomass or ammonia. However, progress in these areas has been hindered by the limited availability of detailed experimental measurements focusing on these scenarios. Regarding oxy-fuel combustion, the 100 kW OXYCOAL-AC test facility of the Institute of Heat and Mass Transfer (WSA) from the RWTH Aachen University needs to be mentioned [49, 167, 207, 208]. This facility offers comprehensive data on pulverized coal flames operating under both, oxy-fuel and air atmospheres. In the context of biomass combustion, the Brigham Young University (BYU) Burner Flow Reactor (BFR) stands out as a significant experimental facility, where Damstedt et al. [24, 25] conducted comprehensive measurements of various coal and biomass single and co-firing systems, providing valuable insights into combustion dynamics. The Central Research Institute of Electric Power Industry (CRIEPI) jet flame plays a crucial role in studying the co-firing of coal and ammonia, offering detailed experimental datasets comparing co-firing scenarios with single firings of coal or ammonia [164, 165]. In the following, numerical efforts considering oxy-fuel combustion, biomass combustion, and coal co-firing scenarios shall be briefly reviewed.

In the context of oxy-fuel combustion, Edge et al. [27] utilized LES to study oxy-fired pulverized coal combustion, highlighting the improved predictive capabilities of LES in terms of recirculation zones and flame properties compared to RANS simulations. Chen and Ghoniem [20] conducted LES and RANS approaches to investigate oxy-fuel combustion of lignite coal, revealing LES's superior prediction for flow dynamics, flame characteristics, and char combustion in the CO_2-rich environment, where gasification reactions were locally significant in fuel-rich zones and char consumption was dominated by oxidation reactions. Franchetti et al. [35] performed LES to investigate oxy-coal combustion in the 100 kW OXYCOAL-AC test facility at Aachen University, revealing good agreement with mean velocity measurements and demonstrating the potential of LES for complex oxy-coal combustion burners and industrial furnace applications. Nicolai et al. [106] conducted LES using a sophisticated modeling framework that combines a detailed solid fuel kinetic mechanism with a flamelet approach to investigate oxy-fuel combustion's potential for carbon capture in coal-fired power plants, focusing on the impact of adjustable oxygen content in recirculated flue gas on solid fuel conversion in various oxy-fuel swirl flames.

In the context of biomass combustion, similar modeling techniques utilized in coal combustion can be adapted with minor adjustments, owing to the comparable nature of the combustion process in both solid fuels [199]. Unlike coal, biomass typically possesses a lower energy density and higher moisture content. Backreedy et al. [7] conducted RANS simulations to examine the co-firing of pulverized coal and biomass, with a specific emphasis on the burnout characteristics of larger diameter biomass particles. Their findings revealed that small wood particles exhibited rapid combustion, whereas the combustion rate of larger particles was influenced by their inherent composition, size, and shape. Ma et al. [89] focused on the development of a RANS model to simulate biomass combustion in existing coal-fired furnaces, investigating the effects of potassium release and NO_x formation. Ghenai and Janajreh [37] conducted a comprehensive RANS analysis of co-firing biomass with coal, considering gas and particle phases, turbulence effects on chemical reactions, and the reduction of NO_x and CO_2 emissions through co-combustion. Black et al. [13] focused on using RANS to analyze the impact of oxy-fuel combustion of coal and biomass in a full-scale utility boiler. They studied the effects of different fuel and combustion atmospheres on heat transfer characteristics, particularly in the context of converting to biomass firing under various combustion conditions. The aforementioned studies were solely based on numerical results from RANS simulations of industrial-scale biomass combustion and biomass co-combustion with coal, lacking experimental comparisons. However, Yin et al. [205] performed a RANS study on co-firing wheat straw with coal, comparing their numerical findings to experimental data. They identified that intra-particle heat and mass transfer had a secondary influence on biomass conversion and proposed a robust modeling approach for biomass/coal co-firing, highlighting substantial discrepancies in burnout characteristics between the two fuels. Rabaçal et al. [131] studied the impact of devolatilization and char combustion mode modeling on the structure of a large-scale biomass and coal co-firing flame using LES and comparing it with experimental data, finding that devolatilization modeling had a significant impact on the flame structure, while the char combustion mode model had a minor influence on the predicted outcomes for the tested conditions. Wen et al. [196] conducted LES of a 40 kW self-sustained pulverized torrefied biomass furnace in air and oxy-fuel atmospheres using an extended flamelet model, revealing differences in flame structures and thermochemical variable distributions due to distinct flow dynamics, while also observing significant effects on emissions, particularly for the furnace with staged oxidizer combustion.

The co-firing of coal with ammonia presents a promising approach to achieve a substantial reduction in CO_2 emissions and facilitate the defossilization of coal-fired power plants. Yamamoto et al. [204] studied the co-firing of coal and ammonia with a horizontal single burner and found that optimal conditions for minimum NO emissions were achieved at a co-firing rate of 20 % with ammonia injection located 1 m away from the burner, resulting in NO levels similar to those observed in pure coal-fired cases. Zhang et al. [209] conducted a study on an 8.5 MW combustion facility with a single swirl burner, performing RANS simulations with simple chemistry using a global reaction mechanism, and found that co-firing ratios above 40 % led to a significant increase in unburned ammonia in the flue gas. Additionally, they observed that using an 80 % co-firing ratio resulted in the highest NO emissions, while further increasing the co-firing ratio reduced NO emissions. Ishihara et al. [63, 64] confirmed these findings using 0D network calculations of perfectly stirred reactors with detailed chemistry, consistent with the studies by Yamamoto et al. [204] and Zhang et al. [209].

The studies above have employed various models to address turbulence-chemistry interaction (TCI), each offering varying levels of accuracy in predicting species concentrations. Given the critical importance of accurate species prediction in pulverized coal combustion, the following section will provide a brief overview of commonly used models in this domain. Despite the exponential growth in computational power, simulations of turbulent multiphase flows with detailed chemistry remain too expensive for practical industrial applications. Notably, coal combustion is a complex process involving several hundreds of species and thousands of reactions for a detailed description, making it infeasible to directly solve transport equations for all species in numerical simulations. Consequently, simplified combustion models that rely on strong assumptions, such as the eddy break-up (EBU) model [158] or the eddy dissipation concept (EDC) [92], are commonly employed in PCC simulations. While these simplistic models exhibit satisfactory performance in certain scenarios, they possess notable limitations, such as being based on the assumption of infinitely fast chemistry. The simplification of chemical kinetics in such models can lead to inaccurate predictions of crucial flame properties, including pollutant formation and flame temperature. To address these limitations, more advanced models have been developed in recent years, such as the transported probability density function (PDF) model [122], the conditional moment closure (CMC) model [72], and the flamelet model [114], which offer improved capabilities in mitigating the aforementioned weaknesses. The flamelet model [114] represents an advantageous and effective approach for incorporating detailed reaction mechanisms, thereby enabling a precise description of the gas phase in coal combustion. Notably, the flamelet model achieves this precision with a relatively lower computational burden, as it only solves for a small number of transport equations. Central to this framework is the precalculation and storage of thermochemical properties in flamelet tables, wherein a set of transported control variables is employed to access the tabulated data during simulation run time. Several variations of the flamelet model have been proposed, including those based on non-premixed (e.g. [137, 179, 180, 192]) and premixed flamelets (e.g. [73, 74, 182]). One extension of the flamelet model is the flamelet/progress variable (FPV) model introduced by Pierce and Moin [117], where a progress variable is employed as a trajectory variable. The FPV model has gained significant popularity in the field of pulverized coal flame simulations due to its good trade-off between accuracy and performance and has been extensively applied in various applications [3, 95–97, 188, 192], including the simulations conducted as part of this work. In the following section, the objectives and contributions of this work are outlined and the general structure of this thesis is provided.

1.3 Objectives and contribution

The present work focuses on the LES of turbulent reactive multiphase flows employing advanced flamelet approaches. Specifically, the research investigates solid fuel systems that utilize coal as a primary fuel source. The simulations in this work were carried out in the scope of the DFG project "Multi-dimensional Flamelet Modelling for the LES of Pulverized Coal Flames" (grant number 238057103). The primary objective of this research is the development of multi-dimensional flamelet models specifically tailored for LES, aiming to enhance the accuracy of predicting pollutant formation during the combustion of solid fuels. Substantial progress has been made in this domain. Two test flames were extensively examined, and the simulations were carefully validated against experimental data. To address specific challenges encountered in the research, a series of models were developed and presented in the three published papers of this work. These models account for (1) experimental artifacts arising from species probe measurements, (2) the co-firing of coal and ammonia, a relatively new approach to reduce CO_2 emissions in coal-fired power plants, and (3) the improvement of nitrogen oxides (NO_x) emission prediction. Overall, this study contributes to the advancement of flamelet modeling in LES, providing valuable insights and improvements in predicting pollutant formation in solid fuel combustion processes.

The structure of this work is as follows: Chapter 2 provides the theoretical background on reactive solid fuel systems. It encompasses the governing equations for reactive multiphase flows, the description of turbulence and combustion, and an overview of the fundamental processes involved in coal conversion. Chapter 3 focuses on modeling strategies for reactive solid fuel systems. It discusses the commonly used modeling paradigms for turbulent flows, including DNS, RANS simulation, and LES. The chapter also presents the subgrid models employed in the LES. Additionally, it addresses combustion modeling, and in particular flamelet approaches, radiation modeling, and the treatment of the dispersed phase in coal conversion. Chapter 4 deals with the numerical schemes utilized to solve the governing equations. Chapter 5 showcases the published journal papers produced during this work, which employ the models and methods introduced in the preceding chapters. Two flame setups are examined: a coaxial hydrogen-piloted pulverized coal flame operated by the Central Research Institute of Electric Power Industry (CRIEPI) in Japan (sections 5.1 and 5.2) and a semi-industrial swirl-stabilized pulverized coal flame operated by Brigham Young University (BYU) in Utah, USA (section 5.3). Section 5.1 applies a four-dimensional flamelet/progress variable (FPV) approach, employing two mixture fractions for the hydrogen pilot and coal volatiles, along with the total enthalpy and a progress variable, to describe the thermochemical state. The investigation focuses on experimental artifacts in gas species measurements using suction probes and introduces a newly developed probe correction modeling approach. Section 5.2 extends the flamelet description to include co-firing of coal and ammonia by introducing an additional mixture fraction. Consequently, the FPV approach encompasses five dimensions. This work presents and tests a newly developed reaction mechanism in the LES framework. The mechanism describes the detailed chemistry of ammonia and the oxidation of coal volatiles and tars. Section 5.3 investigates the formation of NO_x in a semi-industrial swirl-stabilized pulverized coal flame. A four-dimensional FPV approach is used, considering mixture fractions of volatiles and char off-gases. Two different approaches to model NO species are compared. One approach extracts the NO species directly from the flamelet library, while the second approach involves solving an additional transport equation for NO, in which the reaction source term is split into a formation and a rescaled consumption part. This separation allows for a better representation of the forward- and backward reactions of NO. Chapter 6 summarizes the findings of this research and provides an outlook on future research directions.

Chapter 2

Theoretical background

The following chapter provides the theoretical background necessary to describe complex reactive multiphase systems. Multiphase flows encompass the dynamics of two-phase systems in which one phase is dispersed, indicating the presence of discrete elements that lack material connectivity, i.e. in pulverized coal flames. In this work, particle and gas phase are treated separately via an Euler-Lagrange framework and linked via two-phase coupling terms. The primary focus of this chapter is the introduction of the governing equations that describe reactive multiphase flows. The interphase source terms are explicitly incorporated into the respective equations to account for their influence on the system dynamics. However, to provide a more comprehensive understanding of these terms and their closure, a detailed explanation is deferred to the subsequent modeling section (Section 3.5). Following the presentation of the governing equations, the chapter proceeds to define and characterize turbulence, a vital aspect for understanding the complex dynamics inherent in these systems. Subsequently, combustion processes are addressed, where reactants undergo chemical reactions leading to the formation of products. Here, the reaction kinetics and the different modes that may be encountered during combustion are described. The final section of this chapter provides an introductory overview of the fundamental equations that describe the combustion of solid fuels, with a specific emphasis on the detailed examination of coal combustion.

2.1 Reacting multiphase fluid flow

2.1.1 Multiphase conservation equations

The mathematical and physical fundamentals of reacting fluid flow will be described first. Most engineering applications use the continuum assumption to describe the reactive gas phase of a multicomponent system, which allows the description of its motion by partial differential equations. It is important to note a clear distinction between the terms “multicomponent” and “multiphase” in this context. Multicomponent flows involve the simultaneous movement of different chemical species within a single phase, whereas multiphase flows pertain to the coexistence and interactions of multiple distinct phases. The continuum assumption neglects the molecular motion of a fluid and assumes that a large number of molecules are present in a given volume. To justify the continuum assumption, the mean free path length of the molecules λ_m must therefore be small compared to the characteristic system length scale l_s. This ratio is described by the Knudsen number Kn; thus, it must hold:

$$Kn = \frac{\lambda_m}{l_s} \ll 1. \tag{2.1}$$

In the following section, the governing conservation equations for mass, momentum, species and energy are briefly summarized. For a more detailed explanation, the reader is referred to classical textbooks (i.e. Williams [202], Poinsot and Veynante [121]).

Conservation of mass

Conservation of mass implies that mass in a given control volume $dV = dx \cdot dy \cdot dz$ can neither be produced nor destroyed, and only changes through fluxes across the respective surface boundaries or interphase mass transfer. The temporal evolution of mass in a control volume can be described in differential form through:

$$\frac{\partial \rho}{\partial t} + \frac{\partial \rho u_i}{\partial x_i} = \dot{S}_{\text{mass}} \tag{2.2}$$

On the left-hand side (LHS), the first term denotes the change of the mixture density ρ in time t, while the second term represents the convective transport of mass over the volume boundaries in i^{th} direction using the spatial coordinate x_i and the velocity u_i. To account for the interphase mass transfer between solid and gas phase during solid fuel combustion (i.e. through the release of volatiles and char from coal particles to the gas phase), a mass source term $\dot{S}_{\text{mass}}$ has been added to the right-hand side (RHS) of Eq. 2.2.

Conservation of momentum

Similar to the mass, the momentum ρu_i is also a conserved quantity. The governing equation describes the temporal and spatial evolution of momentum, taking into account all acting forces on a fluid element, and reads:

$$\frac{\partial \rho u_i}{\partial t} + \frac{\partial \rho u_i u_j}{\partial x_j} = -\frac{\partial p}{\partial x_i} + \frac{\partial \tau_{ij}}{\partial x_j} + \rho g_i + \dot{S}_{\text{mom}} \tag{2.3}$$

The first and second term on the LHS are the accumulation and convection terms, respectively. The RHS describes the sum of all acting forces on the fluid, considering forces due to pressure p, viscous stresses τ_{ij} and a volume force due to gravity, in which the i^{th} component of the gravitational acceleration g_i is considered. The last term $\dot{S}_{\text{mom}}$ takes into account additional forces due to interphase momentum transfer between solid and gas phase (i.e. the effect of particle acceleration on the gas phase). In this work, only Newtonian fluids are considered, for which the viscous stresses are proportional to the strain rate of the flow. Thus, the stress tensor can be described through the dynamic viscosity μ, and is given by:

$$\tau_{ij} = \mu \left(\frac{\partial u_i}{\partial x_j} + \frac{\partial u_j}{\partial x_i} \right) - \frac{2}{3} \mu \frac{\partial u_k}{\partial x_k} \delta_{ij} \tag{2.4}$$

where δ_{ij} denotes the Kronecker delta ($\delta_{ij} = 1$ for $i = j$, $\delta_{ij} = 0$ for $i \neq j$).

Conservation of species

The gas phase of a reactive flow consists not only of a single species α, but rather of a mixture composition of a number of N_{s} species. To distinguish the different species α in a mixture, the mass fraction Y_α is used, which is defined as:

$$Y_\alpha = \frac{m_\alpha}{m_{\text{t}}} = \frac{m_\alpha}{\sum_{i=1}^{N_{\text{s}}} m_i} \tag{2.5}$$

The species mass fraction relates the mass of a single species m_α to the total mass m_{t} of the composition (defined as the sum of all species masses excluding the mass of dispersed particles). The temporal and spatial evolution of the species mass fraction is described by the conservation equation:

$$\frac{\partial \rho Y_\alpha}{\partial t} + \frac{\partial \rho Y_\alpha u_j}{\partial x_j} = -\frac{\partial \rho V_{\alpha,j} Y_\alpha}{\partial x_j} + \dot{\omega}_\alpha + \dot{S}_{Y_\alpha} \tag{2.6}$$

Again, the two terms on the LHS are the accumulation and convection terms of Y_α, while the terms on the RHS denote the diffusion flux with the species diffusion velocity $V_{\alpha,i}$, the chemical source term $\dot{\omega}_\alpha$, describing the net rate of production and destruction by chemical reactions of species α, and the source term $\dot{S}_{Y_\alpha}$, accounting for the interphase mass transfer between solid and gas phase, respectively. The diffusion velocity $V_{\alpha,j}$ needs modeling for closure. The complete evaluation can be achieved by solving the Stefan-Maxwell equations, which account for the effect of mass diffusion due to concentration gradients, diffusion due to a pressure gradient, a body force, and the Soret effect [121]. This approach requires the solution of a system of equations of size N_s^2, which quickly becomes too expensive with an increasing number of species. Thus, more simplified models are usually used. One of these models is the Hirschfelder-Curtiss approximation, which reads [50]:

$$V_{\alpha,i} = -\frac{D_\alpha}{X_\alpha}\frac{\partial X_\alpha}{\partial x_i} \tag{2.7}$$

Here, D_α and X_α are the diffusion coefficient and the mole fraction of species α in the mixture. To ensure continuity, the diffusive fluxes in Eq. 2.6 need to sum up to zero ($\sum_{\alpha=1}^{N_\mathrm{s}} V_{\alpha,i}Y_\alpha = 0$). As Eq. 2.7 does not calculate the exact diffusion velocities, this requirement is not fulfilled, and a correction velocity V_i^c needs to be added [121]:

$$V_{\alpha,i} = -\frac{D_\alpha}{X_\alpha}\frac{\partial X_\alpha}{\partial x_i} + V_i^c = -\frac{D_\alpha}{X_\alpha}\frac{\partial X_\alpha}{\partial x_i} + \sum_{\alpha=1}^{N_\mathrm{s}} D_\alpha \frac{W_\alpha}{W}\frac{\partial X_\alpha}{\partial x_i} \tag{2.8}$$

where W_α and W are the molecular weights of species α and the mixture. The latter can be calculated as:

$$W = \left(\sum_{\alpha=1}^{N_\mathrm{s}} \frac{Y_\alpha}{W_\alpha}\right)^{-1} \tag{2.9}$$

Further simplifying this approach by assuming equal diffusivities, corresponding to Fick's law, leads to the correction velocity becoming obsolete. An additional simplification is the so called unity Lewis number approach, in which the species diffusion D_α and the thermal diffusion $D_{th} = \lambda/(\rho c_p)$ are assumed to be equal. The latter is used in this work. The Lewis number equation reads:

$$Le = \frac{D_{th}}{D_\alpha} = \frac{\lambda}{\rho c_p D} \tag{2.10}$$

Here, D_{th}, D, λ and c_p are the thermal diffusivity, the diffusion coefficient in the mixture, the thermal conductivity and the mean specific heat capacity of the mixture at constant pressure. A unity Lewis number assumption implies, that $D_\alpha = D_{th} = D$, as all respective species diffusivities are assumed to be equal. However, this assumption becomes invalid in the presence of hydrogen, characterized by its high diffusivity. The burner configurations in sections 5.1 and 5.2 incorporate hydrogen as pilot fuel, and thus, differential diffusion effects may occur. Given the low heat input of hydrogen to coal ($\sim 2.8\,\%$) and the turbulent nature of these flames, it is assumed that differential diffusion will have a negligible impact. Consequently, the unity Lewis number assumption is employed in this context. The assumption allows to define a single Schmidt number in a multi-component flow, according to $Sc = \mu/\rho D$. Substituting this into Eq. 2.3 leads to the simplified species conservation equation which is used in this work:

$$\frac{\partial \rho Y_\alpha}{\partial t} + \frac{\partial \rho Y_\alpha u_j}{\partial x_j} = \frac{\partial}{\partial x_j}\left(\frac{\mu}{Sc}\frac{\partial Y_\alpha}{\partial x_j}\right) + \dot{\omega}_\alpha + \dot{S}_{Y_\alpha} \tag{2.11}$$

Conservation of energy

While the conservation of energy in a fluid flow can be described by various quantities [121], the total enthalpy h of the mixture, defined as the sum of sensible enthalpy h_s and enthalpy of formation h_c, is used in this work. It is defined as:

$$h = h_\mathrm{s} + h_\mathrm{c} = \sum_{\alpha=1}^{N_\mathrm{s}} \int_{T_0}^{T} Y_\alpha c_{p,\alpha} dT + \sum_{\alpha=1}^{N_\mathrm{s}} Y_\alpha \Delta h_{\mathrm{f},\alpha}^\circ \tag{2.12}$$

where $c_{p,\alpha}$ and $\Delta h^{\circ}_{\mathrm{f},\alpha}$ are the specific heat capacity of species α at constant pressure and the formation enthalpy of species α at reference temperature T_0. The transport equation of the total enthalpy reads:

$$\frac{\partial \rho h}{\partial t} + \frac{\partial \rho h u_j}{\partial x_j} = \frac{Dp}{Dt} - \frac{\partial q_j}{\partial x_j} + \tau_{ij}\frac{\partial u_i}{\partial x_j} + \dot{Q}_{\mathrm{rad}} + \rho \sum_{\alpha=1}^{N_{\mathrm{s}}} Y_\alpha f_{\alpha,j} V_{\alpha,j} + \dot{S}_{\mathrm{h}} \tag{2.13}$$

where $f_{\alpha,j}$ are the body force components acting on species α. Assuming a low Mach number Ma flow for the solid fuel combustion investigated in this work, where $Ma = u/c \leq 0.3$ is defined as the ratio between the velocity u and the speed of sound c, yields several simplifications. Assuming negligibly small pressure changes, $\frac{Dp}{Dt}$ is neglected and thus, the density is solely dependent on the thermochemical state, rather than pressure. Additionally, viscous heating and volumetric forces can be neglected. Thus, the simplified energy conservation equation for low Mach numbers reads:

$$\frac{\partial \rho h}{\partial t} + \frac{\partial \rho h u_j}{\partial x_j} = -\frac{\partial q_j}{\partial x_j} + \dot{Q}_{\mathrm{rad}} + \dot{S}_{\mathrm{h}} \tag{2.14}$$

The terms on the RHS denote the enthalpy flux q_j, an additional source term for enthalpy changes due to radiative heat transfer $\dot{Q}_{\mathrm{rad}}$ and an additional source term for the interphase heat transfer between solid and gas phase $\dot{S}_{\mathrm{h}}$. The heat flux can be derived using Fourier's law as:

$$q_j = -\frac{\lambda}{c_p}\frac{\partial h}{\partial x_j} + \sum_{\alpha=1}^{N_{\mathrm{s}}} h_\alpha \frac{\partial Y_\alpha}{\partial x_i}\left(\frac{\lambda}{c_p} - \rho D_\alpha\right) \tag{2.15}$$

where the heat conduction and species diffusion are considered. The last term on the RHS vanishes if the unity Lewis number assumption is valid. Hence, using a unity Lewis number assumption, Eq. 2.16 can be rewritten as:

$$\frac{\partial \rho h}{\partial t} + \frac{\partial \rho h u_j}{\partial x_j} = \frac{\partial}{\partial x_j}\left(\frac{\mu}{Pr}\frac{\partial h}{\partial x_j}\right) + \dot{Q}_{\mathrm{rad}} + \dot{S}_{\mathrm{h}} \tag{2.16}$$

where Pr is the Prandtl number, defined as $Pr = c_p\mu/\lambda$.

Equation of state

As outlined in the previous section, the solid fuel combustion system investigated in this work are operated in the low Mach regime. For this regime, negligibly small pressure changes can be assumed. In order to relate the other state variables, the ideal gas law is used:

$$\rho = \frac{p}{T}\frac{W}{R} \tag{2.17}$$

where R is the universal gas constant. The mean molecular mass W is calculated via Eq. 2.9

2.2 Turbulence

Flows can be distinguished as either laminar or turbulent. The previously introduced governing equations for reacting flows describe both, laminar and turbulent conditions. In a laminar flow, the fluid flows in layers and no cross flows or rotating structures occur perpendicular to the flow direction. Turbulent flows, on the other hand, are characterized by rotating structures, which are also referred to as eddies, varying in size and intensity. Flows in engineering applications are usually turbulent. Especially for combustion applications, the properties of turbulent flows are advantageous. The significantly higher mixing and heat transfer allow a much more compact configuration, which is favorable for the design of burners (or combustors). Osborne Reynolds found that the appearance of turbulence depends on the ratio of inertial (non-linear) forces acting on the flow, to stabilizing viscous (frictional) forces [134]. The ratio is nowadays known as the Reynolds number and can be described by:

$$Re = \frac{\rho u L}{\mu} \tag{2.18}$$

where u and L are a characteristic velocity and length scale, depending on the flow problem. The latter can be e.g., a pipe diameter (used for pipe flows) or the length of a plate (used for free streams). Critical Reynolds numbers define the transitional point, above which inertial forces dominate, causing disturbances and forcing the flow to become turbulent. As mentioned above, turbulent flows are marked by rotating structures or eddies. These can be further characterized by the size of the scales of turbulent motion. Richardson introduced the concept of the energy cascade [136], stating that a turbulent flow is characterized by a large number of eddies of different sizes, while energy is transferred from the larger scales to the smaller scales. These eddies differ in characteristic sizes l, characteristic velocities u and characteristic timescales t. The largest turbulent scale (eddy) is proportional to the flow problem, and thus, depending on the geometry. While turbulent eddies exhibit random and chaotic behavior, the large scales break up into smaller scales and transfer their kinetic energy to the smaller ones. The energy cascade repeats until viscous forces dominate and force the smallest eddies to dissipate completely, and hence, transfer the remaining energy into heat due to molecular friction. The smallest possible scale an eddy can reach before it is dissipated into heat is called Kolmogorov scale η_K. Kolmogorov further developed the concept of the energy cascade [76, 77]. He found that the rate, at which kinetic energy is fed to the largest scales, must be equal to the rate at which the smallest scales dissipate energy into heat. Based on this finding, the Kolmogorov microscales were derived, which read:

$$\eta_\mathrm{K} = \left(\frac{\nu^3}{\epsilon}\right)^{1/4}, \quad \tau_\mathrm{K} = \left(\frac{\nu}{\epsilon}\right)^{1/2}, \quad v_\mathrm{K} = (\nu\epsilon)^{1/4} \tag{2.19}$$

Here, τ_K, v_K and ϵ are the Kolmogorov time scale, the Kolmogorov velocity scale and the dissipation rate, respectively. As the production of kinetic energy through the largest scales dictates the dissipation rate, it can be calculated by the ratio of the energy of the largest eddies u_0^2 and

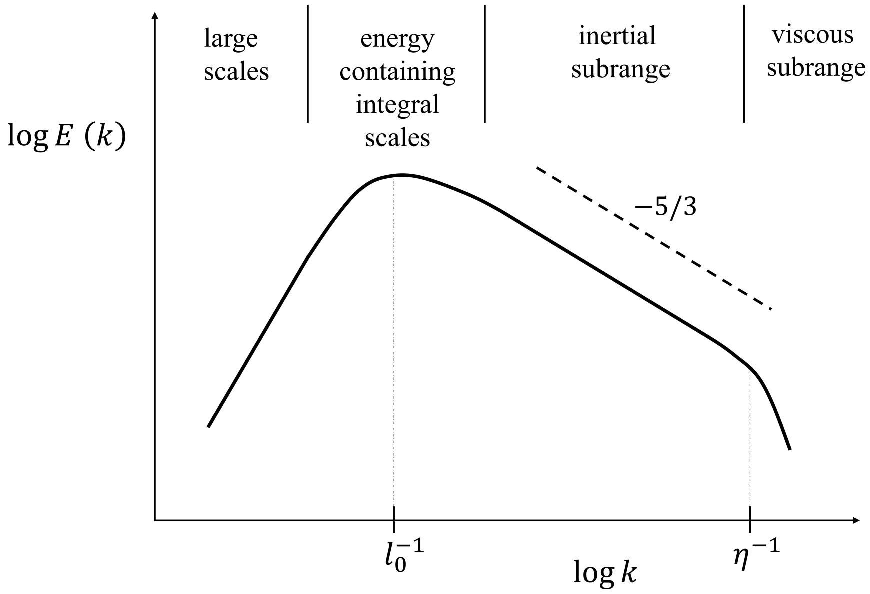

Figure 2.1: Schematic distribution of the turbulent kinetic energy spectrum (as shown by Peters [115]).

the characteristic time $t_0 = l_0/u_0$, where u_0 and l_0 are the length and velocity scale of the largest eddies. The characteristic velocity u_0 is in the same order as the turbulent velocity fluctuation u' of the flow problem. Thus, the dissipation rate reads:

$$\epsilon \sim \frac{u_0^2}{t_0} = \frac{u_0^3}{l_0} \tag{2.20}$$

Using Eq. 2.19, this proportionality can be further derived to:

$$\frac{\eta_\mathrm{K}}{l_0} \sim Re_0^{-3/4} \tag{2.21}$$

where Re_0 is the Reynolds number of the largest turbulent scales.

Figure 2.1 shows the theoretical shape of the resulting energy spectrum, derived by Kolmogorov, showing the turbulent kinetic energy E and the wave number k, defined as $k = 2\pi/l$. The integral length scale l_0^{-1} denotes the wave number, at which the eddies contain the maximum turbulent kinetic energy. Based on the idea that small eddies receive energy from the larger eddies, which is dissipated by viscosity past a certain wave number, two ranges occur, the inertial subrange and the viscous subrange. In the inertial subrange, the turbulent kinetic energy scales with an exponent of $-5/3$. It ends with the wave number reaching the inverse Kolmogorov scale η_K.

2.3 Combustion

Section 2.1 presented the governing equations for the description of reactive and non-reactive fluid flow. However, the concept of combustion has not yet been sufficiently clarified. Combustion can be primarily defined as an exothermic oxidation reaction of fuel and oxidizer. The fuel source can be either gaseous, liquid or solid, while in this work gaseous and solid fuels are investigated. The process of chemical conversion from reactants to products is included in the species conservation equation (Eq. 2.11) through the species source term, which in turn, needs closure. In the context of this work, the source term can be related mainly to exothermic combustion reactions, whereas chemical conversion can also take place through endothermic reactions (occuring e.g., in industrial chemistry or photosynthesis). The conversion of reactants into products usually does not proceed linearly via one global chemical reaction of two species, but rather involves a large number of intermediate elementary reactions and species, which are summarized in detailed reaction mechanisms. If the complexity (and thus the number of species and reactions) of a reaction mechanism increases, e.g., as is the case in the presence of large hydrocarbons, it is suitable to describe its conversion by reduced reaction mechanisms, considering only the most important species and reaction pathways. The following section will introduce the reaction kinetics, followed by the reaction mechanisms used in this work. Subsequently, the different modes of combustion are briefly outlined.

2.3.1 Chemical kinetics

A chemical reaction occurs, if species collide, breaking molecular bonds and forming new species. The chemical conversion of two species A_2 and B_2 into $2AB$ can be simplified as:

$$A_2 + B_2 \rightleftharpoons 2AB \tag{2.22}$$

where the arrows denote forward- and backward reactions of A_2 and B_2 into $2AB$ and vice versa. However, reactants are usually not converted directly into products by a single collision of the respective species, resulting in a number of intermediate species and intermediate reactions. A reaction system with a number of N_r reactions and N_s species occurs, which can be generalized by its stoichiometric equation:

$$\sum_{\alpha=1}^{N_\mathrm{s}} v'_{\alpha\gamma}\chi_\alpha \rightleftharpoons \sum_{\alpha=1}^{N_\mathrm{s}} v''_{\alpha\gamma}\chi_\alpha, \quad \gamma = 1...N_\mathrm{r} \tag{2.23}$$

Here, $v'_{\alpha\gamma}$, $v''_{\alpha\gamma}$ and χ_α denote the molar stoichiometric coefficients of the reactants and the products for species α and reaction γ, while χ_α describes the chemical species symbol of α. The reaction rate of a reaction γ can be expressed as the net rate of its forward- and backward reaction rates:

$$q_\gamma = k_{\mathrm{f},\gamma} \prod_{\alpha=1}^{N_\mathrm{s}} (c_\alpha)^{v'_{\alpha\gamma}} - k_{\mathrm{b},\gamma} \prod_{\alpha=1}^{N_\mathrm{s}} (c_\alpha)^{v''_{\alpha\gamma}} \tag{2.24}$$

where the first and second term on the RHS refer to the forward- and backward reaction rates, with $k_{\mathrm{f},\gamma}$ and $k_{\mathrm{b},\gamma}$ being the associated specific rate constants and $c_\alpha = \rho Y_\alpha / W_\alpha$ being the molar species concentration, respectively. The specific rate constants k_γ can be calculated using an Arrhenius expression:

$$k_\gamma = A_\gamma T^{n_\gamma}\, e^{\left(-\frac{E_{\mathrm{A},\gamma}}{R_\mathrm{u} T}\right)} \tag{2.25}$$

where A_γ, $E_{\mathrm{A},\gamma}$, and n_γ are the pre-exponential factor, the activation energy, and the temperature exponent. The equilibrium constant $K_\gamma = k_{\mathrm{f},\gamma}/k_{\mathrm{b},\gamma}$ relates the forward- and backward specific rate constants. The required source term $\dot{\omega}_\alpha$ of Eq. 2.11 can be derived from the summation over all reactions as:

$$\dot{\omega}_\alpha = \sum_{\gamma=1}^{N_\mathrm{r}} \dot{\omega}_{\gamma,\alpha} = W_\alpha \sum_{\gamma=1}^{N_\mathrm{r}} (v''_{\alpha\gamma} - v'_{\alpha\gamma}) q_\gamma \tag{2.26}$$

Depending on the complexity of the fuel, the respective reaction mechanism can easily cover several thousand reactions and hundreds of species. For each reaction, the individual specific rate constant k_γ must be calculated, making its direct use for the detailed description of the combustion process computationally expensive. Thus, reduced mechanisms are developed, covering only major species and reactions in a specific range of temperature and pressure, and simpler models are used to describe the combustion process. These detailed reaction pathways or specially reduced mechanisms are required for a detailed pollutant prediction.

Reduced reaction mechanisms

In this work, four reduced chemical reaction mechanisms are used:

1. A mechanism for pulverized coal flames by Tufano et al. [132, 170] (52 species, 452 reactions)

2. A mechanism for pulverized coal flames including the most important $\mathrm{NO_x}$ formation mechanisms (prompt-, thermal-, fuel-$\mathrm{NO_x}$, and the via $\mathrm{N_2O}$ pathway) by Shamooni et al. [145] (120 species, 1551 reactions)

3. A mechanism for pure ammonia flames by the Chemical Reaction Engineering and Chemical Kinetics Lab (CRECK) modeling group [157, 159] (31 species, 203 reactions)

4. A mechanism for the co-firing of coal and ammonia including the most import $\mathrm{NO_x}$ formation mechanisms by Meller et al. [97] (129 species, 1664 reactions)

2.3.2 Combustion modes

Combustion can be classified into two idealized regimes: premixed and non-premixed. Premixed combustion describes a homogeneous premixing of fuel and oxidizer before ignition takes place, whereas in non-premixed combustion, fuel and oxidizer are fed separately to the reaction zone. Classic configurations for both regimes are illustrated in Fig. 2.2, showing a flat flame (premixed) and a counterflow flame configuration (non-premixed). In real applications, perfectly premixed, or perfectly non-premixed combustions rarely occur, as either the separately supplied fuel and oxidizer streams partially mix before ignition or the premixed mixture is not homogeneously mixed. In this case, the combustion is referred to as partially premixed combustion. However, the regimes of premixed and non-premixed combustion shall be discussed briefly in the following sections.

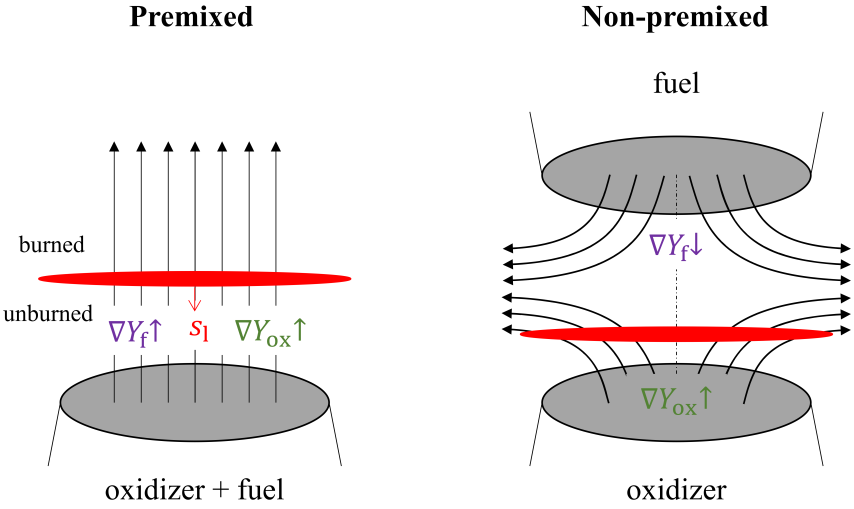

Figure 2.2: Illustration of a premixed flame (left) and a non-premixed flame configuration (right). ∇Y_f and ∇Y_ox denote the mixture fraction gradients of fuel (f) and oxidizer (ox).

Premixed combustion

As stated above, in premixed combustion, both, fuel and oxidizer are homogeneously mixed in advance before ignition. A flame thereby only forms if the mixture lies within the flammability limit. When both, the oxidizer and fuel undergo complete conversion in a chemical reaction, it is characterized as a stoichiometric mixture. In such cases, the reactants are consumed entirely, aligning precisely with the balanced chemical equation, without any excess of either component. In contrast, a mixture is called lean if there is an excess of oxidizer in the mixture and thus, oxygen is present in the exhaust gas. A rich mixture, on the other hand, has an insufficient amount of oxygen in the unburned mixture for a complete conversion, resulting in fuel still being present in the exhaust gas. An important quantity describing this relationship is the equivalence ratio, which reads:

$$\Phi = \frac{(Y_\mathrm{f}/Y_\mathrm{ox})_\mathrm{u}}{(Y_\mathrm{f}/Y_\mathrm{ox})_\mathrm{u,st}} \tag{2.27}$$

It relates the present ratio of the mixture fractions of fuel Y_f and oxidizer Y_ox in the unburned state (subscript u) to the ratio at stoichiometric conditions (subscript st). By definition, $\Phi > 1$, if the mixture is rich, $\Phi < 1$, if the mixture is lean, and $\Phi = 1$, if the mixture is stoichiometric. The flame front in a premixed combustion always propagates towards the unburned mixture. An important quantity for the characterization of premixed flames is hence the laminar flame speed s_l at which the flame front propagates, and which can nowadays directly be computed from one-dimensional flames using specialized reaction kinetic libraries, e.g., the Cantera software [41]. The laminar flame speed depends on the unburned mixture composition, its temperature and pressure. Another important quantity for premixed flames is the laminar flame thickness δ_l, for which different definitions exist [121]. An often used definition is the thermal flame thickness δ_th, relating the difference of the temperatures at a burned (b) and unburned (u) state to its maximum gradient, which reads:

$$\delta_\mathrm{th} = \frac{T_\mathrm{b} - T_\mathrm{u}}{\max|\frac{\partial T}{\partial x}|} \tag{2.28}$$

Here, the flame thickness is calculated using a one-dimensional (1D) temperature profile. The structure of a laminar premixed flame is marked by three regions, a preheat zone, where fuel and oxidizer are preheated, a reaction zone, where the predominant chemical conversion occurs, and a post-oxidation zone, where radicals recombine and slow species are formed until chemical equilibrium is achieved. The chemical reaction progress in a premixed flame can be described through a progress variable Y_p, which ranges from zero (for unburned reactants) to unity (for fully burned products). The progress variable has no unique definition and must be defined case-specifically. One criterion to be fulfilled is the monotonicity in the entire flame. The most common definition is a linear combination of different product species mass fractions, which is also used in this work. The general expression of the progress variable Y_p definition then reads:

$$Y_\mathrm{p} = \sum b_\alpha Y_\alpha \tag{2.29}$$

Here, b_α is a weighting factor for species α, which is used to better account for relevant small concentration products in the exhaust gas; e.g., for pulverized coal flames, a factor of 10 is often used for NO species to better account for $\mathrm{NO_x}$ formation in the definition of Y_p; see, i.e., the parameter study by Luo et al. [88]. It should be noted that, for a complex, multi-fuel stream problem, the definition of Y_p should include products of each respective fuel source. For most large hydrocarbon fuels, a linear combination of species mass fractions $\mathrm{CO_2}$, CO, and $\mathrm{H_2O}$ is sufficient. From the definition of the progress variable, a normalized progress variable c (or $Y_\mathrm{p,norm}$) can be derived, which reads:

$$c = \frac{Y_\mathrm{p} - Y_\mathrm{p}^\mathrm{u}}{Y_\mathrm{p}^\mathrm{b} - Y_\mathrm{p}^\mathrm{u}} \tag{2.30}$$

Again, superscript b and u denote the burned and unburned state, respectively.

Non-premixed combustion

In non-premixed combustion, the introduction of fuel and oxidizer occurs separately, leading to the formation of a reaction zone where the two streams interact. Within this zone, chemical conversion takes place on a significantly smaller time scale compared to the mixing of oxidizer and fuel. Consequently, the combustion rate of a non-premixed flame is diffusion-dependent, lacking self-induced propagation and a characteristic flame speed, as typically found in premixed combustion. Unlike premixed flames, which possess a well-defined characteristic flame thickness, non-premixed combustion exhibits a flame thickness that relies solely on the stretch and strain induced by the local flow conditions of oxidizer and fuel. When the local flow velocity exceeds a critical value, quenching can occur due to the inadequate heat release of the combustion compared to the heat transported away from the reaction front. Given the diffusion-dependent nature of the flame burning rate, the problem can be simplified to a mixing problem, where the focus shifts to understanding and analyzing the mixing processes involved. Thus, a mixture fraction Z, describing the mixture of fuel (f) and oxidizer (ox) in a specific volume, can be derived [115]:

$$Z = \frac{m_\mathrm{f}}{m_\mathrm{f} + m_\mathrm{ox}} \tag{2.31}$$

where m_f and m_ox are the masses of fuel and oxidizer. The mixture fraction is zero for the pure oxidizer ($Z = 0$) and unity for pure fuel ($Z = 1$). In the context of the mixture fraction, it is important to acknowledge the challenge of accurately determining the mass of species involved due to their varying composition during the reaction. To address this limitation and provide a more general formulation, an alternative approach relates the mixture fraction to the chemical elements present in the system, as their mass is conserved throughout the reaction. The mass fraction Z_j of element j can be derived, as [115]:

$$Z_j = \sum_{\alpha}^{N_\mathrm{s}} \frac{a_{\alpha j} W_j}{W_\alpha} Y_\alpha \tag{2.32}$$

Here, $a_{\alpha j}$ describes the number of all elements j in a molecule of species α. For hydrocarbon fuels ($\mathrm{C}_m\mathrm{H}_n$), Bilger [10] introduced a mixture fraction definition that incorporates the mass fractions of elemental carbon (Z_C), hydrogen (Z_H), and oxygen (Z_O). This formulation provides a more comprehensive representation of the mixture composition by considering the individual elemental contributions of the fuel components. It reads:

$$Z = \frac{Z_\mathrm{C}/(mW_\mathrm{C}) + Z_\mathrm{H}/(nW_\mathrm{H}) + 2(Y_{\mathrm{O_2,ox}} - Z_\mathrm{O})/(\nu'_{\mathrm{O_2}} W_{\mathrm{O_2}})}{Z_\mathrm{C,f}/(mW_\mathrm{C}) + Z_\mathrm{H,f}/(nW_\mathrm{H}) + 2Y_{\mathrm{O_2,ox}}/(\nu'_{\mathrm{O_2}} W_{\mathrm{O_2}})} \tag{2.33}$$

The aforementioned formula can be obtained through numerical simulations or experimental measurements of mass fractions. Instead of directly solving the equation, typically necessitating a direct numerical simulation (DNS) with detailed chemistry for turbulent flows, it is common in CFD to employ a transport equation for the mixture fraction Z to characterize the mixing phenomena within the system. It reads:

$$\frac{\partial \rho Z}{\partial t} + \frac{\partial \rho u_j Z}{\partial x_j} = \frac{\partial}{\partial x_j}\left(\rho D \frac{\partial Z}{\partial x_j}\right) \tag{2.34}$$

Again, the unity Lewis number assumption applies for all species.

2.4 Pulverized coal combustion (PCC)

In the following section, the theoretical basics of pulverized coal combustion shall be discussed. Since the coal composition varies depending on its source, the characterization of coal will be discussed first. The crucial processes describing coal conversion are devolatilization and volatile combustion (also known als pyrolysis), as well as char burnout. These processes are described subsequently. A description of the numerical modeling is given in section 3.4.

2.4.1 Coal characterization

Given the abundant presence of coal worldwide, efforts have been made to characterize ("rank") different coals in terms of specific similarities (e.g. volatile matter, moisture content, total carbon content, specific energy, burnout characteristics, etc.). While several systems for a general classification of coal exist [155], the simplest and one of the most used methodologies to classify coal is the definition of a coal rank based on its age and hence the maturity of the coal. A schematic representation of this classification is given in the often used van Krevelen diagram [175], shown in Fig. 2.3. Van Krevelen has mapped various samples of coals and biomasses with respect to the atomic ratios of H/C and O/C, excluding moisture and ash. Coal is formed by the coalification of plant biomass over a period of millions of years. The longer the coalification process continues, the lower the oxygen (O) and hydrogen (H) content in the coal becomes. As a result, the relative proportion of pure carbon (C) increases, reaching (almost) 100 % in pure graphite. A low rank refers to coal with a relatively high oxygen and hydrogen content (upper right direction in

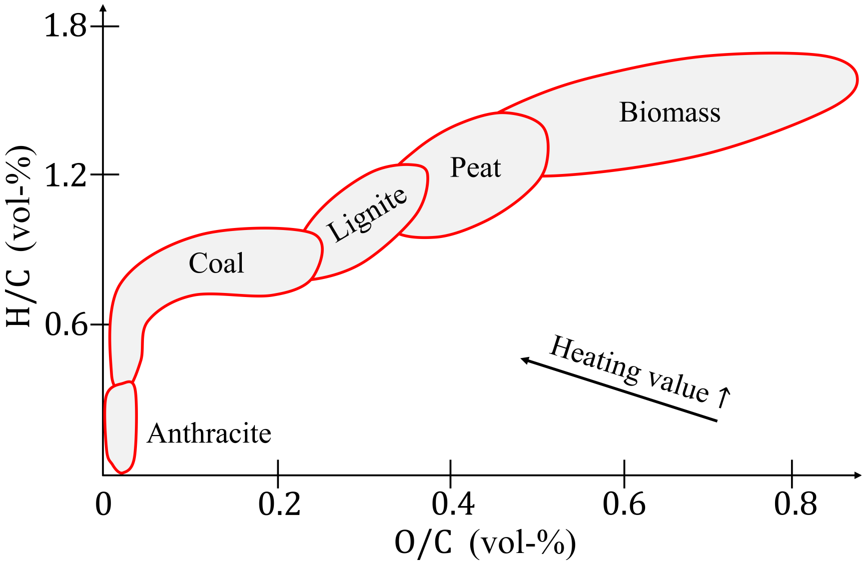

Figure 2.3: Van Krevelen diagram for different solid fuels. Adapted from [127].

Fig. 2.3). A high coal rank, on the other hand, characterizes a relatively high carbon content. The rank in Fig. 2.3 increases towards the origin; the origin corresponds to pure graphite. From a low rank to a high rank, the known coals can be classified as [198]: lignite, sub-bituminous coal, bituminous coal, semi-bituminous coal, and anthracite. The coal classification into different ranks gives only a brief overview of its composition; further physical and chemical properties are required for the modeling of its conversion processes. Thus, the coal composition is described via proximate and ultimate analyses, which shall be described next.

Proximate analysis

The proximate analysis gives the mass-weighted proportions of moisture, ash, volatiles, and fixed carbon in the coal. Proximate analysis is performed under standardized tests that ensure the same conditions for different coals [108]. As the moisture concentration in coal increases, the heat of combustion decreases (see Fig. 2.3). Ash is typically attributed to calcium and magnesium carbonates, alkali chlorides, iron pyrites or hydrated alumina silicates [198]. High moisture and ash contents decrease the rank of the coal, as both materials are referred to as non-combustible. The volatile matter and the amount of fixed carbon represent the combustible materials. The volatile gas is released after the coal particle is heated up; it usually consists of carbon monoxide, carbon dioxide, methane, water, alkanes, and alkenes. Its accurate description is of high importance in the modeling of coal conversion and will be further discussed in section 3.4.1. The rank of coal usually decreases as the volatile content increases. After evaporation and devolatilization, the coal residue consists only of ash and fixed carbon. The latter is subsequently oxidized through char burnout reactions. As shown in Fig. 2.3, the coal rank increases with increasing fixed carbon content.

Ultimate analysis

The ultimate analysis gives the mass-weighted amounts of carbon (C), hydrogen (H), nitrogen (N), sulphur (S), and oxygen (O) in the coal type being analyzed. The analysis only considers the combustible constituents of the coal. In this context, the term dry and ash-free basis (*daf*) is often used, referring to the elemental composition of coal without the influence of moisture and inorganic ash.

Coal properties

In addition to the atomic proportions of the various elements mentioned above, the higher heating value (HHV) - also known as gross calorific value (GCV) - or the lower heating value (LHV) - also known as net calorific value (NCV) - is often given. The HHV thereby indicates the amount of heat released during the combustion of the fuel, assuming that the products have reached ambient conditions ($T = 25\,^{\circ}\mathrm{C}$) again. The LHV takes into account the heat that is released, assuming that the products have reached a temperature at which the water vapor remains in the gaseous state (typically around $T \sim 105\,^{\circ}\mathrm{C}$).

The HHV, compared to the LHV, therefore includes the latent heat of the water in the products, that is released by vaporization. The HHV of coals varies between $\sim 25\,\mathrm{MJ/kg}$ for lower ranks and $\sim 30-37\,\mathrm{MJ/kg}$ for higher ranks [198].

As coal is a porous medium, two types of coal particle density must be distinguished, the true density $\rho_{\mathrm{p,true}}$ and the bulk density $\rho_{\mathrm{p,bulk}}$. While the true density refers to the density of a pore free particle, the bulk density $\rho_{\mathrm{p,bulk}}$ considers the pores inside a coal particle. The latter is used in this work, it will be referred to as the particle density ρ_{p} in the subsequent text. The porosity of a coal particle is derived by the ratio of both quantities to:

$$\theta_{\mathrm{p}} = 1 - \frac{\rho_{\mathrm{p,bulk}}}{\rho_{\mathrm{p,true}}} \tag{2.35}$$

Merrick's approach [98] allows the determination of the true density of a coal particle on a *daf* basis, using:

$$\frac{1}{\rho_{\mathrm{p,true},daf}} = \sum_{\alpha=1}^{5} m_{e,\alpha} \frac{Y_{\mathrm{p},\alpha}}{A_{w,\alpha}} \tag{2.36}$$

where $Y_{\mathrm{p},\alpha}$ are the respective elemental mass fractions from the ultimate analysis with $\alpha \in \{\mathrm{C, H, N, S, O}\}$, and $A_{w,\alpha}$ are the atomic weights of the respective elements. The elemental coefficients $m_{e,\alpha}$ are taken from [98] and were originally determined via linear regression analysis on data from literature. The bulk density is obtained experimentally, usually ranging from $1000-1500$ kg/m^3 for coal particles. For the coals used in this work, an initial particle density of $\rho_{\mathrm{p}} = 1100\,\mathrm{kg/m^3}$ is assumed. The particle density is changed initially due to the release of volatile matter during the devolatilization step. In this process, the particle diameter is assumed to be constant. However, in the subsequent process during char combustion, the particle density is assumed to stay constant, while the particle diameter is decreasing. Apart from that, the particle size may change due to particle swelling, which varies for different coal types. In this study, particle swelling is neglected, although models exist that address it (e.g. [146, 147]). In fact, the impact of particle swelling and shrinkage on gas phase quantities was found to be insignificant according to Muto et al. [103], while Attili et al. [6] noted only a minor effect on small particles and no effect on large particles.

To correctly predict particle heat up and heat exchange with the gas phase, it is of great importance to accurately determine the particle's specific heat capacity $c_{p,\mathrm{p}}$. In this work, the method by Merrick [98] and Brewster et al. [16] is used, following the approach by Stöllinger et al. [163], assuming that the heat capacity of coal only depends on the composition of volatiles, char and ash. The particle's heat capacity is then computed via Eq. 2.37:

$$c_{p,\mathrm{p}} = Y_{\mathrm{p,VM}}\, c_{p,\mathrm{VM}} + Y_{\mathrm{p,FC}}\, c_{p,\mathrm{FC}} + Y_{\mathrm{p,ash}}\, c_{p,\mathrm{ash}} \tag{2.37}$$

where $Y_{\mathrm{p,VM}}$, $Y_{\mathrm{p,FC}}$, and $Y_{\mathrm{p,ash}}$ are the respective particle mass fractions of volatile matter, fixed carbon and ash, and $c_{p,\mathrm{VM}}$, $c_{p,\mathrm{FC}}$, and $c_{p,\mathrm{ash}}$ are the corresponding heat capacities. The heat capacity of ash in J/(kg K) is calculated as:

$$c_{p,\mathrm{ash}} = 539.9 + 0.586\, T_{\mathrm{p}} \tag{2.38}$$

where T_{p} is the particle temperature. The heat capacities of volatile matter (VM) and fixed carbon (FC) are then calculated as:

$$c_{p,\alpha} = \frac{R_{\mathrm{u}}}{W_\alpha}\left[g_1\left(\frac{380}{T_{\mathrm{p}}}\right) + 2\,g_1\left(\frac{1800}{T_{\mathrm{p}}}\right)\right] \tag{2.39}$$

where $\alpha \in \{\mathrm{VM,\ FC}\}$, W_α is the respective mean atomic weight, and $g_1(x)$ is calculated as $g_1(x) = e^x / \left(\frac{e^x - 1^2}{x}\right)$.

In this work, two different coals are investigated, “Coal 5” [1] and a high volatile bituminous “Blind Canyon” [25] coal. The proximate and ultimate analyses are given in Table 2.1.

Table 2.1: Properties of “Coal 5” [1] and the high bituminous “Blind Canyon” coal [25], showing proximate analysis (PA) and ultimate analysis (UA) on a dry and ash-free (*daf*) basis.

“Coal 5” [1]				“Blind Canyon” [25]			
PA [wt%]		UA [wt%]		PA [wt%]		UA [wt%]	
Ash	14.2	C	70.30	Ash	7.89	C	74.8
Volatiles	32.6	H	4.57	Volatiles	40.6	H	5.08
Fixed carbon	52.4	N	1.66	Fixed carbon	51.5	N	1.53
Moisture	0.8	S	0.45	Moisture	2.1	S	0.58
		O	8.78			O	10.1

2.4.2 Coal conversion processes

As indicated in the previous sections, two processes are the main driving forces during coal conversion, the pyrolysis (also known as devolatilization) step, and the char combustion step. Upon heating coal particles, the thermal energy causes the disruption of chemical bonds within the coal’s molecular structure. Consequently, the broken molecular structures are released into the gas phase as volatile gases, consisting of both, light gases and tars. The volatile composition varies depending on the coal type and its modeling will be further discussed in section 3.4.1. This step is referred to as pyrolysis or devolatilization step. In burner configurations, the coal particles experience typical heating rates of $10^4 - 10^5\,\mathrm{K/s}$ [198]. The early stages of PCC are driven by pyrolysis and the subsequent volatile combustion. The rapid volatile combustion causes a strong temperature increase and is a crucial sub-process for flame stabilization and the subsequent occuring char combustion. After the majority of the volatiles are released, the char combustion starts simultaneously to the devolatilization. This process takes place at a significantly slower conversion rate, resulting in a significant time difference between the two processes. The conversion of char is described by heterogeneous surface reactions, caused by the diffusion of oxidizer from the ambient gas into the porous surface structure of the coal particle. Thus, the rate at which char is converted not only depends on the porosity of the particles and the composition of the coal, but, in particular, on the surrounding gas. After the complete burnout of the char particle, ash remains. Ash has a minor impact on the coal combustion process itself and is therefore often neglected in the modeling, but should be mentioned for the sake of completeness due to its negative effects in industrial applications (e.g., fouling of attached heat exchanger surfaces through catalysis, induced by the mineral content in the ash). If the moisture content in the proximate analysis is significant, evaporation must be considered in the modeling, which is often specified as the first of three coal conversion steps. Considering the very low moisture content of the coals investigated (see Tab. 2.1), the modeling of evaporation is neglected and will not be further discussed in this work. Finally, the total mass loss rate of the coal particles $\frac{dm_{\mathrm{p}}}{dt}$ can be described by the previously mentioned processes to:

$$\frac{dm_{\mathrm{p}}}{dt} = \cancel{-\dot{m}_{\mathrm{p,evap}}} - \dot{m}_{\mathrm{p,vol}} - \dot{m}_{\mathrm{p,char}} \tag{2.40}$$

where $\dot{m}_{\mathrm{p,evap}}$, $\dot{m}_{\mathrm{p,vol}}$, and $\dot{m}_{\mathrm{p,char}}$ are the neglected drying rate due to evaporation and the mass losses due to devolatilization and char combustion. The total mass released from the coal particle is subsequently added to the gas phase as a source term in Eq. 2.2.

In the following sections, the underlying physical and chemical phenomena of pyrolysis (devolatilization) and char combustion will be briefly discussed. Their modeling approaches will be outlined in section 3.4.

Pyrolysis

Once coal particles are heated, the pyrolysis or devolatilization process begins and volatile gases are released into the gas phase, consisting of light gases and heavy tars. A distinction is made between two stages of pyrolysis, the primary and secondary pyrolysis [47]. During primary pyrolysis, chemical bonds in the macromolecular coal structure break and new molecular fragments form. At the beginning of the heating process, lighter volatiles are emitted from the coal, and as the temperature increases, aromatic rings within the coal structure start to break apart. Subsequently, heavier volatiles, including large hydrocarbons and tars, are released. The majority of these volatiles enter the surrounding gas phase directly. Meanwhile, as the char structure forms and establishes new stable bonds, smaller fragments become trapped within it, which may also form new bonds with the solid material. The volatile composition primarily consists of the species CO, CO_2, H_2O, light hydrocarbons (H_2 and CH_4), heavy hydrocarbons and tars [155]. Accordingly, secondary pyrolysis describes the decomposition of volatile gas with the surrounding gas and depends primarily on environmental factors, such as the ambient gas composition and the temperature. To summarize, primary pyrolysis dictates the volatile composition of a coal, its devolatilization rates and how much total volatile gas yield is released, while secondary pyrolysis determines the volatile species after decomposition under different atmospheres. Although the proximate analysis gives a yield of the volatile matter, the actual volatile yield in a PCC burner can strongly deviate from it. Badzioch and Hawksley [8] measured the actual volatile yield of various coals under high heating rates and compared it to the proximate analysis of the respective coal. They found that high temperatures can cause more carbon to be released, increasing the amount of carbon in the volatile yield. As a result, both, the total amount of volatile gas and the volatile composition are affected. A parameter that describes the deviation between actual volatile matter under high heating rates $Y_{\mathrm{p,VM}}$ and the measured volatile matter of the proximate analysis under standard conditions $Y_{\mathrm{p,VM,prox}}$ is the Q-factor, which reads:

$$Q = \frac{Y_{\mathrm{p,VM}}}{Y_{\mathrm{p,VM,prox}}} \tag{2.41}$$

The Q-factor strongly depends on the heating rates and thus, the burner configuration, as well as the coal properties. Q-factors up to 2.0 can occur [155], however, the Q-factor in experimental flames and burners usually ranges between $1.0-1.7$. In the modeling, a single Q-factor is typically used for all particles.

The correct modeling of volatile release rates, as well as the modeling of volatile compositions is of high importance for the accurate prediction of PCC in numerical simulations. Modeling approaches for volatile release rates and volatile compositions will be further discussed in section 3.4.

Char conversion

Char conversion takes place predominantly after the primary pyrolysis, however, it can also occur simultaneously to the pyrolysis. Char represents the remaining coal particle after all volatiles have been released. Its composition consists largely of carbon and a minor amount of mineral matter (ash). Char conversion happens on a time scale that is at least one order of magnitude slower than pyrolysis, and thus, dictates the time needed for complete coal conversion. For technical applications, it is economically desirable to reach a conversion rate of at least 99.5 % [52]. Thus, the fundamental processes involved in char conversion need to be discussed. This section is mainly based on the description by Hasse et al. [47].

Although char conversion is usually modeled separately from pyrolysis, it is strongly dependent on the prior pyrolysis, as the char structure is being formed in this step already. A transition process that can occur at high temperatures and depends on the temperature evolution of pyrolysis is the char thermal annealing, in which the char matrix is restructured, the porosity is reduced, and a decrease in the char reactivity is caused by the reduction of the specific surface area of the char particle.

Char conversion depends on heterogeneous surface reactions on the porous char particle, hence, an important parameter is the intrinsic (inner) surface area of the particle. Smoot and Smith [79] classified the conversion of char into three zones (nowadays known as the idealized "three-zones" theory), which are schematically illustrated in Fig. 2.4. It should be noted that the model illustrates an idealized char conversion process, which in reality, usually does not occur. Although in reality additional transition zones exist, these are typically neglected in the modeling. The first zone represents the kinetic regime, in which at low temperatures, the char conversion rate is dictated by reaction kinetics alone. The reaction rate at the char surface is slow compared to the species transport of the surrounding oxidizing gases to the char particle. As a result, a uniform concentration profile evolves inside the particle. The second zone refers to the pore diffusion regime. In this zone, the mean temperature increases and consequently, the chemical reaction rate substantially increases. The reaction rate is now predominantly limited by both, chemical reaction and pore diffusion processes. With increasing temperature, the chemical time scales become faster. The diffusion time scales into the porous char particle are now slower, thus, a radial concentration gradient of the reactive species is formed inside the particle. In the third zone, the film diffusion regime, film diffusion controls the char reaction rate. High temperatures are present, causing the reaction kinetics to become faster than the transport from the bulk particle to the outer particle surface. Heterogeneous surface reactions convert all reactants immediately, and the concentration of reactive species in the porous particle drops to nearly zero. A concentration gradient of reactive species is formed mainly in the particle boundary layer, hence, this zone is particularly affected by particle-gas interactions. To determine the correct regime, not only the temperature, but also the particle size is a determining factor. In summary, the char conversion process is dominated by either chemistry or transport phenomena, which need to be considered in the modeling approach.

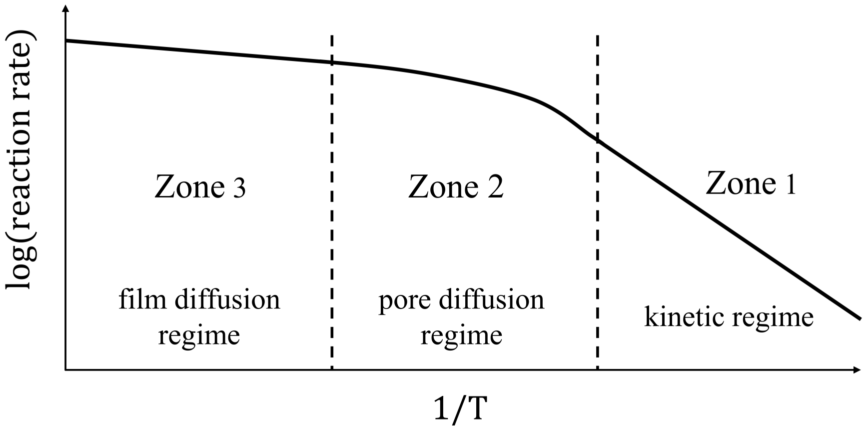

Figure 2.4: Three-Zones model for char conversion, showing the rate controlling regimes. Adapted from [79].

Chapter 3

Modeling of reactive solid fuel systems

In the present chapter, the modeling strategies used to describe reactive solid fuel systems are presented. Initially, the modeling approaches for turbulent flows are discussed, and an overview of the most commonly utilized paradigms is provided. Subsequently, the models utilized to describe combustion in the gas phase are explained, followed by an explanation of the models used to represent coal conversion. Finally, the models applied to describe the dispersed phase are presented, highlighting the coupling strategies employed for both, the solid and gas phases.

3.1 Turbulent flow modeling

The Navier-Stokes equations introduced in chapter 2 can be utilized to describe reactive and non-reactive turbulent flows, assuming appropriate initial and boundary conditions. Numerical methods are widely used in this context, since analytical solutions typically require strong assumptions and are only possible for very simple flow problems. To solve a flow problem numerically, the investigated domain can be divided (discretized) into finite volumes, allowing to solve the governing equations for each of these volumes in time and space. The discretized grid is considered to be Cartesian and equidistant with a cell width of Δ in all directions. A detailed description of the numerical methods and discretization schemes will be given in section 4. To resolve all scales of a turbulent flow problem, the discretized cell width must be smaller than the smallest occurring scale, the Kolmogorov scale η_K (Eq. 2.19), hence $\Delta < \eta_\mathrm{K}$. In this case, the simulation requires no further modeling and is termed a direct numerical simulation (DNS). However, the resolution of all turbulent scales is accompanied by significant computational costs, which increase drastically for high Reynolds numbers and thus, very small Kolmogorov scales. This makes the DNS of technical applications with typically high Reynolds numbers often unfeasible. As a result of this dilemma, several simulation strategies have emerged that resolve and model different contributions of the turbulent kinetic energy spectrum, allowing larger grid sizes with reduced computational costs.

The three most commonly used paradigms and their resolved and modeled contributions of the turbulent kinetic energy spectrum are shown in Fig. 3.1. Together with the DNS, the Reynolds-averaged Navier-Stokes (RANS) simulation and the large eddy simulation (LES) have become the standard approaches for simulating turbulent flows. RANS simulations model most of the turbulent kinetic energy by resolving only time-averaged quantities and using a modeled viscosity

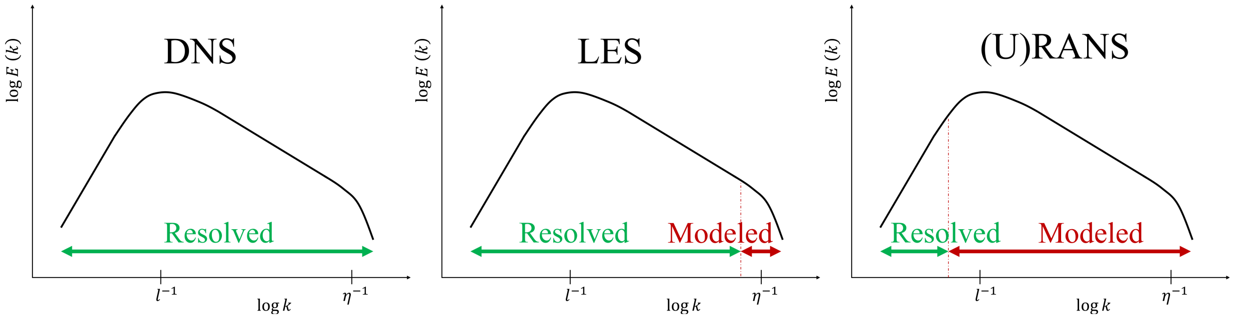

Figure 3.1: Schematic distribution of the resolved and modeled turbulent kinetic energy spectrum for the three paradigms DNS, LES, and (unsteady) RANS simulation.

for incorporating the effect of turbulence on the flow field. In contrast, LES lies between DNS and RANS simulation, by resolving most of the energy-carrying scales and modeling only the smallest, dissipative scales, which are assumed to be isotropic. Generally, a larger modeled part of the turbulent scales allows the use of larger cell sizes and thus, leads to lowered computational costs. In the ensuing content, all three paradigms shall be explained in further detail.

3.1.1 Direct numerical simulation (DNS)

In DNS, all turbulent scales of the flow problem are resolved, thus, no further turbulence modeling is required when solving the governing conservation equations (Eqs. 2.2, 2.3, 2.11, and 2.16). Therefore, DNS provides the most accurate, albeit the computationally most expensive simulation approach. Assuming, that the Kolmogorov length scale η_{K} is the smallest possible scale occuring in the flow problem - it must be noted that other scales may be even smaller (e.g., accurate resolution of the flame front, mixing length scale or particle boundary layers) - the discretized cell width Δ must not exceed this length scale. Given this condition, the computational cost scales with the separation of the smallest scales and hence, the Reynolds number. Considering the proportionality of the largest turbulent scale and the smallest possible scale (Kolmogorov scale), given in Eq. 2.23, the number of cells in each direction must be $N_i = l_0/\eta_{\mathrm{K}}$, leading to a total required mesh resolution N_{DNS} for a three-dimensional (3D) DNS of:

$$N_{\mathrm{DNS}} > \left(\frac{l_0}{\eta_{\mathrm{K}}}\right)^3 \sim Re_0^{9/4} \tag{3.1}$$

If the smallest turbulent scales are to be discretized with equal accuracy both, spatially and temporally, and assuming a proportional behavior of the time step width Δt and the grid size, the computational effort results to [36]:

$$t_{\mathrm{CPU}} \sim Re_0^3 \tag{3.2}$$

From Equation 3.2, it can be seen that DNS is simply not applicable to most technical flows, where high Reynolds numbers occur. However, DNS serves as a great tool for fundamental research. DNS is a crucial reference for validating and refining models for application in e.g. LES or RANS, helping to improve their accuracy and predictive capabilities. The information derived from DNS studies aids in advancing the understanding of turbulence modeling and enhances the accuracy and reliability of simulations used in practical applications across various fields.

3.1.2 Reynolds-averaged Navier-Stokes (RANS) simulation

In RANS, a Reynolds decomposition into a mean $\overline{\phi}$ and a fluctuating component ϕ' is applied to the governing Navier-Stokes equations. For an arbitrary quantity ϕ, it would read:

$$\phi(t) = \overline{\phi} + \phi'(t) \tag{3.3}$$

Known as Reynolds-averaging, this leads to the solution of a time-averaged quantity $\overline{\phi}$. The classical RANS simulation therefore calculates only the time-averaged mean flow field for the given problem. Mathematically, the Reynolds-averaging results in unclosed terms in the governing equations, requiring adequate modeling. For the momentum equation, the so-called Reynolds stresses $\overline{u_i'u_j'}$, and for the conservation equations for species and enthalpy, turbulent scalar fluxes $\overline{u_i'\phi'}$ appear. A common method to close these equations is the Boussinesq approximation, which describes the unresolved means by a turbulent viscosity μ_{t}, assuming, that energy is only transferred from resolved to unresolved scales [197]. A suitable modeling of the viscosity term is required for an accurate representation of the flow field. Among the most commonly used models, algebraic models (e.g. Prandtl's mixing length model [125]), one-equation models (e.g. the Prandtl - Kolmogorov model [126]), and two equation models (e.g. one of the most popular, the k-ϵ model

[80]) shall be mentioned. In Prandtl's mixing length model, the integral length scale is used to calculate μ_t, while in the one-equation model, an additional transport equation for the turbulent kinetic energy k is solved to derive μ_t. Two-equation models solve two additional equations as the name implies, which are subsequently used to derive μ_t. Most common are the equations for the turbulent kinetic energy k and the dissipation rate ϵ. Besides classical RANS models, which describe the time-averaged mean flow conditions, unsteady RANS (URANS) methods have been developed in order to describe unsteady motions, which are not caused by turbulence. These methods are used, e.g., for the simulation of wall movement in internal combustion engines or rotating turbomachinery. RANS methods have been widely used in industrial applications, especially due to their low computational costs. However, once more detailed information about the flow is needed, RANS simulations often provide unreliable results. Consequently, simulation methods are needed that provide a good trade-off between sufficiently accurate description of turbulent structures in the flow field and cost efficiency. One such paradigm is LES, which will be described in more detail in the following section.

3.1.3 Large eddy simulation (LES)

In LES, only the large turbulent scales are resolved explicitly, while the smallest scales are modeled. The concept is based on the assumption, that the large scales contain most of the energy, which is transferred to the smaller scales. The small scales are then considered to contain little energy, are dissipative, and have an universal and isotropic character. Compared to RANS methods, this approach provides the ability to obtain a time-resolved, more detailed description of complex flows; although less detailed than DNS, it offers significantly lower computational costs, thus, allowing the simulation of larger, more complex flow structures. By modeling only the smallest scales, LES has a significantly lower model error compared to RANS. The separation of turbulent flow structures into large and small scales is achieved through a filter operation, which is then applied to the Navier-Stokes equations. A general formulation of this filter operation applied to an arbitrary quantity ϕ is given by:

$$\overline{\phi}(\boldsymbol{x}) = \int_D \phi(\boldsymbol{x'}) G(\boldsymbol{x} - \boldsymbol{x'}; \Delta) d\boldsymbol{x'} \tag{3.4}$$

where G and Δ are the filter function and the filter width, while D denotes the domain, over which the integration is performed. The filtered quantity is then given by $\overline{\phi}$. Removing the high frequency components of ϕ is mathematically achieved by filtering in either spectral or physical space, of which the methods are thoroughly discussed in many textbooks [36, 121, 124]. This is also the key distinction between LES and RANS simulations. LES employs spatial/spectral filtering instead of time-averaging in order to capture the larger energy-containing scales of turbulence, providing a more detailed representation of flow characteristics. While the sharp Fourier cutoff filter has been widely applied in spectral numerical solution methods, common filters in physical space (in one dimension) are the Gaussian filter:

$$G(x - x'; \Delta) = \left(\frac{6}{\pi \Delta^2}\right)^{1/2} e^{\left[-\frac{6|x-x'|^2}{\Delta^2}\right]} \tag{3.5}$$

or the box filter:

$$G(x - x'; \Delta) = \begin{cases} 1/\Delta & \text{if} \quad |x - x'| \leq \Delta/2 \\ 0 & \text{otherwise} \end{cases} \tag{3.6}$$

However, in most LES applications, implicit filtering of the numerical grid is applied, including the code used in this work. In implicitly filtered LES, the filter width Δ is equal to the grid resolution.

A density-weighted filter operation (also known as Favre-filtering [29]) is applied, as the direct filtering of the governing equations for a variable density flow would lead to additional subgrid correlations ($\overline{\rho'\phi'}$), which in turn require additional modeling. Thus, the Favre operator is applied, which reduces the number of unclosed terms. It reads:

$$\widetilde{\phi} = \frac{\overline{\rho\phi}}{\overline{\rho}} \tag{3.7}$$

where the tilde symbol on an arbitrary quantity $\widetilde{\phi}$ denotes the Favre-filtering. For Reynolds-filtering, the decomposition into resolved and unresolved (or subgrid) scales can be (similar to the Reynolds decomposition in Eq. 3.3) described by:

$$\phi = \overline{\phi} + \phi' \tag{3.8}$$

For Favre-filtering, the decomposition reads:

$$\phi = \widetilde{\phi} + \phi'' \tag{3.9}$$

Favre-filtering is applied to the respective transport equations, expressing density terms by Favre-averages (e.g. $\overline{\rho u_i} = \overline{\rho}\widetilde{u}_i$) and assuming commutativity of derivatives and filtering. Following this, these filtered equations will be discussed in detail.

3.1.3.1 Filtered conservation equations

Favre-filtering applied to the continuity equation with a source term for interphase mass transfer between (coal) particle and gas phase, given in Eq. 2.2, yields the filtered continuity equation:

$$\frac{\partial \overline{\rho}}{\partial t} + \frac{\partial \overline{\rho}\widetilde{u}_j}{\partial x_j} = \overline{\dot{S}}_{\mathrm{mass}} \tag{3.10}$$

Comparing this filtered continuity equation to the unfiltered Eq. 2.2 does not produce any unclosed terms. Applying the Favre-filtering on the momentum equation (Eq. 2.3) yields:

$$\frac{\partial \overline{\rho}\widetilde{u}_i}{\partial t} + \frac{\partial \overline{\rho}\widetilde{u_i u_j}}{\partial x_j} = -\frac{\partial \overline{p}}{\partial x_i} + \frac{\partial \overline{\tau}_{ij}}{\partial x_j} + \overline{\rho} g_i + \overline{\dot{S}}_{\mathrm{mom}} \tag{3.11}$$

with

$$\overline{\tau}_{ij} = \overline{\mu}\left(\frac{\partial \widetilde{u}_i}{\partial x_j} + \frac{\partial \widetilde{u}_j}{\partial x_i}\right) - \frac{2}{3}\overline{\mu}\frac{\partial \widetilde{u}_k}{\partial x_k}\delta_{ij} \tag{3.12}$$

Comparing both, the filtered and unfiltered momentum equation yields an unclosed expression for the nonlinear convection term $\widetilde{u_i u_j} \neq \widetilde{u}_i\widetilde{u}_j$, which requires additional modeling. The term $\widetilde{u_i u_j}$ can be expressed through a so called subgrid stress (SGS) tensor τ_{ij}^{SGS} as:

$$\widetilde{u_i u_j} = \tau_{ij}^{\mathrm{SGS}} + \widetilde{u}_i\widetilde{u}_j \tag{3.13}$$

which is described similar to the Reynolds stress tensor. Inserting Eqs. 3.12 and 3.13 into Eq. 3.11 and rearranging terms yields the final form of the filtered momentum equation:

$$\frac{\partial \overline{\rho}\widetilde{u}_i}{\partial t} + \frac{\partial \overline{\rho}\widetilde{u}_i\widetilde{u}_j}{\partial x_j} = -\frac{\partial \overline{p}}{\partial x_i} + \frac{\partial}{\partial x_j}\left[\overline{\mu}\left(\frac{\partial \widetilde{u}_i}{\partial x_j} + \frac{\partial \widetilde{u}_j}{\partial x_i} - \frac{2}{3}\frac{\partial \widetilde{u}_k}{\partial x_k}\delta_{ij}\right) - \tau_{ij}^{\mathrm{SGS}}\right] + \overline{\rho} g_i + \overline{\dot{S}}_{\mathrm{mom}} \tag{3.14}$$

The only unclosed term now is the subgrid stress tensor τ_{ij}^{SGS}. Its modeling is a key objective in LES modeling. In this work, the Boussinesq approximation is used, a widely applied assumption for closure of this term [197]. As introduced in the RANS modeling section, this assumption treat the effect of the unresolved turbulent scales as an additional turbulent viscosity μ_{t}, implying that energy is carried mostly in one direction, from resolved to unresolved scales, and not vice versa.

The deviatoric part of the subgrid stress tensor $\tau_{ij}^{\text{SGS,D}}$ is described analogous to the stress tensor of a Newtonian fluid. It reads:

$$\tau_{ij}^{\text{SGS,D}} = \tau_{ij}^{\text{SGS}} - \frac{1}{3}\tau_{kk}^{\text{SGS}}\delta_{ij} = -\overline{\rho}\nu_{\text{t}}\left(\frac{\partial \widetilde{u}_i}{\partial x_j} + \frac{\partial \widetilde{u}_j}{\partial x_i} - \frac{2}{3}\delta_{ij}\frac{\partial \widetilde{u}_k}{\partial x_k}\right) \tag{3.15}$$

where ν_{t} is the turbulent kinematic viscosity. The turbulent kinematic viscosity ν_{t} is introduced to model the influence of turbulence on flow behavior by establishing a relationship between turbulent viscosity (or eddy viscosity) μ_{t} and fluid density ρ by means of $\nu_{\text{t}} = \mu_{\text{t}}/\rho$. Both notations, μ_{t} and ν_{t}, are frequently encountered in scientific literature to represent turbulent viscosities in different contexts.

The isotropic part of the subgrid stress τ_{kk}^{SGS} is solved implicitly by adding it to the filtered pressure instead of solving it explicitly. Thus, the newly yielded filtered pseudo-pressure reads:

$$\overline{p}_{\text{mod}} = \overline{p} + \frac{1}{3}\tau_{kk}^{\text{SGS}}\delta_{ij} = \overline{p} + \frac{1}{3}\overline{\rho}\left(\widetilde{u_k^2} - \widetilde{u}_k^2\right) \tag{3.16}$$

This procedure is only valid for low Mach flows, as in this case the Poisson equation is solved to achieve continuity, whereas an explicit modeling is necessary for a fully compressible high Mach description. Applying the Boussinesq approximation on the filtered momentum equation (Eq. 3.14) by inserting Eq. 3.15, and assuming that the subgrid fluctuations of the molecular viscosities are negligible, yields:

$$\frac{\partial \overline{\rho}\widetilde{u}_i}{\partial t} + \frac{\partial \overline{\rho}\widetilde{u}_i\widetilde{u}_j}{\partial x_j} = -\frac{\partial \overline{p}}{\partial x_i} + \frac{\partial}{\partial x_j}\left[(\widetilde{\mu} + \widetilde{\mu}_{\text{t}})\left(\frac{\partial \widetilde{u}_i}{\partial x_j} + \frac{\partial \widetilde{u}_j}{\partial x_i} - \frac{2}{3}\frac{\partial \widetilde{u}_k}{\partial x_k}\delta_{ij}\right)\right] + \overline{\rho}g_i + \overline{\dot{S}}_{\text{mom}} \tag{3.17}$$

The only unclosed term in Eq. 3.17 is now the filtered turbulent viscosity $\widetilde{\mu}_{\text{t}}$. To approximate this term, different SGS models exist, which will be further discussed in section 3.1.3.2.

Furthermore, the Favre-filtering is to be applied to the corresponding scalar transport equations for species Y_α and enthalpy h (Eqs. 2.11 and 2.16), yielding:

$$\frac{\partial \overline{\rho}\widetilde{Y}_\alpha}{\partial t} + \frac{\partial \overline{\rho}\widetilde{Y_\alpha u_j}}{\partial x_j} = \frac{\partial}{\partial x_j}\left(\frac{\widetilde{\mu}}{Sc}\frac{\partial \widetilde{Y}_\alpha}{\partial x_j}\right) + \overline{\dot{\omega}}_\alpha + \overline{\dot{S}}_{Y_\alpha} \tag{3.18}$$

$$\frac{\partial \overline{\rho}\widetilde{h}}{\partial t} + \frac{\partial \overline{\rho}\widetilde{hu_j}}{\partial x_j} = \frac{\partial}{\partial x_j}\left(\frac{\widetilde{\mu}}{Pr}\frac{\partial \widetilde{h}}{\partial x_j}\right) + \overline{\dot{Q}}_{\text{rad}} + \overline{\dot{S}}_{\text{h}} \tag{3.19}$$

Similar to Eq. 3.17, the subgrid fluctuations of the molecular viscosity are assumed to be negligible, allowing for the approximation of these terms by Favre-filtering. Two unclosed scalar flux terms arise in the convective terms from filtering these equations, $\widetilde{Y_\alpha u_j}$ and $\widetilde{hu_j}$. Again, the unclosed scalar fluxes can be split into a resolved and an unresolved part, reading:

$$\widetilde{Y_\alpha u_j} = \widetilde{Y}_\alpha\widetilde{u}_j + g_j^{\text{SGS}}; \quad \widetilde{hu_j} = \widetilde{h}\widetilde{u}_j + q_j^{\text{SGS}} \tag{3.20}$$

where g_j^{SGS} and q_j^{SGS} are the subgrid scale fluxes. The unknown SGS fluxes are approximated through a gradient approach as:

$$\overline{\rho}g_j^{\text{SGS}} = \overline{\rho}\left(\widetilde{Y_\alpha u_j} - \widetilde{Y}_\alpha\widetilde{u}_j\right) = \frac{\widetilde{\mu}_{\text{t}}}{Sc_{\text{t}}}\frac{\partial \widetilde{Y}_\alpha}{\partial x_j} \tag{3.21}$$

$$\overline{\rho}q_j^{\text{SGS}} = \overline{\rho}\left(\widetilde{hu_j} - \widetilde{h}\widetilde{u}_j\right) = \frac{\widetilde{\mu}_{\text{t}}}{Pr_{\text{t}}}\frac{\partial \widetilde{h}}{\partial x_j} \tag{3.22}$$

describing the eddy diffusivities through the turbulent viscosity $\widetilde{\mu}_{\text{t}}$ and a turbulent Schmidt Sc_{t} or Prandtl number Pr_{t}, respectively. Both, Sc_{t} and Pr_{t} were set to a value of 0.7 for the simulations conducted in this work [68]. The remaining unclosed turbulent viscosity can now be treated similarly to the filtered momentum equation (Eq. 3.17). Applying the gradient assumption (Eqs. 3.21 and 3.22) on the filtered transport equations for species Y_α and enthalpy h (Eqs. 3.18 and 3.19) finally yields:

$$\frac{\partial \overline{\rho}\widetilde{Y}_\alpha}{\partial t} + \frac{\partial \overline{\rho}\widetilde{Y}_\alpha \widetilde{u}_j}{\partial x_j} = \frac{\partial}{\partial x_j}\left[\left(\frac{\widetilde{\mu}}{Sc} + \frac{\widetilde{\mu}_\mathrm{t}}{Sc_\mathrm{t}}\right)\frac{\partial \widetilde{Y}_\alpha}{\partial x_j}\right] + \overline{\dot{\omega}}_\alpha + \overline{\dot{S}}_{Y_\alpha} \tag{3.23}$$

$$\frac{\partial \overline{\rho}\widetilde{h}}{\partial t} + \frac{\partial \overline{\rho}\widetilde{h}\widetilde{u}_j}{\partial x_j} = \frac{\partial}{\partial x_j}\left[\left(\frac{\widetilde{\mu}}{Pr} + \frac{\widetilde{\mu}_\mathrm{t}}{Pr_\mathrm{t}}\right)\frac{\partial \widetilde{h}}{\partial x_j}\right] + \overline{\dot{Q}}_\mathrm{rad} + \overline{\dot{S}}_\mathrm{h} \tag{3.24}$$

It needs to be mentioned, that the filtered reaction source term $\overline{\dot{\omega}}_\alpha$ of Eq. 3.23 is highly nonlinear due to the chemical interactions and needs to be modeled. Its modeling will be discussed separately in the combustion modeling section (section 3.2).

3.1.3.2 Subgrid scale (SGS) modeling

The turbulent (eddy) viscosity μ_t is still unclosed and requires modeling. A common approach to model this term is the use of so called eddy viscosity models, which rely on the Boussinesq approximation. Subsequently, the models used in this work shall be presented.

Perhaps the most famous eddy viscosity model is the **Smagorinsky model** [150], which has gained popularity due to its robustness, ease of use and simple formulation, along with a satisfying performance. To model the turbulent viscosity, Smagorinsky proposed the use of a filter size Δ together with a proportionality constant C_m, which shall account for the fact that the computational cell is typically greater than the mixing length scale (as proposed by Prandtl [125]), reading:

$$\mu_\mathrm{t} = \nu_\mathrm{t}\overline{\rho} = \overline{\rho}(C_\mathrm{m}\Delta)^2 D_\mathrm{S}(\widetilde{u}_i) \tag{3.25}$$

The differential operator D_S, which depends on the filtered velocity field, can be calculated as:

$$D_\mathrm{S} = \sqrt{2\widetilde{S}_{ij}\widetilde{S}_{ij}} \quad \text{and} \quad \widetilde{S}_{ij} = \frac{1}{2}\left(\frac{\partial \widetilde{u}_i}{\partial x_j} + \frac{\partial \widetilde{u}_j}{\partial x_i}\right) \tag{3.26}$$

with $\widetilde{S}_{ij}$ being the filtered strain rate tensor. The model constant C_m is chosen depending on the grid, typically ranging between $0.05 < C_\mathrm{m} < 0.2$. A limitation that arises in this model is the occurrence of artificial damping of the flow in regions of pure shear or in the near-wall region (where the flow is generally anisotropic) due to the overprediction of the turbulent viscosity. Several newer models address this problem of the classical Smagorinsky model, among which two were applied in this thesis and will be presented in the following: the Sensor-enhanced Smagorinsky model by Hasslberger et al. [48] and the Sigma model by Nicoud et al. [107].

The **Sensor-enhanced Smagorinsky model** applies a subgrid activity sensor to the standard Smagorinsky model to correct and better predict the subgrid scale dissipation of the standard model. Depending on the flow condition, the sensor calculates values between zero and the actual value for the turbulent viscosity, that would result from the standard Smagorinsky model. A primary advantage of the sensor model is that it demonstrates much better prediction of transitional flows, as well as much better near-wall scaling (which is predicted incorrectly using the standard Smagorinsky model), at almost insignificant additional computational cost. The model formulation is based on a coherent structure function F_CS, which is calculated as the second invariant of the subgrid scale velocity gradient tensor normalized by its magnitude. It reads:

$$F_\mathrm{CS} = \frac{Q}{E}, \quad \text{with} \quad Q = \frac{1}{2}\left(\widetilde{\Omega}_{ij}\widetilde{\Omega}_{ij} - \widetilde{S}_{ij}\widetilde{S}_{ij}\right), \quad \text{and} \quad E = \frac{1}{2}\left(\widetilde{\Omega}_{ij}\widetilde{\Omega}_{ij} + \widetilde{S}_{ij}\widetilde{S}_{ij}\right) \tag{3.27}$$

where $\widetilde{\Omega}_{ij} = 0.5\left(\partial\widetilde{u}_i/x_j - \partial\widetilde{u}_j/x_i\right)$ is the filtered rotation rate tensor. According to this formulation, the limits of the coherent structure function are $-1 \leq F_\mathrm{CS} \leq +1$. Finally, the Sensor-enhanced Smagorinsky model reads:

$$\mu_\mathrm{t} = \mu_\mathrm{t,smago}|\widehat{F}_\mathrm{CS} - F_\mathrm{CS}|^{3/2}C_\mathrm{sensor} = \overline{\rho}(C_\mathrm{m}\Delta)^2 D_\mathrm{S}(\widetilde{u}_i)|\widehat{F}_\mathrm{CS} - F_\mathrm{CS}|^{3/2}C_\mathrm{sensor} \tag{3.28}$$

where $\mu_{\mathrm{t,smago}}$ denotes the turbulent viscosity, calculated by the standard Smagorinsky model. The model compares the coherent structure function on two different scales, the implicitly-filtered grid and a newly introduced explicitly-filtered test grid, denoted by $(\widehat{\cdot})$. The test filter for an arbitrary quantity ϕ is defined as [4]:

$$\widehat{\phi}_{i,j,k} = \sum_{l=-1}^{+1} \sum_{m=-1}^{+1} \sum_{n=-1}^{+1} b_l \cdot b_m \cdot b_n \cdot \phi_{i+l,j+m,k+n} \tag{3.29}$$

with the weighting coefficients $(b_{-1}, b_0, b_{+1}) = (C, 1-2C, C)$ and $C = 1/12$. Thus, the considered cell and its direct neighbour cells $(l, m, n \in \{-1, 0, +1\})$ are used for secondary filtering. A sensor model constant C_{sensor} of 1/0.16 is recommended for central differencing schemes (CDS), whereas a value of 1/0.13 is recommended for quadratic upstream interpolation for convective kinematics (QUICK) schemes. According to this model formulation, for a fully resolved flow field ($\widehat{F}_{\mathrm{CS}} = F_{\mathrm{CS}}$), the subgrid scale dissipation is zero. Given the Sensor-enhanced Smagorinsky model's observed advancements in predicting near-wall scaling, this relatively novel model has been implemented into the LES framework and utilized in the recent publication detailed in section 5.3, wherein a semi-industrial burner simulation is conducted, encompassing the inclusion of burner walls.

Another widely used eddy viscosity model is Nicoud's **Sigma model** [107], which is based on Eq. 3.25, using a different differential operator D_σ and a different model constant C_{m}. The differential operator is constructed such that it reaches zero in regions of pure shear or in near-wall regions. For this purpose, the singular values of the resolved velocity gradient tensor $\widetilde{g}_{ij} = \partial \widetilde{u}_i / \partial x_j$ are used. At first, the invariants I_1, I_2, and I_3 of the matrix $G_{ij} = \widetilde{g}_{ki}\widetilde{g}_{kj}$ are determined, reading:

$$I_1 = \mathrm{tr}(G_{ij}), \qquad I_2 = \frac{1}{2}\left[\mathrm{tr}(G_{ij})^2 - \mathrm{tr}(G_{ik}G_{kj})\right], \qquad I_3 = \det(G_{ij}) \tag{3.30}$$

with tr and det being the trace and determinant of the matrix. Further, angles are computed from the invariants:

$$\alpha_1 = \frac{I_1^2}{9} - \frac{I_2}{3}, \qquad \alpha_2 = \frac{I_1^3}{27} - \frac{I_1 I_2}{6} + \frac{I_3}{2}, \qquad \alpha_3 = \frac{1}{3}\mathrm{arccos}\left(\alpha_2 \alpha_1^{-3/2}\right) \tag{3.31}$$

Using both, Eqs. 3.30 and 3.31, the singular values of $\widetilde{g}_{ij}$ can then be computed as:

$$\begin{aligned} \sigma_1 &= \left(\frac{I_1}{3} + 2\sqrt{\alpha_1}\cos(\alpha_3)\right)^{1/2}, \\ \sigma_2 &= \left(\frac{I_1}{3} - 2\sqrt{\alpha_1}\cos\left(\frac{\pi}{3} + \alpha_3\right)\right)^{1/2}, \\ \sigma_3 &= \left(\frac{I_1}{3} - 2\sqrt{\alpha_1}\cos\left(\frac{\pi}{3} - \alpha_3\right)\right)^{1/2} \end{aligned} \tag{3.32}$$

Finally, the differential operator D_σ is calculated from the singular values, according to:

$$D_\sigma = \frac{\sigma_3(\sigma_1 - \sigma_2)(\sigma_2 - \sigma_3)}{\sigma_1^2} \quad \text{with} \quad \sigma_1 \geq \sigma_2 \geq \sigma_3 \geq 0 \tag{3.33}$$

Nicoud tested different model constants on different test cases and obtained promising results for $1.3 \leq C_{\mathrm{m}} \leq 1.5$. The model is well established for application in the LES of combustion processes, predicting no turbulent viscosity for solid body rotations and thermal expansion. The Sigma model is used in the simulations of the first two published studies of this work, presented in sections 5.1 and 5.2. These investigations entail the use of a laboratory-scale burner featuring a free-flow configuration and the absence of burner walls; for both cases, a model constant C_{m} of 1.5 is used.

3.2 Combustion modeling

This section deals with the approaches used to describe the turbulent combustion process during solid fuel conversion, as present in pulverized coal combustion. The chemical conversion from a fuel source and an oxidizer is described by a series of reactions and species, which can be summarized in a reaction mechanism, serving as a thermochemical database. Depending on the specific combustion problem, several hundred species and several thousand reactions may be required for a detailed characterization. The coupling of the chemical conversion with the LES flow solver is accomplished via the filtered reaction rate $\overline{\dot{\omega}}_\alpha$ in Eq. 3.23. The reaction rate is then calculated from the specific reaction mechanism used. The development of reaction mechanisms is based on complex experiments and detailed molecular dynamics simulations, which provide reliable results only for a specific fuel and in a specific operating range.

The use of a reaction mechanism in LES (1) may require additional transport equations to be solved for the respective species, (2) depending on the number of species, consideration of the chemistry may become very time consuming and computational expensive, and (3) additional modeling of the interaction of turbulence and chemistry at the subgrid scale is essential, as the reaction rate $\overline{\dot{\omega}}_\alpha$ in Eq. 3.23 appears in its filtered form.

Several modeling approaches exist to couple the chemistry with the flow solver. Subsequently, emphasis will be placed on two methods: the direct solution of reaction mechanisms by finite rate chemistry (FRC) and the use of flamelet-based tabulation approaches. Although the former model is not used in this work, it is briefly outlined for the sake of completeness and to illustrate advantages and disadvantages of both methods.

3.2.1 Finite rate chemistry (FRC)

The FRC method is based on the concept of calculating reaction rates locally for each species, taking into account the respective mixture composition, temperature, and pressure. This entails solving an individual transport equation for each species within a given reaction mechanism. However, utilizing detailed reaction mechanisms, which often consist of hundreds of species, becomes computationally intensive and impractical for two-dimensional (2D) or three-dimensional (3D) simulations. To address this challenge, reduced mechanisms are often employed. These reduced mechanisms are derived from detailed mechanisms using various techniques such as genetic algorithms [148, 149], directed relation graph (DRG) analysis [86], path flux analysis (PFA) [133] or sensitivity analysis [173]. These methods identify and eliminate irrelevant reactions and species from the mechanism, while maintaining the desired prediction accuracy by predefining objective functions for, e.g., flame speed and temperature profiles. Gruhlke et al. [43] recently applied the FRC method in LES to investigate a complex gas turbine combustion chamber. Their study demonstrates the successful implementation of the FRC method in a realistic engineering scenario. Given the interaction of turbulence and chemistry across all scales, various modeling approaches are utilized to account for the subgrid turbulence-chemistry interaction in LES. In their investigation, Gruhlke et al. employed the dynamic thickened flame model [81] to address turbulence-chemistry interaction.

However, the use of FRC for the LES of pulverized coal flames is not practically feasible due to the extensive number of species and reactions involved in coal conversion. The complexity of coal combustion processes necessitates handling a large number of species and reactions, which poses computational challenges. Even when employing reduced mechanisms, a significant number of species are retained. For instance, in this study, the reduced CRECK mechanisms used contain 52, 120 and 129 species [97, 132, 145, 170]. This substantial number of species makes the direct application of FRC in LES unfeasible.

In recent years, flamelet-based tabulation methods have emerged as an alternative approach, gaining attention for their ability to provide detailed insights into thermochemical states with relatively low computational requirements. These methods have been applied in the simulations conducted in this work and will be discussed further in the subsequent section.

3.2.2 Flamelet-based tabulation approaches

Flamelet-based tabulation approaches rely on the fundamental assumption that a turbulent flame can be characterized as an ensemble of laminar 1D flames known as flamelets. This assumption holds when the time scale associated with the turbulent flow greatly exceeds the time scale of chemical reactions. Essentially, it implies that the chemical conversion occurring at the inner flame front is significantly faster than flow separation phenomena. The Damköhler number Da serves as a metric for assessing this relationship, quantifying the ratio of the turbulent time scale τ_t to the chemical time scale τ_c. The Damköhler number can be expressed as follows:

$$Da = \frac{\tau_\mathrm{t}}{\tau_\mathrm{c}} \tag{3.34}$$

A high Damköhler number thereby indicates that chemical reactions occur more rapidly compared to turbulence effects. In the context of flamelet modeling, this implies that chemical reactions are more dominant than turbulence mixing. In such cases, the Kolmogorov length scale, which represents the smallest eddies in the turbulent flow, tends to be much larger than the thickness of the inner reaction layer. This indicates that the turbulent eddies are relatively large compared to the region where significant chemical reactions occur (inner reaction layer). Consequently, variations in the flame structure in the tangential direction are expected to be minimal, while changes occur predominantly perpendicular to the flame front. As a result, these perpendicular changes can be effectively described by an ensemble of 1D flames, known as flamelets. The flamelet concept is not limited to one-dimensional problems; it can also be applied to model multi-dimensional turbulent flames. The fundamental idea of the flamelet model can be traced back to Williams [201], who introduced the concept. The flamelet equations, which provide the mathematical formulation for describing the behavior of flamelets, were initially formulated by Peters [114]. Flamelet models offer a significant advantage compared to the FRC model by enabling pre-calculation of 1D flames using detailed or reduced reaction mechanisms. These mechanisms can be solved using kinetic libraries such as Chemkin [67], Cantera [41], or FlameMaster [118]. The latter was utilized in this work. Computational costs associated with 1D flame calculations are comparatively lower than those required for 2D or 3D simulations. The 1D flame computations produce flamelet solutions that are parameterized using predefined trajectory variables, and these solutions are then stored in a flamelet table. During the simulation, the flamelet table is accessed based on the trajectory variables, allowing for the retrieval of various thermochemical states. This approach offers a significant advantage since it only necessitates solving transport equations for the trajectory variables, eliminating the need for individual transport equations for each species. This stands in contrast to the FRC approach, which requires solving individual transport equations for each species, resulting in a substantial reduction in computational effort with flamelets.

For premixed flames, the progress variable c (as defined in Eq. 2.30) is employed as the trajectory variable in flamelet models. On the other hand, for non-premixed flames, the mixture fraction Z (as defined in Eq. 2.31) serves as the trajectory variable. It is important to note that this choice of trajectory variable implies an assumption about the overall underlying flame structure, which can be premixed, non-premixed, or even partially-premixed. Therefore, the modeling approach must be selected accordingly, depending on the specific combustion problem under investigation.

Both premixed and non-premixed flamelet approaches have been extensively developed in recent years, building upon the foundational concept introduced by Peters [114]. Notable advancements in this field include the intrinsic low-dimensional manifolds (ILDM) approach by Maas and Pope [90, 91], the flame-prolongation of ILDM (FPI) by Gicquel et al. [38], the premixed flamelet-generated manifolds (PFGM) approach by van Oijen et al. [176, 177], and the flamelet/progress variable (FPV) approach by Pierce and Moin [117]. The latter was employed in this work. Hereinafter, flamelet models applied to PCC simulations shall be examined and necessary adaptions for the use of flamelet models to PCC flames will be presented.

3.2.2.1 Flamelet modeling for solid fuel combustion

Both premixed and non-premixed flamelet models have demonstrated successful applications to PCC flames. However, selecting the appropriate combustion state for PCC flames is often not straightforward. In the case of single particle combustion, it can be considered non-premixed since the fuel and oxidizer come into contact separately. Nonetheless, the situation may vary in complex burner configurations. For example, in burners with strong recirculation zones, such as swirl-stabilized burners, both premixed and non-premixed (and also partially-premixed) regions can form. Similarly, in the co-firing of coal and a premixed secondary fuel source, both premixed and non-premixed states may be present. Therefore, the choice between premixed and non-premixed flamelet models for PCC flames requires careful consideration and analysis of the specific combustion conditions and characteristics.

Among the premixed flamelet models, Knappstein et al. [73] employed a premixed FGM model to investigate the devolatilization of coal in a premixed flat flame configuration. The study involved the impingement of coal particles on a laminar flame front, and the model's predictions were compared to experimental data, demonstrating favorable agreement. In a subsequent study, Knappstein et al. [74] expanded the premixed FGM model to incorporate an additional mixture fraction, enabling the consideration of char combustion alongside devolatilization. By comparing the model results to detailed chemistry solutions using a generic test case, they achieved good agreement. Vascellari et al. [181] utilized a premixed FPV approach to examine a laminar stagnation pulverized coal flame based on a premixed composition. The obtained results were compared to a reference model, which accounted for full species transport and direct chemistry determination. The comparison revealed good agreement in terms of the main species profiles and temperature, with only minor deviations observed in the flame and post-flame zone.

Among other researchers, Vascellari et al. [179, 180] employed non-premixed flamelet models. The focus of their investigations was on single particle combustion, specifically examining the devolatilization process using unsteady laminar diffusion flamelets. In their initial study [179], a laminar flamelet approach was employed, which was subsequently extended to a FPV approach in a later investigation [180]. The results obtained by Vascellari et al. exhibited a high level of agreement with experimental data and fully resolved simulations employing detailed chemistry. Notably, their models demonstrated good predictive capability in terms of ignition and volatile combustion phenomena. Watanabe et al. [183] introduced a flamelet model based on two mixture fractions for volatile gases and char off-gases. This model was applied to a two-dimensional pulverized coal jet flame and compared to results obtained from detailed chemistry simulations. The flamelet model exhibited a good representation of turbulent structures; however, it predicted slightly faster ignitions compared to the detailed chemistry simulations. In a subsequent study [184], the flamelet model was extended to incorporate a third mixture fraction, accounting for coal moisture. A LES of a large-scale test furnace was conducted, resulting in favorable agreement with experimental data. The extended flamelet model demonstrated its capability in accurately capturing the combustion processes within the furnace. Rieth et al. [137, 139] utilized a non-premixed steady flamelet model for the investigation of a semi-industrial swirl-stabilized coal furnace, characterized by the presence of recirculation zones. The model considered mixture fractions for volatiles and char off-gases, and the obtained results were compared to detailed experimental measurements. The overall flow field, including main species concentrations and velocities, was well reproduced by the flamelet model. In another study, Rieth et al. [141] applied a FPV approach to the pulverized coal combustion in a turbulent mixing layer and validated it using detailed DNS data with direct chemistry integration. The results indicated that the FPV approach was suitable for representing the complex reacting multiphase flow; however, slight deviations were observed in premixed regions.

Depending on the specific application scenario, both non-premixed and premixed flamelet approaches have shown successful applications in simulating pulverized coal flames. However, in order to determine the superior model, Messig et al. [99] conducted a study comparing both approaches using pulverized coal counterflow flames. The investigation focused solely on devolatilization as the coal model, and the results were compared to reference solutions obtained from fully resolved simulations employing direct chemistry. The findings indicated that both non-premixed and premixed flamelet approaches were capable of accurately predicting the behavior of pulverized coal flames. However, the non-premixed approach exhibited slightly better results, while the premixed approach exhibited larger deviations, particularly concerning temperature and species concentrations, especially under rich conditions. Similar observations were made by Wen et al. [193, 194], who evaluated various premixed and non-premixed flamelet approaches using DNS data provided by Rieth et al. [141]. Once again, the premixed flamelet models showed larger deviations compared to the non-premixed flamelet models.

Based on these recent results, the present work focuses solely on the simulation of pulverized coal flames using a FPV approach based on non-premixed flamelets. The subsequent section will provide a more detailed explanation of this chosen approach.

3.2.2.2 Non-premixed combustion modeling

In this section, the flamelet/progress variable (FPV) approach by Pierce and Moin [117] based on non-premixed flamelets is outlined. First, the theoretical background of the model is presented, followed by the extensions of the model necessary to be applied to PCC simulations, namely the consideration of heat losses, as well as several mixture fractions to cover all relevant gas streams. Finally, the used coupling strategy of the turbulence-chemistry interaction (TCI) between LES and the flamelet table is discussed.

Flamelet/progress variable (FPV) approach

The flamelet model is rooted in the concept that a turbulent diffusion flame can be characterized by a collection of laminar one-dimensional flamelets. This approach allows for the description of complex flame structures through the combination of simpler flame solutions. In the flamelet model, a conserved transported scalar is selected to represent the flamelet's thermochemical states. This scalar serves as a means to access the relevant information from the flamelet library, thereby reducing the number of transported scalars while retaining the crucial details provided by detailed chemical kinetics. In the case of the non-premixed flamelet model, the mixture fraction is often employed as a suitable conserved scalar for this purpose. The mixture fraction represents the local fuel-oxidizer mixing ratio and enables the characterization of different combustion regimes within the flame. The one-dimensional steady flamelet equations in the mixture fraction space are derived through a coordinate transformation from the physical space to the mixture fraction space, reading [114]:

$$\rho \frac{\partial \phi_k}{\partial \tau} = \rho \frac{\chi}{2} \frac{\partial^2 \phi_k}{\partial Z^2} + \dot{\omega}_k \tag{3.35}$$

In Eq. 3.35, τ is a time-like coordinate, χ is the dissipation rate of the conserved scalar, ϕ_k is either the species mass fraction or the temperature, while $\dot{\omega}_k$ describes the respective source terms of ϕ_k. The scalar dissipation rate, representing the coupling of the flamelet solution with the flow field, is defined as:

$$\chi = 2 D_Z \left(\nabla Z\right)^2 \tag{3.36}$$

where D_Z is the molecular diffusivity of the mixture fraction Z and ∇Z is the gradient of Z. The determination of the Z-dependent profile of χ, which necessitates modeling, can be achieved by derivation from a steady counterflow flame. To accurately describe this profile, the concept of the stoichiometric scalar dissipation rate χ_{st} is introduced. This scalar dissipation rate serves as a crucial parameter that enables a unique characterization of the profile. All thermochemical quantities ϕ can now be parameterized as a function of the mixture fraction and the scalar dissipation rate, resulting in:

$$\phi = \phi\left(Z, \chi_{\mathrm{st}}\right) \tag{3.37}$$

where χ_{st} is the scalar dissipation rate at the stoichiometric mixture fraction $Z = Z_{\mathrm{st}}$. Solving these equations can then be illustrated by the so-called S-shaped curve [115], which is shown in Fig. 3.2. By systematically varying the scalar dissipation rate from zero to a critical quenching limit, corresponding to the point at which the flame extinguishes, a range of flamelet solutions can be obtained. Each solution corresponds to a specific combination of mixture fraction and scalar dissipation rate, capturing the diverse characteristics of the flame. This parameterization offers a comprehensive representation of the combustion process, allowing for a detailed understanding of how the flame structure and thermochemical properties are influenced by the interplay between mixture fraction and scalar dissipation rate. The S-shaped curve can be partitioned into three

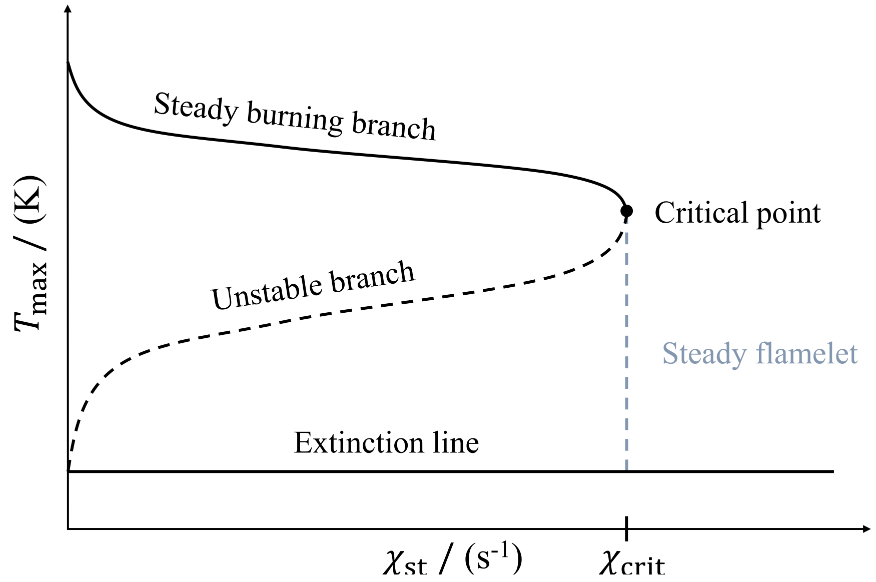

Figure 3.2: Schematic representation of the S-shaped curve showing the maximum temperature T_{max} as a function of stoichiometric scalar dissipation rate χ_{st} for a full set of flamelet solutions. Adapted from [105].

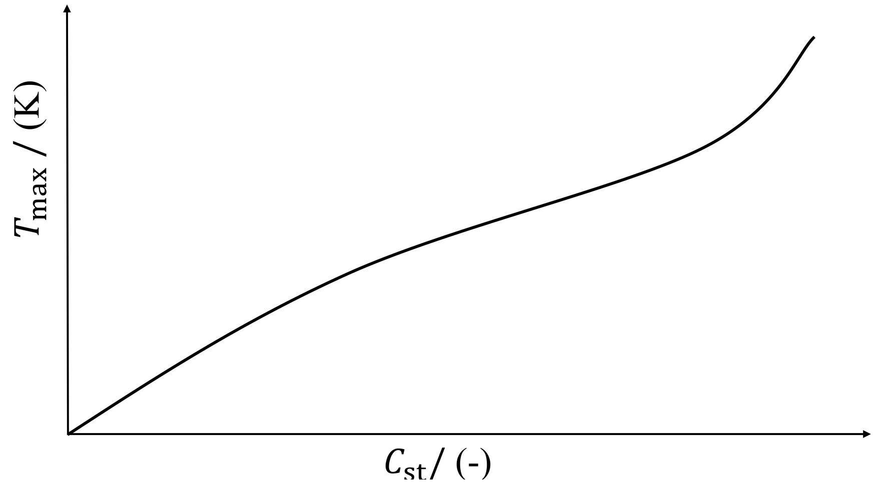

Figure 3.3: Schematic representation of the remapped flamelet solutions onto a reactive scalar C_{st} describing the flame progress as used in the FPV approach.

distinct sections: the stable branch, the unstable branch, and the extinction line. Along the stable branch, an increase of the scalar dissipation rate is accompanied by a gradual decrease of the maximum temperature until it reaches a critical point denoted as χ_{crit}. At this critical point, the temperature drops to a significantly low level, making it unable to sustain combustion reactions within the flame. Subsequently, two possible scenarios arise based on the trajectory of the flame. If the scalar dissipation rate continues to increase beyond χ_{crit}, the flame extinguishes. Consequently, the flame trajectory aligns with the extinction line, signifying the termination of combustion. Conversely, if the scalar dissipation rate is reduced at the critical point, the flame remains in equilibrium, maintaining a balance between chemical reactions and transport processes. As a result, the maximum temperature progressively decreases as the scalar dissipation rate decreases. In this scenario, the flame trajectory follows the unstable branch until it eventually reaches flame extinction. The extinction line describes the non-burning solution, as no chemical reactions occur. From Fig. 3.2, it can be illustrated that several solutions exist for a range of scalar dissipation rates, implying that no unique parametrization in terms of $\chi = \chi_{\mathrm{st}}$ is possible. The steady flamelet model (see Fig. 3.2), by contrast, neglects the unstable branch. However, it clearly shows that at the point $\chi = \chi_{\mathrm{crit}}$, a discontinuity appears and the flamelet region between χ_{crit} and the extinction line cannot be accurately represented.

Pierce and Moin [117] proposed a model that uses a reactive scalar C instead of the scalar dissipation rate, which is able to uniquely describe the flame states of all three regions of the S-shaped curve. They suggested formulating the reactive scalar C from a linear combination of the main reaction products, such that the monotonicity criterion is fulfilled. In this work, this definition is maintained and different linear combinations of occurring product species mass fractions are chosen case-dependent.

Hence, the FPV approach parameterizes all thermochemical quantities as a function of the mixture fraction Z and the reactive scalar C, reading:

$$\phi = \phi\,(Z, C) \tag{3.38}$$

The 1D counterflow flames are thus, first calculated in Z-space for an ensemble of stoichiometric scalar dissipation rates along the S-shaped curve and subsequently remapped onto a reactive scalar. Figure 3.3 shows the remapped flamelet solutions onto a reactive scalar C describing the flame progress and showing the unique representation of all flame states. The FPV approach is able to better account for unsteady processes such as extinction and re-ignition phenomena, while still employing a steady flamelet solution.

The application of the FPV approach to PCC simulations requires several extensions. In PCC flames, the accurate modeling of two significant interphase mass transfer phenomena is crucial: devolatilization and char burnout. These phenomena are fundamental to capturing the essential characteristics of PCC flames and should be adequately incorporated in PCC simulations. This results in two mixture fractions that interact with the surrounding oxidizer stream. Moreover, in cases where a pilot stream is used for flame stabilization, or the co-firing of coal with a secondary fuel source is investigated (as in section 5.2), further mixture fractions are necessary. Hence, in the present work, both, two mixture fraction, as well as three mixture fraction approaches are used. Hasse and Peters [46] introduced a two mixture fraction approach to effectively model split injection in Diesel engines. This approach has proven to be successful and has been subsequently applied to PCC simulations by several researchers (e.g. [3, 141, 191]). To overcome numerical issues in accessing the table and to increase simulation stability, Hasse and Peters proposed a coordinate transformation from a unit triangle in the composition space to a unit square space by introducing a new mixture fraction parameter. The general approach can be seen in Fig. 3.4. The transformed parameters are then given by:

$$Z = Z_1 + Z_2 \quad \text{and} \quad A = \frac{Z_2}{Z_1 + Z_2 + \epsilon} \tag{3.39}$$

where ϵ denotes a small positive number ($\epsilon = 10^{-6}$) required for numerical stability.

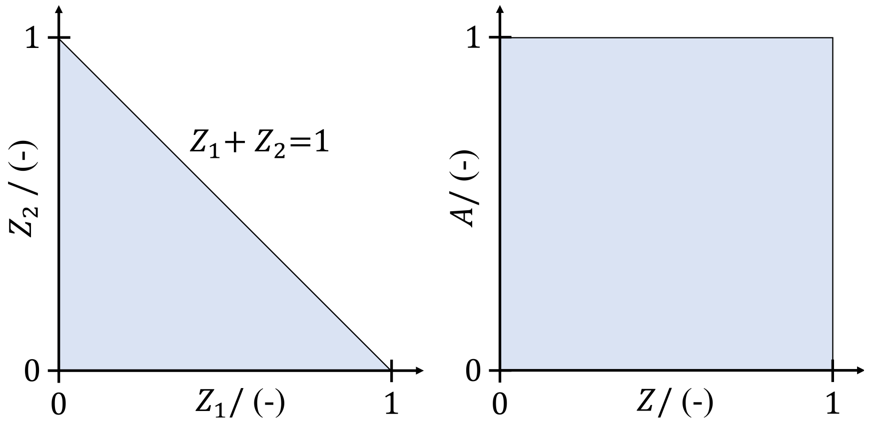

Figure 3.4: Schematic representation of the transformation from a unit triangle in composition space (Z_1, Z_2) to a unit square space (Z, A), according to [46].

Wen et al. [192] have extended this approach to consider three mixture fractions. Here, the unit pyramid space resulting from three mixture fractions (Z_1, Z_2, and Z_3) is transformed into a unit cubic space (ranging from 0 to 1) to describe all possible states of mixing between fuel and oxidizer. The procedure is shown in Fig. 3.5. In this model, another transformed mixture fraction parameter is introduced, yielding the transformed parameters:

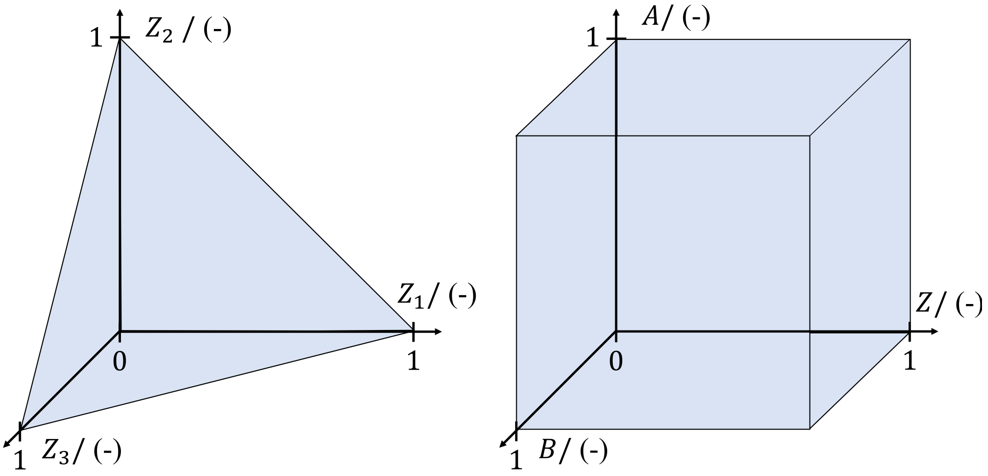

Figure 3.5: Schematic representation of the transformation from a unit pyramid in composition space (Z_1, Z_2, Z_3) to a unit cubic space (Z, A, B), according to [192].

$$Z = Z_1 + Z_2 + Z_3 \quad \text{and} \quad A = \frac{Z_2}{Z_1 + Z_2 + \epsilon} \quad \text{and} \quad B = \frac{Z_1 + Z_2}{Z_1 + Z_2 + Z_3 + \epsilon} \tag{3.40}$$

Both variants are applied in the simulations of this work.

Another extension of the FPV model to the simulation of PCC flames is the inclusion of heat losses. The interaction of hot exhaust gas with cold coal particles can lead to strong heat losses, which have to be considered in the flamelet modeling. Messig et al. [99] has demonstrated the importance of correctly describing heat losses in pulverized coal flames. They proposed to solve the individual flamelet solutions with successively reduced or increased boundary temperatures for the fuel and oxidizer sides, whereas equal temperatures are used at both sides. These flamelet solutions are then stored as a function of the enthalpy. The same approach is used in this work. Decreasing the boundary temperatures can thus, account for the heat loss process, while increasing the boundary temperatures can account for the heat gain process. Hence, the non-premixed

1D flamelets are solved at different boundary temperatures first (e.g., 273 K, 300 K, 600 K, 800 K, depending on the case), and subsequently, the solutions are remapped onto the enthalpy. Following this approach, the flamelet solutions along this trajectory can be parameterized by the enthalpy and stored as a separate dimension in the flamelet library. Proch et al. [129] introduced an alternative methodology to account for interphase heat transfer by adjusting the source term in the flamelet temperature equations through the application of a constant factor λ. A constant value of $\lambda = 1$ thereby corresponds to adiabatic flamelet conditions. By varying this factor, non-adiabatic flamelet solutions at varying enthalpy levels are obtained. Using this methodology, wider enthalpy ranges can be accessed, corresponding to enthalpy levels in real flames. Notably, the absence of a linear relationship between enthalpy and λ necessitates an iterative procedure for the extraction of table data. In this work, solely the first approach based on the linear variation of the boundary temperatures is applied, while the latter approach is mentioned for the sake of completeness.

Finally, depending on the number of considered mixture fractions in the simulations of this work, the parameterization of the thermochemical state yields either:

$$\phi = \phi\left(Z, A, C, h\right) \quad \text{or} \quad \phi = \phi\left(Z, A, B, C, h\right) \tag{3.41}$$

3.2.2.3 Subgrid probability density function (PDF) modeling

Coupling tabulated chemistry approaches to LES requires further modeling, since only Favre-filtered quantities are available to retrieve data from the flamelet library and the distribution of the transported scalars within the subgrid is not known. Directly retrieving the table data via a Favre-filtered scalar does not yield the Favre-filtered state $\widetilde{\phi}$, thus, for Eq. 3.41, it holds:

$$\widetilde{\phi} \neq \phi\left(\widetilde{Z}, \widetilde{A}, \widetilde{B}, \widetilde{C}, \widetilde{h}\right) \tag{3.42}$$

To obtain the Favre-filtered state, the distribution of the transported scalars within the subgrid is required, hence, the subgrid probability/filtered density function (PDF/FDF) needs to be known [117]. The works of Givi [39] and Pope [123] should be mentioned in this context, who first proposed the use of presumed or transported PDFs for LES [39] and introduced a description of the FDF [123].

The presumed PDF is constructed using the first two moments of a scalar. For the Favre subgrid PDF $\widetilde{P}$ in mixture fraction space Z, this would be the mixture fraction average $\widetilde{Z}$ and variance $\widetilde{Z''^2}$. A Favre-filtered quantity $\widetilde{\psi}$ can then be obtained by integrating the joint-scalar PDF. For the transported scalar Z, it reads:

$$\widetilde{\psi} = \int_0^1 \psi\left(Z\right) \widetilde{P}\left(Z, \widetilde{Z}, \widetilde{Z''^2}\right) dZ \tag{3.43}$$

where the Favre subgrid PDF $\widetilde{P}$ results from the Favre-averaging procedure. Popular subgrid PDFs in the context of LES are the beta PDF and the top-hat PDF, whereas the top-hat PDF was used for the LES of PCC in this work. For the sake of clarity, both distributions shall be explained subsequently. The introduction of the beta PDF in the context of LES dates back to the work of Cook & Riley [23]. The model reads:

$$\widetilde{P}\left(Z, \widetilde{Z}, \widetilde{Z''^2}\right) = Z^{a-1}\left(1 - Z\right)^{b-1} \Gamma\left(a + b\right)\left(\Gamma\left(a\right)\Gamma\left(b\right)\right) \tag{3.44}$$

$$\text{with} \qquad a = \widetilde{Z}c, \qquad b = \left(1 - \widetilde{Z}\right)c \qquad \text{and} \qquad c = \frac{\left(\widetilde{Z} - \widetilde{Z}^2 - \widetilde{Z''^2}\right)}{\widetilde{Z''^2}} \tag{3.45}$$

where Γ is the gamma function. Although the beta PDF is able to well predict the subgrid behavior of many test cases compared to DNS data, it has difficulties when it comes to multi-stream mixture problems, as it is defined for one mixture fraction and adds one table dimension.

To overcome this issue, Floyd et al. [33] proposed the top-hat PDF model. Within a LES cell, the model assumes a constant gradient of Z. It is based on the assumption, that on the subgrid scale, all values of Z have an equal probability to occur in a certain lower and upper limit of Z, forming a top-hat shape within this range. Thus, the distribution reads:

$$\widetilde{P}\left(Z, \widetilde{Z}, \widetilde{Z''^2}\right) = \begin{cases} t_0 & \text{if} \quad Z_a \leq Z \leq Z_b \\ 0 & \text{if} \quad \text{otherwise.} \end{cases} \tag{3.46}$$

$$\text{with} \qquad Z_a = \widetilde{Z} - \frac{1}{2}\sqrt{12\widetilde{Z''^2}}, \qquad Z_b = \widetilde{Z} + \frac{1}{2}\sqrt{12\widetilde{Z''^2}} \qquad \text{and} \qquad t_0 = \frac{1}{Z_b - Z_a} \tag{3.47}$$

where Z_a and Z_b are the limits of Z and t_0 is the width, computed from the first two moments of Z, $\widetilde{Z}$ and $\widetilde{Z''^2}$.

To properly describe the thermochemical state in the gas phase of a system, a single mixture fraction as a trajectory variable is often not sufficient, and an extension to further tracking scalars is applied; these can be, i.e., as used in the applications to this thesis (see section 5), further mixture fractions, the enthalpy, or a variable to describe the reaction progress. Multiple tracking scalars also require further subgrid modeling to accurately describe the TCI. One possibility is to form the entire joint PDF and solve further variance transport equations for the individual tracking scalars. This may quickly become intractable for multiple tracking scalars. A way to simplify this, which was also used in this work, is to express multiple mixture fractions as the sum of the respective mixture fractions and construct the subgrid PDF based only on the mixture fraction sum. In this work, complex multiphase flows with multiple mixture fractions are investigated. The use of a joint beta-PDF for the subgrid modeling of the mixture fractions was omitted here, since even simplifying different mixture fractions by using the mixture fraction sum, a pre-integration and tabulation of $\widetilde{Z''^2}$ would be necessary, which requires an extension of the flamelet look-up table by at least one dimension. For the application cases in sections 5.1 and 5.3, this approach would require a look-up table with at least five dimensions (two mixture fractions, progress variable, enthalpy, and $\widetilde{Z''^2}$); for the application case in section 5.2, a look-up table with at least six dimensions (three mixture fractions, progress variable, enthalpy, and $\widetilde{Z''^2}$) would be necessary. The increasing dimensionality of the flamelet tables implies a larger amount of data that needs to be stored and accessed during the simulation. This results in an augmented memory demand, potentially exceeding the available resources. The computational cost associated with accessing and manipulating these extensive tables can become prohibitively expensive, adversely impacting the overall computational performance. Therefore, the aforementioned top-hat approach [33] was used instead, as the dimensionality does not increase using this method. The joint subgrid PDF for two mixture fractions using a top-hat PDF approach would read:

$$\widetilde{P}\left(Z_1, Z_2, \widetilde{Z_1}, \widetilde{Z_1''^2}, \widetilde{Z_2}, \widetilde{Z_2''^2}\right) = \begin{cases} t_0 & \text{if} \quad Z_{1,a} \leq Z_1 \leq Z_{1,b}, \quad Z_{2,a} \leq Z_2 \leq Z_{2,b} \\ 0 & \text{if} \quad \text{otherwise.} \end{cases} \tag{3.48}$$

$$\text{with} \qquad t_0 = \frac{1}{\left(Z_{1,b} - Z_{1,a}\right)\left(Z_{2,b} - Z_{2,a}\right)} \tag{3.49}$$

where $Z_{1,a}$, $Z_{2,a}$, $Z_{1,b}$, and $Z_{2,b}$ are calculated similar to Eq. 3.47. However, for simplification, in this work the different mixture fractions are summed up (e.g., $\widetilde{Z} = \widetilde{Z_1} + \widetilde{Z_2}$ for the application cases in sections 5.1 and 5.3, $\widetilde{Z} = \widetilde{Z_1} + \widetilde{Z_2} + \widetilde{Z_3}$ for the application case in section 5.2) so that the subgrid PDF can be applied to $\widetilde{Z}$ only and Eqs. 3.46 and 3.47 can be used for both, two mixture fraction and three mixture fraction problems.

An additional transport equation is then solved to obtain the variance of the sum of all mixture fractions $\widetilde{Z''^2}$, following the derivation of Pera et al. [112] and using the parameters that have been tested for spray flame LES [142, 166]. The transport equation reads:

$$\frac{\partial \overline{\rho} \widetilde{Z''^2}}{\partial t} + \frac{\partial \overline{\rho} \widetilde{Z''^2} \widetilde{u}_j}{\partial x_j} = \frac{\partial}{\partial x_j} \left[\left(\frac{\widetilde{\mu}}{Sc} + \frac{\widetilde{\mu}_\mathrm{t}}{Sc_\mathrm{t}} \right) \frac{\partial \widetilde{Z''^2}}{\partial x_j} \right] + \frac{2\widetilde{\mu}_\mathrm{t}}{Sc_\mathrm{t}} \left(\frac{\partial \widetilde{Z}}{\partial x_j} \right)^2 - 2\overline{\dot{S}}_{\chi Z} + \overline{\dot{S}}_\mathrm{p} \tag{3.50}$$

where the third and fourth terms on the RHS are source terms due to the unresolved scalar dissipation rate and due to the subgrid effect of the particles on the mixture fraction variance, assuming that particle mass is released on the subgrid scale, following the adaption by Rieth et al. [137] for the simulation of PCC. The former term is modeled by:

$$\overline{\dot{S}}_{\chi Z} = C_\chi \frac{\widetilde{\mu}_\mathrm{t}}{Sc_\mathrm{t}} \frac{\widetilde{Z''^2}}{\Delta^2} \tag{3.51}$$

In Eq. 3.51, $C_\chi = 8.0$ is a subgrid dissipation rate constant, taken from [137]. The fourth term on the RHS of Eq. 3.50 is then modeled by [51]:

$$\overline{\dot{S}}_\mathrm{p} = C_\mathrm{p} \widetilde{Z''^2} \frac{\overline{\dot{S}}_{Y_\alpha}}{\widetilde{Z}} \tag{3.52}$$

where $C_\mathrm{p} = 0.5$ is a model constant, taken from Tillou et al. [166] and $\overline{\dot{S}}_{Y_\alpha}$ is the particle source term according to volatile and char off-gas mass release, as described in section 3.5.3.

For further tracking scalars beside the mixture fractions, statistical independence is assumed and their PDF is modeled by a Dirac distribution. The joint PDF can then be described as a product of a marginal PDF and a conditional PDF, yielding:

$$\widetilde{P}(Z, Y) = \widetilde{P}(Z)\, \widetilde{P}(Y|Z) \tag{3.53}$$

where Y describes a transported scalar following a Dirac PDF, reading:

$$\widetilde{P}(Y|Z) = \delta\left(Y - \widetilde{Y|Z}\right) \tag{3.54}$$

Thus, a Favre-filtered quantity $\widetilde{\psi}$ depending on Z and Y can then be obtained by integrating the joint-scalar PDF as:

$$\widetilde{\psi} = \int_0^1 \int_0^1 \psi(Z, Y)\, \widetilde{P}\left(Z, \widetilde{Z}, \widetilde{Z''^2}\right) \delta\left(Y - \widetilde{Y|Z}\right) dZ\, dY \tag{3.55}$$

Considering the sifting property of a Dirac PDF $\left(\int f(x)\delta(x - x_0)\, dx = f(x_0)\right)$ [122], Eq. 3.55 can be reformulated to:

$$\widetilde{\psi} = \int_0^1 \psi\left(Z, Y = \widetilde{Y|Z}\right) \widetilde{P}\left(Z, \widetilde{Z}, \widetilde{Z''^2}\right) dZ \tag{3.56}$$

The aforementioned statistical independence of the respective tracking scalars then allows the simplification $\widetilde{Y|Z} = \widetilde{Y}$. Finally, an arbitrary Favre-filtered quantity $\widetilde{\psi}$ can be expressed as function of $\widetilde{Z}$, $\widetilde{Z''^2}$ and $\widetilde{Y}$, so that Eq. 3.42 becomes valid.

3.3 Radiation modeling

In combustion simulations, heat transfer by radiation is often neglected as a consequence of the high computational cost involved. However, whereas heat transfer rates due to convection and conduction increase linearly with the temperature difference, the radiative heat transfer rate increases with the fourth power of the temperature difference. Especially in realistic furnaces (such as the swirl-stabilized PCC burner flow reactor studied in section 5.3), radiation effects can have a significant impact on the total heat transfer and thus, should be considered in the modeling. In this work, the models implemented by Cavallo Marincola are used. A detailed description can be found in the PhD thesis of Cavallo Marincola [18], to which the interested reader is referred to. Subsequently, the basic concepts of modeling radiation effects shall be briefly outlined. To describe the radiative energy intensity I through a medium at a point r for a specific direction $\hat{s}$, a general radiative transfer equation (RTE) can be derived, which reads:

$$\frac{dI}{ds} = \kappa\left(r\right) I_{\mathrm{b}}\left(r\right) - \kappa\left(r\right) I\left(r,\hat{s}\right) - \sigma_{\mathrm{sc}}\left(r\right) I\left(r,\hat{s}\right) + \frac{\sigma_{\mathrm{sc}}\left(r\right)}{4\pi}\int_{4\pi} I\left(r,\hat{s}\right)\Phi\left(r,\hat{s}_i,\hat{s}\right) d\Omega_i \tag{3.57}$$

In Eq. 3.57, κ and σ_{sc} denote the absorption and scattering coefficients, I_{b} describes the black-body intensity, given as $I_{\mathrm{b}} = \sigma T^4/\pi$, where $\sigma \approx 5.6704\text{E-}8\,\mathrm{W/(m^2K^4)}$ is the Stefan-Boltzmann constant. The terms on the RHS of Eq. 3.57 describe the energy emission, the energy absorption, and the attenuation and augmentation due to scattering, respectively, while the latter is given by the integral over all unit angles Ω_i, taking into account the probability Φ of a ray with direction $\hat{s}_i$ to be scattered into a different direction $\hat{s}$. The discrete ordinates method (DOM) is used to discretize and solve the general RTE. The DOM was first proposed by Chandrasekhar [19] and further developed for general heat transfer by Truelove [168] and Fiveland [30]. Using this method, the general RTE is discretized in n different directions $\hat{s}_j$. Thus, the integral of the last term on the RHS of Eq. 3.57 can be reformulated as:

$$\int_{4\pi} f\left(\hat{s}\right) d\Omega = \sum_{j=1}^{n} w_j f\left(\hat{s}_j\right) \tag{3.58}$$

Here, w_j denotes the quadrature weight for each direction. The discretized formulation of the general RTE (Eq. 3.57) then reads:

$$\frac{dI}{ds} = \kappa\left(r\right) I_{\mathrm{b}}\left(r\right) - \kappa\left(r\right) I\left(r,\hat{s}\right) - \sigma_{\mathrm{sc}}\left(r\right) I\left(r,\hat{s}\right) + \frac{\sigma_{\mathrm{sc}}\left(r\right)}{4\pi}\sum_{j=1}^{n} w_j I\left(r,\hat{s}_j\right)\Phi\left(r,\hat{s}_i,\hat{s}_j\right) \tag{3.59}$$

The RTE can be iteratively solved for each direction, provided that the absorption and scattering coefficients at each point in the domain are known. The iteration scheme is outside the scope of this work. For a detailed explanation, the reader is referred to [18]. The sum of all intensities acting on a given control volume then represents the incident radiation G, which can be discretized by:

$$G = \int_{4\pi} I\left(\hat{s}\right) d\Omega \approx \sum_{j=1}^{n} w_j I_j \tag{3.60}$$

Finally, the radiative source term ∇q can be derived by:

$$\nabla q = \kappa\left(4\pi I_{\mathrm{b}} - \int_{4\pi} I\left(\hat{s}\right) d\Omega\right) \approx \kappa\left(4\pi I_{\mathrm{b}} - G\right) \tag{3.61}$$

The RTE is discretized and solved in 80 directions using a S8 approximation. The grey weighted sum of grey gases (GWSGG) model is used to model gas phase spectral properties. The model parameters are taken from the work by Kangwanpongpan et al. [66]. Particle radiative heat transfer through absorption, scattering and emission is considered in this work, while the latter is derived from a correlation function with the char burnout, which will be described in more detail in section 3.5.2.

The interplay between turbulence and radiation presents a dynamic exchange: radiation influences both, the flow and species concentration fields, while simultaneously being influenced by turbulent fluctuations within the flow field. Turbulence-radiation interaction requires additional modeling. In the context of RANS simulations, which yield time-averaged flow fields, it is imperative to account for turbulence-radiation interaction to prevent significant errors. However, in LES, turbulence-radiation interaction is primarily relevant at a subgrid scale, diminishing its overall importance.

Similar to the work of Cavallo Marincola [18], this work omits consideration of turbulence-radiation interaction, assuming a sufficiently well-resolved grid. Consequently, the absorption coefficient κ, blackbody intensity I_b, and radiative source term ∇q are approximated under the assumption that any correlation between fluctuations in intensity and the local absorption coefficient can be neglected:

$$\overline{\kappa\left(T,p\right)} \approx \kappa\left(\widetilde{T},\widetilde{p}\right) \tag{3.62}$$

$$\overline{I_\mathrm{b}\left(T\right)} \approx I_\mathrm{b}\left(\widetilde{T}\right) \tag{3.63}$$

$$\overline{\nabla q\left(T,Y_\alpha,p\right)} \approx \nabla q\left(\widetilde{T},\widetilde{Y_\alpha},\widetilde{p}\right) \tag{3.64}$$

3.4 Coal conversion modeling

The following section aims to outline the modeling approaches used to represent coal combustion. First, the modeling of the devolatilization process shall be described, followed by a brief review of the modeling approaches used to describe the volatile composition. Subsequently, the modeling of the char conversion is discussed.

3.4.1 Devolatilization modeling

The volatile release rate depends on the pyrolysis characteristics of the specific coal type. A number of different detailed models exist for the modeling of the devolatilization rate, treating the pyrolysis of coal as one or multiple chemical reactions. A general distinction is made between the more simplistic empirical models, which describe the overall devolatilization process by one or more Arrhenius-type expressions, and the more complex network models, which characterize the coal structure in greater detail. Empirical models are very sensitive to fit and give accurate predictions only for the fitted operational range of conditions. Nonetheless, they are often preferred to network models, since these models are associated with a high computational costs. This limits the use of network models in large-scale simulations.

Empirical models range from the simplest single first order (SFOR) model by Badzioch and Hawksley [8], which describes the devolatilization rate by one Arrhenius-type expression, to multi-step models such as the two-competing model (TCM) by Kobayashi [75], which takes into account two Arrhenius-type expressions. An extension of these models is the distributed activation energy (DAE) model [5, 120], which considers a large number of independent, parallel reactions that feature different activation energies. The most popular network models include the chemical percolation devolatilization (CPD) model by Grant et al. [42] and later on extended by Fletcher et al. [31, 32], the flash-distillation chain-statistics (FLASHCHAIN) model by Niksa and Kerstein [109], and the functional group-depolymerization, vaporization and crosslinking (FG-DVC) model by Solomon et al. [156], all of which are similar in the level of detail in the description of the coal structure, yet feature differences among the characterization of the macromolecular structure.

Despite the range of detailed models available to describe the devolatilization process, in this work solely the computational cost-efficient SFOR model is used [8], which shall be explained in more detail hereinafter. For a detailed description of all of the above mentioned models, the interested reader is referred to the review by Hasse et al. [47].

The SFOR model by Badzioch and Hawksley [8] is one of the simplest devolatilization models, describing the overall volatile release by a single reaction rate. The coal conversion can thus be described in simplified fashion via Eq. 3.65:

$$\text{Coal} \xrightarrow{k_\mathrm{devol}} \text{Char} + \text{Tar} + \text{Gas} \tag{3.65}$$

The devolatilization rate k_{devol} is then described by a simple Arrhenius-type expression, reading:

$$k_{\mathrm{devol}} = A e^{[E_{\mathrm{A}}/(R T_{\mathrm{p}})]} \tag{3.66}$$

where A and E_{A} are the pre-exponential factor and the activation energy, which need to be fitted to the pyrolysis characteristics of the specific coal type.

The rate constants of the SFOR model are fitted via the particle kinetics preprocessor (PKP) developed by Vascellari et al. [178]. The PKP tool iteratively fits new rate constants using detailed reference solutions (in this work, CPD is used). The general approach is as follows: First, based on the proximate and ultimate analysis of the coal being studied, the kinetic parameters are determined using the selected detailed model. An initial estimate of the expected occurring heating rates of the particle history is chosen to determine volatile yields and pyrolysis rates using the detailed model. Subsequently, the model parameters for the empirical model are calibrated. In turn, these are used in the LES and the new heating rates are extracted from the simulation, which again are used to run the detailed model in PKP.

Ideally, the iterative process is repeated until the solution converges and realistic heating rates are achieved. However, this procedure is often not feasible in LES. Thus, in this work, the initial estimate of the heating rates was chosen based on previous studies from comparable burner setups with similar coal types. The empirical model calibration was then performed with one or two iteration loops based on coarse grid simulations. Figure 3.6 shows the general workflow of the particle kinetics preprocessor to determine the empirical model constants.

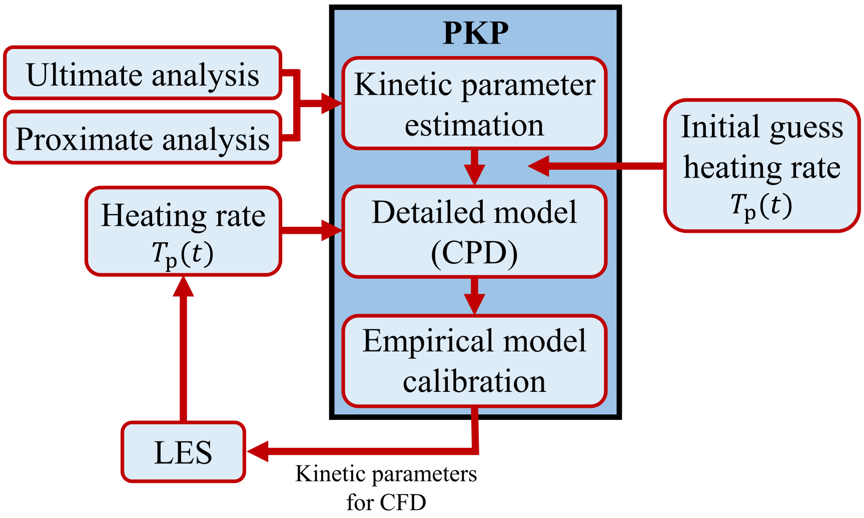

Figure 3.6: Schematic representation of the particle kinetics preprocessor (PKP) workflow. Adapted from [178].

Finally, the devolatilization mass flow can be expressed as:

$$\dot{m}_{\mathrm{p,vol}} = k_{\mathrm{devol}} \left(m_{\mathrm{p,VM,0}} - m_{\mathrm{p,VM}} \right) \tag{3.67}$$

taking into account the difference of the initial volatile mass $m_{\mathrm{p,VM,0}}$ (considering the corrected volatile yield at high heating rates, as described by Eq. 2.41) and the current volatile mass $m_{\mathrm{p,VM}}$ of a computational particle. During the volatile release process, the particle diameter d_{p} is assumed to stay constant, while the particle density is decreasing, depending on the change of particle mass, reading:

$$\rho_{\mathrm{p}} = 6 \frac{m_{\mathrm{p}}}{\pi d_{\mathrm{p}}^3} \tag{3.68}$$

The volatile gases are assumed to be released from the coal particle at particle temperature.

3.4.2 Volatile composition modeling

In this work, two approaches to determine the volatile gas composition were adopted to be used for the subsequent 1D flamelet simulations in order to generate the flamelet library. These shall be briefly outlined next.

In section 5.1, similar to the work of a previous collaborator Rieth et al. [137], the volatile composition was determined by applying the approach of Stöllinger et al. [163], using the extended formulations of Petersen and Werther [116]. In this approach, the atomic composition of the volatile gas is initially determined by subtracting the residual carbon from the ultimate analysis, which results from the volatile yield under high heating rates (see Eq. 2.41). The released volatiles are then determined using three splitting factors ξ (accounting for the carbon products CO, tar and C_2H_4) via a stoichiometrically consistent equation:

$$\begin{aligned}
\mathrm{C}_{\nu_\mathrm{C}}\mathrm{H}_{\nu_\mathrm{H}}\mathrm{O}_{\nu_\mathrm{O}}\mathrm{S}_{\nu_\mathrm{S}}\mathrm{N}_{\nu_\mathrm{N}} \rightarrow\ & \nu_\mathrm{S}\mathrm{H_2S} + \frac{1}{2}\nu_\mathrm{N}\mathrm{N_2} + \xi_\mathrm{CO}\nu_\mathrm{O}\mathrm{CO} + \frac{1}{2}\left(1-\xi_\mathrm{CO}\right)\nu_\mathrm{O}\mathrm{CO_2} \\
& + \left[\left(1 - 2\xi_{\mathrm{C_2H_4}} - 6\xi_\mathrm{tar}\right)\nu_\mathrm{C} - \frac{1}{2}\left(\xi_\mathrm{CO}+1\right)\nu_\mathrm{O}\right]\mathrm{CH_4} \\
& + \left[\frac{1}{2}\nu_\mathrm{H} - 2\left(1-\xi_{\mathrm{C_2H_4}} - 4.5\xi_\mathrm{tar}\right)\nu_\mathrm{C} + \left(\xi_\mathrm{CO}+1\right)\nu_\mathrm{O} - \nu_\mathrm{S}\right]\mathrm{H_2} \\
& + \xi_{\mathrm{C_2H_4}}\nu_\mathrm{C}\mathrm{C_2H_4} + \xi_\mathrm{tar}\nu_\mathrm{C}\mathrm{C_6H_6}
\end{aligned} \tag{3.69}$$

where ν_i are the mole fractions of the components C, H, O, S, N, respectively. cDue to the results of the ultimate analysis for the coal composition in the case of section 5.1, sulphur is neglected, and thus, $\nu_\mathrm{S} = 0$. The splitting factors are chosen such that the atomic composition is maintained and were set to: $\xi_\mathrm{CO} = 1.0$, $\xi_\mathrm{tar} = 0.0$ and $\xi_{\mathrm{C_2H_4}} = 0.59$, assuming a negligibly small tar yield and high amounts of CO instead of CO_2, similar to the work of Rieth et al. [137]. The splitting factors have to be chosen such that positive mass fractions result and that the weighted heating values of the volatile gas composition and the fixed carbon, based on mass fractions on a dry and ash-free basis, align with the experimentally determined coal heating value. Further information can be found in section 5.1.

In sections 5.2 and 5.3, the volatile composition was determined using the CRECK-S-C model [100], applying the detailed approach of Debiagi et al. [26]. The model is able to determine devolatilization rates and detailed product compositions. This is achieved by integrating the instantaneous volatile release rates over time, which allows the determination of the overall predicted volatile yield. A detailed description of this model is beyond the scope of this work. The interested reader is referred to the works of Migliavacca et al. [100] and Debiagi et al. [26], a good overview can also be found in the PhD Thesis by Nicolai [105]. Further information on the modeled volatile compositions used for the simulations in this work can be found in sections 5.2 and 5.3.

3.4.3 Char conversion modeling

After the volatiles are released, char combustion takes place. In this process, the remaining carbon in the coal particle is oxidized via heterogeneous surface reactions. As introduced in section 2.4.2, char combustion can either be kinetically limited or diffusion limited (see Fig. 2.4). Factors such as char porosity, char reactivity, specific surface area of the particle, particle temperature and temperature histories, such as the concentration of the oxidizer and the effect of ash inhibition play an essential role for the char conversion rate. Thus, its accurate modeling requires plenty of information about the coal's physical and chemical properties, which are often neither known, nor well understood. As a result, the current char combustion model is based on the limited available data and is generally simple.

In this work, Smith's intrinsic reaction rate model is used [152], which will be described next. For a comprehensive overview of the applied equations, the interested reader is referred to the works of Stöllinger et al. [163] and Rieth et al. [137].

The model assumes CO to be the only immediate species after char oxidation, just taking into account the predominant elementary reaction at high temperature char combustion:

$$\mathrm{C}_{\mathrm{char}} + \frac{1}{2}\,\mathrm{O}_2 \rightarrow \mathrm{CO} \tag{3.70}$$

The total char off-gas rate can then be determined as:

$$\dot{m}_{\mathrm{p,char}} = X_{\mathrm{O}_2}\, p_0\, \pi\, d_{\mathrm{p}}^2\, \frac{R_{\mathrm{ox}}\, R_{\mathrm{char}}}{R_{\mathrm{ox}} + R_{\mathrm{char}}} \tag{3.71}$$

Here, X_{O_2} and p_0 are the oxygen mole fraction the coal particle experiences and the atmospheric pressure, respectively. Further, R_{ox} and R_{char} are the bulk molecular mass diffusion rates of oxygen and char. The former can be calculated as:

$$R_{\mathrm{ox}} = C_{\mathrm{diff}}\, \frac{T_m^{0.75}}{d_{\mathrm{p}}} \tag{3.72}$$

using the mass diffusion-limited rate constant $C_{\mathrm{diff}} = 5.0\,\mathrm{E}{-12}\,\mathrm{s\,K^{-0.75}}$ and the mean temperature between particle and gas phase, given as $T_m = (\widetilde{T} + T_{\mathrm{p}})/2$. The mass diffusion rate R_{char} is governed by:

$$R_{\mathrm{char}} = \eta \rho_{\mathrm{p}} S_a \frac{d_{\mathrm{p}}}{6} k_i \tag{3.73}$$

taking into account the effectiveness factor η, the specific internal surface area S_a, and the intrinsic reactivity k_i. The latter is determined from an Arrhenius expression as:

$$k_i = A_i\, e^{-\frac{E_i}{R T_{\mathrm{p}}}} \tag{3.74}$$

Both, the pre-exponential factor A_i and the activation energy E_i are taken from the work by Stöllinger et al. [163], taking values of $A_i = 0.052\,\mathrm{kg/(m^2\,s\,Pa)}$ and $E_i = 161500\,\mathrm{J/(kmol\,K)}$. The specific internal surface area S_a depends on the char burnout b_{char} and the initial surface area $S_{a,0}$. It reads:

$$S_a = S_{a,0}\,(1 - b_{\mathrm{char}}) \sqrt{\frac{b_{\mathrm{char}}}{\theta_{\mathrm{p}}} + 1 - b_{\mathrm{char}}} \qquad \text{with} \qquad b_{\mathrm{char}} = 1 - \frac{m_{\mathrm{p,FC}}}{m_{\mathrm{p,FC,0}}} \tag{3.75}$$

Here, $m_{\mathrm{p,FC}}$, $m_{\mathrm{p,FC,0}}$, and θ_{p} are the current and initial fixed carbon contents of the coal particle and the coal porosity, respectively, taking a value of $\theta_{\mathrm{p}} = 0.7$. The initial surface area $S_{a,0}$ can be approximated by [200]:

$$S_{a,0} = 1546300\, Y_{\mathrm{p,FC}}^2 - 2834900\, Y_{\mathrm{p,FC}} + 1301700 \tag{3.76}$$

using the mass fraction of the fixed carbon content on a *daf* basis $Y_{\mathrm{p,FC}}$, as explained in section 2.4. The effectiveness factor η is calculated as a function of the Thiele modulus ϕ, reading:

$$\eta = \frac{3}{\phi^2}\,(\phi \coth \phi - 1) \tag{3.77}$$

The Thiele modulus ϕ is then determined as:

$$\phi = \frac{d_{\mathrm{p}}}{2} \left(\frac{S_{\mathrm{O}_2}\, S_a\, \rho_{\mathrm{p}}\, k_i\, X_{\mathrm{O}_2}\, p_0}{D_e\, \rho\, Y_{\mathrm{O}_2}} \right)^{1/2} \tag{3.78}$$

Here, $S_{\mathrm{O}_2} \approx 1.33$ denotes the stoichiometric oxygen mass required for the heterogeneous surface reaction in Eq. 3.70. The effectiveness factor η accounts for the resistance due to pore diffusion, considering the effective diffusion coefficient in the particle pores D_e, given by:

$$D_e = \frac{\theta_{\mathrm{p}}}{\tau^2} \left(\frac{1}{D_{Kn}} + \frac{1}{D_{\mathrm{ox}}} \right)^{-1} \tag{3.79}$$

where τ is the pore tortuosity, taking a value of $\tau = \sqrt{2}$. Further, D_{Kn} and D_{ox} describe the Knudsen and the oxygen diffusion coefficient. According to Eq. 3.79, bulk and Knudsen diffusion are assumed to take place in parallel. The Knudsen diffusion coefficient is calculated as:

$$D_{Kn} = C_{Kn} \overline{r}_{\mathrm{pore}} \sqrt{\frac{T_{\mathrm{p}}}{M_{\mathrm{O}_2}}} \tag{3.80}$$

where $C_{Kn} = 97\,\mathrm{kg}^{0.5}\,\mathrm{m}\,\mathrm{K}^{-0.5}\,\mathrm{kmol}^{-0.5}\,\mathrm{s}^{-1}$ is a dimensional constant and M_{O_2} is the molecular weight of oxygen. The mean pore radius $\overline{r}_{\mathrm{pore}}$ is governed by:

$$\overline{r}_{\mathrm{pore}} = \frac{2\theta_{\mathrm{p}}\sqrt{\tau}}{S_a \rho_{\mathrm{p}}} \tag{3.81}$$

Finally, the diffusion coefficient of oxygen D_{ox} is calculated by:

$$D_{\mathrm{ox}} = D_0 \left(\frac{T_m}{T_0} \right)^{1.75} \tag{3.82}$$

where D_0 is a binary diffusion coefficient for O_2 in N_2, given as $D_0 = 3.13\,\mathrm{E{-}4}\,\mathrm{m}^2/\mathrm{s}$ at a reference temperature $T_0 = 1500\,\mathrm{K}$ (at one atmosphere), following the work by Baum and Street [9].

During the char conversion process, the particle density does not change, while the particle diameter is decreasing depending on the change of particle mass, reading:

$$d_{\mathrm{p}} = \left(\frac{m_{\mathrm{p,FC}}}{\rho_{\mathrm{p}}} \frac{6}{\pi} \right)^{1/3} \tag{3.83}$$

3.5 Dispersed phase modeling

This section deals with the modeling of the dispersed phase. Particles are described in a Lagrangian manner in *PsiPhi*. The underlying equations for the description of Lagrangian particles in a reactive turbulent flow are presented first, addressing the description of the particle motion and the interphase heat exchange. Finally, the coupling terms for the interaction of the gas- and solid phase are clarified, closing the equations in section 3.1.3.1.

3.5.1 Particle motion

Particle motion is driven by multiple forces. These forces include drag and lift, which arise from the exchange of momentum between the fluid and the particle. Additionally, there is a gravitational force acting on the particle due to its mass, as well as a buoyancy force exerted by the fluid in the opposite direction. Moreover, a thermophoretic force emerges as a result of temperature gradients within the flow. A Brownian force, describing irregular and erratic thermal motion, contributes to the particle's overall motion. It is evident that the description of the complex particle motion depends on many factors and assumptions have to be made to simplify its mathematical description.

In this work, all particles are assumed to be spherical and non-deformable. A uniform temperature throughout the particle is assumed (i.e., the conductivity across the particle is infinite). A dilute particle phase is assumed, implying no direct particle-to-particle interactions, and thus, particle collisions, coalescence, or agglomeration are neglected. As the solid particles have a much greater density than the surrounding gas, the only interacting forces are assumed to be the drag force and the gravitational force. An important quantity for the description of the particle drag force is the particle Reynolds number Re_{p}, which is given by:

$$Re_{\mathrm{p}} = \frac{\rho |u - u_{\mathrm{p}}| d_{\mathrm{p}}}{\mu} \tag{3.84}$$

Here, $|u - u_\mathrm{p}|$ is the relative velocity between both, gas (u) and particle (u_p) phases, and d_p is the particle diameter. A quantity describing the relevance of the particle inertia for its motion in a moving fluid is the Stokes number. In order to describe the dimensionless Stokes number, the particle relaxation time should be introduced first. The particle relaxation time τ_p describes the time required for a particle accelerated by drag to reach its equilibrium state again. It reads:

$$\tau_\mathrm{p}^{-1} = \frac{3}{4}\frac{\rho\, c_\mathrm{D}}{\rho_\mathrm{p}\, d_\mathrm{p}}|u - u_\mathrm{p}| \tag{3.85}$$

where c_D and ρ_p are the drag coefficient and the particle density. The Stokes number St can then be written as:

$$St = \frac{\tau_\mathrm{p}|u|}{d_\mathrm{p}} \tag{3.86}$$

For $St \ll 1$, the particle follows the local fluid streamlines. Conversely, if the particle Stokes number is large, the particle inertia is predominant, and the particle will follow its initial trajectory. A further dimensionless quantity to characterize particle motion is the Froude number Fr, which describes the ratio of inertial forces to gravitational forces acting on a particle. It reads:

$$Fr^2 = \frac{|u|^2}{d_\mathrm{p}|g|} \tag{3.87}$$

Thus, a low Froude number indicates that particle dynamics are governed predominantly by gravitational forces, whereas a high Froude number suggests negligible influence of gravitational force. In the context of turbulent pulverized coal flames, however, the Froude number plays a minor role and is mentioned for the sake of completeness. Ultimately, the particle trajectory and acceleration can be determined accordingly:

$$\frac{dx_\mathrm{p}}{dt} = u_\mathrm{p} \tag{3.88}$$

$$a_\mathrm{p} = \frac{du_\mathrm{p}}{dt} = \frac{F_\mathrm{D}}{m_\mathrm{p}} + \frac{F_\mathrm{G}}{m_\mathrm{p}} \tag{3.89}$$

Here, x_p and a_p are the particle position and acceleration, while F_D and F_G are the drag force and the gravitational force, calculated as:

$$F_\mathrm{G} = m_\mathrm{p}\left(1 - \frac{\rho}{\rho_\mathrm{p}}\right) g \tag{3.90}$$

$$F_\mathrm{D} = \frac{m_\mathrm{p}}{\tau_\mathrm{p}}\left(u - u_\mathrm{p}\right) = \frac{3}{4}\frac{\rho\, m_\mathrm{p}}{\rho_\mathrm{p}\, d_\mathrm{p}}\, c_\mathrm{D}\left(u - u_\mathrm{p}\right)|u - u_\mathrm{p}| \tag{3.91}$$

The particle Reynolds number Re_p and the drag coefficient c_D show an empirical correlation. Thus, c_D can be expressed by Re_p, following the drag law for spherical particles by Schiller and Naumann [144]:

$$c_\mathrm{D} = \begin{cases} \frac{24}{Re_\mathrm{p}}\left(1 + \frac{Re_\mathrm{p}^{2/3}}{6}\right) & \text{if} \quad Re_\mathrm{p} \le 1000 \\ 0.424 & \text{if} \quad Re_\mathrm{p} > 1000 \end{cases} \tag{3.92}$$

This correlation demonstrates that at high particle Reynolds numbers ($Re_\mathrm{p} > 1000$), the drag coefficient becomes asymptotically independent of the particle Reynolds number, whereas in the transition region ($Re_\mathrm{p} \le 1000$), inertial effects significantly influence the drag coefficient.

However, in LES only the large scales are resolved, while the subgrid scales need to be modeled. For the LES of PCC, the particle sizes are usually much smaller than the smallest resolved scales, which implies that the effect of the unresolved part of the turbulent scales on the particle motion has to be addressed. Since the smallest scales behave quasi-randomly and in an isotropic manner, stochastic methods are particularly suitable to describe this effect on the particle trajectory. In this work, the impact of the subgrid scales on the particle trajectories is described by a decomposition of each particle acceleration equation (Eq. 3.89), balancing the particle acceleration and all acting forces onto the particle, into deterministic and stochastic components, the latter accounting for subgrid effects, as proposed in previous works by Bini and Jones [11, 12]. The particle position and acceleration of a stochastic particle can then be obtained by Eq. 3.88 and:

$$du_{\mathrm{p}} = \left(1 - \frac{\overline{\rho}}{\rho_{\mathrm{p}}}\right) g \; dt + \frac{\widetilde{u} - u_{\mathrm{p}}}{\tau_{\mathrm{p}}} \; dt + \sqrt{C_0 \frac{k_{\mathrm{SGS}}}{\tau_{\mathrm{p,t}}}} \; dW \tag{3.93}$$

The first two terms on the RHS of Eq. 3.88 account for the gravity/buoyancy forces and the drag force acting on the particle due to the resolved scales (similar to Eqs. 3.90 and 3.91). The last term on the RHS represents the subgrid scale effects on the particle dynamics, with $C_0 = 1$ being the dispersion constant and k_{SGS} being the subgrid scale kinetic energy of the gas phase. The latter can be calculated as:

$$k_{\mathrm{SGS}} = 2\,\Delta\, C_{\mathrm{m}}^{2/3}\, \widetilde{S}_{ij}\, \widetilde{S}_{ij} \tag{3.94}$$

assuming an equilibrium of the subgrid scales. Again, C_{m} is the subgrid scale model constant, $\widetilde{S}_{ij}$ is the filtered strain rate tensor and Δ is the cell width. The turbulent particle relaxation time $\tau_{\mathrm{p,t}}$ is given by:

$$\tau_{\mathrm{p,t}} = \tau_{\mathrm{p}} \left(\frac{\tau_{\mathrm{p}}\, k_{\mathrm{SGS}}^{1/2}}{\Delta} \right)^{0.6} \tag{3.95}$$

The last term on the RHS of Eq. 3.93 is further scaled with the incremental Wiener process dW, a three-dimensional random variable obtained from a normal distribution with zero mean and a variance equaling $\sqrt{dt}$ [122]. For a detailed description of the statistical method used, the reader is referred to the original works by Bini and Jones [11, 12].

3.5.2 Particle heat transfer

In PCC, heat transfer between gas and particle phase occurs mainly through convective heat exchange, radiative emission of the particle and absorption from the gas phase, and heat releases through devolatilization and char combustion with the latter capable of both elevating and reducing the particle temperature. The various heat transfer processes are illustrated in Fig. 3.7. The infinite conductivity through the particle adopted in the modeling is sketched by a uniform temperature. The particle temperature balance equation is governed by the net heat transfer on the particle surface, reading:

$$\underbrace{\frac{dT_{\mathrm{p}}}{dt}}_{\text{Accumulation}} = \underbrace{\frac{1}{\tau_{\mathrm{con}}}\,(T - T_{\mathrm{p}})}_{\text{Convection}} + \underbrace{\frac{\epsilon_{\mathrm{p}}\, A_{\mathrm{p}}}{m_{\mathrm{p}}\, c_{p,\mathrm{p}}}\,(G - 4\,\pi\, I_{\mathrm{b,p}})}_{\text{Radiation}} + \underbrace{\frac{\dot{q}_{\mathrm{vol}}}{m_{\mathrm{p}}\, c_{p,\mathrm{p}}}}_{\text{Devolatilization}} + \underbrace{\frac{\dot{q}_{\mathrm{char}}}{m_{\mathrm{p}}\, c_{p,\mathrm{p}}}}_{\text{Char burnout}} \tag{3.96}$$

where the term on the LHS denotes the temporal evolution of the particle temperature and the terms on the RHS denote the heat transfer due to convection, radiation, devolatilization, and char burnout, respectively. In Eq. 3.96, τ_{con} is the convective time scale, ϵ_{p} is the particle emissivity, A_{p} is the projected particle area ($A_{\mathrm{p}} = \pi\, d_{\mathrm{p}}^2/4$), G is the incident radiation (obtained by the DOM, as described in section 3.3), $I_{\mathrm{b,p}}$ is the blackbody radiation intensity of the particle (calculated as $I_{\mathrm{b,p}} = \sigma\, T_{\mathrm{p}}^4/\pi$, where σ is the Stefan-Boltzmann constant), $c_{p,\mathrm{p}}$ is the particle heat capacity, while $\dot{q}_{\mathrm{vol}}$ and $\dot{q}_{\mathrm{char}}$ are the heat fluxes due to devolatilization and char burnout. The convective time scale τ_{con} can be determined as:

$$\tau_{\mathrm{con}} = \frac{1}{6}\,\frac{Pr}{Nu}\,\frac{c_{p,\mathrm{p}}}{c_p}\,\frac{\rho_{\mathrm{p}}\, d_{\mathrm{p}}^2}{\mu} \tag{3.97}$$

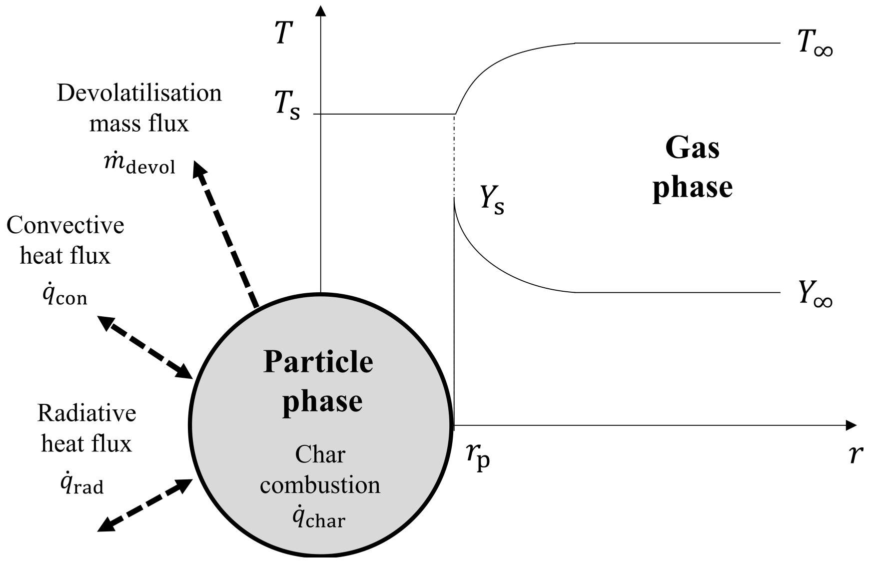

Figure 3.7: Schematic representation of the heat transfer processes occurring in PCC (adapted from [82]). The subscript "s" denote the particle surface quantity.

where c_p is the heat capacity of the mixture in the gas phase and the Prandtl number Pr is assumed to be constant ($Pr = 0.7$). The Nusselt number Nu is calculated using the Ranz-Marshall correlation [93], reading:

$$Nu = 2 + 0.552 Re_{\mathrm{p}}^{1/2} Pr^{1/3} \tag{3.98}$$

The particle emissivity ϵ_{p} is estimated as a function of the char burnout, following the approach by Stoellinger et al. [163], reading:

$$\epsilon_{\mathrm{p}} = \epsilon_{\mathrm{coal}} - \left(\epsilon_{\mathrm{ash}} - \epsilon_{\mathrm{coal}}\right) \frac{\left(1 - Y_{\mathrm{p,VM,0}}\right) m_{\mathrm{p,0}} - m_{\mathrm{p}}}{\left(1 - Y_{\mathrm{p,VM,0}}\right) m_{\mathrm{p,0}} - \left(1 - Y_{\mathrm{p,VM,0}} - Y_{\mathrm{p,FC,0}}\right) m_{\mathrm{p,0}}} \tag{3.99}$$

with the emissivities of the unreacted particle $\epsilon_{\mathrm{coal}} = 0.9$ and ash particle $\epsilon_{\mathrm{ash}} = 0.5$, the mass fractions of volatile matter $Y_{\mathrm{p,VM,0}}$, and char $Y_{\mathrm{p,FC,0}}$, the particle mass at initial state $m_{\mathrm{p,0}}$, and the current particle mass m_{p}.

The heat flux due to devolatilization $\dot{q}_{\mathrm{vol}} = \dot{m}_{\mathrm{p,vol}}\, h_{\mathrm{vol}}$ presents the latent heat of devolatilization and can thus be neglected in Eq. 3.96. The heat flux resulting from char combustion is determined based on the assumption that only one heterogeneous reaction occurs, which is represented as $\mathrm{C_{char}} + 0.5\,\mathrm{O_2} \rightarrow \mathrm{CO}$. Hence, the particle initially absorbs heat due to the partial oxidation from C to CO, and subsequently releases heat due to the release of CO into the gas phase at gas temperature. The heat flux due to char combustion $\dot{q}_{\mathrm{char}}$ can be detetermined as:

$$\dot{q}_{\mathrm{char}} = -\dot{m}_{\mathrm{p,char}} \left[\left(S_{\mathrm{O_2}} + 1\right) h_{\mathrm{CO}} - S_{\mathrm{O_2}}\, h_{\mathrm{O_2}} - h_{\mathrm{char}} \right] \tag{3.100}$$

Here, $S_{\mathrm{O_2}}$ is the stoichiometric oxygen mass required for the heterogeneous char reaction, h_{CO} and $h_{\mathrm{O_2}}$ are the enthalpies of species CO and $\mathrm{O_2}$ at gas temperature, and h_{char} is the enthalpy of the char at particle temperature. The particle heat capacity is calculated using Eq. 2.37.

A blowing correction is applied in the simulations of this work to account for the influence of rapid devolatilization on the particle's momentum and convective heat transfer. The blowing correction B is governed following the approach by Stöllinger et al. [163]. It reads:

$$B = \frac{Pr}{2\,\pi\, d_{\mathrm{p}}\, \mu}\, \dot{m}_{\mathrm{p,vol}} \tag{3.101}$$

Equation 3.101 is then applied to the Nusselt number Nu (Eq. 3.98) and the particle relaxation time τ_p Eq. 3.85 as:

$$\tau_\mathrm{p}^* = \tau_\mathrm{p}\,(1+B) \tag{3.102}$$

$$Nu^* = Nu\;e^{-0.6B} \tag{3.103}$$

Finally, the corrected values of Nu and τ_p, denoted by (*), are used in the aforementioned equations.

3.5.3 Interphase coupling terms

The Favre-filtered transport equations 3.10, 3.17, 3.23, and 3.24 contain filtered source terms that account for the solid-gas interphase exchange, which can be generally described as:

$$\overline{\dot{S}}_\phi = \frac{1}{\Delta^3}\sum_{\mathrm{p}=1}^{N_\mathrm{p}} \dot{S}_{\mathrm{p},\phi} \tag{3.104}$$

Here, N_p is the total number of particles within a cell volume and $\dot{S}_{\mathrm{p},\phi}$ is the arising source term of a given particle.

In terms of the Favre-filtered continuity equation (Eq. 3.10), the source term is obtained from the particle mass released into the gas phase, originating from the devolatilization and the char burnout:

$$\overline{\dot{S}}_\mathrm{mass} = \frac{1}{\Delta^3}\sum_{\mathrm{p}=1}^{N_\mathrm{p}} \dot{m}_\mathrm{p} = \frac{1}{\Delta^3}\sum_{\mathrm{p}=1}^{N_\mathrm{p}} \dot{m}_\mathrm{p,vol} + \frac{1}{\Delta^3}\sum_{\mathrm{p}=1}^{N_\mathrm{p}} \dot{m}_\mathrm{p,char} \tag{3.105}$$

The interphase momentum transfer from the particle to the gas phase, as described by Eq. 3.17, considers the contributions of particle drag and momentum. It is calculated as follows:

$$\overline{\dot{S}}_\mathrm{mom} = \frac{1}{\Delta^3}\sum_{\mathrm{p}=1}^{N_\mathrm{p}} F_\mathrm{D,p} + \frac{1}{\Delta^3}\widetilde{u}_i\sum_{\mathrm{p}=1}^{N_\mathrm{p}} \dot{m}_\mathrm{p} = \frac{1}{\Delta^3}\sum_{\mathrm{p}=1}^{N_\mathrm{p}} F_\mathrm{D,p} + \frac{1}{\Delta^3}\widetilde{u}_i\sum_{\mathrm{p}=1}^{N_\mathrm{p}} \dot{m}_\mathrm{p,vol} + \frac{1}{\Delta^3}\widetilde{u}_i\sum_{\mathrm{p}=1}^{N_\mathrm{p}} \dot{m}_\mathrm{p,char} \tag{3.106}$$

The species source term in Eq. 3.23 results from the species mass released into the gas phase due to devolatilization as well as the consumption and release of species due to char combustion. It can be calculated as:

$$\overline{\dot{S}}_{Y_\alpha} = \frac{1}{\Delta^3}\sum_{\mathrm{p}=1}^{N_\mathrm{p}} \dot{m}_\mathrm{p}\,Y_{\mathrm{p},\alpha} = \frac{1}{\Delta^3}\sum_{\mathrm{p}=1}^{N_\mathrm{p}} \dot{m}_\mathrm{p,vol}\,Y_{\mathrm{p,VM},\alpha} + \frac{1}{\Delta^3}\sum_{\mathrm{p}=1}^{N_\mathrm{p}} \dot{m}_\mathrm{p,char}\,Y_{\mathrm{p,FC},\alpha} \tag{3.107}$$

Finally, the enthalpy source term in Eq. 3.24 is computed as:

$$\overline{\dot{S}}_\mathrm{h} = \frac{1}{\Delta^3}\sum_{\mathrm{p}=1}^{N_\mathrm{p}} \left[\frac{m_\mathrm{p}\,c_{p,\mathrm{p}}}{\tau_\mathrm{con}}\left(\widetilde{T}-T_\mathrm{p}\right) + \dot{m}_\mathrm{p,vol}\,h_\mathrm{vol} + \dot{m}_\mathrm{p,char}\,h^*_\mathrm{char}\right] + \dot{Q}_\mathrm{rad} \tag{3.108}$$

with the radiative enthalpy source term:

$$\dot{Q}_\mathrm{rad} = -\epsilon_\mathrm{p}\frac{\pi\,d_\mathrm{p}^2}{4}\,(4\,\pi\,I_\mathrm{b,p} - G) \tag{3.109}$$

The first term on the RHS of Eq. 3.108 corresponds to the particle heat transfer due to convection (similar to Eq. 3.96). The second and third term on the RHS correspond to the particle heat transfer due to devolatilization and char combustion, respectively. Here, h_vol denotes the volatile enthalpy at particle temperature, and h^*_char denotes the corrected enthalpy of the char species, only taking into account the heat released by the particle, which is calculated similar to Eq. 3.100:

$$h^*_\mathrm{char} = (S_{\mathrm{O}_2}+1)h_\mathrm{CO} - S_{\mathrm{O}_2}h_{\mathrm{O}_2} \tag{3.110}$$

using the enthalpies calculated at gas phase temperature. The last term on the RHS of Eq. 3.108 corresponds to the radiative enthalpy source term obtained by the DOM, as described in section 3.3.

Chapter 4

Numerical treatment

The previously introduced transport equations for reactive fluids (Eq. 2.2, 2.3, 2.11, and 2.16) require numerical solution methods, since an analytical solution is only possible for particularly simplified problems. To achieve this, the computational domain is discretized into a number of smaller elements, for which the governing equations are solved. For the discretization of the conservation equations, different methods can be applied, e.g., the finite element method (FEM), the finite difference method (FDM), spectral methods, or the finite volume method (FVM), which are widely described in the literature (see e.g. [36]). The latter method is applied in most CFD solvers because it ensures conservation irrespective of the shape used for the finite volumes, and thus, allows to simulate complex geometries. The simulations performed for this work are conducted with the in-house code *PsiPhi*, which also utilizes the FVM and shall be further explained. Following the introduction of the FVM, spatial and temporal discretization methods used in the CFD solver *PsiPhi*, as well as the pressure-velocity coupling, which plays a special role in the low-Mach regime, are described. This is followed by the numerical treatment of the Lagrangian particles, and finally, special strategies for the initialization of PCC simulations are given.

A numerical solution method can be described by distinct steps: a spatial discretization of the solution, in which a spatially distributed variable is described by a vector of discrete values, the definition of discrete spatial operators, and the temporal discretization, which defines rules to calculate the solution at the subsequent time step. It should be noted that the spatial discretization also includes the discretization of the initial conditions as well as the boundary conditions. To illustrate the discretization steps, a general transport equation for a generic scalar ϕ is given:

$$\underbrace{\frac{\partial \phi}{\partial t}}_{\text{Accumulation}} + \underbrace{\frac{\partial (\phi u_j)}{\partial x_j}}_{\text{Convection}} = \underbrace{\frac{\partial}{\partial x_j}\left(D_\phi \frac{\partial \phi}{\partial x_j}\right)}_{\text{Diffusion}} + \underbrace{\dot{\omega}_\phi}_{\text{Source}} \tag{4.1}$$

The transport equation can be divided into distinct terms: an accumulation term representing the temporal evolution of the scalar ϕ, a convection term describing the advection following a local velocity field u_j, and a diffusion term determining its spatial diffusion rate. Additionally, a source term is included, which represents all changes caused by volumetric terms, e.g., the interaction between the solid and the gas phase or chemical conversion in the gas phase.

4.1 Finite volume method (FVM)

The FVM discretizes the numerical domain into a finite number of adjacent volumes (cells), in which the conservation equations can be solved. Starting from the conservation equation for a generic scalar ϕ, Eq. 4.1 is first integrated over a finite volume V. The integral form then reads:

$$\int_V \frac{\partial \phi}{\partial t} dV + \int_V \frac{\partial (\phi u_j)}{\partial x_j} dV = \int_V \frac{\partial}{\partial x_j}\left(D_\phi \frac{\partial \phi}{\partial x_j}\right) dV + \int_V \dot{\omega}_\phi dV \tag{4.2}$$

By applying the Gauss theorem to the transport terms, which reads $\int_V \nabla \cdot \phi \, dV = \int_A \phi \cdot \boldsymbol{n} \, dA$, the volume integral of the divergence fields can be reformulated by the fluxes through the volume surfaces as:

$$\int_V \frac{\partial \phi}{\partial t} \, dV + \int_A (\phi u_j) \, n_j \, dA = \int_A \left(D_\phi \frac{\partial \phi}{\partial x_j}\right) n_j \, dA + \int_V \dot{\omega}_\phi \, dV \tag{4.3}$$

where $\boldsymbol{n}$ describes the normal vector of the surface. The equations for each discretized volume are then solved, yielding a volume-averaged solution for ϕ on the center of the cell for each volume. A Cartesian grid with uniform cubic cells ($\Delta_x = \Delta_y = \Delta_z = \Delta$) is used for spatial discretization in *PsiPhi*. Figure 4.1 illustrates a 2D uniform cell and its adjacent cells, along with the terminology used in this work. Capital letters denote quantities at the cell centers, while lower case letters denote quantities at the cell surfaces.

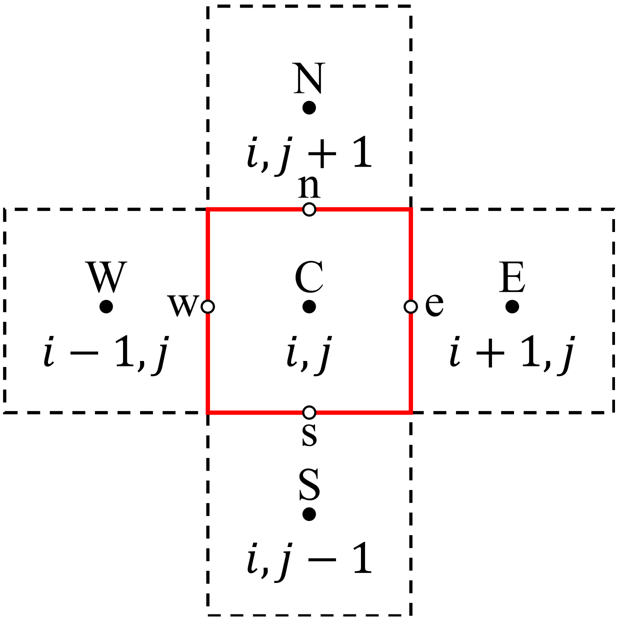

Figure 4.1: Illustration of a 2D Cartesian cell and its adjacent cells.

4.1.1 Discretization of volume integrals

Both terms, the accumulation and source term in Eq. 4.3 require the integration over the volume V. Using the previously made assumptions, that the cell value of ϕ is equal to the value on the cell center C and that the cells are of uniform cubic shape, the integration of ϕ over the volume can be simplified as:

$$\int_V \phi \, dV = \phi_{\mathrm{C}} \, \Delta_x \, \Delta_y \, \Delta_z = \phi_{\mathrm{C}} \, \Delta^3 \tag{4.4}$$

4.1.2 Discretization of convective fluxes

The convective term in Eq. 4.3 requires the integral over the closed cell surface A; in terms of cubic cells, the integration can be approximated by:

$$\int_A \phi \, u_j \, n_j \, dA \approx \sum_f \phi_f \, u_f \, n_f \, \Delta \, A_f \tag{4.5}$$

Hence, the surface integration is approximated by summation of the respective fluxes over all six cell faces f (north (n), east (e), south (s), west (w), top (t), bottom (b)). As the values at the cell faces f are unknown, various discretization schemes serve to obtain these via interpolation, whereby the choice of the scheme also entails different accuracies, computational costs, and stability behavior. Hereinafter, the discretization schemes used shall be briefly explained, assuming a flow direction from west to east for simplicity.

Upwind differencing scheme (UDS)

The most basic discretization scheme is the upwind differencing scheme (UDS), which approximates the value of ϕ_f at the cell face using the value of ϕ from the upstream cell center. In the specified flow direction, the flux through the cell face e yields:

$$\phi_\mathrm{e} = \phi_\mathrm{C} \tag{4.6}$$

Albeit the scheme is very robust, the first-order accurate scheme often leads to unphysically smooth scalar fields caused by excessive numerical diffusion. Thus, it is preferable to use higher-order accurate schemes, particularly for LES.

Central differencing scheme (CDS)

A second-order accurate discretization scheme is the central differencing scheme (CDS), which determines the value of ϕ_f at the cell face by averaging the two adjacent cell centers. For ϕ_e, the CDS reads:

$$\phi_\mathrm{e} = \frac{1}{2}(\phi_\mathrm{C} + \phi_\mathrm{E}) \tag{4.7}$$

A drawback of this method is the occurrence of oscillations if the flow scales are not fully resolved and thus, the fields are not smooth enough, leading to unphysical values. Because a low Mach formulation is used in this work, the convective terms in the momentum equations are discretized by the second-order accurate CDS, as the implicit calculation of the pressure field tends to dampen numerical oscillations. Meanwhile, the transport equations for reactive scalars lack implicit treatment, while the values are also strictly bounded. Thus, CDS can not be used in that regard and other higher-order accurate spatial methods with improved stability are required.

Total variation diminishing (TVD) scheme

For the convective fluxes of scalars, the total variation diminishing (TVD) scheme with a CHARM limiter function, proposed by Zhou et al. [211], is applied in this work. The TVD scheme combines the advantages of the UDS and the CDS by blending both schemes, taking the local solution into account. Thus, for smooth fields, the high accuracy of the CDS can be mostly maintained, whereas the robustness of the UDS is used in the presence of steep gradients and extrema, resulting in a non-oscillating, stable solution. Applying the TVD scheme on the flux over the eastern surface ϕ_e reads:

$$\phi_\mathrm{e} = \phi_\mathrm{C} + \frac{1}{2}B(r)\left(\phi_\mathrm{C} - \phi_\mathrm{E}\right) \tag{4.8}$$

where $B(r)$ denotes the flux limiter function, which depends on the ratio of adjacent gradients r, defined as:

$$r = \frac{\phi_\mathrm{W} - \phi_\mathrm{C}}{\phi_\mathrm{C} - \phi_\mathrm{E}} \tag{4.9}$$

The CHARM limiter function [211] is used for $B(r)$, which is computed as:

$$B(r) = \begin{cases} \frac{r(3r+1)}{(r+1)^2} & \text{if} \quad r > 0 \\ 0 & \text{if} \quad r \leq 0 \end{cases} \tag{4.10}$$

Hence, for sharp gradients (e.g. $r \leq 0$), the first-order accurate UDS is used, while for smooth fields, r is close to unity and the second-order accurate CDS is applied.

4.1.3 Discretization of diffusive fluxes

To determine the diffusive fluxes in Eq. 4.3, the derivatives of ϕ on the cell surfaces are needed. In this work, the diffusive fluxes are computed by a second-order accurate CDS. Expressing the diffusive flux term by the sum of the adjacent surface fluxes yields:

$$\int_A \left(D_\phi \frac{\partial \phi}{\partial x_j} \right) n_j \, dA = \sum_f \left[D_\phi \frac{\partial \phi}{\partial x_j} \right]_f n_f \, \Delta \, A_f \tag{4.11}$$

Thus, for uniform, cubic cells, the diffusion flux across the eastern surface $F_{D,\mathrm{e}}$ can be approximated by:

$$F_{D,\mathrm{e}} = \left[D_\phi \frac{\partial \phi}{\partial x_j} \right]_\mathrm{e} n_\mathrm{e} \, \Delta \, A_\mathrm{e} = \left[D_\phi \frac{\phi_\mathrm{E} - \phi_\mathrm{C}}{\Delta} \right] \Delta \, A_\mathrm{e} \tag{4.12}$$

4.1.4 Time integration

After the previously described spatial discretization, the accumulation term in in Eq. 4.1 needs to be discretized in time. The physical simulation run time is split into small, discrete time steps Δt. Rearranging Eq. 4.1 by splitting the time-dependent accumulation term from the remaining terms and introducing RHS(ϕ) as the sum of the terms on the right-hand side, yields:

$$\frac{\partial \phi}{\partial t} = \underbrace{-\frac{\partial (\phi u_j)}{\partial x_j} + \frac{\partial}{\partial x_j} \left(D_\phi \frac{\partial \phi}{\partial x_j} \right) + \dot{\omega}_\phi}_{\mathrm{RHS}(\phi)} \tag{4.13}$$

For discretization of the accumulation term, different schemes exist. A distinction must be made between explicit, implicit, and hybrid explicit-implicit schemes. Explicit schemes rely on the current time step to update the flow field values. They are typically easier to implement and computationally less expensive, but they might come with stability limitations, requiring smaller time steps for convergence. On the other hand, implicit schemes consider the new time step, which means they involve solving a system of equations at each time step. Implicit schemes are often more stable, allowing for larger time steps, but they are computationally more demanding compared to explicit schemes. The smaller the time step, the more accurate the prediction of the transport equation to be solved. As the size of the chosen time step has a considerable influence on the computational costs, similar to the discretized grid, a trade-off must be found, which allows an efficient computation at a sufficiently accurate time step. The *CFL* condition, named after Courant, Friedrichs, and Lewy [83], can be used to determine the maximum time step width. It reads:

$$CFL = \frac{|u_i| \Delta t}{\Delta} \tag{4.14}$$

Hence, the *CFL* condition indicates the maximum number of cells across which the information of an arbitrary quantity moves per time step. For explicit time integration schemes, the *CFL* number should be ≤ 1, and thus, the information from ϕ should not be transported further than one cell over one time step to assure a stable time integration. However, implicit time integration schemes allow higher *CFL* numbers. In the simulations of this work, an explicit time integration was performed, using a third-order accurate low-storage Runge-Kutta scheme [102], which shall be introduced in the following section.

Runge-Kutta scheme

The Runge-Kutta scheme is an extension to the standard explicit Euler scheme. The explicit Euler scheme can be applied to calculate ϕ^{n+1}, where $n+1$ describes the time $t + \Delta t$ (to be read as superscript), using the current time step $n(t)$, reading:

$$\phi^{n+1} \approx \phi^n + \Delta t \, \mathrm{RHS}(\phi^n) \tag{4.15}$$

Although the Runge-Kutta scheme is globally only first-order accurate, a more robust and accurate scheme is used in this work. The Runge-Kutta scheme involves dividing a time step into several sub-steps and using a combination of function evaluations at different points within each sub-step to approximate the solution at the next time step. While basic first-order Runge-Kutta methods exist, more advanced and accurate schemes with higher orders are widely used. In the present work, a third-order low-storage Runge-Kutta scheme is applied. This scheme involves three separate explicit-Euler sub-steps, each assigned with specific weights. In each sub-step, the time advancement relies on the solution obtained from the previous sub-step. The low-storage manner [203] refers to the fact that not all sub-steps need to be stored in memory. Instead, only the current Runge-Kutta step and the previous sub-step need to be stored, reducing the memory requirements during computation. The general formulation for the Runge-Kutta steps then reads:

$$\phi^{n_m} = \phi^{n_{m-1}} + b_m q_m \tag{4.16}$$

$$q_m = a_m q_{m-1} + \Delta t \,\mathrm{RHS}(\phi^{n_{m-1}}) \tag{4.17}$$

where m is the number of the respective sub-step and a and b are weighting factors. The three sub-steps can then be formulated as:

$$\begin{aligned}
\phi^{n_1} &= \phi^{n} + b_1\, q_1, & q_1 &= \Delta t \,\mathrm{RHS}\,(\phi^{n}) \\
\phi^{n_2} &= \phi^{n_1} + b_2\, q_2, & q_2 &= a_2\, q_1 + \Delta t \,\mathrm{RHS}\,(\phi^{n_1}) \\
\phi^{n_3} &= \phi^{n_2} + b_3\, q_3, & q_3 &= a_3\, q_2 + \Delta t \,\mathrm{RHS}\,(\phi^{n_2})
\end{aligned} \tag{4.18}$$

The weighting factors are taken from Williamson [203], reading:

$$\begin{aligned}
a_1 &= 0; & b_1 &= 1/3; & w_1 &= 1/3 \\
a_2 &= -5/9; & b_2 &= 15/16; & w_2 &= 5/12 \\
a_3 &= -153/128; & b_3 &= 8/15; & w_3 &= 1/4
\end{aligned} \tag{4.19}$$

with w_m being the weighting factors to determine the sub-step time, according to:

$$t^m = t^{m-1} + \Delta t\, w_m \tag{4.20}$$

4.1.5 Pressure correction

For the description of compressible flow problems, momentum and continuity equations must be solved along with the energy equation, where the coupling of pressure, temperature and density is accomplished by the equation of state. In this work, however, a variable density low Mach formulation has been used, where the pressure is decoupled from the transported density and energy. Instead, a target density is defined in terms of reactive scalars and the assumption of a constant background pressure. Inconsistencies among transported density and target density may appear and violate continuity. To overcome this issue, a predictor-corrector scheme is used. In the preceding predictor step, the density and momentum conservation equations are solved, where the pressure gradient terms are omitted, resulting in an initial guess of the fields at the next time step. A Poisson-type equation can be formulated to yield a pressure parameter field that corrects the continuity error. Poisson type equations must be solved using iterative methods. Iterative solvers in the *PsiPhi* code are the Gauss-Seidel scheme with successive over-relaxation and the Jacobi-preconditioned conjugated gradient solver. The latter was applied in the simulations of this work. The momentum interpolation method of Rhie and Chow [135] is used to determine a pressure gradient on the cell surfaces that can be finally applied to the velocity correction, needed for the fluxes in the momentum equation, thus, preventing pressure-velocity decoupling (and occurring checkerboard patterns in the pressure field). In the following corrector step, the corrected velocities are used along with the pressure gradients, calculated from the pressure parameter field, to integrate all conserved quantities in time. For further details on the implementation in the *PsiPhi* code, the interested reader is referred to the works of Kempf, Stein, and Proch [68, 128, 160].

4.1.6 Boundary conditions

In the previous sections, the set of equations necessary to describe a flow problem were introduced and the spatial and temporal discretization schemes used were presented. In order to solve a certain flow problem, and thus, impose the correct flow behavior, appropriate, case-specific initial and boundary conditions are required, which will be explained subsequently. Case-specific initial conditions for the solution of reactive flows may require additional modeling. This will be separately discussed in section 4.3.

The vast majority of potential boundary conditions can be formulated as combination of two basic types: the Dirichlet boundary condition and the von-Neumann boundary condition. The Dirichlet boundary condition sets a fixed value for a specific quantity ϕ (e.g., velocity, temperature, chemical composition, etc.). The von-Neumann boundary condition sets a fixed value for the gradient of a specific quantity ϕ in the face normal direction. When the face normal gradient is set to zero, it results in a diffusive flux of zero on the face, which is commonly referred to as the zero gradient boundary condition. It reads:

$$\frac{\partial \phi}{\partial x_j} n_j = 0 \tag{4.21}$$

Inlet

At the inlet plane, Dirichlet boundary conditions are applied to the momentum, as well as the density and other transported quantities, reading:

$$\phi = \phi_{\text{inlet}} \tag{4.22}$$

In most cases, the flow at the inlet surface is already turbulent, requiring the knowledge of velocity fluctuations and special treatment in the modeling is necessary to obtain accurate results. Turbulence is artificially superimposed onto the inlet velocity using the inflow generator by Klein [71] in an extension for arbitrary grids by Kempf [69]. The inflow generator uses a given Reynolds stress tensor and a turbulent length-scale to superimpose fluctuations on the inlet velocity field. The boundary condition for the pressure correction method depends on the boundary condition applied to the momentum equation and is set complementary to the latter. Hence, a zero-gradient boundary condition is set for the pressure. A fixed pressure value at the inlet is not necessary as the pressure correction method only relies on pressure gradients and curvature, rather than the absolute pressure value.

Outlet

For open boundaries, a von-Neumann boundary condition is used for the momentum, as well as the density and other scalar quantities. Analogous to its application at the inlet plane, the boundary condition for pressure is set complementary. Therefore, a Dirichlet boundary condition is used for the pressure at open boundaries. The pressure is usually set to zero to minimize the influence of round-off errors.

Walls

For the description of walls in *PsiPhi*, the immersed boundary method is applied. In this approach, a regular cubic mesh is used for the whole domain, leading to computational cells inside the walls. Initially, the discretized governing equations are solved for all cells including the cells inside the walls. Subsequently, the quantities inside the wall cells are set to values such that they mimic walls. Velocities and thus, convective fluxes at surfaces adjacent to wall cells are set to zero by a Dirichlet boundary condition. To avoid diffusion through the wall, the diffusive fluxes for cells adjacent to walls are also set to zero in the wall direction using a von-Neumann boundary condition. A Dirichlet boundary condition is used in the cell adjacent to the flow domain by setting it to the respective value (e.g., a fixed wall temperature, etc.). To maintain zero gradient conditions in the pressure correction method, an average pressure value based on the neighboring fluid cells is set inside the immersed boundary cells during each iteration step. Using this methodology, complex geometries often require a large number of cells for a sufficient resolution in the given framework. The simple geometries encountered in the burners studied allow an efficient computation with moderate resolution. The methodology simplifies the representation of walls, but does not account for the problem of near-wall resolution in LES. In the subsequent text, the subscript IB is used when referring to immersed boundaries.

4.2 Lagrangian particles

The temporal discretization of Lagrangian particle quantities is consistent with the temporal discretization of Eulerian quantities. The spatial discretization, i.e., the projection of Eulerian (gas phase) onto Lagrangian (particle) quantities and vice versa, however, shall be briefly explained. The mapping process is based on a second-order trilinear interpolation scheme. To illustrate the interpolation scheme, a Lagrangian particle inside a 3D grid and the cell centers to be used for interpolation are shown in Fig. 4.2. The interpolation scheme uses the cell centers of the 8 nearest cells (assuming the particle is not located exactly on the cell center). Initially, weighting factors for the contributions of the respective nearest cell centers to determine the particle location need to be obtained. Each weighting factor w has a positive $w(^{+})$ and a negative contribution $w(^{-})$, determining the weighting to/from the nearest cell center in positive and negative direction, respectively. The weighting factor $w(i^{-})$, giving the contribution of the nearest cell center in negative x-direction x_{C}^{-}, i.e., would yield:

$$w(i^{-}) = \frac{x_{\mathrm{C}}^{+} - x_{\mathrm{p}}}{\Delta} \tag{4.23}$$

where x_{p} and x_{C}^{+} are the particle distance in x-direction and the distance of the nearest cell center in positive x-direction from the particle location. Accordingly, the weighting factor for x_{C}^{+} is simply given by:

$$w(i^{+}) = 1 - w(i^{-}) \tag{4.24}$$

Similarly, the weighting factors for the remaining cell centers ($w(j^{-})$, $w(j^{+})$, $w(k^{-})$, and $w(k^{+})$) can be computed. Finally, the general expression for a 3D interpolation from Eulerian to Lagrangian phase reads:

$$\phi_{\mathrm{p}} = \sum_{i\in[i^{-},\,i^{+}]} \sum_{j\in[j^{-},\,j^{+}]} \sum_{k\in[k^{-},\,k^{+}]} w(i)\, w(j)\, w(k)\, \phi(i,j,k) \tag{4.25}$$

Conversely, the 3D interpolation from Lagrangian particle phase to the nearest Eulerian cell centers can be computed as:

$$\phi(i^{-},\, j^{-},\, k^{-}) = w(i^{-})\, w(j^{-})\, w(k^{-})\, \phi_{\mathrm{p}} \tag{4.26}$$

$$\phi(i^{-},\, j^{-},\, k^{+}) = w(i^{-})\, w(j^{-})\, w(k^{+})\, \phi_{\mathrm{p}} \tag{4.27}$$

$$\phi(i^{-},\, j^{+},\, k^{-}) = w(i^{-})\, w(j^{+})\, w(k^{-})\, \phi_{\mathrm{p}} \tag{4.28}$$

$$\phi(i^{-},\, j^{+},\, k^{+}) = w(i^{-})\, w(j^{+})\, w(k^{+})\, \phi_{\mathrm{p}} \tag{4.29}$$

$$\phi(i^{+},\, j^{-},\, k^{-}) = w(i^{+})\, w(j^{-})\, w(k^{-})\, \phi_{\mathrm{p}} \tag{4.30}$$

$$\phi(i^{+},\, j^{-},\, k^{+}) = w(i^{+})\, w(j^{-})\, w(k^{+})\, \phi_{\mathrm{p}} \tag{4.31}$$

$$\phi(i^{+},\, j^{+},\, k^{-}) = w(i^{+})\, w(j^{+})\, w(k^{-})\, \phi_{\mathrm{p}} \tag{4.32}$$

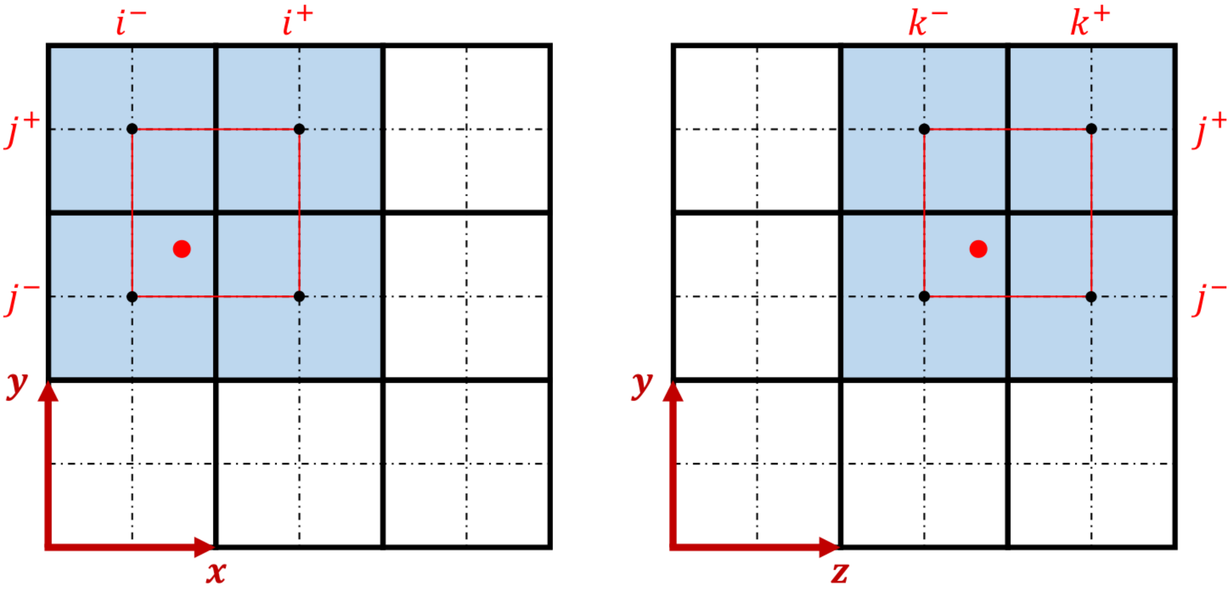

Figure 4.2: Sketch of a Lagrangian particle inside a 3D Cartesian grid and the cell centers to be used for standard interpolation.

$$\phi(i^+,\, j^+,\, k^+) = w(i^+)\, w(j^+)\, w(k^+)\, \phi_\mathrm{p} \tag{4.33}$$

Close to walls, the interpolation scheme only considers fluid cells and no immersed boundaries. Therefore, a factor f is introduced for the interpolation, which corrects the weighting of the closest cell centers in the near-wall region, i .e., if immersed boundary cells need to be excluded from the interpolation. The factor f reads:

$$f^{-1} = \sum_{i\in[i^-,i^+]} \sum_{j\in[j^-,j^+]} \sum_{k\in[k^-,k^+]} w(i)\, w(j)\, w(k)\, I_\mathrm{IB}(i,j,k) \tag{4.34}$$

Here, $I_\mathrm{IB}(i,j,k)$ is the indicator for the immersed boundary, taking a value of 1, if a fluid cell is present, and a value of 0, if a wall cell is present. This correction is considered by multiplying f and $I_\mathrm{IB}(i,j,k)$ in the interpolation scheme. For Eqs. 4.25 and 4.26, this would yield:

$$\phi_\mathrm{p} = \sum_{i\in[i^-,i^+]} \sum_{j\in[j^-,j^+]} \sum_{k\in[k^-,k^+]} f \cdot w(i)\, w(j)\, w(k)\, \phi(i,j,k)\, I_\mathrm{IB}(i,j,k) \tag{4.35}$$

and

$$\phi(i^-,j^-,k^-) = f \cdot w(i^-)\, w(j^-)\, w(k^-)\, \phi_\mathrm{p}\, I_\mathrm{IB}(i,j,k) \tag{4.36}$$

Similarly, the correction is applied to Eqs. 4.27 - 4.33.

4.3 Initialization of pulverized coal combustion (PCC) simulations

In this work, the investigation focuses on two distinct flame setups, a laboratory-scale coal burner (sections 5.1 and 5.2), and a semi-industrial coal furnace equipped with a swirl-burner (section 5.3), each requiring specific considerations for combustion initialization. The first flame setup flows into a free environment, thus, outlet boundary conditions are used for the lateral boundaries and for the outlet. The second flame setup is surrounded by walls, represented by immersed boundaries. Here, the wall temperature is set to a constant temperature. In case of the laboratory-scale burner setup, initialization of the flame is accomplished by setting the domain area around the pilot fuel stream inlet (see Fig. 5.2) as burned ($Y_\mathrm{PV} = 1.0$), and thus, achieving ignition by feedback after fuel injection; the fuel injection starts at the first time step. However, this initialization technique does not lead to successful ignition when applied to the semi-industrial coal furnace. The presence of a high swirl in the flame results in immediate flame extinction. To address this issue, an alternative method is adopted. Specifically, a central region in the flame domain directly after the fuel inlet (see Fig. 5.20) is designated as "burned" ($Y_{\mathrm{PV}} = 1.0$), while an annular area surrounding this region is defined as "partially burned" ($Y_{\mathrm{PV}} = 0.5$) for initialization. This modification enables the successful formation of the flame subsequent to fuel injection in the second flame configuration.

Chapter 5

Applications

The objective of this chapter is to provide an in-depth analysis of the LES of PCC flames. Three published papers will be presented, which will offer a critical evaluation of their methodologies and results. The papers investigate various aspects of the LES of coal combustion, including the validation of numerical models against experimental data, the effect of experimental artifacts on the prediction accuracy of species quantities, and the development of multi-dimensional flamelet models for use in new measures to reduce carbon dioxide emissions occurring during coal firing, e.g., the co-firing of coal and ammonia. In this work, two distinct burner setups have been the focus of investigation: the CRIEPI coal jet flame [1, 161, 164, 165] and the BYU burner flow reactor (BFR) [24, 25].

The CRIEPI coal jet flame is a well-established laboratory-scale burner, widely employed to investigate the behavior of coal single- and co-firing in power generation. In contrast, the BFR is a swirl-stabilized pulverized coal flame on a semi-industrial scale that exhibits highly turbulent behavior and is characterized by the presence of internal and external recirculation zones, thus rendering it particularly challenging for LES. The burner has proven to be well-suited for studying coal firing-related emissions, particularly NO_x formation processes, thanks to the availability of extensive measurement data.

The chapter is organized as follows: first, the two publications presenting LES of the CRIEPI coal jet flame are shown, followed by a publication that features the LES of the BYU burner flow reactor.

The primary objective of the first paper [95] is to validate the numerical model used to simulate coal combustion in a laboratory-scale burner setup. The simulation involves a 4D-FPV approach that takes into account two mixture fractions for the hydrogen pilot and the volatile gas, as well as a progress variable definition and enthalpy. The simulation neglects char burnout, as it has negligible influence due to the short residence time of the particles in the flame domain. The paper provides a comprehensive analysis of the combustion behavior and verifies the model's accuracy by comparing it against experimental data. Furthermore, the species comparability is enhanced by modeling experimental artifacts of the suction probe, resulting in much improved agreement with the experimental data.

The second paper [97] investigates the impact of co-firing coal and ammonia on the combustion behavior of the same flame setup, utilizing FPV-LES. The FPV approach is extended to include an additional mixture fraction for ammonia, resulting in a 5D-FPV approach. A reduced reaction mechanism is generated and validated to comprehensively represent the combustion of both, coal and ammonia. The findings of this paper reveal that the inclusion of ammonia has a substantial influence on the flame structure, species and temperature distribution. A detailed description of the ammonia chemistry is necessary to achieve accurate results, as demonstrated by the improved agreement between the newly generated mechanism and experimental data compared to an existing coal mechanism (not specifically designed for ammonia combustion).

The third paper [96] investigates two approaches to model NO_x species that form during coal combustion by analyzing a semi-industrial swirl-stabilized burner setup utilizing FPV-LES. The first approach directly retrieves the NO species from the flamelet table, while the second method solves a separate transport equation for NO. In the second approach, the source term is split into a formation and a rescaled consumption part to better account for forward- and backward reactions of NO. The paper highlights the need for the additional transport equation for NO, showing a much improved prediction.

This chapter of the thesis aims to provide a detailed and comprehensive overview of the research conducted during the time spent at the Chair of Fluid Dynamics at the University of Duisburg-Essen. The papers intend to highlight the potential of LES as a valuable tool for advancing our comprehension of turbulent combustion phenomena in these burners, and showcase the importance of further research in the field of solid fuel combustion.

5.1 Numerical Analysis of a Turbulent Pulverized Coal Flame Using a Flamelet/Progress Variable Approach and Modeling Experimental Artifacts [95]

This section of chapter 5 including all text, figures and tables is published in the journal Energy and Fuels 'D. Meller, T. Lipkowicz, M. Rieth, O. T. Stein, A. Kronenburg, C. Hasse, and A. M. Kempf. Numerical Analysis of a Turbulent Pulverized Coal Flame Using a Flamelet/Progress Variable Approach and Modeling Experimental Artifacts. Energy and Fuels, 35(9):7133–7143, 2021.' [95] and is reprinted with permission from American Chemical Society (ACS).
Contributor Roles Taxonomy: D. Meller developed the code, ran the simulations and wrote the original manuscript draft. T. Lipkowicz and M. Rieth developed code, provided discussions of the results and contributed to the manuscript. O. T. Stein, A. Kronenburg, C. Hasse, and A. M. Kempf provided discussions of the results and contributed to the manuscript.

Abstract

A coaxial burner with a hydrogen-supported pulverized coal flame, operated by the Central Research Institute of Electric Power Industry (CRIEPI, Japan), is investigated numerically. The flame is modeled using massively parallel Large Eddy Simulation (LES). A flamelet/progress variable (FPV) approach is used for modeling the complex multiphase flow of the laboratory coal flame. A four-dimensional tabulation method based on non-premixed flamelets is introduced, which uses two mixture fractions for the hydrogen pilot and coal volatiles, respectively, as well as the absolute enthalpy and the reaction progress to parameterize the thermochemical space. Simulations are compared to the experiments in terms of temperature, gas-phase velocities (with and without consideration of buoyancy), as well as the gas compositions along the centerline and in radial direction at different heights. The effect of the suction probe on the scalar field measurements is tested by simulating this probing, observing relative changes up to 50 % in various quantities and locations. By considering these probe effects, the agreement between experiment and simulation can be improved significantly; at the same time, the simulation also provides the unperturbed scalar fields, without probing effects. The new flamelet model gives a robust and cost effective prediction of the investigated laboratory flame - provided that the probing effects are considered.

5.1.1 Introduction

Pulverized coal combustion (PCC) is one of the major sources for the world's electricity production. The important role of PCC is forecasted to continue over the next decades. The by-products of PCC, such as NO_x, SO_x, CO_2, and unburned hydrocarbons are known to have a negative impact on the environment, but great efforts are made to achieve highly efficient combustion and to minimize emissions. To obtain deeper insight into the highly complex processes involved in PCC, computational fluid dynamics (CFD) has become very important in the recent years. The prediction accuracy of CFD strongly depends on the numerical modeling of turbulence, with the three major paradigms direct numerical simulation (DNS), large eddy simulation (LES), and Reynolds-averaged Navier-Stokes (RANS) simulation. Compared with RANS, the balance between improved prediction accuracy and moderately increased computational cost makes LES a powerful tool for the simulation of PCC since its early applications by Kurose, Makino, and other research groups [34, 78, 111, 130, 162, 184]. The deep insight provided by such simulations would be very difficult to obtain through experiments [53] alone, because exact measurements in such hostile environments are very challenging, underlining the importance of numerical simulations for characterizing PCC flames. However, although computational power is growing exponentially, simulations of turbulent multiphase flows with detailed chemistry remain too expensive for industrial applications. Combustion models that are based on strong assumptions, such as the eddy break up (EBU) model [158] are often used and have already been applied to the present flame [34, 45, 162]. Although such simple models perform well in specific areas, they have significant weaknesses. The EBU model is based on the infinitely fast chemistry assumption. Simplifying the actual chemical kinetics can lead to an inaccurate (or even no) prediction of important flame properties (e.g., pollutant formation, flame temperature, etc.). More advanced models can overcome some of these weaknesses, like the transported probability density function (PDF) model [122], the conditional moment closure (CMC) model [72] and the flamelet model [115]. The final approach used here in its extended version refers to the flamelet/progress variable (FPV) model by Pierce and Moin [117]. Flamelet models describe the detailed homogeneous kinetics in complex turbulent flows at a reduced computational cost, and hence, are often used in LES, including applications to PCC simulations [138, 184, 187, 189]. In this model, thermochemical quantities are precomputed and stored in flamelet look-up tables (FLUT). Specific trajectory variables, which are transported in the flow solver, couple the chemistry table with the flow field. In particular, the FPV approach uses a progress variable as a major trajectory variable for table access.

Watanabe and Yamamoto were the first to propose a FPV model for two fuel streams which considers devolatilization and char combustion and showed its applicability for PCC simulations on a two-dimensional DNS PCC jet field [183]. They achieved good agreement of the overall representation of turbulent structures and combustion, although the ignition process occurred too early in the FPV-DNS. In a subsequent study, they coupled the flamelet model with LES by introducing a presumed PDF to take the subgrid scale turbulence-chemistry interaction (TCI) into account [184]. They extended the model to include another mixture fraction for coal moisture and tested it on a laboratory coal jet flame, obtaining good results in terms of ignition. Vascellari et al. used an extended FPV approach in fully resolved simulations to correctly reproduce the flame structure of single coal particles before and during the ignition process [180]. Wen et al. performed fully resolved laminar counterflow PCC flame simulations with FPV and compared their results to the ones from simulations with detailed chemistry integration, finding a good agreement [190]. Rieth et al. tested the FPV approach performing carrier-phase DNS of a reacting mixing layer with entrained coal particles [141]. It was found that the FPV approach was in accordance with the reference carrier-phase DNS, although discrepancies appeared in zones where premixing and highly unsteady extinction and re-ignition occur, as these effects are difficult to capture by steady non-premixed FPV modeling.

In the present work, we apply the FPV approach to simulate the latest experiments of a coaxial burner with a hydrogen-supported PCC flame, experimentally investigated by CRIEPI [1, 53–55]. The flame is a target flame of the biennial workshop on measurement and simulation of coal and biomass conversion (CBC) and serves as reference flame for model development with its large experimental data base [1, 53–55]. The original flame configuration with methane as pilot gas has been widely studied by RANS simulations, LES and even DNS [3, 17, 34, 44, 45, 70, 138, 162, 188, 210]. Direct comparison of the various numerical datasets and the experiments have been conducted within the CBC workshop series, but potential measurement difficulties (volume-averaging of the gas sampling probe, limited accuracy of pyrometry experiments) and different modeling strategies (in terms of grid, modeling, model parameters, inflow settings, etc.) made it difficult to clearly highlight an advanced modeling strategy over others. Franchetti et al. developed a simple method for modeling pyrometer measurements in their LES of the original flame and were among the first to get reasonable temperature data [34]. While the mean velocity fields were relatively well captured by all simulations contributing to CBC, significant differences were evident in terms of species predictions as well as axial temperature distributions. For example, Rieth et al. [138], Stein et al. [162] and Khan et al. [70] predicted that O_2 is consumed (and CO_2 is formed) further upstream than in the DNS of Hara et al. [44]. The axial temperature distributions matched with the species distributions, but predicted different maximum temperatures and overshoots of different magnitudes [34, 44, 70, 138, 162].

Wen et al. [188] and Akaotsu et al. [3] tested the FPV approach on the original flame configuration by LES. Wen et al. found that the EBU model performed less well than the flamelet model [188]. Akaotsu et al. stated that premixed and diffusion combustion modes coexist even in the downstream region of the flame and that char combustion is negligible in the region of interest [3]. Both studies used two mixture fractions for char off-gases and volatiles and replaced the pilot stream with volatile gas. Recently, the experimentalists at CRIEPI have introduced a new testcase, which uses hydrogen as pilot gas instead of methane and aims to minimize the relative heat input by the pilot to set a stronger focus on coal combustion [1]. For the new flame, the temperature was measured by thermocouples to provide more accurate data than the pyrometer in the original experiment. A first simulation was conducted by Ahn et al., who obtained much better results in terms of temperature (likely due to the thermocouple measurement) [1]. However, the species prediction still showed some notable deviations from the experiments. This may have been related to spatial averaging effects occurring in the gas sampling experiments, which will be an object of study in the present work. Here, we neglect the very small effect of char burnout and only two mixture fractions for volatiles and the pilot gas are considered in the FPV approach. Furthermore, a method is introduced to correct the volume-averaging error during species measurement. The two main objectives of the present work can be summarized as follows:

- Apply the FPV model to the new flame configuration focusing on the combustion of the pilot gas and coal volatiles.
- Enhance the comparability of the species composition by modeling the suction probing and give a guidance for future modelers.

5.1.2 Modeling

5.1.2.1 FPV governing equations and tabulation method

The FPV approach describes the thermochemical state using a limited number of control variables. The CRIEPI jet flame consists of a hydrogen pilot and the main, coal-particle-laden air jet. Hydrogen is highly diffusive and thus, effects due to differential diffusion can be expected in the hydrogen pilot. The extension of the FPV method to differential diffusion is conceptually complex [119]. In the present case, the thermal heat input of hydrogen (0.11 kW) to coal (3.76 kW) is about 2.8 % of the total heat input. Hence, we assume that differential diffusion effects are small in the present setup and we employ an FPV approach that is based on the assumption of unity Lewis number. To accurately describe thermochemical conversion in the present flame, three mixture fractions Z_j would be necessary to distinguish the pilot stream Z_{pil}, as well as the volatiles Z_{vol}, and the char off-gases Z_{char}.

$$Z_j = \frac{m_j}{m_{\mathrm{ox}} + m_{\mathrm{vol}} + m_{\mathrm{char}} + m_{\mathrm{pil}}} \tag{5.1}$$

Each of the mixture fractions for the volatiles, char off-gases, and the pilot describes the mass fraction of the respective fuel in the mixture consisting of oxidizer (m_{ox}) and fuel (m_{vol}, m_{char}, and m_{pil}). However, a three-Z flamelet model would need at least five dimensions (three mixture fractions, enthalpy and progress variable) using a top-hat PDF [110], and more dimensions with a beta-PDF. To avoid an intractable dimensionality of the chemistry table, the impact of the char surface reactions on the gas phase has been neglected in this work. The recent FPV simulation of the original flame configuration by Akaotsu et al. [3] showed that the char off-gas mixture fraction is in the order of 10^{-2}, indicating that the influence of char combustion is negligible, which is confirmed by earlier studies [34, 138, 162, 210]. Char conversion is hence neglected in the current simulation, in view of the similarity of the old and new flame, with similar thermochemical states and similar flame structures (no recirculation zones, relatively low residence time of the coal particles).

The flamelet model is thus based on the mixture fraction for volatiles Z_{vol}, the mixture fraction for the hydrogen pilot Z_{pil}, a progress variable Y_{PV}, and the absolute enthalpy h to account for the strong interphase heat transfer between solid and gas phase during combustion.

The overall FPV approach is similar to the approach used by Rieth et al. [141]. The Favre-filtered transport equations for mass and momentum, as well as the ones for the mixture fractions, the progress variable, and the absolute enthalpy, are solved to simulate the reactive flow problem.

$$\frac{\partial}{\partial t}\bar{\rho} + \frac{\partial}{\partial x_i}\bar{\rho}\tilde{u}_i = \bar{\dot{S}}_\rho \tag{5.2}$$

$$\frac{\partial}{\partial t}\bar{\rho}\tilde{u}_i + \frac{\partial}{\partial x_j}\bar{\rho}\tilde{u}_i\tilde{u}_j = -\frac{\partial}{\partial x_i}\bar{p} + \frac{\partial}{\partial x_j}\bar{\tau}_{ji} + \bar{\dot{S}}_{u_i} \tag{5.3}$$

$$\frac{\partial}{\partial t}\bar{\rho}\tilde{Z}_{\mathrm{pil}} + \frac{\partial}{\partial x_i}\bar{\rho}\tilde{u}_i\tilde{Z}_{\mathrm{pil}} = \frac{\partial}{\partial x_i}\left[\left(\frac{\bar{\mu}}{Sc} + \frac{\mu_{\mathrm{SGS}}}{Sc_{\mathrm{t}}}\right)\frac{\partial \tilde{Z}_{\mathrm{pil}}}{\partial x_i}\right] \tag{5.4}$$

$$\frac{\partial}{\partial t}\bar{\rho}\tilde{Z}_{\mathrm{vol}} + \frac{\partial}{\partial x_i}\bar{\rho}\tilde{u}_i\tilde{Z}_{\mathrm{vol}} = \frac{\partial}{\partial x_i}\left[\left(\frac{\bar{\mu}}{Sc} + \frac{\mu_{\mathrm{SGS}}}{Sc_{\mathrm{t}}}\right)\frac{\partial \tilde{Z}_{\mathrm{vol}}}{\partial x_i}\right] + \bar{\dot{S}}_{Z_{\mathrm{vol}}} \tag{5.5}$$

$$\frac{\partial}{\partial t}\bar{\rho}\tilde{Y}_{\mathrm{PV}} + \frac{\partial}{\partial x_i}\bar{\rho}\tilde{u}_i\tilde{Y}_{\mathrm{PV}} = \frac{\partial}{\partial x_i}\left[\left(\frac{\bar{\mu}}{Sc} + \frac{\mu_{\mathrm{SGS}}}{Sc_{\mathrm{t}}}\right)\frac{\partial \tilde{Y}_{\mathrm{PV}}}{\partial x_i}\right] + \bar{\dot{\omega}}_{Y_{\mathrm{PV}}} \tag{5.6}$$

$$\frac{\partial}{\partial t}\bar{\rho}\tilde{h} + \frac{\partial}{\partial x_i}\bar{\rho}\tilde{u}_i\tilde{h} = \frac{\partial}{\partial x_i}\left[\left(\frac{\bar{\mu}}{Pr} + \frac{\mu_{\mathrm{SGS}}}{Pr_{\mathrm{t}}}\right)\frac{\partial \tilde{h}}{\partial x_i}\right] + \bar{\dot{S}}_h \tag{5.7}$$

The equations follow the standard nomenclature for combustion LES. The Sigma model with a (static) model constant of 1.5 serves as subgrid-scale model for the LES [107], assuming a constant turbulent Schmidt- and Prandtl number of $Sc_{\mathrm{t}} = Pr_{\mathrm{t}} = 0.7$ and a unity Lewis number ($Sc = Pr = 0.7$). The progress variable Y_{PV} in Eq. (5.6) is defined as a linear combination of the species mass fractions for H_2O and CO_2, hence $Y_{\mathrm{PV}} = Y_{\mathrm{H_2O}} + Y_{\mathrm{CO_2}}$. Different definitions of the progress variable were tested for monotonicity between thermochemical quantities and Y_{PV}. It was found that the monotonic criterion was fulfilled when using $Y_{\mathrm{H_2O}}$ and $Y_{\mathrm{CO_2}}$. The absolute enthalpy in Eq. (5.7) is defined as the sum of sensible and standard formation enthalpy. The source term $\bar{\dot{S}}_\rho$ in the continuity equation corresponds to the mass release from devolatilization. Unlike the transport equation for the hydrogen pilot gas, the volatile mixture fraction contains a source term $\bar{\dot{S}}_{Z_{\mathrm{vol}}}$ which also refers to the mass release during devolatilization. In Eq. (5.6), $\bar{\dot{\omega}}_{Y_{\mathrm{PV}}}$ describes the progress variable source term due to chemical reactions, obtained from the flamelet library. The source term $\bar{\dot{S}}_h$ in Eq. (5.7) refers to the enthalpy exchange of the gas phase with the particles (due to convection and devolatilization) and due to radiation.

The table was generated by calculating one-dimensional steady non-premixed flamelets using the FlameMaster code by Pitsch [118]. As proposed by Hasse and Peters [46] to prevent numerical issues, two parameters for the transformed mixture fractions are introduced to parameterize the table:

$$Z = Z_{\mathrm{vol}} + Z_{\mathrm{pil}} \tag{5.8}$$

$$X = \frac{Z_{\mathrm{pil}}}{Z_{\mathrm{vol}} + Z_{\mathrm{pil}}} \tag{5.9}$$

In Eqs. (5.8) and (5.9), Z is the mixture fraction sum and X is the mixture fraction of hydrogen in the fuel. These two parameters are applied to describe the overall mixing process and are used for table access.

Flamelet calculations have been performed by varying the mixture fraction Z at a constant mixture fraction X and a constant boundary temperature, which will be discussed in more detail below. Individual flamelets were calculated using the "Arclength Continuation Method" [118]. Using this method, the scalar dissipation rate χ is varied in a certain range after each calculation until the solutions of the equations represent all branches of the well known S-shaped curve [115]. All thermochemical quantities can then be represented as quantities of mixture fraction Z and scalar dissipation rate χ. Figure 5.1 (left) shows an example of the calculated S-shaped curve for $X = 0.2$. The mixture fraction X is varied in steps of 0.1 in subsequent calculations. The third and fourth trajectory variables are the normalized progress variable $Y_{\mathrm{PV,norm}}$ and the normalized enthalpy H_{norm}.

$$Y_{\mathrm{PV,norm}} = \frac{Y_{\mathrm{PV}} - Y_{\mathrm{PV,min}}}{Y_{\mathrm{PV,max}} - Y_{\mathrm{PV,min}}} \tag{5.10}$$

$$H_{\mathrm{norm}} = \frac{H\left(Z,X\right) - H_{\mathrm{min}}\left(Z,X\right)}{H_{\mathrm{max}}\left(Z,X\right) - H_{\mathrm{min}}\left(Z,X\right)} \tag{5.11}$$

Here, Y_{min} and Y_{max} are the minimum and maximum progress variables in the respective S-shaped curve of each diffusion flamelet. The normalized enthalpy is obtained from the flow field, where $H_{\mathrm{min}}\left(Z,X\right)$ and $H_{\mathrm{max}}\left(Z,X\right)$ are the minimum and maximum enthalpies at specific values of Z and X. Considering the strong interphase heat transfer during coal combustion, to account for a correct temperature and species prediction in the flow field using FPV, Messig et al. [99] demonstrated the importance of the correct enthalpy implementation in the look-up tables. Similar to the table generation using FlameMaster, they used different input stream temperatures for the fuel and air side in order to achieve different enthalpy levels, calculating adiabatic non-premixed flamelets. The heat gain process is represented by elevating both the fuel and air boundary temperatures in the 1D simulations compared to the original coal particle temperature. The heat loss process is represented by successively lowering the boundary temperatures on both sides. Due to the linear variation of the enthalpy, this allows to directly extract the table values. Wen et al. [194] found that for PCC, the heat loss is more important than the heat gain process. To keep the computational effort low and the table size moderate, four different input stream temperatures were used for enthalpy variation in this work (273 K, 300 K, 600 K, 800 K).
According to Fig. 5.1 (left), the representation of the flamelet solutions in scalar dissipation rate space results in multiple solutions for several scalar dissipation rates. By remapping the data onto the defined progress variable space, which is the main component of the FPV approach, a unique representation of the entire S-shaped curve is achieved. Figure 5.1 (right) shows the remapped data onto the progress variable space. In the following table generation process, the values in between the respective dimensions were linearly interpolated to achieve an equally spaced table grid. For a detailed description of the FPV approach and the underlying equations, the reader is referred to Pierce and Moin[117], and Ihme et al. [59, 60].

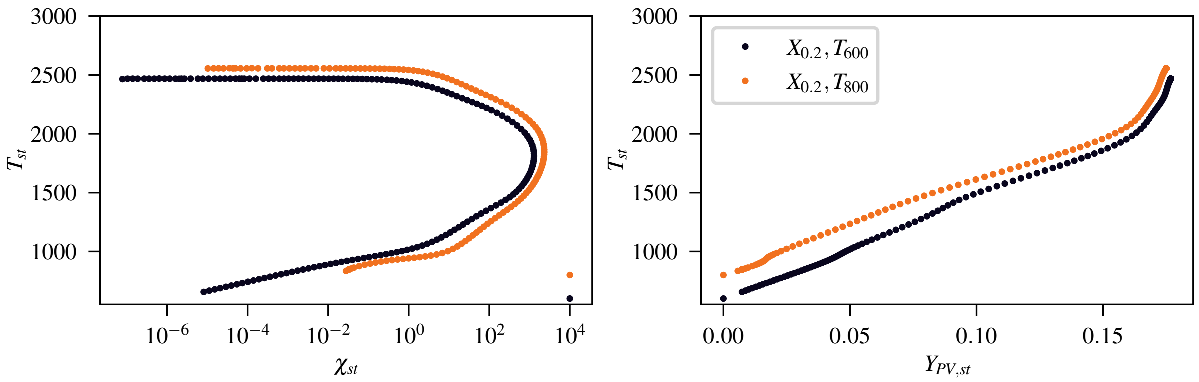

Figure 5.1: Temperature T_{st} as a function of scalar dissipation rate χ_{st} along the entire S-shaped curve (left) and temperature as a function of remapped flamelet data onto progress variable space $Y_{\mathrm{PV,st}}$ (right). The subscript "st" refers to the stoichiometric quantities. Both plots show FlameMaster calculations for $X = 0.2$ and the input stream temperatures $T = 600$ and 800 K.

5.1.2.2 PCC submodels and chemistry

“Coal 5” [1] was employed for the laboratory flame, its properties and the resulting modeled gas composition are presented in Tab. 5.4. The approach of Stoellinger and Petersen was used to obtain the volatile gas composition [116, 163]. The elements in the coal are distributed among common species in the volatile gas, found under high heating rate conditions. The splitting factors of the approach are chosen such that the LHV of the modeled gas composition matches the experimental one. The small amount of sulphur in the coal has been neglected and was added to the carbon content. Since CO_2 occurs in the progress variable definition, all the oxygen is distributed assigned to CO in the present case. The LHV of the modeled gas composition has the best match with the experimental one, assigning the remaining carbon in the volatile content solely to C_2H_4. The remaining hydrogen and nitrogen are distributed among H_2 and N_2, respectively. The final modeled volatile gas composition consists of N_2, H_2, CO and C_2H_4. The particle size distribution was imposed stochastically, using a measured size distribution taken from Ahn et al. [1].

The reduced CRECK mechanism with 52 species and 452 reactions was considered to calculate the non-premixed flamelets [132, 170]. The table dimensions are 263 x 11 x 11 x 101 in mixture fraction sum, mixture fraction ratio, normalized enthalpy and normalized progress variable space, respectively.

Coal particles are treated in a Lagrangian manner and are described by the models used by Rieth et al. [137, 141]. Devolatilization is described by the single first order reaction (SFOR) model by Badzioch & Hawksley [8], which has been tested with the CRIEPI flame in previous studies [34, 138, 186]. The model constants have been fitted based on the coal ultimate analysis, using the particle kinetics preprocessor (PKP) tool developed at TU Darmstadt [178]. The single rate parameters were $k = 875.06 \cdot 10^5\,\mathrm{s}^{-1}$ and $E = 688.69 \cdot 10^5\,\mathrm{J\,kmol^{-1}\,K^{-1}}$ for the pre-exponential factor and the activation energy, respectively. For the devolatilization model, a Q-factor of 1.64 has been used, which was also calculated by the particle kinetics preprocessor. (The Q-factor describes the ratio of the expected high temperature volatile yield on a dry ash-free basis compared to the proximate volatile matter.) It has been shown that the accurate description of the devolatilization is mandatory for a good prediction of the flame stabilization, as it has a direct impact on the flame structure [2]. Particle swelling is neglected, as Muto et al. [104] have shown that it has a negligible effect. Particle sizes are modeled as constant during the devolatilization process.

Table 5.1: Properties of “Coal 5” [1] and modeled gas composition

Ultimate analysis (dry) [wt%]		Proximate analysis [wt%]	
C	70.30	Ash	14.2
H	4.57	Volatile matter	32.6
N	1.66	Fixed carbon	52.4
S	0.45	Moisture	0.8
O	8.78		
LHV	27.90 MJ/kg		

Modeled gas composition (mass fractions)

C_2H_4	CO	H_2	N_2
0.4006	0.4672	0.0816	0.0505

5.1.3 Numerical simulation

5.1.3.1 Experimental background

The investigated flame has been developed by CRIEPI in Japan [1, 53–55]. New experimental studies with a hydrogen-supported flame instead of the previous methane pilot flame have been performed by Ahn et al. [1]. The main jet with a diameter of 6 mm is fed with pulverized coal and air. A wall of 0.5 mm wall thickness separates the main jet from the annular hydrogen pilot stream, which has a channel width of 0.5 mm. The outer wall thickness is 1.0 mm. The burner setup is illustrated in Fig. 5.2. For a detailed explanation, the reader is referred to Hwang, Ahn and their respective coworkers [1, 53–55]. The experimental data is taken from the proceedings of coal and biomass conversion (CBC) in 2019 [161] and from the paper by Ahn et al [1]. The temperature was measured with a K-type sheated thermocouple, particle velocities were measured by particle image velocimetry (PIV); and gas concentrations were obtained from a gas analyzer using a ceramic suction probe, inserted in axial direction into the flame, which determines volume-averaged values over the sucked-in volume [1]. A more detailed description of the suction probe and an approach to consider the resulting volume-averaged data in the numerical evaluation is given in the section “Post processing and probe correction”.

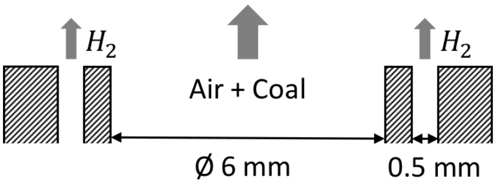

Figure 5.2: Setup of the investigated coaxial burner.

5.1.3.2 Numerical details

The LES calculations have been performed using the in-house code *PsiPhi*, which has been widely used and validated for the simulation of combustion processes [21, 61, 84, 137]. The code uses a low-Mach finite volume method (FVM) with a conjugated gradient solver and a Jacobi preconditioner. An equidistant and orthogonal Cartesian grid is used with a second-order accurate central differencing scheme (CDS) for the spatial discretization of diffusive fluxes and the convective flux of momentum. Convective scalar fluxes are discretized using a total variation diminishing (TVD) scheme with CHARM limiter [211]. For explicit time discretization, a third order low-storage Runge-Kutta scheme is applied [102]. Radiative heat transfer is modeled using the discrete ordinates method (DOM) with the S8 quadrature grey weighted sum of grey gases model (GWSGG) [30, 168]. The model parameters have been taken from Kangwanpongpan et al [66].

The coupling of the Eulerian and Lagrangian phases (for gas and particles) is made by a second-order trilinear interpolation scheme. Massively distributed domain decomposition for Lagrangian and Eulerian fields is achieved by the message passing interface (MPI).

A zero-gradient boundary condition is used at the outlet whereas a Dirichlet boundary condition is set at all other boundaries for all transported quantities. A zero-gradient boundary condition is used for pressure at the inlet and a Dirichlet boundary condition is set at all other boundaries. Pseudo-turbulence is generated for the main jet velocity at the inlet plane using the inflow generator by Klein [71] in an efficient implementation [69]. A turbulent lengthscale of 0.6 mm and a value of $0.45\,\mathrm{m^2\,s^{-2}}$ for the normal Reynolds stresses have been set.

5.1.3.3 Numerical setup

The experimental conditions, which are used in the simulation, are shown in Tab. 5.3 [1, 161]. The main jet time-averaged velocity profile is approximated using a power-law profile to match the profile from experiments at 30 mm height.

$$u = u_1 \left(1 - \frac{r}{r_1}\right)^{4.5} \tag{5.12}$$

Here, u_1 is the maximum main jet velocity on the centerline, initially set to 12.0 m/s (taken from Ahn et al. [1]), and r_1 is the inner radius of 3.0 mm. The discretized velocity profile is rescaled to match the volume flow rate of the experiment. The coflow and surrounding flow use a flat velocity profile with a constant coflow velocity of 1.5 m/s, which was measured in the experiment. Temperatures for the main and coflow inlet have been set to 350 K, the surrounding flow temperature to 300 K. Buoyant has been considered in accost direction.

Simulations were conducted on a Cartesian mesh with cubic cells of $\Delta = 0.4$ mm in width. In order to achieve a stable solution at this mesh size, the *CFL* condition was limited to a value of 0.7. The initialization of the flame is conducted by setting up a domain filled with air at ambient temperature, whereby the area around the coflow inlet is set to burned ($Y_{\mathrm{PV}} = 1.0$). By using this procedure, pilot gas is ignited by feedback immediately after injection. The injection of the pilot gas and the particle-laden air begins at the first time step.

Table 5.2: Experimental conditions [1]

Name	Unit	Value
Coal feed rate	[g/min]	7.75
Air flow rate	[$\mathrm{l_N}$/min]	12.0
H_2 flow rate	[$\mathrm{l_N}$/min]	0.6
Coal heat input	[kW @ LHV]	3.76
H_2 heat input	[kW @ LHV]	0.11
Air/coal ratio	[kg/kg]	2.0
$\mathrm{Re_{jet}}$	[-]	3008
Equivalence ratio (coal)	[-]	4.64

The computational domain consists of a rectangular box with 210 mm in x-direction and 60 mm in y- and z-direction, respectively, leading to a total number of approximately 11.8 Mio. cells. The simulations were performed on 1,694 cores on SuperMUC and MagnitUDE and cost around 40,000 core-h to simulate a physical run-time of around 5 s. The first 300,000 time steps were run without the radiation model, statistical samples were taken between time steps 350,000 and 400,000.

5.1.3.4 Parameter and sensitivity studies

Sensitivity studies were made to test the influence of various models and parameters. First, it was found that radiation has a negligible impact on the results. Because the addition of radiation causes a considerable increase in computational cost, it was only considered after about 3/4 of the physical run time and only used for the final simulations. Furthermore, the effect of domain size on the flame spread has been studied. Therefore, simulations were made with twice the width and depth of the domain. The influence on the flame spread has been found to be negligible with the considered range. Different velocity profiles for the main jet at the inlet were investigated as well. It was found that the use of a top-hat velocity profile slightly decreases the maximum temperature at the jet break-up point on the centerline, corresponding to an increase in flame spread further downstream, while the velocity profile no longer matched the experimental data. A power-law profile showed best agreement with the experiments close to the burner and was therefore used throughout the simulations. The jet spread and break-up point were highly sensitive regarding the exponent of the power-law profile. Thus, the exponent was chosen such that the velocity profile matched the experimental data at 30 mm height. In a final test, the high temperature zone of the diffusion flame between the pilot gas and the ambient air was expanded by setting a higher temperature (800 K) in close proximity to the burner geometry (up to 2.5 mm from the hydrogen pilot), since simulations by Ahn et al. [1] showed a significantly higher temperature in this region. The expanded pilot flame showed negligible impact on the jet in terms of spreading and break-up point. Supplementary simulation results for the latter studies can be found in the supporting information section (see Appendix section 7).

For the sensitivity studies and the determination of the right model parameters and setup, as well as for the table testing, around 50 additional simulations have been performed.

5.1.3.5 Post processing and probe correction

A limitation of the available experimental data results from the use of gas suction probes. Such probes sample data from a relatively large gas volume, and in the process, smoothen the investigated fields. To still permit a comparison between the simulations and the measurements, the computational results were smoothened in a way that attempts to mimic the probing effect. The probe, which is inserted in axial direction into the flame, has an inner diameter of 2 mm and an outer diameter of 4 mm. The volume flow rate Q_{ref} of the suction probe is specified as approximately 2 l/min at a reference temperature of $T_{\mathrm{ref}} = 300\,\mathrm{K}$; the volume flow rate Q is corrected at each grid point with respect to the temperature T using the ideal gas law. This flow rate is then used to calculate the diameter of the stream tube that is sucked into the probe:

$$d_{\mathrm{pc}} = 2\sqrt{\frac{Q}{u\,\pi}} = 2\sqrt{\frac{Q_{\mathrm{ref}}\,T}{T_{\mathrm{ref}}\,u\,\pi}} \tag{5.13}$$

Subsequently, computed results at each point are averaged (filtered) over a circle of the given diameter, resulting in data that is comparable to the measurements, or “probe-corrected” (indicated by subscript “pc”). The effective diameter d_{pc} is independent of the probe diameter and depends only on the gas temperature and the axial velocity, provided that the volume flow of the suction probe is known. It should be emphasized that the suction probing, and thus, the probe correction in this work is only applied to the species measurements.

5.1.4 Results

Figure 5.3 (a) shows the time-averaged (top) and the instantaneous gas temperature (bottom) on the central y-z plane of the computational domain. The time-averaged temperature distribution shows two reaction zones, one just downstream of the nozzle exit, where pure hydrogen is burned (from 0 mm height), which increases the temperature to release the volatiles; the second reaction zone is due to the volatile combustion (from approximately 40 mm height). Figure 5.3 (b) shows the time-averaged axial temperature profile along the centerline of the burner. Temperature correlates with the reaction progress, and hence, is a function of species concentration. In the simulation, the temperature increases too far upstream and reaches a peak slightly higher than in the experiment. This behavior is slightly unexpected, as the species mole fraction of O_2 is in good agreement between experiment and simulation, as shown in Fig. 5.3 (c). The axial distribution of CO_2 in Fig. 5.3 (c) is underpredicted in the simulation, which can be attributed to several reasons. Since oxygen is exclusively bound to Y_{CO} in the present volatile gas composition, there is no direct release of CO_2 by devolatilization. This means that all CO_2 in the downstream region must be formed by the further oxidation of CO to CO_2. Alternatively, adding CO_2 to the volatile mixture would release further CO_2, which could improve the downstream comparison with the experiments. However, because CO_2 was chosen as a contributor to the reaction progress variable in the present study, and to avoid model inconsistencies, this species was omitted from the volatile mixture, in favor of CO. Furthermore, as already reported in previous studies [3, 44, 188], some CO may further be oxidized to CO_2 during probe measurements in the experiment [53], leading

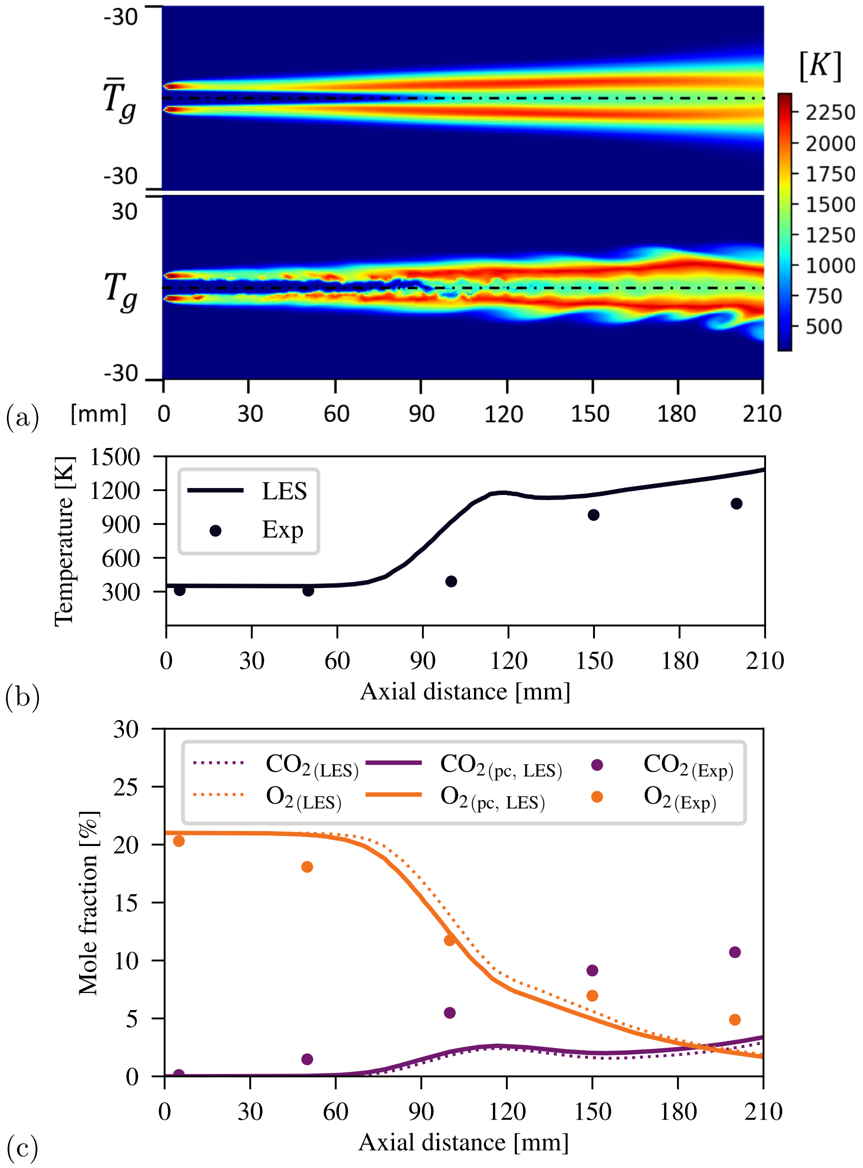

Figure 5.3: (a) Time-averaged (top) and instantaneous (bottom) temperature along the y-z plane. (b) Time-averaged axial temperature along the centerline of the burner. (c) Time-averaged mole fractions of CO_2 and O_2 along the centerline of the burner. The subscript "pc" refers to the probe-corrected profiles.

to a bias of measured CO_2 and CO species. It is also worth noting that numerical results of the previous burner configuration (employing a CH_4 pilot) showed a similar inconsistency between temperature and species [1, 34, 44, 70, 138, 162].

Figure 5.4 presents time-averaged mole fraction contours on the y-z plane of H_2O, O_2, CO_2, CO and volatiles. H_2O is formed during hydrogen combustion in the first reaction zone. O_2 is mostly consumed in the two reaction zones. CO_2 and CO are mainly produced in the second zone, where the coal particles release volatiles and burn with the surrounding oxidizer. CO_2 is formed in the outer zones, where enough O_2 from both sides is available (main jet and surrounding flow). The formation of CO is mainly favored in the inner, oxygen-poor, hot reaction zone. The mole fraction contour of volatiles shows a consistent distribution. Thus, it can be assumed, that CO is mainly coming from the unburned volatile gas - again pointing to the oxygen distribution in the volatile gas composition. Before presenting radial scalar profiles, the impact of the probe correction shall be discussed. Figure 5.5 shows the time-averaged axial gas velocity over the

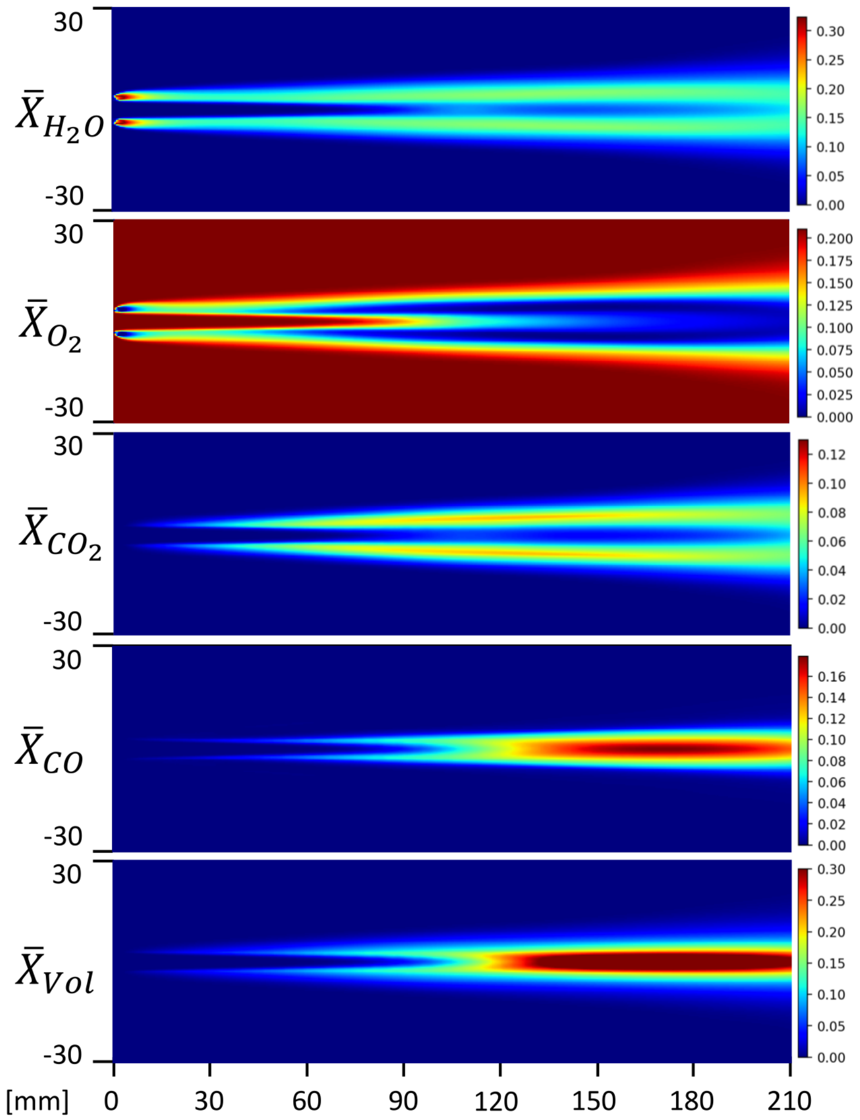

Figure 5.4: Time-averaged gaseous mole fractions of H_2O, O_2, CO_2, CO and volatiles along the y-z plane.

radius at 30 mm and 90 mm from the burner. For the sake of completeness, the influence on the velocity profile with and without consideration of buoyancy is briefly discussed here. Comparing the velocity predictions with and without buoyancy demonstrates that the effect of the latter can be considered negligible. The velocity profiles of the experimental data in Fig. 5.5 show that the flow field widens and the peak velocity decreases with increasing downstream distance. The same trend can be observed in the simulation, which shows a good agreement with the experiment.

Figure 5.6 shows the respective probe correction diameter d_{pc} profiles at 30 mm and 90 mm from the burner. There is an inverse relation of the temperature and the velocity in the correction diameter equation, as d_{pc} scales with $\mathrm{T}^{1/2}\,u^{-1/2}$ (see Fig. 5.5 and Eq. (5.13)). High velocities, as present on the centerline, lead to relatively small diameters over which the probe sucks in gas. As soon as the temperature rises (see Fig. 5.3 (a)), the gas expands, and with that, the correction diameter increases significantly with, consequently, the effect of spatial filtering, as seen in the following.

Along the centerline, the effect of probe correction is moderate (see Fig. 5.3 (c)), as the high velocity leads to a very small stream tube diameter of the gas that is being drawn into the probe (as shown in Fig. 5.6 for r → 0 mm), and hence, there is only a small spatial filtering effect and

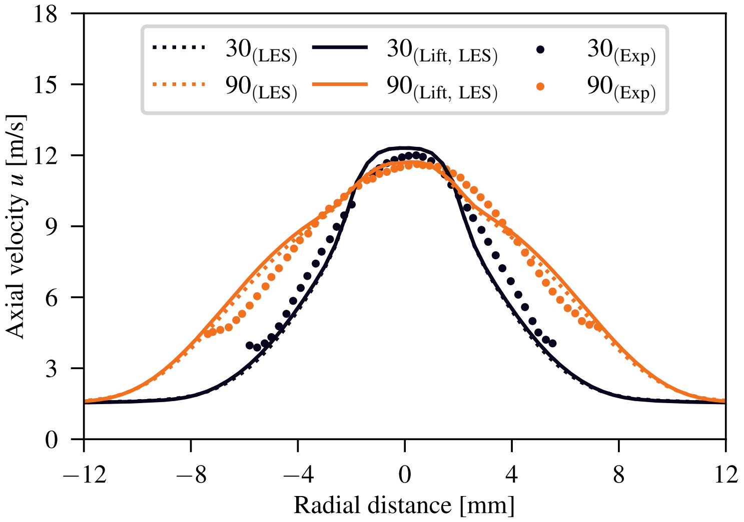

Figure 5.5: Time-averaged axial velocity profiles at different heights (millimeters) for the simulations with ("lift") and without consideration of buoyancy and the experiment. The labels 30 and 90 indicate the respective heights above the burner in millimeters.

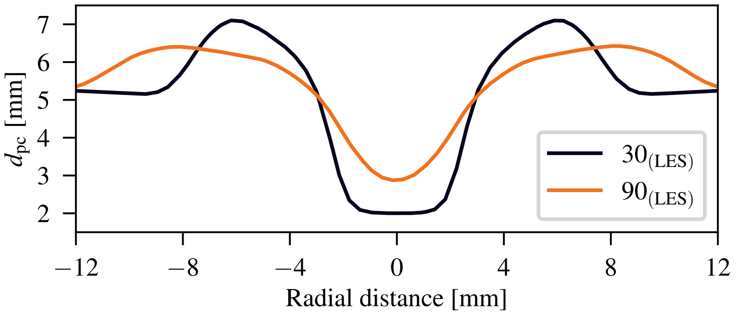

Figure 5.6: Probe correction diameter d_{pc} profiles at different heights (millimeters). The labels 30 and 90 indicate the respective heights above the burner in millimeters.

change in the result. This will change significantly away from the centerline.

Figure 5.7 shows radial profiles of time-averaged mole fractions of CO_2 and CO at different heights. The strong influence of the probing diameter on the measurement can be seen (e.g., for CO_2 at 50 mm height), where relative changes up to 50 % occur. At a height of 150 mm, the concentration of CO increases significantly, especially in the main jet area. This is likely caused by the early temperature rise and volatile release. Figure 5.8 shows the radial time-averaged mole fractions of O_2 and volatiles at different heights. From a height of 100 mm, the peak of the volatile concentration shifts from the outer reaction zone towards the centerline. The high temperature favors the release of volatiles. The radial evolution of the oxygen concentration shows a good agreement with the experiment even further downstream.

In regions of high volatile mole fractions (Fig. 5.8, e.g., at 150 mm height and 0 mm radial distance), the prediction of CO_2 and CO (Fig. 5.7) take opposite trends. While CO_2 is underestimated, CO is overestimated. Here, the authors refer again to the two possible reasons mentioned above. The effect of spatial filtering, and thus, the change in results increases significantly with rising temperatures and low axial velocities. These factors lead to a relatively large correction diameter, over which the suction probe sucks in gas, and with that, the probe affect the results even further.

As a result, we strongly encourage the use of the presented probe correction method for comparisons of numerical results with similarly obtained experimental data. In the authors' opinion, a

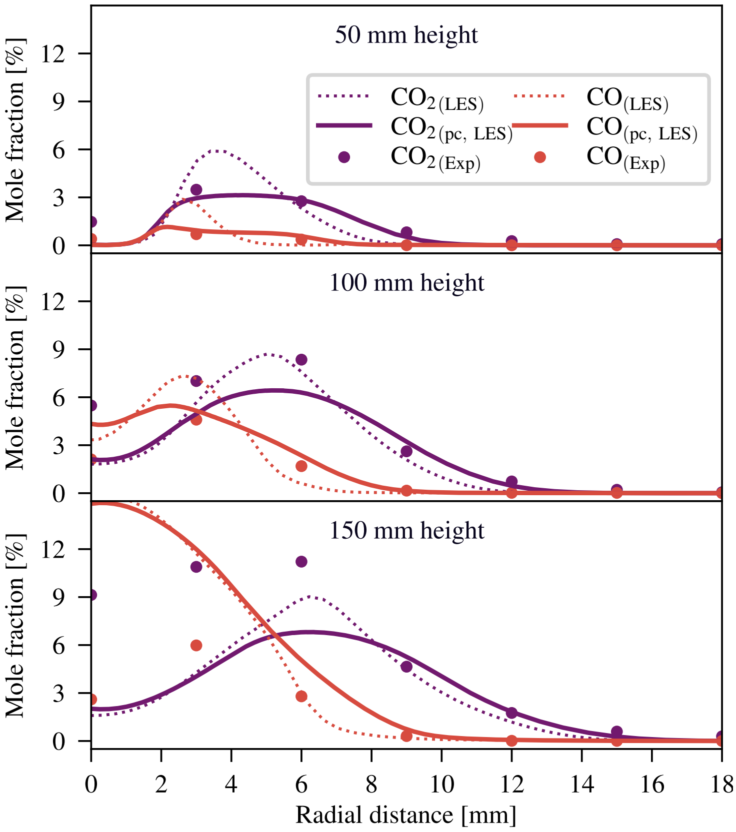

Figure 5.7: Time-averaged mole fractions of CO_2 and CO at different heights. The subscript "pc" refers to the probe-corrected profiles.

comparability between experiment and simulation for this flame is only possible considering the probe correction effect.

5.1.5 Discussion

Deviations between experiment and simulation arise both on the experimental and the simulation side, and we discuss experimental errors first. The temperature measurement by thermocouples faces challenges of its own, especially in regions of strong flame oscillations, as is the case at the flame tip. The adhesion of particles to the probe of the thermocouple can lead to further inaccuracies in the measurements. The volume-averaging of the suction probe has a great impact on the species measurements in regions of high temperature and low axial velocities and can strongly affect the prediction accuracy, as have been shown in this study. Furthermore, the oxidation of some CO to CO_2 during probe measurement may influence the species prediction additionally.

On the numerical simulation side, the calibration of the devolatilization parameters of the one-step model to the coal data, as well as the correct determination of the volatile composition and the table values calculated from it may have a strong impact on the results. Devolatilization is a highly complex heterogeneous process, while its modeling is usually constrained to a relatively narrow range of temperatures. Previous studies on the CRIEPI flame showed how difficult it is to correctly predict the mean gas temperature and species composition along the burner axis simultaneously [1, 34, 44, 70, 138, 162]. Considering the factors mentioned above, the present simulations show promising results that capture the experimental data well, especially in terms of gas composition, when considering the simple probe correction suggested here.

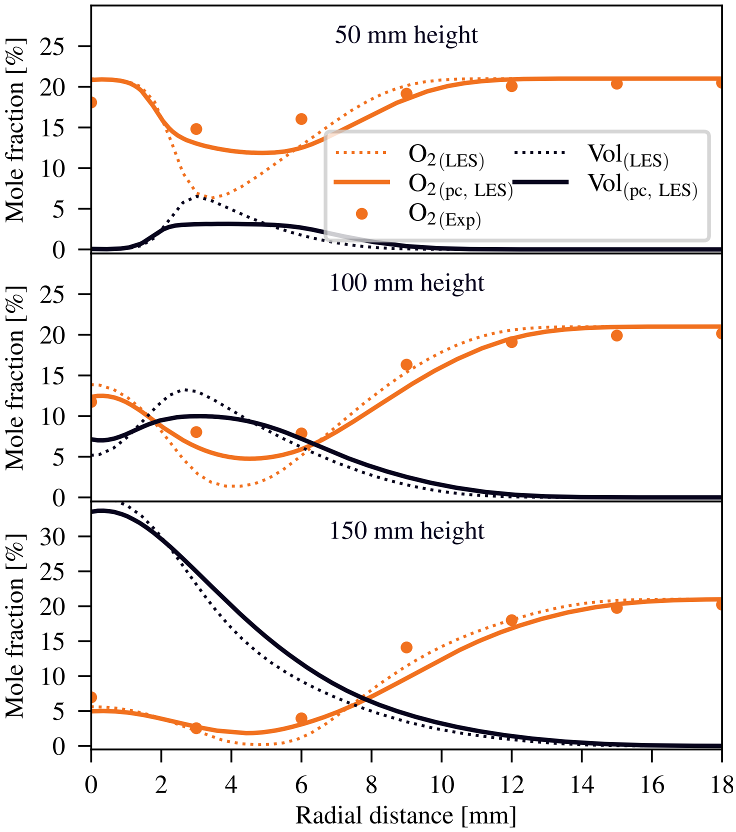

Figure 5.8: Time-averaged mole fractions of O_2 and volatiles at different heights. The subscript “pc” refers to the probe-corrected profiles.

5.1.6 Conclusions

A coaxial burner with a hydrogen-supported pulverized coal flame was investigated numerically by LES. A flamelet/progress variable approach was used to describe the thermochemical processes. The flamelet model was tested for a coal flame LES as one of the first simulations conducted on the new configuration of the investigated flame and showed a good performance. It was emphasized that this approach is well suited for the simulation of pulverized coal flames like the CRIEPI flame. The inclusion of the probe diameter in the evaluation allowed for a meaningful comparison between the experiment and simulation and showed a good agreement of the species concentrations.

The two main objectives of the paper, (1) to apply the FPV model to the new flame configuration considering only pilot and volatile gases and (2) to enhance the comparability of the gas composition by considering the modeling of the suction probe, have been achieved. The FPV approach was shown to be a cost-effective method to pre-tabulate the thermochemical flame characteristics and to give an accurate prediction of the gas composition.

In the authors’ opinion, without the simple probe correction, a meaningful comparison between experiment and simulation is not possible in this case. We highly recommend this probe correction method for future modeling attempts of the present flame.

5.1.7 Acknowledgement

The authors gratefully acknowledge the financial support through the German Research Foundation (DFG, project 238057103), the Gauss Centre for Supercomputing e.V. (www.gauss-centre.eu) for funding this project by providing computing time on the GCS Supercomputer SUPERMUC at Leibniz Supercomputing Centre (www.lrz.de) through project grant pn68nu and the Center for Computational Sciences and Simulation (CCSS) for providing computing time on the Supercomputer MagnitUDE (DFG grants INST 20876/209-1 FUGG, INST 20876/243-1 FUGG) at the Zentrum fuer Informations- und Mediendienste (ZIM). We are grateful to our colleagues at CRIEPI for providing the detailed experimental basis.

This paper is dedicated to the late Mário Costa, a good friend and remarkable scientist who is fondly remembered and greatly missed.

5.2 Evaluation of ammonia co-firing in the CRIEPI coal jet flame using a three mixture fraction FPV-LES [97]

This section of chapter 5 including all text, figures and tables is published in the Proceedings of the Combustion Institute 'D. Meller, L. Engelmann, P. Wollny, K. Tainaka, H. Watanabe, P. Debiagi, O. T. Stein, and A. M. Kempf. Evaluation of ammonia co-firing in the CRIEPI coal jet flame using a three mixture fraction FPV-LES. Proceedings of the Combustion Institute, 39(3):3615–3624, 2023.' [97] and is reprinted with permission from Elsevier.
Contributor Roles Taxonomy: D. Meller developed the code, ran the simulations and wrote the original manuscript draft. K. Tainaka and H. Watanabe performed experiments and contributed to the manuscript. L. Engelmann, P. Wollny, P. Debiagi, O. T. Stein and A. M. Kempf provided discussions of the results and contributed to the manuscript.

Abstract

Highly resolved large eddy simulations (LES) are performed to investigate co-firing of coal and ammonia in a burner experiment conducted by the Central Research Institute of Electric Power Industry (CRIEPI) in Japan. The coaxial burner with a hydrogen supported pulverized coal flame is modeled using the in-house code *PsiPhi*. A three mixture fraction flamelet/progress variable (FPV) approach is employed to simulate coal particle conversion due to devolatilization, hydrogen combustion, and ammonia combustion. Three cases are investigated and compared to each other: 1) a coal combustion case, injecting air and coal particles, 2) an ammonia combustion case, injecting a mixture of ammonia and air, and 3) a co-firing combustion case, injecting a mixture of coal, ammonia and air in the center tube. Two mechanisms are used to build the chemistry table and are compared against each other: a reduced CRECK mechanism with 120 reaction species and 1551 elementary reactions, originally reduced for coal combustion modeling, and a newly introduced reduced CRECK mechanism with 129 reaction species and 1644 elementary reactions, including the detailed NH_3 reaction paths in addition to the coal chemistry. Species are compared for the coal case and temperature fields are compared for both the coal and co-firing case. Normalized LIF signals for OH and NH are presented for all three cases. The gas composition profiles are in good agreement with the experiment and the temperature fields are consistent with previous results for the pure coal flames. For pure ammonia and for ammonia co-firing, the new mechanism shows an improved prediction of the reaction zone.

5.2.1 Introduction

Many countries are still relying on firing coal to meet their electrical base load. Thus, it is necessary to take measures to reduce emissions of carbon dioxide (CO_2) and nitric oxides (NO_x) to meet sustainability targets. One measure to reduce CO_2 emissions is the co-firing of ammonia (NH_3) as carbon-free hydrogen (energy) carrier, providing an opportunity to defossilise coal-fired power plants and their fuels.

Yamamoto et al. [204] investigated the co-firing of coal and NH_3 using a horizontal single burner. They found that the NH_3 injection position in the furnace affects the NO emissions. Minimum NO emissions were reached at a co-firing rate of 20 % with an injection position of 1 m distance from the burner - NO emissions were comparable to pure coal-fired cases.

Experiments are of great value for the engineering of such burners, but are increasingly supported by computational fluid dynamics (CFD) that can provide deeper and more accurate insights into the harsh environment during pulverized coal combustion (PCC).

Zhang et al. [209] investigated the influence of the NH_3 co-firing ratio on a 8.5 MW_{th} combustion facility with a single swirl burner, using 3D Reynolds-averaged Navier-Stokes (RANS) simulations and a global reaction mechanism. They found, at co-firing ratios above 40 %, a strong increase in unburned NH_3 in the flue gas. Using a co-firing ratio of 80 % led to the highest NO emissions, while a decrease of NO was observed when the co-firing ratio was increased even further. Ishihara et al. [63, 64] could reproduce the findings of Yamamoto et al. [204] and Zhang et al. [209] with 0D network calculations of perfectly stirred reactors while using detailed chemistry.

A powerful tool with a good trade-off between accurate predictions of PCC and computational cost is large eddy simulation (LES). The major advantage of LES compared to RANS approaches is the more realistic treatment of turbulence-chemistry interactions (TCI). Particularly for presumed-PDF flamelet approaches, LES is advantageous over RANS, since LES avoids the modeling of the entire joint-PDF of the governing flamelet variables since a major part of the TCI is already resolved, while only the subgrid PDF/FDF remains to be modeled. While LES has been widely used for PCC simulations [34, 78, 162, 184], co-firing of coal and NH_3 is yet to be investigated. An important aim in the numerical modeling of PCC is the accurate species prediction. While initial PCC-LES are based on simple combustion models (eddy breakup, eddy dissipation), the flamelet model has gained importance [114]. It offers the possibility to take into account detailed reaction mechanisms at comparatively low computational cost. In this approach, thermochemical quantities are precomputed and stored in flamelet tables, while transported control variables are used to access the tabulated data. An extension of this model is the flamelet/progress variable (FPV) model by Pierce and Moin [117], in which a progress variable is used as trajectory variable. The FPV model has been widely applied to PCC simulations [3, 95, 188, 192]. Wen et al. [192] introduced a three mixture fraction flamelet model for laminar PCC, considering devolatilization, char combustion and a pilot stream.

In the present work, co-firing of coal and NH_3 is studied using a three mixture fraction FPV-LES approach. The Central Research Institute of Electric Power Industry (CRIEPI, Japan) has conducted the experiments, using a hydrogen piloted coal flame [1, 161, 164, 165]. A detailed description of the oxidation of volatiles including large hydrocarbons for tar with a simultaneously accurate description of NH_3 oxidation, when NH_3 not only occurs in small concentrations as a volatile but is also fired as a major fuel species, is provided for the first time, while FPV-LES is used for an advanced description of TCI.

The objectives of the present study are as follows: to generate a reduced reaction mechanism covering the detailed ammonia chemistry coupled to an existing mechanism for coal volatiles and tars for use in co-firing environments and to demonstrate its advantages by comparison with experiments, using highly resolved FPV-LES. To the authors state of knowledge, this is the first work on the co-firing of coal and NH_3 using FPV-LES while presenting the first reduced, dedicated mechanism for co-firing purposes.

5.2.2 Experimental background

Figure 5.9 shows the geometry of the laboratory scale burner. It consists of an inner tube with a diameter of 6 mm and a coaxial pilot channel with a width of 0.5 mm, feeding pure hydrogen to stabilize the flame. Both channels are separated by a wall with a thickness of 0.5 mm; the thickness of the outer wall is 1.0 mm. The burner is operated in the following modes: 1) pure coal combustion (C), with coal particles and air flowing in the main stream, 2) pure ammonia combustion (A), with a mixture of air and NH_3 flowing in the main stream, and 3) the co-firing of coal and ammonia (CA), with coal particles and a mixture of air and NH_3 flowing in the main stream. Table 5.3 shows the experimental conditions. The coal type is “Coal 5” from the original paper [1], its properties are given in Table 5.4.

A gas analyzer with a ceramic suction probe is used to measure species concentrations. The temperature is measured using a K-type sheated thermocouple. Planar laser-induced fluorescence (PLIF) provides OH and NH signals at a height of 15 mm, to target high temperature and NH_3 reaction zones. Experimental data for case C are taken from the paper by Ahn et al. [1] and the proceedings of the workshop on coal and biomass conversion (CBC) [161]. Experimental data for cases A and CA are taken from [164, 165].

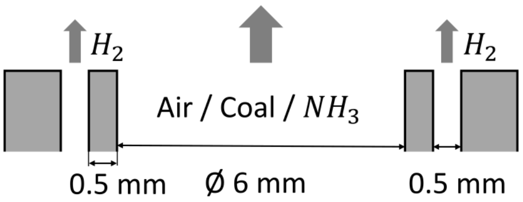

Figure 5.9: Setup of the investigated coaxial burner.

Table 5.3: Experimental conditions [165] - Standard liters l_N are given at 293.15 K and 1 bar.

Case	C	A	CA
	Coal	NH_3	Co-firing
Air [l_N/min]	12.0	9.6	9.6
NH_3 [l_N/min]	0.0	2.4	2.4
H_2 [l_N/min]	0.6	0.6	0.6
Coal feed [g/h]	465.1	0.0	297.4
Heat input [kW] (main fuel)	3.63	0.58	2.9
Reynolds number	3008	3056	3056
Equivalence ratio	4.64	0.91	4.61

Table 5.4: Properties of "Coal 5" [1] showing proximate analysis (PA) and ultimate analysis (UA) on a dry ash-free basis.

PA [wt%]		UA [wt%]	
Ash	14.2	C	70.30
Volatiles	32.6	H	4.57
Fixed carbon	52.4	N	1.66
Moisture	0.8	S	0.45
LHV [MJ/kg]	**27.9**	O	8.78

5.2.3 5D-FPV approach

The present jet flame relies on four sources of gaseous fuel, the first resulting from the outer hydrogen pilot, the second from the NH_3/air stream and the third and fourth from the volatile matter and the char, from the coal particles. To accurately describe these fuel streams, four mixture fractions are required. Studies of the original configuration of the CRIEPI flame by Franchetti et al. [34], Wen et al. [192] and Akaotsu et al. [3] show that char reactions are negligible in the (relatively short) region of interest. There is no experimental evidence for a strongly different behavior in the new flame setup. Hence, to limit the complexity of the chemistry table, the influence of char combustion is neglected in this work. Thus, three mixture fractions $Z_j = Y_j/(Y_{\mathrm{ox}} + Y_{\mathrm{vol}} + Y_{\mathrm{ammo}} + Y_{\mathrm{pil}})$ are introduced to describe the mixing of the three fuel streams, indicated by $j \in \{\mathrm{pil}, \mathrm{ammo}, \mathrm{vol}\}$ for the pilot stream, the ammonia stream, and the volatile stream, with the ambient air. In the present work, the pilot stream is described by a separate mixture fraction and is treated as pure H_2. As proposed by Hasse and Peters [46], to prevent numerical issues during table access and to improve simulation stability, a coordinate transformation from a unit pyramid space (Z_{pil}, Z_{vol} and Z_{ammo}) to a unit cubic space is performed, following the three-mixture fraction flamelet approach by Wen et al. [192]. Three non-dimensional parameters are used, $Z = Z_{\mathrm{pil}} + Z_{\mathrm{vol}} + Z_{\mathrm{ammo}}$, $A = Z_{\mathrm{pil}}/(Z_{\mathrm{pil}} + Z_{\mathrm{vol}} + \epsilon)$ and $B = (Z_{\mathrm{pil}} + Z_{\mathrm{vol}})/(Z_{\mathrm{pil}} + Z_{\mathrm{vol}} + Z_{\mathrm{ammo}} + \epsilon)$, where ϵ denotes a small positive number required for numerical stability. These parameters (ranging from 0 to 1) describe all possible states of mixing.

To fill the table for all these states, the non-premixed flamelet equations [114] are solved in “FlameMaster” (by Pitsch) [118] for varying values of A and B (0, 0.2, 0.4, 0.6, 0.8, 1) to represent the interphase mass transfer. The gas composition on the fuel side of the flamelet equations is calculated from $Y_{\mathrm{fuel,A,B}} = (1-B)Y_{\mathrm{ammo,p}} + B(1-A)Y_{\mathrm{vol,p}} + ABY_{\mathrm{pil,p}}$, where $Y_{\mathrm{ammo,p}}$, $Y_{\mathrm{vol,p}}$, and $Y_{\mathrm{pil,p}}$ are the pure ammonia, volatiles, and pilot stream mass fractions. The composition of the oxidizer side is set to air. The stoichiometric mixture fractions for the fuel mixtures range between $\mathrm{Z}_{\mathrm{pil,st}}$ =0.028 for hydrogen, $\mathrm{Z}_{\mathrm{ammo,st}}$ =0.140 for ammonia, and $\mathrm{Z}_{\mathrm{vol,st}}$ =0.094 for volatiles. Similar to the work of Messig et al. [99], different input stream temperatures for the fuel T_{f} and oxidizer T_{ox} side are set to vary the enthalpy levels when solving the non-premixed flamelet equations, to account for the strong interphase heat transfer during coal conversion. Three different input stream temperatures $T_{\mathrm{Boundary}} = T_{\mathrm{f}} = T_{\mathrm{ox}}$ are considered in the table (300 K, 600 K, 800 K), with linear interpolation conducted during table access. The scalar dissipation rate χ is varied when solving the non-premixed flamelet equations in mixture fraction space to account for different strain rates. Since the relative heat input of the hydrogen pilot in case C is relatively small (2.8 %), we assume that differential diffusion effects are small in the present setup. Thus, the one-dimensional steady non-premixed flamelet equations are solved based on the assumption of unity Lewis number. The thermochemical quantities given by the flamelet solutions are then parameterized using the control variables. Besides the mixture fractions, a progress variable is needed, which is defined as a linear combination of key product species following $Y_{\mathrm{PV}} = Y_{\mathrm{CO_2}} + Y_{\mathrm{CO}} + Y_{\mathrm{H_2O}} + 10\ Y_{\mathrm{NO}}$. Here, $Y_{\mathrm{H_2O}}$ serves for the combustion of all three mixture fractions, while $Y_{\mathrm{CO_2}}$ and Y_{CO} describe the volatile combustion. The contribution of Y_{NO} is added to account for nitrogen species resulting from NH_3 and volatiles, the prefactor of the last term is based on the parameter study by Luo et al. [88]. The normalized enthalpy H_{norm} and the normalized progress variable $Y_{\mathrm{PV,norm}}$ are used for table access, following the equations from previous work [95].

The final table parameterization follows $\Psi = F(A, B, Z, Y_{\mathrm{PV,norm}}, H_{\mathrm{norm}})$ for the thermochemical quantities Ψ. To provide the trajectory variables, transport equations for Z_{pil}, Z_{vol}, Z_{ammo}, Y_{PV} and the total enthalpy H are solved, using the equations presented in a previous paper [95]. The transport equation of the progress variable contains a further source term, which takes into account the mass transfer between solid and gas phase, whereby only the volatile species, contribute to it [99]. The variance of the sum of all mixture fractions $\widetilde{Z''^2}$ is solved via transport equation [112], using the parameters that have been tested for spray flame LES [142, 166]. The table is pre-integrated to be used with an assumed top-hat pdf based on the filtered mixture fraction sum $\widetilde{Z}$ and the subgrid mixture fraction variance $\widetilde{Z''^2}$ for turbulence-chemistry interaction modeling [110]. The table dimensions are 6 x 6 x 132 x 51 x 6 in A x B x Z x $Y_{\mathrm{PV,norm}}$ x H_{norm} space resulting in a total of 1,454,112 points and requiring a storage space of 644 MB in uncompressed ASCII format.

5.2.4 Homogeneous chemistry

First, a reduced CRECK mechanism consisting of 120 species and 1551 elementary reactions is used [145]. The mechanism was developed and optimized to predict emissions of NO_x as a pollutant - but not to describe the combustion of ammonia. The mechanism includes three NO_x formation paths, fuel-, prompt- and thermal-NO_x, and has shown good performance in the context of modeling pulverized coal flames with detailed NO_x chemistry already [145].

The introduction of NH_3 as a co-fuel in the co-firing of coal and NH_3 fundamentally changes the flame behavior, making it advisable to develop a reduced mechanism that describes the combustion behavior of NH_3. A new reaction mechanism is generated, combining the reaction paths for the pure NH_3 combustion from the CRECK modeling group [157, 159] (31 species and 203 elementary reactions, *CNH*$_3$) and the aforementioned reduced CRECK mechanism (*C120*) [145]. The new mechanism results from merging species and reactions from *C120* and *CNH*$_3$, followed by excluding duplicate species and reactions. Duplicate reactions showed equal reaction rates, avoiding any inconsistencies. The new mechanism includes 129 species and 1644 elementary reactions (*C129*). Mechanism *C129* is the only mechanism containing all necessary species for the complete fuel composition (volatiles, NH_3, H_2), considering a detailed description of the oxidation of volatiles including large hydrocarbons for tar, while simultaneously considering an accurate description of NH_3 oxidation (for use if NH_3 is fired as fuel at high concentrations). A reaction path diagram for NH_3 oxidation following nitrogen of mechanisms *C120*, *C129*, and CNH_3 at 1800 K and a detailed analysis can be found as supplemental material (see Appendix section 7). The new mechanism *C129* includes more detailed reaction pathways. The reaction pathway $NH_2 \rightarrow N_2H_2 \rightarrow NNH \rightarrow N_2$ is completely ignored in *C120*. Mechanism *C129* shows a better prediction of the reduction of NO. The following paragraphs compare the different mechanisms. For the characterization of fuels and the development and optimization of reaction mechanisms, the laminar flame speed is particularly important. Capturing the laminar flame speed of a fuel-air mixture at relevant equivalence ratios is a fundamental requirement, even for a partially premixed coal flame. Figure 5.10 shows the laminar flame speeds S_L of NH_3 at different equivalence ratios Φ, calculated with Cantera [41], for the pure NH_3 mechanism (CNH_3) [157, 159], the reduced CRECK mechanism with 120 species (*C120*) [145] and the new mechanism (*C129*). Experimental data collected by Ronney [143] under microgravity conditions as well as recent results by Mei et al. [94] (under gravity) are shown.

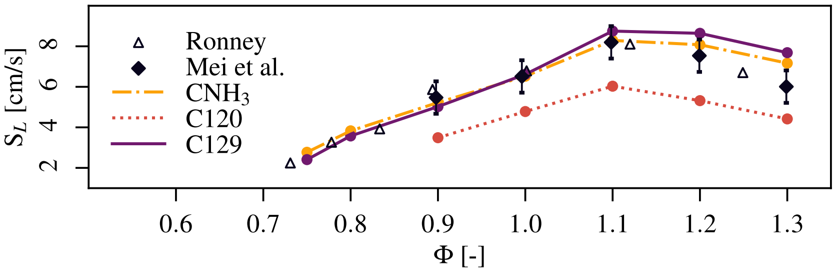

Figure 5.10: Laminar flame speed of NH_3 at different equivalence ratios for $p = 1\,\text{bar}$ and $T = 298\,\text{K}$.

While *C120* underestimates the laminar flame speed of NH_3 for all investigated equivalence ratios, mechanisms *C129* and CNH_3 are in good agreement with the experimental data at lean, stoichiometric and slightly rich conditions. The paper considers three mechanisms that need to be compared and checked for consistency. In a further step, 1D counterflow flames are calculated with FlameMaster for different values of A and B, and a wide range of scalar dissipation rates from equilibrium to near extinction. For the quantitative comparison of the mechanisms shown in Figs. 5.11 - 5.13, scalar dissipation rates were selected such that all three mechanisms resulted in a converged flame solution. In the following figures, the x-axis is clipped to show only relevant changes. Figure 5.11 shows the temperature as well as the mass fractions for NO, OH and NH over the mixture fraction Z for pure NH_3 combustion (e.g. $A = 0$, $B = 0$) for all three mechanisms. The trends of T and Y_{OH} match for all three mechanisms, while mechanisms *C120* and *C129* show slightly lower values for Y_{NH}. The mass fraction Y_{NO} is in good agreement for *C129* and the reference mechanism CNH_3, while *C120* shows slightly lower values.

Figures 5.12 and 5.13 show the same plots for different mixtures of volatiles and hydrogen, and volatiles and pure NH_3 at different scalar dissipation rates. Although the curves for T and Y_{OH} show almost identical trends, there are the expected deviations for Y_{NO} and Y_{NH}. Mechanism *C120* shows slightly higher values for Y_{NO} and Y_{NH}, while the deviations for Y_{NO} increase as the proportion of NH_3 in the fuel mixture increases. This reflects well the findings from the reaction path analysis, as *C129* shows a better prediction of NO reduction.

In summary, both mechanisms show very similar results for the 1D counterflow flames. Differences arise for Y_{NO} and Y_{NH} with increasing amount of NH_3, with *C129* showing better agreement

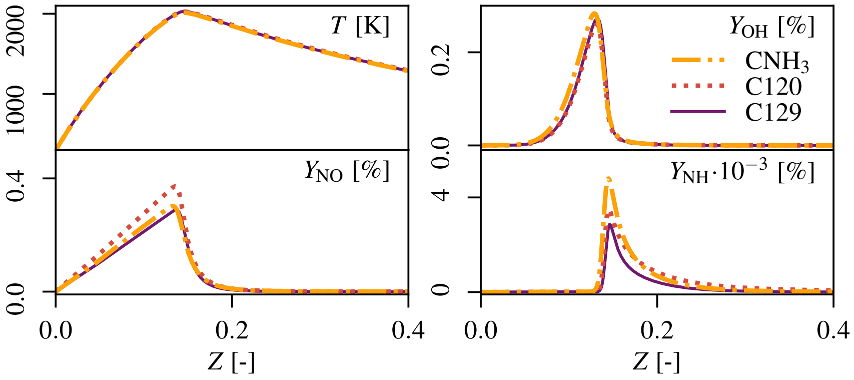

Figure 5.11: 1D counterflow flames at $T_f = T_{ox} = 300\,\mathrm{K}$, $\chi = 1\,\mathrm{s}^{-1}$ and $p = 1\,\mathrm{bar}$ for $A = 0.0$ and $B = 0.0$.

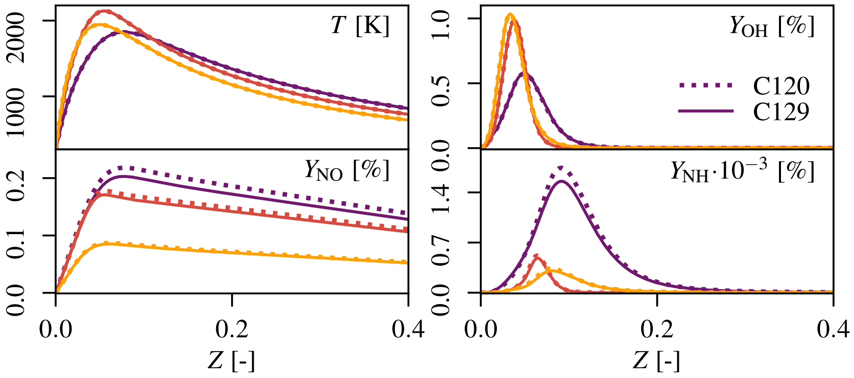

Figure 5.12: 1D counterflow flames at 300 K and 1 bar for $B = 1.0$ and $A = 0.4$ ($\chi = 19\,\mathrm{s}^{-1}$, purple), $A = 0.6$ ($\chi = 1\,\mathrm{s}^{-1}$, red) and $A = 0.8$ ($\chi = 1\,\mathrm{s}^{-1}$, yellow).

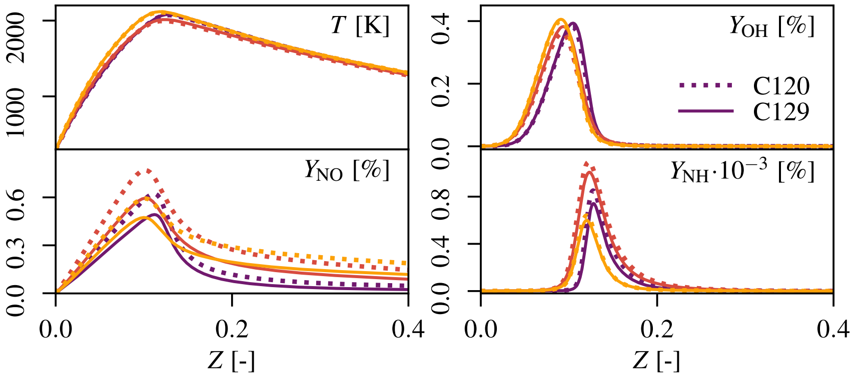

Figure 5.13: 1D counterflow flames at 300 K and 1 bar for $A = 0.0$ and $B = 0.4$ ($\chi = 0.1\,\mathrm{s}^{-1}$, purple), $B = 0.6$ ($\chi = 1\,\mathrm{s}^{-1}$, red) and $B = 0.8$ ($\chi = 1\,\mathrm{s}^{-1}$, yellow).

with the reference mechanism *CNH3* for pure ammonia. The 1D counterflow flames reflect the findings in the reaction path analysis well.

5.2.5 Coal conversion modeling

Coal particles are described in a Lagrangian framework using the models used by Rieth et al. [137]. The single first order reaction (SFOR) model by Badzioch & Hawksley [8] is used to describe devolatilization. The model constants are fitted based on the coal ultimate analysis using the particle kinetics preprocessor (PKP) [178] and have been taken from our previous work on this burner geometry [95]. The fitted parameters for the pre-exponential factor and the activation energy read $k = 875.06 \cdot 10^5\,\mathrm{s}^{-1}$ and $E = 688.69 \cdot 10^5\,\mathrm{J/(kmol\,K)}$, respectively. A Q-factor of 1.64 is used to account for the volatile yield at high temperatures. Table 5.5 shows the modeled pure volatile gas ($A = 0$ and $B = 1$) based on which the mixtures between the three fuels have been calculated. The composition of volatiles is obtained using the CRECK-S-C model, following the new, detailed approach by Debiagi et al. [26], which is able to predict coal devolatilization rates including detailed product composition. The instantaneous volatile release rates were integrated over time, allowing to define the overall predicted yield of volatiles.

Table 5.5: Modeled volatile gas composition Y [%].

H_2	2.2	C_5H_5N	9.2	$C_{10}H_{12}$	12.0
CO	11.9	HCN	6.5	$C_6H_6O_2$	13.5
CO_2	3.0	C_2H_4	1.6	C_6H_5OH	10.3
CH_4	0.1	H_2O	3.8	$C_{16}H_{10}$	23.2
NH_3	2.7				

Particle swelling is neglected, as Muto et al. [104] reported a negligible influence. A blowing correction is applied to account for the rapid effect of devolatilization on the momentum and energy equations of the particle [163]. The particle size distribution was taken from Ahn et al. [1]. Particle motion is governed by drag and gravity [162]. A Wiener process models the influence of subgrid turbulence on the particles [12, 65], taking into account the particle relaxation time and the subgrid kinetic energy. Favre-filtered transport equations for total mass, momentum, and the respective control variables from the FPV-approach are solved to describe the gas phase, following the equations from [95]. Subgrid fluxes are closed with Nicoud's Sigma model [107], assuming a constant turbulent Schmidt- and Prandtl number of 0.7 and a unity Lewis number. An additional transport equation for NO is solved, splitting the NO source term into a formation and a rescaled consumption part, following the work of Wen et al. [191].

5.2.6 Numerical setup and post processing

The in-house code *PsiPhi* is used to perform the massively parallel LES [95, 137, 138]. The code uses a low-Mach finite volume method (FVM) with a conjugate gradient solver and Jacobi preconditioner. An equidistant, orthogonal Cartesian grid is used. Diffusive fluxes and the convective flux of momentum are discretized by a second-order accurate central differencing scheme (CDS), while convective scalar fluxes are discretized through a total variation diminishing (TVD) scheme with a CHARM limiter [211]. Time integration is performed by an explicit third-order low-storage Runge-Kutta scheme [102]. Previous studies of the flame [34, 95] show that radiative heat transfer in this flame is negligible, as there are no confining combustor walls considered which would typically emit, absorb, or reflect heat, and hence, influence particle and gas temperature. Considering its computational cost, radiative heat transfer has been excluded from the detailed mechanism comparison. A comparison of the radiation influence for mechanism *C129* and cases C and CA is available as supplemental material. The Lagrangian and Eulerian phases are coupled through second-order trilinear interpolation. The domain decomposition for both Lagrangian and Eulerian fields is achieved by the message passing interface (MPI). The inflow generator by Klein [69, 71] is used to generate turbulent perturbations for the main jet velocity at the inlet plane, using a turbulent lengthscale of 0.6 mm and a value of $0.45\,\mathrm{m^2/s^2}$ for the diagonal Reynolds stresses. For the transported quantities, a zero-gradient boundary condition is used at the outlet whereas a Dirichlet boundary condition is used at all other boundaries. For pressure, a zero-gradient boundary condition is set at the inlet whereas ambient pressure is set at all other boundaries. The inlet velocity profile and flame initialization are taken from previous work [95]. Simulations are conducted on two different grids. For the coarse (fine) simulations, cubic cells of $\Delta = 0.4$ (0.1) mm are used throughout a rectangular domain, spanning 217.6 (30.0) mm / 64 (25) mm / 64 (25) mm in x-, y- and z-direction, resulting in approximately 14 (19) million cells. The *CFL* number is limited to a value of 0.7 to achieve a stable solution. Simulations are performed on 2,048 cores on the HPC system HAWK at a computational cost of 30,000 - 40,000 core-h for the coarse and fine simulations. Statistical samples are taken between time steps 150,000 and 200,000. For the post-processing of species mole fractions, a probe-correction technique [95] is used to account for the diameter over which the suction probe gathers samples in the experiments.

5.2.7 Results and discussion

The discussion starts for the pure coal case C, for which the most complete experimental data is available. Figure 5.14 shows radial profiles of mean mole fractions X_{O_2}, X_{CO_2}, X_{CO} and X_{NO} at 50 mm and 100 mm from the burner for both mechanisms. Both mechanisms give a good prediction. Since case C has only very small amounts of nitric species in the volatile gas, the changes between the mechanisms are small, as expected. The consideration of the more detailed NH_3 kinetics influences the oxygen reduction to a certain extent (see i.e. X_{O_2} at 50 mm height). The fundamentally theoretical basis of mechanism *C129* should be considered as the reference result.

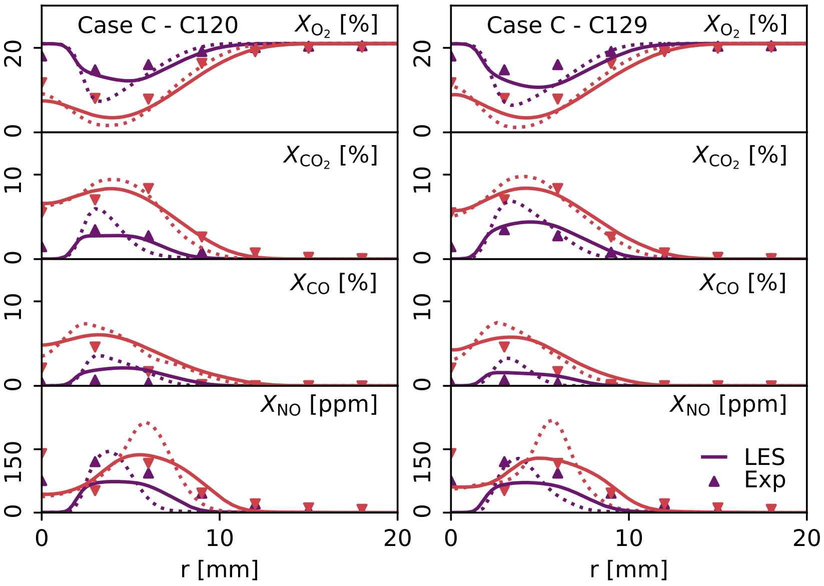

Figure 5.14: Mean mole fractions X_{O_2}, X_{CO_2}, X_{CO} and X_{NO} of *C120* (left) and *C129* (right) for case C at 50 mm (purple) and 100 mm (red) height above the burner. Raw values are dotted, probe-corrected values [95] are shown with solid lines.

After this initial validation of the simulation setup (and the validation performed in our previous work [95]), the general flame behavior of cases A and CA are investigated. Figure 5.15 shows the mean temperature fields from mechanisms *C120* (left) and *C129* (right) for the three respective cases and the mean temperature field of *CNH*$_3$ for case A. The pure coal combustion case (C) shows an early breakup of the main jet. Two hot temperature zones - due to the hydrogen flame and the volatile combustion - are formed. Minor differences between the two investigated mechanisms are evident due to the already present N-species in the volatile gas. *C129* shows a slightly earlier temperature rise above 20 mm height. The co-firing case (CA) shows a weak breakup of the main jet compared to case C. Both mechanisms act very similarly while the hot temperature zone with *C129* seems slightly thicker. The pure combustion of NH_3 (case A) shows again an even weaker breakup of the main jet. Compared to case CA, the hot temperature zone is thinner (since no coal particles are injected). Ammonia burns in the peripheral regions where the mixture of air and NH_3 meets the hydrogen flame. All three mechanisms act very similarly, while *C120* yields slightly lower temperatures attributable to the lower laminar flame speed.

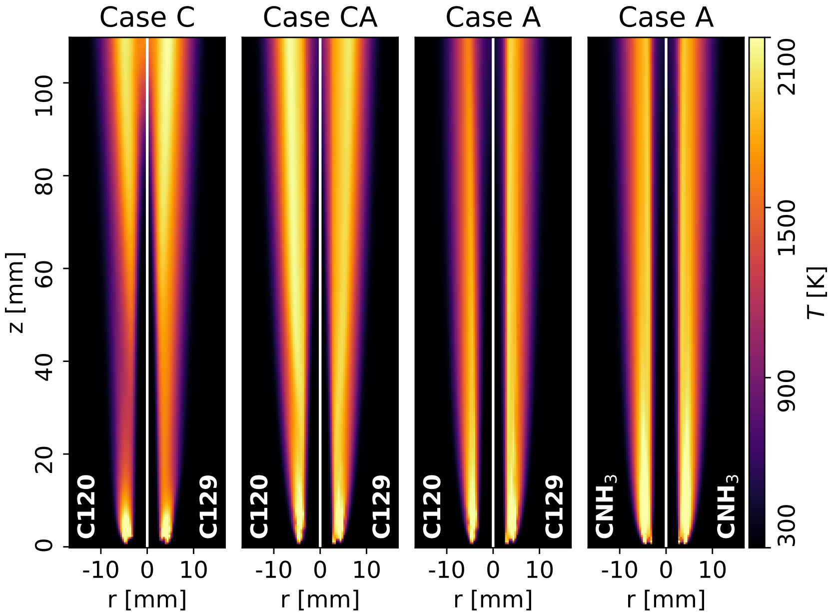

Figure 5.15: Mean temperature of *C120* (left) and *C129* (right) in the y-plane for all three cases and mean temperature of *CNH*$_3$ for case A. (The figure shows only a section of the entire simulated domain.)

Figure 5.16 shows the instantaneous (left) and mean (right) $X_{\mathrm{O_2}}$ mole fractions of mechanism *C129* for all cases and mechanism *CNH*$_3$ for case A. Case C shows more turbulence due to lower temperatures (in the upstream region), and hence, higher local Reynolds numbers. While oxygen is completely consumed at around 120 mm, case CA shows still a thin oxygen zone even further downstream. Case A shows the weakest breakup of the inner jet. Oxygen consumption is low compared to the other cases. Overall, the addition of NH_3 causes the flame to be stabilized by the early ammonia combustion. The axial point of the jet breakup moves further downstream, while the weakest breakup can be observed when no particles are injected.

Figure 5.17 shows the axial mean temperature along the centerline for the cases C and CA. The simulation shows an earlier temperature rise and a slightly higher temperature further downstream compared to the experiment for both cases, which has also been observed in our previous studies for case C [95]. In fact, experimental species data shows that ignition has occurred at 100 mm height (cf. red lines in Fig. 5.14 for r → 0), while the experimental temperature data at this point has only risen slightly, indicating no ignition. Turbulent fluctuations in the region of the flame tip (i.e. 100 mm height) might affect the temperature measurement by thermocouples. It is worth noting that other research groups observed a similar inconsistency between temperature and species on their numerical results of the previous burner configuration (employing a CH_4 pilot) [138, 162] and of the present burner configuration [1]. The differences between *C120* and *C129* are small for both cases.

Figure 5.18 shows species concentrations 15 mm above the burner, obtained from the fine grid. Normalized OH and NH LIF measurements, as well as normalized mole fractions X_{OH}, X_{NH} and the mixture fraction of the volatiles Z_{vol} are shown. Normalization is applied based on the highest value in all cases (C, A, CA) for each mechanism, respectively. For case C, the experiment shows two peaks for OH, while the simulations show only one peak. The peaks indicate the reaction

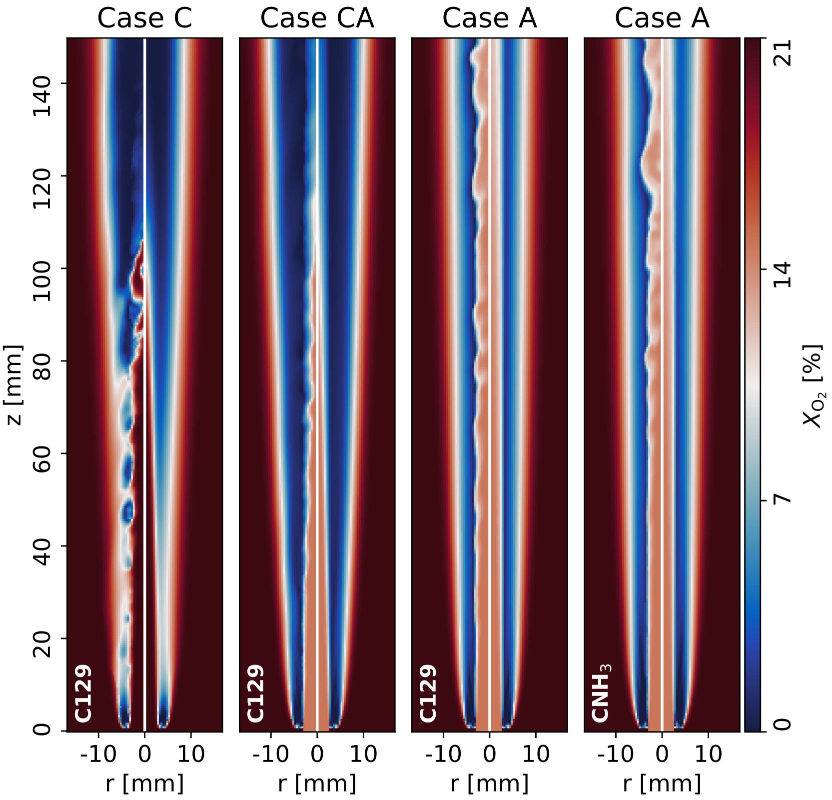

Figure 5.16: Instantaneous (left) and mean (right) X_{O_2} mole fractions of *C129* for all cases and *CNH*$_3$ for case A. (The figure shows only a section of the entire simulated domain.)

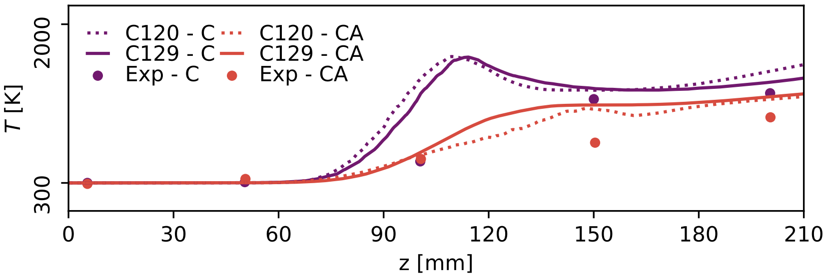

Figure 5.17: Axial mean temperature for cases C and CA.

fronts with the surrounding air. The profiles shown are located relatively close to the burner, where the influence of the hydrogen pilot is still comparatively strong. The limiting grid resolution of the thin annular region due to the uniform grid arrangement of the code slightly influences predictions in the near-burner region. However, since the hydrogen pilot merely serves to ignite the coal/ammonia flame and the grid resolution in the middle and downstream region is high, it do not unduly affect the major results.

The largest volatile concentration shows up in close proximity to the flame front and decreases to zero within the flame front due to volatile combustion. For case A, the location of OH of both mechanisms is in reasonable agreement with the experiment. Since there is no coal inflow, there is also no volatile release. The NH concentration increases at the edge of the flame front in the inner high temperature zone due to reduction of NH_3 from the mixture of NH_3 and air. The location is much better predicted by *C129* compared to *C120*. For case CA, both, NH and OH fit well with the experiment for both mechanisms, while *C129* has a slightly better prediction of

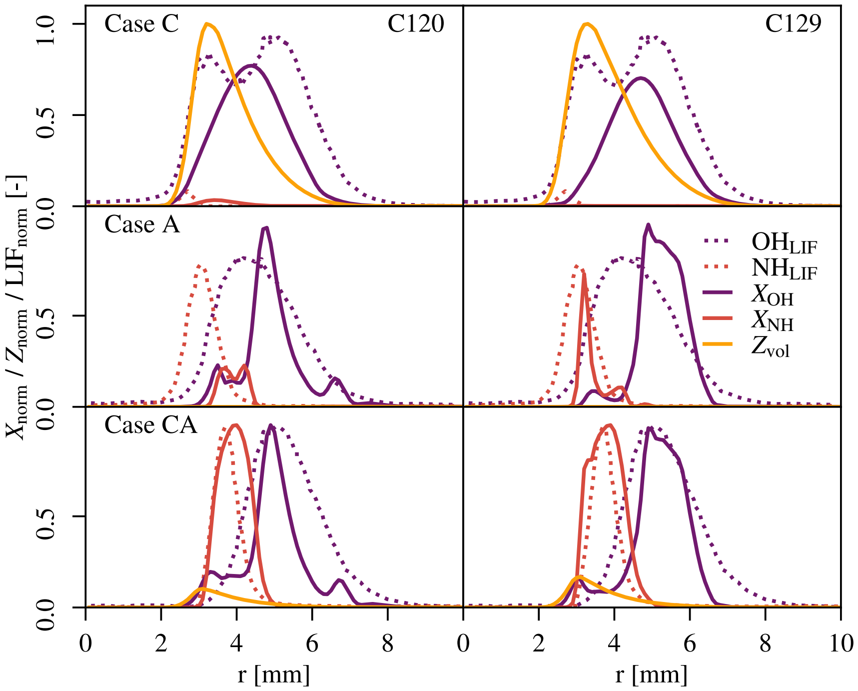

Figure 5.18: Normalized OH and NH LIF measurements, normalized mole fractions of X_{OH}, X_{NH} and normalized mixture fraction Z_{vol} at 15 mm height above the burner.

the location of the NH reaction zone. The volatile release in case CA is lower since the coal/air mass ratio is lower.

Figure 5.19 shows the mole fraction X_{NO} at 15 mm (yellow), 50 mm (purple) and 100 mm (red) height for both mechanisms and cases A and CA. While differences in NO production for case C are small due to the low NH_3 concentration in the coal volatiles (see Fig. 5.14), differences in NO production are evident (as expected) for cases A and CA. Mechanism *C129* yields slightly more NO further downstream in case A. Comparing this to the temperature profiles in Fig. 5.15, *C129* predicts higher temperatures for case A, thus, more NO is formed. Since no measurements are available at present to fully evaluate the results for cases A and CA, this remains future work.

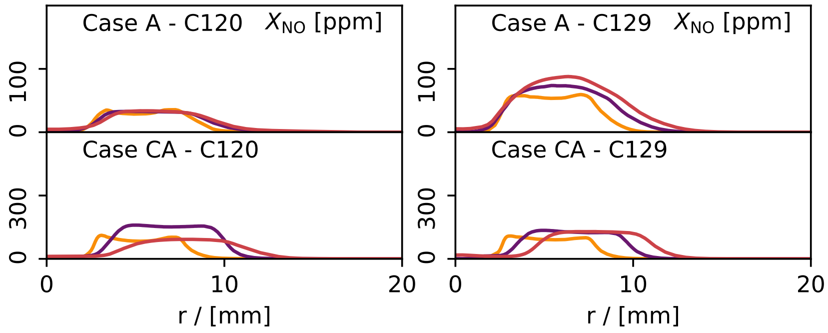

Figure 5.19: Mean mole fraction X_{NO} from *C120* (left) and *C129* (right) for cases A and CA at 15 mm (yellow), 50 mm (purple) and 100 mm (red) height above the burner. Only probe-corrected values [95] are shown.

5.2.8 Conclusion

The co-firing of coal and NH_3 was studied using a three mixture fraction FPV-LES approach. The major advantage of the LES in this work is the more realistic treatment of TCI compared to RANS approaches. LES is also a necessary requirement for the probe correction applied. Two mechanisms were compared against each other, one being an existing reduced CRECK mechanism for coal combustion. A new mechanism specifically for ammonia co-firing has been generated from existing (reduced) CRECK mechanisms. The new mechanism *C129* provides for the first time a detailed description of the volatile combustion, considering large hydrocarbons for tar, and NH_3 oxidation, considering NH_3 not only in small concentrations as a volatile, but also as a major fuel species. The new mechanism *C129* shows good agreement with the reference mechanism CNH_3 with respect to the laminar flame speed of NH_3 in 1D simulations.

Three cases were studied, 1) a coal and air case, 2) a pure NH_3 and air case, and finally 3) the co-firing of coal and a mixture of NH_3 and air. Axial temperature profiles and radial species concentrations were compared. While the temperature profiles in the simulations showed a slightly earlier rise compared to the experiment (which is consistent with other simulations of that flame series), the species trends of both mechanisms for case C fit well. The LIF measurements of OH and NH were reasonably matched by both mechanisms, with *C129* showing better predictions for the location and amount of the NH reaction zones for cases with ammonia (A, CA). The new mechanism is available as supplementary material to this paper.

5.2.9 Acknowledgments

The authors gratefully acknowledge the financial support through the German Research Foundation (DFG, project 238057103) and the Gauss Centre for Supercomputing e.V. for supporting this project (grant DUEHAWK2021) by providing computing time on the GCS Supercomputer HAWK at Höchstleistungsrechenzentrum Stuttgart. We thank Dr. A. Shamooni for helpful discussions on the chemical kinetics.

5.3 Exhaust Gas Recirculation (EGR) analysis of a swirl-stabilized pulverized coal flame with focus on NO_x release using FPV-LES [96]

This section of chapter 5 including all text, figures and tables is published in the journal Fuel 'D. Meller, L. Engelmann, O. T. Stein, and A. M. Kempf. Exhaust Gas Recirculation (EGR) analysis of a swirl-stabilized pulverized coal flame with focus on NO_x release using FPV-LES. Fuel, 343:127939, 2023.' [96] and is reprinted with permission from Elsevier.
Contributor Roles Taxonomy: D. Meller developed the code, ran the simulations and wrote the original manuscript draft. L. Engelmann developed code, provided a discussion of the results and contributed to the manuscript. O. T. Stein and A. M. Kempf provided discussions of the results and contributed to the manuscript.

Abstract

Highly-resolved large eddy simulations (LES) are performed to investigate the combustion characteristics and the NO_x-formation in the swirl-induced recirculation zones of the Brigham Young University (BYU) burner flow reactor (BFR). The simulations are performed using the in-house LES tool *PsiPhi*, utilizing a flamelet/progress variable (FPV) approach to model the reactive multiphase flow. Four dimensions are used to parameterize the thermochemical quantities consisting of two mixture fractions for volatiles and char burnout, the total enthalpy and a progress variable, defined by a linear combination of key product species mass fractions. A reduced CRECK mechanism with 120 species and 1551 reactions is used, including all NO_x-formation mechanisms (prompt-, fuel-, thermal-, and pathway via N_2O). Devolatilization, char burnout and radiation effects are considered in the LES. Radial profiles of major gas species are compared with experimental data, leading to an overall good agreement. Two variants to determine NO species were investigated: 1) the direct extraction of NO from the flamelet table and 2) the solution of an additional transport equation for NO with a modified NO source term, split into a formation and a rescaled consumption part. The solution of an additional transport equation for NO is clearly superior and necessary for pulverized coal simulations, showing a much improved prediction of forward- and backward reactions of NO inside the furnace, while the direct extraction of NO from the flamelet table greatly overpredicts its formation.

5.3.1 Introduction

While countries such as the USA and Germany have reduced the generation of electricity from fossil fuels, economically emerging nations such as India and Bangladesh have drastically increased their coal-fired power generation to meet the basic demand. Accordingly, a global abandonment of coal-firing in the coming years is highly unlikely. The drastic reduction of environmentally and climate damaging emissions in coal combustion processes is thus essential to help open the way to a climate-friendly future and a clean transition to new power generation technologies.

Combustion optimization techniques help to increase fuel burnout and promote emission reduction, such as nitrogen oxides (NO_x) reduction by swirl optimization in low-NO_x burners. NO_x is formed in almost all combustion processes. A general distinction is made between three NO_x sources, thermal-NO_x, prompt-NO_x and fuel-NO_x. Thermal-NO_x is formed by thermal dissociation of atmospheric nitrogen at high temperatures ($> 1800\,\mathrm{K}$), which accounts for a large proportion of NO_x emissions, especially for fuels without fuel-bound nitrogen. Prompt-NO_x is formed at the flame front by hydrocarbon- and hydroxyl radical attacks on atmospheric nitrogen – also at high temperatures. Its proportion is small and usually considered negligible. Fuel-NO_x is formed by oxidation of fuel-bound nitrogen. Its contribution to total NO_x can be as high as 80 % for coal firing [101].

Reactor network models and computational fluid dynamics (CFD) are typically used to predict NO_x-formation in combustors.

CFD has become increasingly important in recent years for the detailed study of combustion processes, which are often difficult to study experimentally due to the hostile environment. The accuracy of such simulations strongly depends on the description of turbulent mixing. While direct numerical simulation (DNS) provides the highest accuracy, albeit at the highest cost, large eddy simulation (LES) has established itself as a powerful tool with a good trade-off between accuracy and computational cost, and has already been widely used in PCC. The first applications of PCC-LES were performed by Kurose and Makino [78], followed by other researchers [34, 162, 184].

The application of CFD with detailed chemistry and several hundred species is still too expensive at industrial scale, which makes it necessary to model such chemical processes to lower the computational demand for chemical kinetics closures. While some gas phase combustion models like the eddy break up (EBU) model [158] are based on the assumption of infinitely fast chemistry and often result in inaccurate species predictions, more advanced models such as the transported probability density function (PDF) model [122], the conditional moment closure (CMC) model [72] or the flamelet model [115] can eliminate some of the weaknesses and show better predictions. The latter model is used in this work. In the flamelet model, the thermochemical quantities are not solved directly in the simulation, but are pre-tabulated in flamelet look-up tables (FLUT). The table is then coupled to the flow field via defined trajectory variables. The model used in this work uses the extended flamelet/progress variable (FPV) approach [117]. In this model, a defined progress variable is used as the trajectory variable for table access. It has been widely applied to PCC simulations and demonstrated its accuracy and performance [95, 141, 183, 184].

Although flamelet models can describe the chemical states in reasonable detail, they often struggle to adapt to NO_x-formation mechanisms: The characteristic time scales for the NO_x-formation mechanisms are usually longer than the characteristic flamelet time scale, in particular for the thermal-NO_x mechanism [58, 101]. Fuel-bound nitrogen in PCC has a different characteristic time scale again and complicates the formulation of the flamelet modeling. The interphase mass and heat transfers in PCC flames and the interactions between the different fuel streams further complicate the formulation.

Flamelet strategies for NO_x-formation have already been developed for pure gas flames [15, 40, 58], while the extension to PCC flames with fuel-bound nitrogen has not been widely investigated. Two strategies have been established, 1) to read the NO_x species with a modified reaction progress variable and 2) to solve additional NO_x transport equations for the NO_x mass fractions. Wen et al. [191] investigated both strategies, using solid fuel counterflow flames for two different coals with fuel-bound nitrogen. A combination of both variants, the solution of an additional transport equation for NO, where the NO source term was divided into a formation and a rescaled consumption part under consideration of a modified reaction progress variable, showed the best overall result. While the work of Wen et al. [191] laid the foundation for NO_x prediction in PCC flames, not all aspects (such as turbulence interactions) of industrial coal combustion were considered.

The purpose of the present work is to close this gap by applying this model to a large-scale industrial burner, considering the effect of strong turbulence. The chosen experimental facility is the burner flow reactor (BFR) of Brigham Young University (BYU). In the work of Damstedt [25], this burner has been extensively investigated experimentally, both in single firing and in co-firing of different fuels. Massively parallel highly resolved FPV-LES of the BFR combustor are performed using a four-dimensional flamelet table based on the trajectory variables a) progress variable, b) total enthalpy, c) a mixture fraction for volatiles and d) a mixture fraction for the char burnout. An additional transport equation for NO species is considered following the approach of Wen et al. [191]. Species are investigated inside and outside the internal and external recirculation zones with special emphasis on turbulence effects and NO_x prediction.

5.3.2 Coal combustion modeling

5.3.2.1 Solid phase

Coal particles are described in a Lagrangian framework, using models described by Rieth et al. [137]. The particle motion is described by the balance of the inertial forces and the forces acting on the particle, i.e., gravity and buoyancy forces, drag and a turbulent drag force taking into account the interaction of unresolved flow scales with the particle. The Schiller-Naumann correlation was used for the drag coefficient [22, 144]. The interaction between unresolved flow scales and the particle were modeled as a Wiener process, following the equations by Bini and Jones [12]. The change of thermal energy of the coal particle is derived from the balance of heat transfer, taking into account convective heat exchange with the gas, radiative absorption and emission, and heat exchange due to devolatilization and char combustion. Devolatilization and char combustion describe the conversion of coal. The devolatilization process is described by the single first order reaction (SFOR) model by Badzioch & Hawksley [8]. The single rate parameters used were $k = 2.51\mathrm{E7}\,\mathrm{s}^{-1}$ and $E = 1.06\mathrm{E8}\,\mathrm{J/(kmolK)}$, the Q-factor was set to 1.60, which accounts for the expected high temperature volatile yield on a dry ash-free basis compared to the proximate volatile matter. These parameters were fitted for a range of heating rates between 10E4 and 10E6 K/s based on the coal ultimate analysis using the particle kinetics preprocessor (PKP) tool developed at TU Darmstadt [178]. Smith's intrinsic model is applied for char conversion [152]. Char conversion is considered as soon as 90 % of the volatiles were released. It assumes CO as the only immediate product of char combustion. To account for the rapid effect of devolatilization in the respective particle equations for momentum and energy, a blowing correction is applied [163].

5.3.2.2 Gas phase

In this study, four trajectory variables describe the FPV approach: a reaction progress variable Y_{PV}, the total enthalpy H, and two mixture fractions for volatiles Z_{vol} and char off-gases Z_{char}. Favre-filtered $(\tilde{.})$ transport equations are solved for the total mass, momentum, total enthalpy H, progress variable Y_{PV}, and for the two mixture fractions due to devolatilization Z_{vol} and char burnout Z_{char}, leading to the following equations:

$$\frac{\partial \bar{\rho}}{\partial t} + \frac{\partial (\bar{\rho}\tilde{u}_i)}{\partial x_i} = \bar{\dot{S}}_{\rho} \tag{5.14}$$

$$\frac{\partial (\bar{\rho}\tilde{u}_i)}{\partial t} + \frac{\partial (\bar{\rho}\tilde{u}_i\tilde{u}_j)}{\partial x_j} = -\frac{\partial \bar{p}}{\partial x_i} + \frac{\partial \bar{\tau}_{ij}}{\partial x_i} + \bar{\dot{S}}_{u_i} \tag{5.15}$$

$$\frac{\partial (\bar{\rho}\tilde{h})}{\partial t} + \frac{\partial (\bar{\rho}\tilde{u}_i\tilde{h})}{\partial x_i} = \frac{\partial}{\partial x_i}\left[\left(\frac{\mu}{Pr} + \frac{\mu_{\mathrm{SGS}}}{Pr_{\mathrm{t}}}\right)\frac{\partial \tilde{h}}{\partial x_i}\right] + \bar{\dot{S}}_h \tag{5.16}$$

$$\frac{\partial (\bar{\rho}\tilde{Y}_{\mathrm{PV}})}{\partial t} + \frac{\partial (\bar{\rho}\tilde{u}_i\tilde{Y}_{\mathrm{PV}})}{\partial x_i} = \frac{\partial}{\partial x_i}\left[\left(\frac{\mu}{Sc} + \frac{\mu_{\mathrm{SGS}}}{Sc_{\mathrm{t}}}\right)\frac{\partial \tilde{Y}_{\mathrm{PV}}}{\partial x_i}\right] + \bar{\dot{\omega}}_{Y_{\mathrm{PV}}} + \bar{\dot{S}}_{Y_{\mathrm{PV}}} \tag{5.17}$$

$$\frac{\partial (\bar{\rho}\tilde{Z}_{\alpha})}{\partial t} + \frac{\partial (\bar{\rho}\tilde{u}_i\tilde{Z}_{\alpha})}{\partial x_i} = \frac{\partial}{\partial x_i}\left[\left(\frac{\mu}{Sc} + \frac{\mu_{\mathrm{SGS}}}{Sc_{\mathrm{t}}}\right)\frac{\partial \tilde{Z}_{\alpha}}{\partial x_i}\right] + \bar{\dot{S}}_{Z_{\alpha}} \tag{5.18}$$

The equations follow the standard nomenclature for combustion LES and are taken from previous studies, to which the reader is referred to for a more detailed description [95, 137]. The Sensor-enhanced Smagorinsky (SES) turbulence model [48] with a (static) model constant of 0.173 and a sensor constant of 1/0.16 is used to close the subgrid-viscosity μ_{SGS} in the LES, assuming a constant turbulent Schmidt- and Prandtl number, as well as a unity Lewis number, hence $Sc_{\mathrm{t}} = Pr_{\mathrm{t}} = 0.7$. The filtered stress tensor in the momentum equation is defineds as $\bar{\tau}_{ij} = (\mu + \mu_{\mathrm{SGS}})\left(\frac{\partial \tilde{u}_j}{\partial x_i} + \frac{\partial \tilde{u}_i}{\partial x_j} - \frac{2}{3}\frac{\partial \tilde{u}_k}{\partial x_k}\delta_{ij}\right)$. In Eq. 5.18, α refers to the mixture fractions for the volatiles and char off-gases, thus α =vol, char. Interphase source terms describe the interphase heat and mass transfer between particles and gas phase, and are taken from previous work by Rieth et al. [137]. The coupling of the Lagrangian and Eulerian phase is established through a second-order trilinear interpolation scheme. In the present work, the flamelet model is extended to accurately describe NO_x-formation mechanisms.

5.3.2.3 FPV modeling and NO modeling

One-dimensional steady non-premixed flamelets were solved using the FlameMaster software [118]. As the amount of light gases, e.g., hydrogen, in the predicted volatile gas composition is very low (see Table 5.8), flamelet calculations were based on the assumption of a unity Lewis number. Scalar dissipation rates χ are varied when solving the non-premixed flamelet equations to cover all areas of the S-shaped curve. From the obtained superimposed 1D flamelets, four trajectory variables were built, which parameterize the table. Two transformed parameters $Z = Z_{\mathrm{vol}} + Z_{\mathrm{char}}$ and $X = Z_{\mathrm{char}}/(Z_{\mathrm{vol}} + Z_{\mathrm{char}} + \epsilon)$ were introduced as trajectory variables, following the suggestion of Hasse and Peters [46], where ϵ represents a small positive number. These parameters are used to describe the overall mixing process. The flamelet equations are solved in Z-space for different values of X (0.0, 0.1, ..., 0.9). The maximum value of X was limited to 0.9 (not 1.0), as the flame did not ignite at $X = 1.0$ due to a lack of hydrogen atoms for the pure char off-gas. This procedure follows the work of Akaotsu et al. [3]. The normalized enthalpy H_{norm} and the normalized progress variable $Y_{\mathrm{PV,norm}}$ were chosen as the third and fourth dimensions for table access. The normalized enthalpy is obtained from the total enthalpy (chemical + sensible) of the flow field. Different input stream temperatures (300 K, 600 K, 800 K) on fuel and oxidizer side are set to vary the enthalpy levels to represent the interphase heat transfer between the particle and gas phase. The progress variable is given by a linear combination of different product species mass fractions $Y_{\mathrm{PV}} = Y_{\mathrm{CO_2}} + Y_{\mathrm{H_2O}} + Y_{\mathrm{H_2}} + 10Y_{\mathrm{NO}}$, where the prefactor of the last term is based on the parameter study from Luo et al. [88].

Wen et al. [191] found that extracting the NO mass fraction directly from the flamelet library can result in significant discrepancies in the presence of fuel-bound NO. They have shown that solving another transport equation for NO with a modified NO source term in combination with a modified progress variable can significantly improve the NO prediction. This approach is used in this work, where the Favre-filtered mass conservation equation, using the same model parameters as described for Eqs. 5.14-5.18, is given by

$$\frac{\partial(\bar{\rho}\tilde{\varphi}_{\mathrm{NO}})}{\partial t} + \frac{\partial(\bar{\rho}\tilde{u}_j\tilde{\varphi}_{\mathrm{NO}})}{\partial x_j} = \frac{\partial}{\partial x_j}\left[\left(\frac{\mu}{Sc} + \frac{\mu_{\mathrm{SGS}}}{Sc_{\mathrm{t}}}\right)\frac{\partial\tilde{\varphi}_{\mathrm{NO}}}{\partial x_j}\right] + \bar{\dot{\omega}}_{\mathrm{NO}} \tag{5.19}$$

The last term $\bar{\dot{\omega}}_{\mathrm{NO}}$ describes the filtered chemical reaction rate of NO. Ihme and Pitsch [58] proposed to split $\bar{\dot{\omega}}_{\mathrm{NO}}$ into a formation and a rescaled consumption part to better account for forward- and backward reactions. Accordingly, $\bar{\dot{\omega}}_{\mathrm{NO}}$ reads

$$\bar{\dot{\omega}}_{\mathrm{NO}} = (\bar{\dot{\omega}}^{+}_{\mathrm{NO}})_{\mathrm{TAB}} + \tilde{\varphi}_{\mathrm{NO}}\left(\frac{\bar{\dot{\omega}}^{-}_{\mathrm{NO}}}{\tilde{Y}_{\mathrm{NO}}}\right)_{\mathrm{TAB}} \tag{5.20}$$

where $(\cdot)_{\mathrm{TAB}}$ indicates that these filtered contributions are precomputed and stored in the flamelet library; $\tilde{\varphi}_{\mathrm{NO}}$ denotes again the filtered NO mass fraction from the transport equation (Eq. 5.19).

The homogeneous reactions are described by the reduced CRECK NO_x mechanism, including 120 species and 1551 reactions [145]. The mechanism covers the detailed description of the oxidation of the volatiles including large hydrocarbons for tar, as well as all important NO_x-formation mechanisms (prompt-, fuel-, thermal-, and pathway via N_2O), enabling the detailed analysis of NO_x-formation. The modeled volatile gas composition (Table 5.8) is obtained using the CRECK-S-C model [26], which is able to predict coal devolatilization rates including a detailed product composition. The instantaneous volatile release rates were integrated over time, allowing to define the overall predicted yield of volatiles. A transport equation, often used in spray flame LES, is solved for the variance of the sum of all mixture fractions $\widetilde{Z''^2}$ [112, 142, 166]. Turbulence-chemistry interaction on the flamelets is treated using a pre-integrated table with an assumed top-hat PDF based on the filtered mixture fraction sum $\widetilde{Z}$ and the subgrid mixture fraction variance $\widetilde{Z''^2}$ [110].

The final table has 263 x 10 x 11 x 101 points in the dimensions of Z, X, H_{norm}, and $Y_{\mathrm{PV,norm}}$, respectively, at a storage requirement of 1.4 GB.

5.3.3 Experimental conditions

Damstedt [25] conducted an experimental study of the flame structure and species with respect to nitrogen chemistry using a low-NO_x burner for coal, biomass and various (co-fired) fuels at different swirl numbers. The present work focuses on the pure coal case only. Figure 5.20 shows the burner geometry and the quarl of the BYU combustion chamber. The burner consists of two independently operating fuel injection tubes and was originally designed for the co-firing of two different fuels.

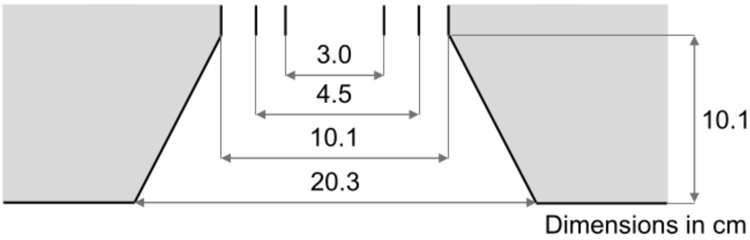

Figure 5.20: Burner and quarl geometry showing central, annular middle and annular outer inlets. The middle inlet is used for co-firing purposes [25].

In the investigated case, coal and carrier air flow through the central inlet, and secondary (swirled) air flows through the outer annulus into the burner quarl. The burner fires into a cylindrical reactor of 2.4 m height and 0.75 m in diameter. Tables 5.6-5.8 show the experimental conditions, the coal composition (high volatile bituminous *Blind Canyon*) and the modeled gas composition. The particle size distribution was given by Damstedt [25]. The flow field was measured via hotwire anemometry at cold conditions.

Table 5.6: Experimental conditions [25].

Center air [kg/h]	11	Annular air [kg/h]	0	Secondary air [kg/h]	160
Center fuel [kg/h]	15.3	Annular fuel [kg/h]	0	Swirl number (-)	1.0

Combustion products were sampled along axial and radial directions inside the flow reactor, using a water-cooled suction probe, and analyzed for individual species mole fractions using a Horiba PG-250 and a FTIR gas analyzer. The accuracies specified by the manufacturer are between 0.1 and 0.5 %, depending on the species. Repeat measurements were conducted to check the reproducibility of the measurements. Measurements of CO_2 showed a high reproducibility with deviations up to 4.6 %. Measurements of O_2 and CO had a significantly lower reproducibility, with deviations of approximately 20.3 % and 15.1 %. Not perfectly distributed fuel and air feeds, as well as the relatively strong flame asymmetry cause the low reproducibility [25].

5.3.4 Numerical setup

The massively parallel LES simulations have been performed using the in-house code *PsiPhi* [28, 95, 137, 141], which uses a low-Mach finite volume method (FVM) with a conjugate gradient

Table 5.7: Ultimate (dry) and proximate analysis of the coal [wt %] [25].

C	74.8	H	5.08	O	10.1	N	1.53	S	0.58
Ash	7.89	Volatile matter	40.6	Fixed C	51.5	Moisture	2.1		

Table 5.8: Modeled volatile gas composition Y [%].

H_2	1.56	H_2O	7.38	CO	12.63	CO_2	5.41	CH_4	6.23
HCN	1.11	NH_3	1.43	C_2H_4	4.71	C_6H_5OH	7.71	$C_6H_6O_2$	4.51
C_5H_5N	9.07	$C_{16}H_{10}$	16.57	$C_{10}H_{12}$	21.66				

solver and Jacobi preconditioner. An equidistant Cartesian grid is used in this code, which provides good numerical accuracy, constant LES-filter width and allows for massively distributed domain decomposition for Lagrangian and Eulerian fields for maximum MPI communication efficiency between CPUs. For the spatial discretization of the diffusive fluxes and the convective flux of momentum, a second-order accurate central differencing scheme (CDS) is used, while for the convective scalar flux discretization, a total variation diminishing (TVD) scheme with a CHARM limiter is applied. The time discretization uses a third order low-storage Runge-Kutta scheme. Radiative heat transfer is considered using the discrete ordinates method (DOM) [30, 168] with a S8 quadrature grey weighted sum of grey gases (GWSGG) model, using the model parameters from Kangwanpongpan et al. [66].

For all transported quantities, a zero-gradient boundary condition is set at the outlet, while a Dirichlet boundary condition is set at the inlet boundary. For pressure, a zero-gradient boundary condition is used at the inlet, while a Dirichlet boundary condition is applied at the outlet. Immersed boundaries describe the furnace walls. The wall temperature is set to a constant value of 800 K as no further data is available from the experiment. A similar approach was used by Rieth et al. [139].

All inlet conditions were taken from Table 5.6. A uniform velocity profile is assigned on the center and secondary air jet. The temperature of the center jet was set to 310 K while the secondary air jet was set to 450 K. Inflow-turbulence is generated at the inlet plane, using an efficient implementation of the inflow generator by Klein [69, 71]. A turbulent length scale of 20 mm and a value of $1.0\,\mathrm{m}^2/\mathrm{s}^2$ for the normal components of the Reynolds stress tensor have shown to give good results.

Simulations were performed on a mesh with cubic cells of $\Delta = 4\,\mathrm{mm}$, describing a domain of 1000 x 750 x 750 mm in size, while the *CFL* number was limited to a value of 0.7 in order to achieve a stable solution. The grid size is chosen similarly to previous studies on this [131] and a similar swirl-stabilized burner [139] using the same solver (utilizing same schemes and numerics). A total of 10 million cells were used for the final simulations, performed on 2,048 cores on HAWK (Stuttgart, Germany). Simulations were run for a total physical simulation time of approximately 18 s (around 210,000 iterations) including the flame initialization. Radiation was enabled after 150,000 iterations. The last 30,000 iterations are used for sampling statistical data. A typical FPV-LES of the reactor costs around 250,000 CPUh.

5.3.5 Cold flow validation

An unreacted simulation was performed and compared to experimental flow field data. Figure 5.21 shows the velocity profiles under cold condition at 15.2 cm distance from the burner quarl for the unreacted LES and the experiment [25]. The experimental data was obtained by sampling through all four reactor windows (north, east, south, west). Individual measurements at the respective reactor windows are shown. Looking at the individual measurements, a slightly asymmetric flame behavior can be seen. The averaged profile in the LES matches the averaged profile in the experiment very well; slight deviations occur at large radii, at which the simulation predicts a weak recirculation zone, which is not observed in the experiment. A possible reason for this may be the insufficient wall resolution (caused by the equidistant grid). The wall resolution is not of much interest in the present case and could only be marginally improved by an affordable grid refinement. The flow field shows the recirculation zone near the centerline and the downward flow from the burner at a radius of around 10 cm.

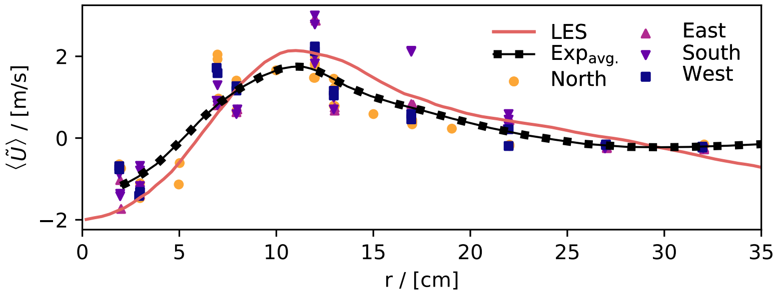

Figure 5.21: Vertical velocity profiles along a radial line at 15.2 cm distance from the burner quarl under cold conditions. The experimental averaged profile is obtained by sampling through all four reactor windows and is taken from Damstedt [25].

5.3.6 Results and discussion

Figure 5.22 shows mean (left) and instantaneous (right) distributions of the axial and radial velocity, gas temperature, volatile mixture fraction, instantaneous particle temperature and burnout, as well as the mean (left) and instantaneous (right) mole fractions of CO, H_2O, O_2, CO_2, NO_{TAB}, and NO in the region near the burner. (Particle quantities are averaged within each cell.) The axial velocity shows the formation of an internal recirculation zone (IRZ) in the top section of the BFR resulting from the swirl. The IRZ forms early in the quarl area and acts comparable to a bluff body for gases, strongly decelerating incoming coal particles from the main jet. An external recirculation zone (ERZ) forms in the upper, outer corners of the BFR, which transports and accumulates hot exhaust products into the corners of the BFR. Most of the secondary air is not recirculated and passes between the inner and outer recirculation zones in a semi-conical jet, interacting with the wall at around 30 cm distance from the burner quarl. Hot combustion products in the IRZ lead to the release of volatiles from the accumulated particles. The low oxygen concentration present in the IRZ prevents direct volatile burning and causes the volatile concentration to increase significantly. In the peripheral regions of the cone-shaped volatile accumulation zone, the concentration drops rapidly and volatile combustion occurs, favored by the presence of large amounts of oxygen. The gas temperature distribution shows an inner semi-conical flame front at the edge regions of the volatile accumulation zone as well as along the secondary air jet.

The particles heat up inside the IRZ and reach the highest temperature in the reaction front. The particle burnout is determined from the initial particle mass $m_{\mathrm{p},0}$ and the instantaneous particle mass m_{p} as $P_{\mathrm{BO}} = 1 - m_{\mathrm{p}}/m_{\mathrm{p},0}$. The particle burnout occasionally reaches levels up to 90 % and shows an average burnout between 60 − 70 % in the investigated domain. The concentrations of CO and H_2O are high in the IRZ due to the volatile release. The oxygen concentration drops to almost zero in the IRZ, since hot combustion exhaust gases are recirculated and force the incoming air to flow between the IRZ and ERZ. Moreover, at the inner edges of the flame front, oxygen is being burned off and the concentration drops rapidly (visible as the edge of the white area between the secondary air jet and the IRZ). These areas match with the temperature distribution and are attributable to the volatile flame front. The reaction zone in

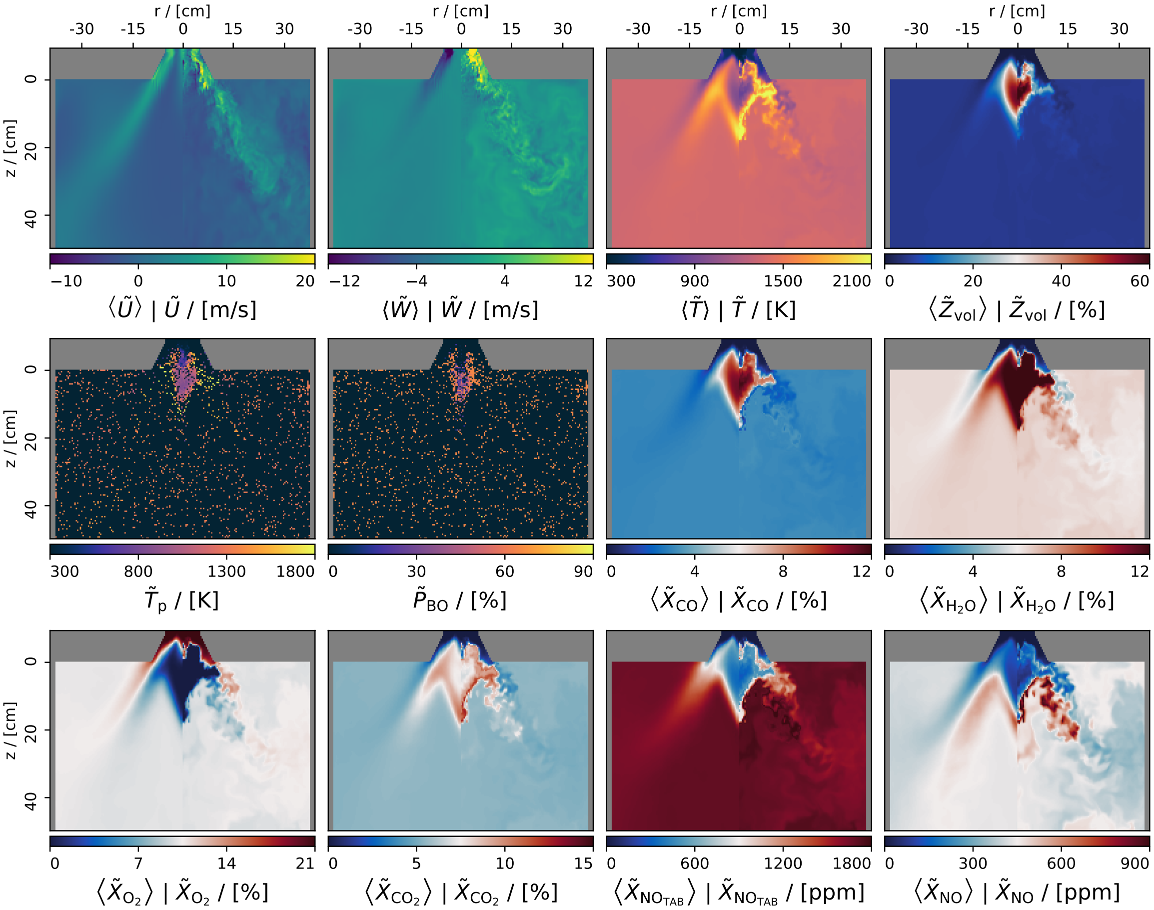

Figure 5.22: Mean (left half of each frame) and instantaneous (right half of each frame) axial and radial velocity, temperature, volatile mixture fraction, instantaneous particle temperature and burnout, CO, H_2O, O_2, CO_2, NO_{TAB} and NO mole fraction distribution.

the flame front and the presence of large oxygen concentrations lead to a strong formation of CO_2.

Figure 5.23 shows the instantaneous mole fraction distributions of NO_{TAB} and NO. The mole fraction NO_{TAB} describes the direct extraction of NO from the flamelet table, while the mole fraction NO refers to the mole fraction solved by an additional transport equation for NO, applying a rescaled consumption source term (Eq. 5.19). Both approaches for the quantification of the NO mole fraction show major differences. Fuel-N is released from the heated coal particles in the IRZ as volatiles. A part of the released nitrogen is assumed to have reduced to N_2 in the fuel-rich region before passing the reaction zone. The presence of high oxygen concentrations promotes the formation of NO, thus, large amounts of NO form in the reaction zone. This can be seen in both approaches, although the increase in NO concentration starts earlier and is much stronger for $X_{NO_{TAB}}$. Further downstream, the concentration of $X_{NO_{TAB}}$ levels off at a value of approximately factor three higher compared to X_{NO}, indicating significantly reduced backward reactions of NO compared to X_{NO}. This is the main issue occuring when directly extracting NO from the flamelet library. A way to overcome this problem is the solution of an additional transport equation for NO, where the NO source term is split into a formation and rescaled consumption part, considering a modified reaction progress variable with Y_{NO} included in the flamelet library. This approach better accounts for forward- and backward reactions of NO and shows a much stronger decrease of NO further downstream, as can be seen for X_{NO}. The mole fraction X_{NO} forms rapidly in the reaction zone and is then reduced due to slow NO destruction reactions. High concentrations of

X_{NO} occur mainly in the hot reaction zone, as expected. In a next step, a quantitative comparison with experimental data is conducted.

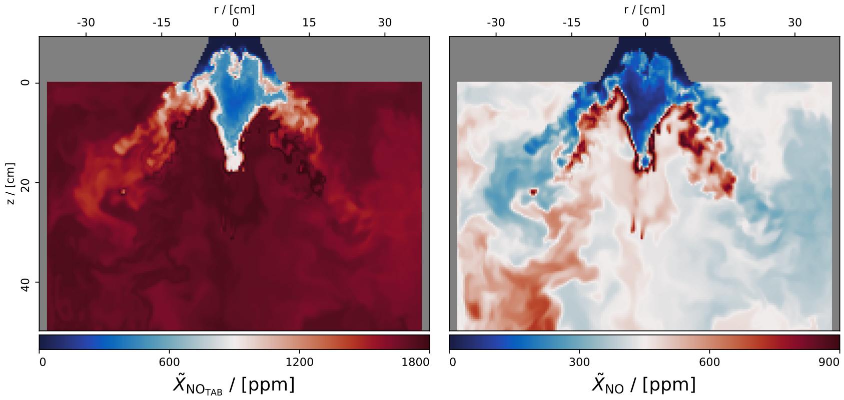

Figure 5.23: Instantaneous mole fraction distributions of $\mathrm{NO_{TAB}}$ and NO. The mole fraction $X_{\mathrm{NO_{TAB}}}$ denotes the direct table extraction, while X_{NO} is solved via Eq. (5.19).

Figure 5.24 shows mean (top) radial distributions of axial velocity, gas temperature, and mole fractions of $\mathrm{NO_{TAB}}$, NO, O_2, CO_2, and H_2O, as well as the respective standard deviations (bottom) at three different axial positions (10.1 cm, 20 cm, and 30 cm distance from the burner quarl). For the species, experimental measurements for 10.1 cm and 20 cm distance from the burner quarl are shown. The experimental data shows a relatively strong asymmetrical flame behavior, while the simulation predicts a symmetrical flame. The mean axial velocity shows both, the swirl induced IRZ and the outer ERZ. While the axial velocity decreases further downstream and the jet spreads to higher radii, it already reaches the outer wall region at a distance of 30 cm. The negative axial velocities for all distances at low radii indicate the IRZ, while the slightly negative axial velocities at large radii at a distance of 10.1 cm indicate the ERZ. The IRZ extends significantly further into the BFR than the ERZ. The radial distribution of the mean gas temperature reveals two reaction zones at a distance of 10.1 cm, a strong reaction zone at the edge of the IRZ, where hot unburned volatile gas meets oxygen-rich air, and a less pronounced reaction zone at the edge of the secondary air jet, where fresh gas reacts with recirculated combustion products. Further downstream, the temperature settles at just below 1400 K, while the edge areas cool slightly due to the wall influence.

The profiles of the mean mole fractions for O_2 and H_2O match the experimental measurements quite well, considering the low reproducibility of O_2 measurements in the experiment and the high fluctuations of the experimental data in Figure 5.24, especially seen at $r = 10$ cm. At this location, the simulation lies within these deviating experimental data points. At $r = -10$ cm, the simulation deviates more strongly, caused by the asymmetrical flame behavior in the experiment, leading to increasingly larger deviations further downstream. The standard deviations of the respective quantities in the simulation are relatively high in the reaction fronts of the highly turbulent IRZ and along the secondary air jet. The oxygen concentration levels off at a distance of 30 cm at around 10 %, indicating incomplete combustion. While the general profile of CO_2 at a distance of 10.1 cm is in agreement with the experimental data, the simulation sightly underpredicts the level of CO_2.

The radial distributions of the mole fraction concentrations $X_{\mathrm{NO_{TAB}}}$ and X_{NO} show again strong differences. $X_{\mathrm{NO_{TAB}}}$ predicts much higher concentrations of NO compared to X_{NO} and the experiment. At a distance of 10.1 cm, the profile of $X_{\mathrm{NO_{TAB}}}$ shows, that NO formation takes place primarily in the reaction zones, although the concentration peaks do not show a sharp separation between the two reaction zones. At a distance of 30 cm, NO levels off at a value just over 1600 ppm, overpredicting the peak mole fraction of X_{NO} at this distance by a factor greater than three. In contrast, X_{NO} from the additional transport equation predicts the same order of

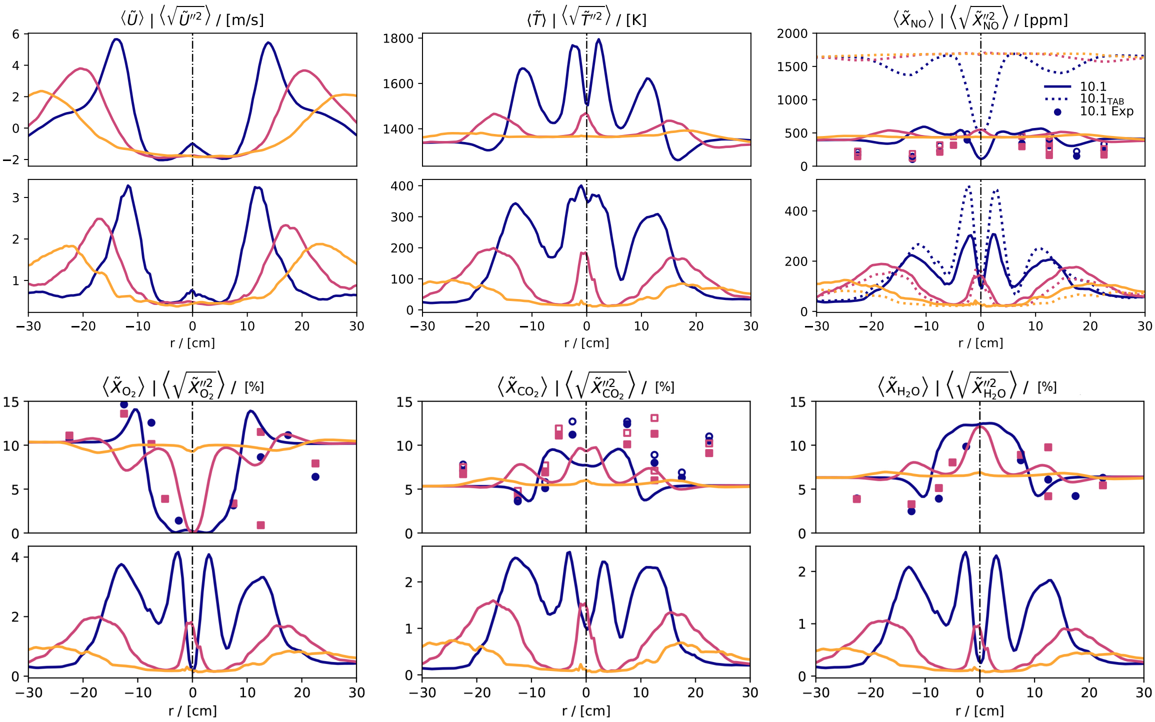

Figure 5.24: Mean (top) radial distributions of axial velocity U, gas temperature T, mole fractions X_{NO}, $X_{\mathrm{NO_{TAB}}}$, $X_{\mathrm{O_2}}$, $X_{\mathrm{CO_2}}$ and $X_{\mathrm{H_2O}}$ and its standard deviations (bottom) at 10.1 cm (blue), 20 cm (red), and 30 cm (yellow) distance from the burner quarl. Experimental data by Horiba (filled) and FTIR gas analyzer (open) are shown.

magnitude as the experiment, although the simulation slightly overpredicts the NO concentration. Again, the effect of the asymmetrical flame behavior in the experiment cause radial deviations. While the simulation profiles at positive radii match the experimental data well, deviations occur for the peak locations of NO at negative radii. As expected, the two reaction zones at a distance of 10.1 cm show small peaks in the concentration of X_{NO}. Further downstream, the locations of the concentration peaks in radial direction follow the temperature peaks before leveling off at a value just below 500 ppm at a distance of 30 cm. High temperatures as well as high oxygen concentrations favor the formation of NO.

While the direct extraction from the flamelet table strongly underpredicts backward reactions of NO in the flow field, overpredicting the experimental measurements of NO by a factor greater than three, a much better prediction was achieved by introducing a transport equation for NO. The consideration of a rescaled NO consumption source term better accounts for forward- and backward reactions of NO. This, in combination with a modified reaction progress variable definition, including Y_{NO}, leads to a much improved prediction of NO formation inside the furnace.

5.3.7 Conclusion

A four-dimensional FPV-LES of the large-scale turbulent low-$\mathrm{NO_x}$ flow reactor operated by the Brigham Young University is presented. A flamelet/progress variable approach is used to account for four classical $\mathrm{NO_x}$ mechanisms (thermal, prompt, fuel, and via $\mathrm{N_2O}$ pathway). The simulation provides additional detail on the general behavior of the low-$\mathrm{NO_x}$ flame; the comparison of main gas species shows a good agreement with the experiment. Two approaches for the determination of the NO mole fraction were investigated: 1) the direct extraction of NO from the flamelet table and 2) the solution of an additional transport equation for NO, in which the NO source term is extracted from the flamelet library using the same modified reaction progress variable as in variant

1), while the transient term $\bar{\dot{\omega}}_{\mathrm{NO}}$ is considered by rescaling the consumption source term. Direct retrieval of the NO mole fraction from the flamelet table overpredicts the experimental measurements by a factor of approximately three, whereas the transport equation approach achieves a much better prediction, better accounting for forward- and backward reactions of NO in the flow field.

5.3.8 Acknowledgments

The authors gratefully acknowledge the financial support through the German Research Foundation (DFG, project 238057103) and the Gauss Centre for Supercomputing e.V. (www.gauss-centre.eu) (grant DUEHAWK2021) for providing computing time on the GCS Supercomputer HAWK at Höchstleistungsrechenzentrum Stuttgart (www.hlrs.de).

Chapter 6

Summary and outlook

6.1 Summary

This work provides a comprehensive study of LES applied to turbulent reacting multiphase flows, specifically focusing on coal combustion across various flame configurations. An Euler-Lagrange framework was employed to accurately represent particle-laden flows.

Three key studies were conducted within this work, utilizing flamelet-based tabulation strategies with a non-premixed FPV approach. Multiple mixture fractions, a progress variable, and enthalpy were selected as trajectory variables for all studies. The inclusion of enthalpy is particularly crucial in capturing the interphase heat transfer between the solid particles and the gas phase. Additionally, to account for the impact of subgrid-scale turbulence, the variance of the subgrid PDF was determined by solving an additional transport equation.

The research focused on two distinct flame setups: a laboratory-scale hydrogen-piloted coal jet flame operated by the CRIEPI institute in Japan and a semi-industrial scale coal furnace equipped with a swirl-stabilized low-$\mathrm{NO_x}$ burner operated by the Brigham Young University. These configurations enabled a comprehensive investigation of coal combustion under different operating conditions and provided insights into coal particle behavior and pollutant formation mechanisms.

In the first study (section 5.1), the numerical investigation of the CRIEPI coal burner involved a coaxial burner configuration with a hydrogen-supported pulverized coal flame. The LES calculations employed a four-dimensional FPV approach, considering two mixture fractions for the hydrogen pilot and volatile gases. The study aimed to assess the performance of the flamelet model in capturing the combustion characteristics of the coal flame. Notably, the flamelet model demonstrated cost-effectiveness through the pre-tabulation of thermochemical flame properties, maintaining accuracy in gas composition prediction. However, inconsistencies were noted in axial temperature prediction, which might be attributed to experimental artifacts. The study also addressed experimental artifacts introduced by the species suction probe used for measurements. A correction technique was applied to improve the agreement between the experimental data and simulation results, taking into account the impact of the suction probe on the scalar field measurements. The simulations revealed relative changes of up to 50 % in various quantities and locations due to the probe effects. This study highlighted the importance of considering experimental artifacts and probe effects in LES and demonstrated the effectiveness of the applied correction technique in enhancing the accuracy of the results.

In the second study (section 5.2), the same burner experiment utilizing the CRIEPI jet burner was further investigated under three different operating conditions, which include the co-firing of coal and ammonia, as well as individual coal and ammonia firing. This study represents one of the pioneering applications of LES in the investigation of coal and ammonia co-firing. To simulate the complex combustion processes in these scenarios, a five-dimensional three-mixture fraction FPV approach was employed. A novel reaction mechanism specifically designed for ammonia co-firing was developed based on existing reduced CRECK mechanisms. This mechanism provides a detailed description of the volatile combustion, considering large hydrocarbons for tar and $\mathrm{NH_3}$ oxidation as major fuel species. The simulations were compared to experimental data, including axial temperature profiles, radial species concentrations, and LIF measurements of OH and NH. The results showed reasonable agreement between the experimental data and simulations, with the newly generated mechanism demonstrating improved predictions for the location and quantity of OH and NH reaction zones in cases where ammonia is present.

The third study (section 5.3) focused on the investigation of a swirl-stabilized low-NO_x burner in a semi-industrial scale coal furnace. A four-dimensional FPV approach was utilized, considering two mixture fractions to account for volatile gases and char burnout. The primary objective of this study was to predict NO_x emissions and investigate the formation mechanisms within a highly turbulent scenario characterized by internal and external recirculation zones (IRZ and ERZ). For generating the flamelet table, an established reduced coal mechanism encompassing major NO_x formation mechanisms, including prompt-, fuel-, thermal-NO_x, and the via N_2O pathway, was chosen. Radiative effects, which may have a significant impact on combustion characteristics, were also taken into consideration in this study. The simulations were compared to experimental data, focusing on radial profiles of major gas species. The results showed an overall good agreement between the simulated profiles and experimental observations. Two approaches for determining NO species were investigated, a direct extraction of NO from the flamelet table and the solution of an additional transport equation for NO with a modified source term. The integration of an additional transport equation for NO with a modified source term in combination with a modified progress variable significantly improved the predictive accuracy of NO. This enhancement is attained by comprehensively accounting for NO production and destruction processes, accomplished by splitting the NO source term into a formation and a rescaled consumption part.

Overall, these studies contributed to a comprehensive understanding of coal combustion dynamics, pollutant formation, and emission reduction strategies. The advanced LES approach combined with flamelet-based tabulation strategies and detailed reaction mechanisms provided valuable insights into the complex interactions and processes occurring during single coal combustion and the co-firing of coal and ammonia. The findings enhanced our ability to predict and control pollutant emissions in coal-fired systems, which is of critical importance for environmental sustainability and the development of cleaner energy technologies. The developed simulation framework shows great applicability not only in pure coal combustion cases, but also in solid fuel systems that aim to greatly reduce carbon dioxide emissions, such as coal and ammonia co-firing. It shows great promise for broader applicability beyond coal to encompass and study also other solid fuel systems, including biomass combustion or iron oxidation/reduction.

6.2 Outlook

The results in this thesis have unveiled a plethora of prospects for future research and advancement in the field of solid fuel combustion. The first study emphasized the significance of understanding and accounting for experimental artifacts to achieve enhanced agreement between experiments and simulations. Although there was a notable improvement in predicting species concentrations, discrepancies remained in predicting the axial temperature profile, possibly caused by other experimental artifacts that have not been modeled in the simulations. The experimental species measurements indicated the presence of a flame close to the burner exit, whereas the temperature measurements suggested flame locations further downstream. It is crucial for future researchers to consider these artifacts and thoroughly investigate other potential sources of experimental artifacts to ensure a comprehensive and accurate representation of the combustion process. This understanding can also help to understand discrepancies between experiment and simulation in other flame configurations.

The second study demonstrated the successful application of LES coupled with flamelet-based tabulation techniques for coal and ammonia co-firing. However, only limited experimental data was available for a more detailed analysis. To facilitate future investigations of this promising CO_2 reduction measure, comprehensive experimental measurements are necessary. Previous research has highlighted the challenges in interpreting axial discrepancies between experimental observations and numerical simulations. In this context, radial profiles of species concentrations, temperature, and velocity are desirable in ensuring the comprehensive analysis of combustion phenomena.

While the impact of char off-gases was neglected in the investigation of the short laboratory-scale burner, it becomes crucial to consider them for larger scale flames, such as semi-industrial applications, requiring additional mixture fractions in the flamelet modeling. So far, only three-mixture fraction flamelet approaches exist in the literature. As co-firing strategies gain interest and research attention for emission reduction, further modeling strategies that account for more than three mixture fractions will be required to accurately capture combustion characteristics in various scenarios. For instance, accurately describing the co-firing of coal and biomass requires accounting for four mixture fractions for volatiles and char off-gases of each fuel, respectively.

The third study demonstrated significantly improved NO prediction by incorporating an additional transport equation with a modified source term. However, the study exclusively focused on NO, neglecting the formation of N_2O, which is a significant contributor to climate change, with a CO_2 equivalent of $298\,\mathrm{kg}_{\mathrm{CO_2}}/\mathrm{kg}_{\mathrm{N_2O}}$. Further research should extend the same approach to study also N_2O formation.

In general, the flamelet-based simulation framework could be extended to incorporate additional physical effects. The consideration of particle fragmentation and particle-wall interactions could be of interest. The latter may lead to slagging in coal combustion, influencing heat transfer to the walls. As of the present, it is worth noting that both, particle fragmentation and particle-wall interactions lack comprehensive theoretical models and are primarily addressed through robust empirical correlations. The integration of such physical models into the flamelet-based simulation tool would not only enhance the accuracy of coal combustion predictions but also offer applicability to other solid fuels, thereby providing significant benefits for future research endeavors in this field.

The flamelet-based simulation framework worked well for CO_2 reduction measures, such as (coal and) ammonia co-firing, and holds promise for broader applicability beyond coal, encompassing other solid fuels such as biomass or metal fuels. In the emerging field of alternative carbon-free energy sources, iron oxidation/reduction is currently undergoing extensive investigation. Looking ahead, the flamelet-based simulation framework offers promising opportunities for modeling and simulating the complex processes associated with iron oxidation/reduction in gas-assisted flames, providing valuable insights to advance this new technology.

Bibliography

[1] S. Ahn, K. Tainaka, H. Watanabe, and T. Kitagawa. Experimental and numerical analysis of turbulent pulverized coal flame in a coaxial burner. *Energy*, 179:727–735, 2019.

[2] S. Y. Ahn, H. Watanabe, and T. Kitagawa. Effect of devolatilization model on flame structure of pulverized coal combustion in a jet-burner system. *J. Mech. Sci. Technol.*, 33, 2019.

[3] S. Akaotsu, Y. Matsushita, H. Aoki, and W. Malalasekera. Application of flamelet/progress-variable approach to the large eddy simulation of a turbulent jet flame of pulverized coals. *Adv. Powder Technol.*, 31(10):4253–4274, 2020.

[4] B. W. Anderson and J. A. Domaradzki. A subgrid-scale model for large-eddy simulation based on the physics of interscale energy transfer in turbulence. *Phys. Fluids*, 24(6):065104, 2012.

[5] D. B. Anthony and J. B. Howard. Coal devolatilization and hydrogastification. *AIChE Journal*, 22(4):625–656, 1976.

[6] A. Attili, P. Farmand, C. Schumann, S. Farazi, B. Böhm, T. Li, C. Geschwindner, J. Köser, A. Dreizler, and H. Pitsch. Numerical Simulations and Experiments of Ignition of Solid Particles in a Laminar Burner: Effects of Slip Velocity and Particle Swelling. *Flow Turbul. Combust.*, 106:515–531, 2021.

[7] R. I. Backreedy, L. M. Fletcher, J. M. Jones, L. Ma, M. Pourkashanian, and A. Williams. Co-firing pulverised coal and biomass: a modeling approach. *Proc. Combust. Inst.*, 30(2): 2955–2964, 2005.

[8] S. Badzioch and P. G. W. Hawksley. Kinetics of Thermal Decomposition of Pulverized Coal Particles. *Ind. Eng. Chem. Process Des. Dev.*, 9(4):521–530, 1970.

[9] M. M. Baum and P. J. Street. Predicting the combustion behaviour of coal particles. *Combust. Sci. Technol.*, 3(5):231–243, 1971.

[10] R. W. Bilger, S. H. Stårner, and R. J. Kee. On reduced mechanisms for methane-air combustion in nonpremixed flames. *Combust. Flame*, 80(2):135–149, 1990.

[11] M. Bini and W. P. Jones. Particle acceleration in turbulent flows: A class of nonlinear stochastic models for intermittency. *Phys. Fluids*, 19(3):035104, 2007.

[12] M. Bini and W. P. Jones. Large-eddy simulation of particle-laden turbulent flows. *J. Fluid Mech.*, 614:207—252, 2008.

[13] S. Black, J. Szuhánszki, A. Pranzitelli, L. Ma, P. J. Stanger, D. B. Ingham, and M. Pourkashanian. Effects of firing coal and biomass under oxy-fuel conditions in a power plant boiler using CFD modelling. *Fuel*, 113:780–786, 2013.

[14] BP. Statistical Review of World Energy 2022. *BP. Statistical Review*, pages available from https://www.bp.com/content/dam/bp/business–sites/en/global/corporate/pdfs/energy–economics/statistical–review/bp–stats–review–2022–full–report.pdf, 2022.

[15] D. Bradley, P. H. Gaskell, X. J. Gu, M. Lawes, and M. J. Scott. Premixed turbulent flame instability and NO formation in a lean-burn swirl burner. *Combust. Flame*, 115(4):515–538, 1998.

[16] B. S. Brewster, L. L. Baxter, and L. D. Smoot. Treatment of coal devolatilization in comprehensive combustion modeling. *Energy Fuels*, 2(4):362–370, 1988.

[17] J. Cai, M. Handa, and M. F. Modest. Eulerian–Eulerian multi-fluid methods for pulverized coal flames with nongray radiation. *Combust. Flame*, 162(4):1550–1565, 2015.

[18] F. Cavallo Marincola. *Large eddy simulation of coal combustion.* PhD thesis, Imperial College London, 2014.

[19] S. Chandrasekhar. *Radiative transfer.* Courier Corporation, 2013.

[20] L. Chen and A. F. Ghoniem. Simulation of Oxy-Coal Combustion in a $100\,\mathrm{kW_{th}}$ Test Facility Using RANS and LES: A Validation Study. *Energy Fuels*, 26(8):4783–4798, 2012.

[21] L. Cifuentes, A. M. Kempf, and C. Dopazo. Local entrainment velocity in a premixed turbulent annular jet flame. *Proc. Combust. Inst.*, 37(2):2493–2501, 2019.

[22] R. Clift, J. Grace, and M. Weber. *Bubbles, drops and particles.* New York: Academic Press, 1978.

[23] A. W. Cook and J. J. Riley. A subgrid model for equilibrium chemistry in turbulent flows. *Phys. Fluids*, 6(8):2868–2870, 1994.

[24] B. Damstedt, J. M. Pederson, D. Hansen, T. Knighton, J. Jones, C. Christensen, L. Baxter, and D. Tree. Biomass cofiring impacts on flame structure and emissions. *Proc. Combust. Inst.*, 31(2):2813–2820, 2007.

[25] B. D. Damstedt. *Structure and nitrogen chemistry in coal, biomass, and co-firing low-NO_x flames.* PhD thesis, Brigham Young University, USA, 2007.

[26] P. Debiagi, C. Ontyd, S. Pielsticker, M. Schiemann, T. Faravelli, R. Kneer, C. Hasse, and V. Scherer. Calibration and validation of a comprehensive kinetic model of coal conversion in inert, air and oxy-fuel conditions using data from multiple test rigs. *Fuel*, 290:119682, 2020.

[27] P. Edge, S. R. Gubba, L. Ma, R. Porter, M. Pourkashanian, and A. Williams. LES modelling of air and oxy-fuel pulverised coal combustion - impact on flame properties. *Proc. Combust. Inst.*, 33(2):2709–2716, 2011.

[28] L. Engelmann, M. Ihme, I. Wlokas, and A. M. Kempf. Towards the Suitability of Information Entropy as an LES Quality Indicator. *Flow Turbul. Combust.*, 108:353–385, 2022.

[29] A. Favre. Statistical equations of turbulent gases. *Problems of hydrodynamics and continuum mechanics*, 231-266, 1969.

[30] W. A. Fiveland. Three-dimensional radiative heat-transfer solutions by the discrete-ordinates method. *J. Thermophys Heat Transfer*, 2(4):309–316, 1988.

[31] T. H. Fletcher, A. R. Kerstein, R. J. Pugmire, and D. M. Grant. Chemical percolation model for devolatilization. 2. Temperature and heating rate effects on product yields. *Energy Fuels*, 4(1):54–60, 1990.

[32] T. H. Fletcher, A. R. Kerstein, R. J. Pugmire, M. S. Solum, and D. M. Grant. Chemical percolation model for devolatilization. 3. Direct use of carbon-13 NMR data to predict effects of coal type. *Energy Fuels*, 6(4):414–431, 1992.

[33] J. Floyd, A. M. Kempf, A. Kronenburg, and R. H. Ram. A simple model for the filtered density function for passive scalar combustion LES. *Combust. Theor. Model.*, 13(4):559–588, 2009.

[34] B. M. Franchetti, F. C. Marincola, S. Navarro-Martinez, and A. M. Kempf. Large Eddy simulation of a pulverised coal jet flame. *Proc. Combust. Inst.*, 34(2):2419–2426, 2013.

[35] B. M. Franchetti, F. Cavallo Marincola, S. Navarro-Martinez, and A. M. Kempf. Large Eddy Simulation of a 100 $\mathrm{kW_{th}}$ swirling oxy-coal furnace. *Fuel*, 181:491–502, 2016.

[36] J. Fröhlich. *Large Eddy Simulation turbulenter Strömungen*. Vieweg+Teubner Verlag Wiesbaden, 2006.

[37] C. Ghenai and I. Janajreh. CFD analysis of the effects of co-firing biomass with coal. *Energy Convers. Manage.*, 51(8):1694–1701, 2010.

[38] O. Gicquel, N. Darabiha, and D. Thévenin. Laminar premixed hydrogen/air counterflow flame simulations using flame prolongation of ILDM with differential diffusion. *Proc. Combust. Inst.*, 28(2):1901–1908, 2000.

[39] P. Givi. Model-free simulations of turbulent reactive flows. *Prog. Energy Combust. Sci.*, 15 (1):1–107, 1989.

[40] G. Godel, P. Domingo, and L. Vervisch. Tabulation of $\mathrm{NO_x}$ chemistry for Large-Eddy Simulation of non-premixed turbulent flames. *Proc. Combust. Inst.*, 32(1):1555–1561, 2009.

[41] D. G. Goodwin, R. L. Speth, H. K. Moffat, and B. W. Weber. Cantera: An Object-oriented Software Toolkit for Chemical Kinetics, Thermodynamics, and Transport Processes. page available from https://www.cantera.org/, 2021.

[42] D. M. Grant, R. J. Pugmire, T. H. Fletcher, and A. R. Kerstein. Chemical model of coal devolatilization using percolation lattice statistics. *Energy Fuels*, 3(2):175–186, 1989.

[43] P. Gruhlke, H. Janbazi, I. Wlokas, C. Beck, and A. M. Kempf. Investigation of a High Karlovitz, High Pressure Premixed Jet Flame with Heat Losses by LES. *Combust. Sci. Technol.*, 192(11):2138–2170, 2020.

[44] T. Hara, M. Muto, T. Kitano, R. Kurose, and S. Komori. Direct numerical simulation of a pulverized coal jet flame employing a global volatile matter reaction scheme based on detailed reaction mechanism. *Combust. Flame*, 162(12):4391–4407, 2015.

[45] N. Hashimoto, R. Kurose, and H. Shirai. Numerical simulation of pulverized coal jet flame employing the TDP model. *Fuel*, 97:277–287, 2012.

[46] C. Hasse and N. Peters. A two mixture fraction flamelet model applied to split injections in a DI Diesel engine. *Proc. Combust. Inst.*, 30(2):2755–2762, 2005.

[47] C. Hasse, P. Debiagi, X. Wen, K. Hildebrandt, M. Vascellari, and T. Faravelli. Advanced modeling approaches for CFD simulations of coal combustion and gasification. *Prog. Energy Combust. Sci.*, 86:100938, 2021.

[48] J. Hasslberger, L. Engelmann, A. M. Kempf, and M. Klein. Robust dynamic adaptation of the Smagorinsky model based on a sub-grid activity sensor. *Phys. Fluids*, 33(1):015117, 2021.

[49] J. Hees, D. Zabrodiec, A. Massmeyer, M. Habermehl, and R. Kneer. Experimental Investigation and Comparison of Pulverized Coal Combustion in CO_2/O_2- and N_2/O_2-Atmospheres. *Flow Turbul. Combust.*, 96:417–431, 2016.

[50] J. O. Hirschfelder, C. F. Curtiss, R. B. Bird, and M. G. Mayer. *Molecular theory of gases and liquids.* Wiley New York, 1964.

[51] C. Hollmann and E. Gutheil. Modeling of turbulent spray diffusion flames including detailed chemistry. *Symp. (Int.) Combust.*, 26(1):1731–1738, 1996.

[52] R. Hurt, J.-K. Sun, and M. Lunden. A Kinetic Model of Carbon Burnout in Pulverized Coal Combustion. *Combust. Flame*, 113(1):181–197, 1998.

[53] S.-M. Hwang, R. Kurose, F. Akamatsu, H. Tsuji, H. Makino, and M. Katsuki. Application of Optical Diagnostics Techniques to a Laboratory-Scale Turbulent Pulverized Coal Flame. *Energy Fuels*, 19(2):382–392, 2005.

[54] S.-M. Hwang, R. Kurose, F. Akamatsu, H. Tsuji, H. Makino, and M. Katsuki. Observation of Detailed Structure of Turbulent Pulverized-Coal Flame by Optical Measurement. *JSME Int J., Ser. B*, 49(4):1316–1327, 2006.

[55] S.-M. Hwang, R. Kurose, F. Akamatsu, H. Tsuji, H. Makino, and M. Katsuki. Observation of Detailed Structure of Turbulent Pulverized-Coal Flame by Optical Measurement. *JSME Int J., Ser. B*, 49(4):1328–1335, 2006.

[56] IEA. Global Energy Review. *IEA. Paris*, pages available from https://www.iea.org/reports/global–energy–review–2020, 2020.

[57] IEA. Coal 2022. *IEA. Paris*, pages available from https://www.iea.org/reports/coal–2022, 2022.

[58] M. Ihme and H. Pitsch. Modeling of radiation and nitric oxide formation in turbulent nonpremixed flames using a flamelet/progress variable formulation. *Phys. Fluids*, 20(5): 055110, 2008.

[59] M. Ihme and Y. C. See. Prediction of autoignition in a lifted methane/air flame using an unsteady flamelet/progress variable model. *Combust. Flame*, 157(10):1850–1862, 2010.

[60] M. Ihme, C. M. Cha, and H. Pitsch. Prediction of local extinction and re-ignition effects in non-premixed turbulent combustion using a flamelet/progress variable approach. *Proc. Combust. Inst.*, 30(1):793–800, 2005.

[61] E. Inanc and A. M. Kempf. Numerical Study of a Pulsed Auto-Igniting Jet Flame with Detailed Tabulated Chemistry. *Fuel*, 252:408–416, 2019.

[62] IPCC. Global Warming of 1.5 °C. *IPCC Special Report*, page available from https://www.ipcc.ch/sr15/, 2018.

[63] S. Ishihara, J. Zhang, and T. Ito. Numerical calculation with detailed chemistry of effect of ammonia co-firing on NO emissions in a coal-fired boiler. *Fuel*, 266:116924, 2020.

[64] S. Ishihara, J. Zhang, and T. Ito. Numerical calculation with detailed chemistry on ammonia co-firing in a coal-fired boiler: Effect of ammonia co-firing ratio on NO emissions. *Fuel*, 274:117742, 2020.

[65] W. P. Jones, S. Lyra, and S. Navarro-Martinez. Large Eddy Simulation of a swirl stabilized spray flame. *Proc. Combust. Inst.*, 33:2153–2160, 2011.

[66] T. Kangwanpongpan, F. H. R. Franca, R. C. da Silva, P. S. Schneider, and H. J. Krautz. New correlations for the weighted-sum-of-gray-gases model in oxy-fuel conditions based on HITEMP 2010 database. *Int. J. Heat Mass Transfer*, 55(25):7419–7433, 2012.

[67] R. J. Kee, F. M. Rupley, and J. A. Miller. The Chemkin thermodynamic data base. *Technical Report SAND87-8215, Sandia National Laboratories*, 1, 1990.

[68] A. M. Kempf. *Large eddy simulation of non-premixed turbulent flames.* PhD thesis, Technical University of Darmstadt, 2004.

[69] A. M. Kempf, S. Wysocki, and M. Pettit. An efficient, parallel low-storage implementation of Klein's turbulence generator for LES and DNS. *Comput. Fluids*, 60:58–60, 2012.

[70] N. Khan, L. Zhao, M. Cleary, R. Bilger, O. T. Stein, and A. Kronenburg. A Mixture Fraction-Based Model for Evaporation, Pyrolysis and Char Conversion of Dilute Fuel Dispersions. *19th Australasian Fluid Mech. Conf., Melbourne, Australia*, 2014.

[71] M. Klein, A. Sadiki, and J. Janicka. A digital filter based generation of inflow data for spatially developing direct numerical or large eddy simulations. *J. Comput. Phys.*, 186(2): 652–665, 2003.

[72] A. Y. Klimenko and R. W. Bilger. Conditional moment closure for turbulent combustion. *Prog. Energy Combust. Sci.*, 25(6):595–687, 1999.

[73] R. Knappstein, G. Kuenne, A. Ketelheun, J. Köser, L. Becker, S. Heuer, M. Schiemann, V. Scherer, A. Dreizler, A. Sadiki, and J. Janicka. Devolatilization and volatiles reaction of individual coal particles in the context of FGM tabulated chemistry. *Combust. Flame*, 169:72–84, 2016.

[74] R. Knappstein, G. Kuenne, H. Nicolai, F. di Mare, A. Sadiki, and J. Janicka. Description of the char conversion process in coal combustion based on premixed FGM chemistry. *Fuel*, 236:124–134, 2019.

[75] H. Kobayashi, J. B. Howard, and A. F. Sarofim. Coal devolatilization at high temperatures. *Proc. Combust. Inst.*, 16(1):411–425, 1977.

[76] A. N. Kolmogorov. Dissipation of Energy in the Locally Isotropic Turbulence. *Proc. Math. Phys. Eng. Sci.*, 434(1890):15–17, 1991.

[77] A. N. Kolmogorov, V. Levin, J. C. R. Hunt, O. M. Phillips, and D. Williams. The local structure of turbulence in incompressible viscous fluid for very large Reynolds numbers. *Proc. R. Soc. London, Ser. A*, 434(1890):9–13, 1991.

[78] R. Kurose and H. Makino. Large eddy simulation of a solid-fuel jet flame. *Combust. Flame*, 135(1):1–16, 2003.

[79] P. J. S. L. Douglas Smoot. *Coal Combustion and Gasification.* Springer New York, NY, 1985.

[80] B. E. Launder and D. B. Spalding. The numerical computation of turbulent flows. *Comput. Methods Appl. Mech. Eng.*, 3(2):269–289, 1974.

[81] J. Legier, T. Poinsot, and D. Veynante. Dynamically thickened flame LES model for premixed and non-premixed turbulent combustion. *Proceedings of the Summer Program*, 157-168, 2000.

[82] C. Lettieri. *Large eddy simulation of two-phase reacting flows.* PhD thesis, Imperial College London, 2010.

[83] R. J. LeVeque. *Finite volume methods for hyperbolic problems.* Cambridge University Press, 2002.

[84] J. T. Lipkowicz, I. Wlokas, and A. M. Kempf. Analysis of mild ignition in a shock tube using a highly resolved 3D-LES and high-order shock-capturing schemes. *Shock Waves*, 29 (4):511–521, 2019.

[85] F. C. Lockwood and A. P. Salooja. The prediction of some pulverized bituminous coal flames in a furnace. *Combust. Flame*, 54(1–3):23–32, 1983.

[86] T. Lu and C. K. Law. A directed relation graph method for mechanism reduction. *Proc. Combust. Inst.*, 30(1):1333–1341, 2005.

[87] K. Luo, H. Wang, J. Fan, and F. Yi. Direct Numerical Simulation of Pulverized Coal Combustion in a Hot Vitiated Co-flow. *Energy Fuels*, 26(10):6128–6136, 2012.

[88] K. Luo, C. Zhao, X. Wen, Z. Gao, Y. Bai, J. Xing, and J. Fan. A priori study of an extended flamelet/progress variable model for NO prediction in pulverized coal flames. *Energy*, 175: 768–780, 2019.

[89] L. Ma, J. M. Jones, M. Pourkashanian, and A. Williams. Modelling the combustion of pulverized biomass in an industrial combustion test furnace. *Fuel*, 86(12):1959–1965, 2007.

[90] U. Maas and S. B. Pope. Simplifying chemical kinetics: Intrinsic low-dimensional manifolds in composition space. *Combust. Flame*, 88(3–4):239–264, 1992.

[91] U. Maas and S. B. Pope. Implementation of simplified chemical kinetics based on intrinsic low-dimensional manifolds. *Symp. (Int.) Combust.*, 24(1):103–112, 1992.

[92] B. F. Magnussen. The eddy dissipation concept: A bridge between science and technology. *ECCOMAS thematic conference on computational combustion*, 21:24, 2005.

[93] W. R. Marshall and W. E. Ranz. Evaporation from drops–Part I. *Chem. Eng. Prog.*, 48 (3):141–146, 1952.

[94] B. Mei, X. Zhang, S. Ma, M. Cui, H. Guo, Z. Cao, and Y. Li. Experimental and kinetic modeling investigation on the laminar flame propagation of ammonia under oxygen enrichment and elevated pressure conditions. *Combust. Flame*, 210:236–246, 2019.

[95] D. Meller, T. Lipkowicz, M. Rieth, O. T. Stein, A. Kronenburg, C. Hasse, and A. M. Kempf. Numerical Analysis of a Turbulent Pulverized Coal Flame Using a Flamelet/Progress Variable Approach and Modeling Experimental Artifacts. *Energy Fuels*, 35(9):7133–7143, 2021.

[96] D. Meller, L. Engelmann, O. T. Stein, and A. M. Kempf. Exhaust Gas Recirculation (EGR) analysis of a swirl-stabilized pulverized coal flame with focus on NO_x release using FPV-LES. *Fuel*, 343:127939, 2023.

[97] D. Meller, L. Engelmann, P. Wollny, K. Tainaka, H. Watanabe, P. Debiagi, O. T. Stein, and A. M. Kempf. Evaluation of ammonia co-firing in the CRIEPI coal jet flame using a three mixture fraction FPV-LES. *Proc. Combust. Inst.*, 39(3):3615–3624, 2023.

[98] D. Merrick. Mathematical models of the thermal decomposition of coal: 2. Specific heats and heats of reaction. *Fuel*, 62:540–546, 1983.

[99] D. Messig, M. Vascellari, and C. Hasse. Flame structure analysis and flamelet progress variable modelling of strained coal flames. *Combust. Theor. Model.*, 21(4):700–721, 2017.

[100] G. Migliavacca, E. Parodi, L. Bonfanti, T. Faravelli, S. Pierucci, and E. Ranzi. A general mathematical model of solid fuels pyrolysis. *Energy*, 30(8):1453–1468, 2005.

[101] J. A. Miller and C. T. Bowman. Mechanism and modeling of nitrogen chemistry in combustion. *Prog. Energy Combust. Sci.*, 15:287–338, 1989.

[102] M. Mohan Rai and P. Moin. Direct simulations of turbulent flow using finite-difference schemes. *J.Comput. Phys.*, 96(1):15–53, 1991.

[103] M. Muto, K. Tanno, and R. Kurose. A DNS study on effect of coal particle swelling due to devolatilization on pulverized coal jet flame. *Fuel*, 184:749–752, 2016.

[104] M. Muto, K. Yuasa, and R. Kurose. Numerical simulation of ignition in pulverized coal combustion with detailed chemical reaction mechanism. *Fuel*, 190:136–144, 2017.

[105] H. Nicolai. *Towards Predictive Simulations of Low-Emission Reactive Solid Fuel Systems.* PhD thesis, Technical University of Darmstadt, 2022.

[106] H. Nicolai, P. Debiagi, J. Janicka, and C. Hasse. Flamelet LES of oxy-fuel swirling flames with different O_2/CO_2 ratios using directly coupled seamless multi-step solid fuel kinetics. *Fuel*, 344:128089, 2023.

[107] F. Nicoud, H. B. Toda, O. Cabrit, S. Bose, and J. Lee. Using singular values to build a subgrid-scale model for large eddy simulations. *Phys. Fluids*, 23(8):085106, 2011.

[108] S. Niksa. *Process Chemistry of Coal Utilization.* Woodhead Publishing, 2020.

[109] S. Niksa and A. R. Kerstein. FLASHCHAIN theory for rapid coal devolatilization kinetics. 1. Formulation. *Energy Fuels*, 5(5):647–665, 1991.

[110] C. Olbricht, O. T. Stein, J. Janicka, J. A. van Oijen, S. Wysocki, and A. M. Kempf. LES of lifted flames in a gas turbine model combustor using top-hat filtered PFGM chemistry. *Fuel*, 96:100–107, 2012.

[111] G. Olenik, O. T. Stein, and A. Kronenburg. LES of swirl-stabilised pulverised coal combustion in IFRF furnace No. 1. *Proc. Combust. Inst.*, 35(3):2819–2828, 2015.

[112] C. Pera, J. Réveillon, L. Vervisch, and P. Domingo. Modeling subgrid scale mixture fraction variance in LES of evaporating spray. *Combust. Flame*, 146:635–648, 2006.

[113] A. A. F. Peters and R. Weber. Mathematical modeling of a 2.4 MW swirling pulverized coal flame. *Combust. Sci. Technol.*, 122(1–6):131–182, 1997.

[114] N. Peters. Laminar diffusion flamelet models in non-premixed turbulent combustion. *Prog. Energy Combust. Sci.*, 10:319–339, 1984.

[115] N. Peters. *Turbulent Combustion.* Cambridge University Press, 2000.

[116] I. Petersen and J. Werther. Experimental investigation and modeling of gasification of sewage sludge in the circulating fluidized bed. *Chem. Eng. Process. Process Intensif.*, 44 (7):717–736, 2005.

[117] C. D. Pierce and P. Moin. Progress-variable approach for large-eddy simulation of non-premixed turbulent combustion. *J. Fluid Mech.*, 504:73–97, 2004.

[118] H. Pitsch. FlameMaster, A Computer Code for Homogeneous Combustion and One-Dimensional Laminar Flame Calculations. *Institute for Technical Mechanic, RWTH Aachen*, pages available from https://www.itv.rwth–aachen.de/downloads/flamemaster/, 1998.

[119] H. Pitsch and N. Peters. A Consistent Flamelet Formulation for Non-Premixed Combustion Considering Differential Diffusion Effects. *Combust. Flame*, 114(1):26–40, 1998.

[120] G. J. Pitt. The kinetic of the evolution of volatile products from coal. *Fuel*, 41:267–274, 1962.

[121] T. Poinsot and D. Veynante. *Theoretical and Numerical Combustion.* R.T. Edwards, 2005.

[122] S. B. Pope. PDF methods for turbulent reactive flows. *Prog. Energy Combust. Sci.*, 11(2): 119–192, 1985.

[123] S. B. Pope. Computations of turbulent combustion: Progress and challenges. *Symp. (Int.) Combust.*, 23(1):591–612, 1991.

[124] S. B. Pope. *Turbulent Flows.* Cambridge University Press, 2000.

[125] L. Prandtl. 7. Bericht über Untersuchungen zur ausgebildeten Turbulenz. *ZAMM - Journal of Applied Mathematics and Mechanics / Zeitschrift für Angewandte Mathematik und Mechanik*, 5(2):136–139, 1925.

[126] L. Prandtl. Über ein neues Formelsystem für die ausgebildete Turbulenz. *Akad. Wiss. Göttingen, Math. Phys. Kl.*, 6–19, 1945.

[127] M. J. Prins, K. J. Ptasinski, and F. J. J. G. Janssen. From coal to biomass gasification: Comparison of thermodynamic efficiency. *Energy*, 32(7):1248–1259, 2007.

[128] F. Proch. *Highly-resolved numerical simulation of turbulent premixed and stratified combustion under adiabatic and non-adiabatic conditions with tabulated chemistry.* PhD thesis, University of Duisburg-Essen, 2016.

[129] F. Proch and A. M. Kempf. Modeling heat loss effects in the large eddy simulation of a model gas turbine combustor with premixed flamelet generated manifolds. *Proc. Combust. Inst.*, 35(3):3337–3345, 2015.

[130] M. Rabaçal, B. M. Franchetti, F. C. Marincola, F. Proch, M. Costa, C. Hasse, and A. M. Kempf. Large Eddy Simulation of coal combustion in a large-scale laboratory furnace. *Proc. Combust. Inst.*, 35(3):3609–3617, 2015.

[131] M. Rabaçal, M. Costa, M. Vascellari, C. Hasse, M. Rieth, and A. M. Kempf. A Large Eddy Simulation Study on the Effect of Devolatilization Modelling and Char Combustion Mode Modelling on the Structure of a Large-Scale, Biomass and Coal Co-Fired Flame. *J. Combust.*, 7036425, 2018.

[132] E. Ranzi, A. Frassoldati, S. Granata, and T. Faravelli. Wide-Range Kinetic Modeling Study of the Pyrolysis, Partial Oxidation, and Combustion of Heavy n-Alkanes. *Ind. Eng. Chem. Res.*, 44(14):5170–5183, 2005.

[133] J. Revel, J. C. Boettner, M. Cathonnet, and J. S. Bachman. Derivation of a global chemical kinetic mechanism for methane ignition and combustion. *J. Chem. Phys.*, 91:365–382, 1994.

[134] O. Reynolds. On the dynamical theory of incompressible viscous fluids and the determination of the criterion. *Philos. Trans. R. Soc. London, Ser. A*, 186:123–164, 1895.

[135] C. M. Rhie and W. L. Chow. Numerical study of the turbulent flow past an airfoil with trailing edge separation. *AIAA Journal*, 21(11):1525–1532, 1983.

[136] L. F. Richardson. *Weather prediction by numerical process.* Cambridge University Press, 2007.

[137] M. Rieth, F. Proch, M. Rabaçal, B. M. Franchetti, F. C. Marincola, and A. M. Kempf. Flamelet LES of a semi-industrial pulverized coal furnace. *Combust. Flame*, 173:39–56, 2016.

[138] M. Rieth, A. G. Clements, M. Rabaçal, F. Proch, O. T. Stein, and A. M. Kempf. Flamelet LES modeling of coal combustion with detailed devolatilization by directly coupled CPD. *Proc. Combust. Inst.*, 36(2):2181–2189, 2017.

[139] M. Rieth, F. Proch, A. G. Clements, M. Rabaçal, and A. M. Kempf. Highly resolved flamelet LES of a semi-industrial scale coal furnace. *Proc. Combust. Inst.*, 36(3):3371–3379, 2017.

[140] M. Rieth, A. M. Kempf, A. Kronenburg, and O. T. Stein. Carrier-phase DNS of pulverized coal particle ignition and volatile burning in a turbulent mixing layer. *Fuel*, 212:364–374, 2018.

[141] M. Rieth, A. M. Kempf, O. T. Stein, A. Kronenburg, C. Hasse, and M. Vascellari. Evaluation of a flamelet/progress variable approach for pulverized coal combustion in a turbulent mixing layer. *Proc. Combust. Inst.*, 37(3):2927–2934, 2019.

[142] A. Rittler, F. Proch, and A. M. Kempf. LES of the Sydney piloted spray flame series with the PFGM/ATF approach and different sub-filter models. *Combust. Flame*, 162:1575–1598, 2015.

[143] P. D. Ronney. Effect of Chemistry and Transport Properties on Near-Limit Flames at Microgravity. *Combust. Sci. Technol.*, 59:123–141, 1988.

[144] L. Schiller and A. Naumann. Über die grundlegenden Berechnungen bei der Schwerkraftaufbereitung. *Zeitschrift des VDI*, 77.12:318–320, 1933.

[145] A. Shamooni, P. Debiagi, B. Wang, T. D. Luu, O. T. Stein, A. Kronenburg, G. Bagheri, A. Stagni, A. Frassoldati, T. Faravelli, A. M. Kempf, X. Wen, and C. Hasse. Carrier-phase DNS of detailed NO_x formation in early-stage pulverized coal combustion with fuel-bound nitrogen. *Fuel*, 291:119998, 2021.

[146] R. C. Shurtz, K. K. Kolste, and T. H. Fletcher. Coal Swelling Model for High Heating Rate Pyrolysis Applications. *Energy Fuels*, 25(5):2163–2173, 2011.

[147] R. C. Shurtz, J. W. Hogge, K. C. Fowers, G. S. Sorensen, and T. H. Fletcher. Coal Swelling Model for Pressurized High Particle Heating Rate Pyrolysis Applications. *Energy Fuels*, 26 (6):3612–3627, 2012.

[148] N. Sikalo, O. Hasemann, C. Schulz, A. M. Kempf, and I. Wlokas. A Genetic Algorithm-Based Method for the Automatic Reduction of Reaction Mechanisms. *Int. J. Chem. Kinet.*, 46(1):41–59, 2014.

[149] N. Sikalo, O. Hasemann, C. Schulz, A. M. Kempf, and I. Wlokas. A genetic algorithm–based method for the optimization of reduced kinetics mechanisms. *Int. J. Chem. Kinet.*, 47(11): 695–723, 2015.

[150] J. S. Smagorinsky. General Circulation Experiments with the Primitive Equations, 1, The Basic Experiment. *Monthly Weather Review*, 91(1):99–164, 1963.

[151] J. P. Smart, K. J. Knill, B. M. Visser, and R. Weber. Reduction of NO_x emissions in a swirled coal flame by particle injection into the internal recirculation zone. *Symp. (Int.) Combust.*, 22(1):1117–1125, 1989.

[152] I. W. Smith. The combustion rates of coal chars: A review. *Symp. (Int.) Combust.*, 19(1): 1045–1065, 1982.

[153] P. J. Smith, T. H. Fletcher, and L. D. Smoot. Model for pulverized coal-fired reactors. *Symp. (Int.) Combust.*, 18(1):1285–1293, 1981.

[154] L. D. Smoot. Modeling of coal-combustion processes. *Prog. Energy Combust. Sci.*, 10(2): 229–267, 1984.

[155] L. D. Smoot and D. T. Pratt. *Pulverized-coal combustion and gasification.* Springer New York, NY, 1979.

[156] P. R. Solomon, D. G. Hamblen, R. Carangelo, M. A. Serio, and G. V. Deshpande. General model of coal devolatilization. *Energy Fuels*, 2(4):405–422, 1988.

[157] Y. Song, L. Marrodán, N. Vin, O. Herbinet, E. Assaf, C. Fittschen, A. Stagni, T. Faravelli, M. Alzueta, and F. Battin-Leclerc. The sensitizing effects of NO_2 and NO on methane low temperature oxidation in a jet stirred reactor. *Proc. Combust. Inst.*, 37:667–675, 2019.

[158] D. B. Spalding. Mixing and chemical reaction in steady confined turbulent flames. *Symp. (Int.) Combust.*, 13(1):649–657, 1971.

[159] A. Stagni, C. Cavallotti, S. Arunthanayothin, Y. Song, O. Herbinet, F. Battin-Leclerc, and T. Faravelli. An experimental, theoretical and kinetic-modeling study of the gas-phase oxidation of ammonia. *React. Chem. Eng.*, 5:696–711, 2020.

[160] O. T. Stein. *Large Eddy Simulation of Combustion in Swirling and Opposed Jet Flows.* PhD thesis, Imperial College London, 2009.

[161] O. T. Stein and H. Watanabe. Target flames: CRIEPI coal jet flame. *Proc. 3rd CBC Workshop, Aachen, Germany*, 69–110, 2019.

[162] O. T. Stein, G. Olenik, A. Kronenburg, F. C. Marincola, B. M. Franchetti, A. M. Kempf, M. Ghiani, M. Vascellari, and C. Hasse. Towards Comprehensive Coal Combustion Modelling for LES. *Flow Turb. Combust.*, 90(4):859–884, 2013.

[163] M. Stoellinger, B. Naud, D. Roekaerts, N. Beishuizen, and S. Heinz. PDF modeling and simulations of pulverized coal combustion - Part 2: Application. *Combust. Flame*, 160(2): 396–410, 2013.

[164] K. Tainaka, A. Yamamoto, M. Kimoto, Y. Ozawa, and S. Hara. Investigation of co-combustion characteristics of pulverized coal and ammonia in a jet flame. *56th Symposium (Japanese) on Combustion*, 2018.

[165] K. Tainaka, S. Sawada, D. Okada, F. Akamatsu, and L. Run. Effects of Co-firing Ammonia on Structure of a Pulverized Coal Jet Flame. *57th Symposium (Japanese) on Combustion*, 2019.

[166] J. Tillou, J.-B. Michel, C. Angelberger, and D. Veynante. Assessing LES models based on tabulated chemistry for the simulation of Diesel spray combustion. *Combust. Flame*, 161: 525–540, 2014.

[167] D. Toporov, P. Bocian, P. Heil, A. Kellermann, H. Stadler, S. Tschunko, M. Förster, and R. Kneer. Detailed investigation of a pulverized fuel swirl flame in CO_2/O_2 atmosphere. *Combust. Flame*, 155(4):605–618, 2008.

[168] J. S. Truelove. Discrete-Ordinate Solutions of the Radiation Transport Equation. *J. Heat Transfer*, 109(4):1048–1051, 1987.

[169] J. S. Truelove and R. G. Williams. Coal combustion models for flame scaling. *Symp. (Int.) Combust.*, 22(1):155–164, 1989.

[170] G. L. Tufano, O. T. Stein, A. Kronenburg, A. Frassoldati, T. Faravelli, L. Deng, A. M. Kempf, M. Vascellari, and C. Hasse. Resolved flow simulation of pulverized coal particle devolatilization and ignition in air- and O_2/CO_2-atmospheres. *Fuel*, 186:285–292, 2016.

[171] G. L. Tufano, O. T. Stein, B. Wang, A. Kronenburg, M. Rieth, and A. M. Kempf. Coal particle volatile combustion and flame interaction. Part I: Characterization of transient and group effects. *Fuel*, 229:262–269, 2018.

[172] G. L. Tufano, O. T. Stein, B. Wang, A. Kronenburg, M. Rieth, and A. M. Kempf. Coal particle volatile combustion and flame interaction. Part II: Effects of particle Reynolds number and turbulence. *Fuel*, 234:723–731, 2018.

[173] T. Turányi. Sensitivity analysis of complex kinetic systems. tools and applications. *J. Math. Chem.*, 5:203–248, 1990.

[174] UNFCCC. Paris agreement. Report of the Conference of the Parties to the United Nations Framework Convention on Climate Change. *Paris*, 21, 2015.

[175] D. W. Van Krevelen. *Coal: typology - physics - chemistry - constitution.* Netherlands, 1993.

[176] J. A. van Oijen and L. P. H. de Goey. Modelling of Premixed Laminar Flames using Flamelet-Generated Manifolds. *Combust. Sci. Technol.*, 161(1):113–137, 2000.

[177] J. A. van Oijen, R. J. M. Bastiaans, and L. P. H. de Goey. Low-dimensional manifolds in direct numerical simulations of premixed turbulent flames. *Proc. Combust. Inst.*, 31(1): 1377–1384, 2007.

[178] M. Vascellari, R. Arora, M. Pollack, and C. Hasse. Simulation of entrained flow gasification with advanced coal conversion submodels. Part 1: Pyrolysis. *Fuel*, 113:654–669, 2013.

[179] M. Vascellari, H. Xu, and C. Hasse. Flamelet modeling of coal particle ignition. *Proc. Combust. Inst.*, 34(2):2445–2452, 2013.

[180] M. Vascellari, G. L. Tufano, O. T. Stein, A. Kronenburg, A. M. Kempf, A. Scholtissek, and C. Hasse. A flamelet/progress variable approach for modeling coal particle ignition. *Fuel*, 201:29–38, 2017. 1st International Workshop on Oxy-Fuel Combustion.

[181] M. Vascellari, D. Messig, A. Scholtissek, C. Hasse, M. Xia, B. Fiorina, and N. Darabiha. Experimental and numerical investigation of a stagnation pulverised coal flame. *Proc. Combust. Inst.*, 37(3):2857–2866, 2019.

[182] K. Wan, L. Vervisch, J. Xia, P. Domingo, Z. Wang, Y. Liu, and K. Cen. Alkali metal emissions in an early-stage pulverized-coal flame: DNS analysis of reacting layers and chemistry tabulation. *Proc. Combust. Inst.*, 37(3):2791–2799, 2019.

[183] J. Watanabe and K. Yamamoto. Flamelet model for pulverized coal combustion. *Proc. Combust. Inst.*, 35(2):2315–2322, 2015.

[184] J. Watanabe, T. Okazaki, K. Yamamoto, K. Kuramashi, and A. Baba. Large-eddy simulation of pulverized coal combustion using flamelet model. *Proc. Combust. Inst.*, 36(2): 2155–2163, 2017.

[185] R. Weber, J. Dugué, A. Sayre, and B. M. Visser. Quarl zone flow field and chemistry of swirling pulverized coal flames: Measurements and computation. *Symp. (Int.) Combust.*, 24(1):1373–1380, 1992.

[186] X. Wen, H. Jin, O. T. Stein, J. Fan, and K. Luo. Large Eddy Simulation of piloted pulverized coal combustion using the velocity-scalar joint filtered density function model. *Fuel*, 158: 494–502, 2015.

[187] X. Wen, K. Luo, Y. Luo, H. I. Kassem, H. Jin, and J. Fan. Large eddy simulation of a semi-industrial scale coal furnace using non-adiabatic three-stream flamelet/progress variable model. *Appl. Energy*, 183:1086–1097, 2016.

[188] X. Wen, K. Luo, H. Jin, and J. Fan. Large eddy simulation of piloted pulverised coal combustion using extended flamelet/progress variable model. *Combust. Theor. Model.*, 21 (5):925–953, 2017.

[189] X. Wen, Y. Luo, K. Luo, H. Jin, and J. Fan. LES of pulverized coal combustion with a multi-regime flamelet model. *Fuel*, 188:661–671, 2017.

[190] X. Wen, H. Wang, Y. Luo, K. Luo, and J. Fan. Evaluation of flamelet/progress variable model for laminar pulverized coal combustion. *Phys. Fluids*, 29(8):083607, 2017.

[191] X. Wen, P. Debiagi, O. T. Stein, A. Kronenburg, A. M. Kempf, and C. Hasse. Flamelet tabulation methods for solid fuel combustion with fuel-bound nitrogen. *Combust. Flame*, 209:155–166, 2019.

[192] X. Wen, Y. Luo, H. Wang, K. Luo, H. Jin, and J. Fan. A three mixture fraction flamelet model for multi-stream laminar pulverized coal combustion. *Proc. Combust. Inst.*, 37:2901–2910, 2019.

[193] X. Wen, M. Rieth, A. Scholtissek, O. T. Stein, H. Wang, K. Luo, A. M. Kempf, A. Kronenburg, J. Fan, and C. Hasse. A comprehensive study of flamelet tabulation methods for pulverized coal combustion in a turbulent mixing layer - Part I: A priori and budget analyses. *Combust. Flame*, 216:439–452, 2020.

[194] X. Wen, M. Rieth, A. Scholtissek, O. T. Stein, H. Wang, K. Luo, A. Kronenburg, J. Fan, and C. Hasse. A comprehensive study of flamelet tabulation methods for pulverized coal combustion in a turbulent mixing layer - Part II: Strong heat losses and multi-mode combustion. *Combust. Flame*, 216:453–467, 2020.

[195] X. Wen, A. Shamooni, O. T. Stein, L. Cai, A. Kronenburg, H. Pitsch, A. M. Kempf, and C. Hasse. Detailed analysis of early-stage $\mathrm{NO_x}$ formation in turbulent pulverized coal combustion with fuel-bound nitrogen. *Proc. Combust. Inst.*, 38(3):4111–4119, 2021.

[196] X. Wen, H. Nicolai, P. Debiagi, D. Zabrodiec, A. Maßmeyer, R. Kneer, and C. Hasse. Flamelet LES of a 40 $\mathrm{kW_{th}}$ pulverized torrefied biomass furnace in air and oxy-fuel atmospheres. *Proc. Combust. Inst.*, 39(4):4563–4572, 2023.

[197] D. C. Wilcox. *Turbulence modeling for CFD.* DCW industries La Canada, CA, 1998.

[198] A. Williams, M. Pourkashanian, J. M. Jones, and N. Skorupska. *Combustion and Gasification of Coal.* Taylor and Francis, 2000.

[199] A. Williams, M. Pourkashanian, and J. M. Jones. Combustion of pulverised coal and biomass. *Prog. Energy Combust. Sci.*, 27(6):587–610, 2001.

[200] A. Williams, R. Backreedy, R. Habib, J. M. Jones, and M. Pourkashanian. Modelling coal combustion: the current position. *Fuel*, 81(5):605–618, 2002.

[201] F. A. Williams. Recent advances in theoretical descriptions of turbulent diffusion flames. *Turbulent mixing in nonreactive and reactive flows*, 189–208, 1975.

[202] F. A. Williams. *Combustion Theory. The Fundamental Theory of Chemically Reacting Flow Systems.* CRC Press., 1985.

[203] J. H. Williamson. Low-storage Runge-Kutta schemes. *J. Comput. Phys.*, 35:48–56, 1980.

[204] A. Yamamoto, M. Kimoto, Y. Ozawa, and S. Hara. Basic co-firing characteristics of ammonia with pulverized coal in a single burner test furnace. *NH_3 Fuel Conference.*, 542ff., 2018.

[205] C. Yin, S. K. Kær, L. Rosendahl, and S. L. Hvid. Co-firing straw with coal in a swirl-stabilized dual-feed burner: Modelling and experimental validation. *Bioresour. Technol.*, 101(11):4169–4178, 2010.

[206] C. F. You, , and X. C. Xu. Coal combustion and its pollution control in China. *Energy*, 35 (11):4467–4472, 2010.

[207] D. Zabrodiec, L. Becker, J. Hees, A. Maßmeyer, M. Habermehl, O. Hatzfeld, A. Dreizler, and R. Kneer. Detailed Analysis of the Velocity Fields from 60 kW Swirl-Stabilized Coal Flames in CO_2/O_2- and N_2/O_2-Atmospheres by Means of Laser Doppler Velocimetry and Particle Image Velocimetry. *Combust. Sci. Technol.*, 189(10):1751–1775, 2017.

[208] D. Zabrodiec, J. Hees, A. Massmeyer, F. vom Lehn, M. Habermehl, O. Hatzfeld, and R. Kneer. Experimental investigation of pulverized coal flames in CO_2/O_2- and N_2/O_2-atmospheres: Comparison of solid particle radiative characteristics. *Fuel*, 201:136–147, 2017.

[209] J. Zhang, T. Ito, H. Ishii, S. Ishihara, and T. Fujimori. Numerical investigation on ammonia co-firing in a pulverized coal combustion facility: Effect of ammonia co-firing ratio. *Fuel*, 267:117166, 2020.

[210] X.-Y. Zhao and D. C. Haworth. Transported PDF modeling of pulverized coal jet flames. *Combust. Flame*, 161(7):1866–1882, 2014.

[211] G. Zhou. *Numerical Simulations of Physical Discontinuities in Single and Multi-Fluid Flows for Arbitrary Mach Numbers.* PhD thesis, Chalmers University of Technology, Gothenburg, 1995.

Chapter 7

Appendix

7.1 Supplemental material to section 5.1

A sensitivity study was performed to investigate the behavior of different velocity profiles for the main jet at the inlet on the axial temperature (see Fig. 7.1), on the radial velocity profile of the axial velocity component u at 30 mm height above the burner inlet (see Fig. 7.2), and on the distribution of the radial CO_2 mole fraction of three heights above the burner inlet (50 mm, 100 mm and 150 mm). Four different profiles were studied: a top-hat velocity profile, a power-law velocity profile with an exponent of 1.5, a power-law velocity profile with an exponent of 4.5, and a thickened diffusion flame at the burner inlet.

The sensitivity study shows that using a top-hat velocity profile slightly lowers the maximum axial temperature (see Fig. 7.1), leads to an earlier flame breakup, which further downstream results in a slightly larger flame spread (see Fig. 7.3). By using a top-hat profile, the results deviate strongly from the experimental data.

Overall, the use of a power-law velocity profile showed the best agreement with the experimental data. Different exponents were investigated, showing a very sensitive behavior in terms of flame spread, jet break up point, and as a consequence also to the axial temperature and radial species profiles. The best agreement with the experimental data was obtained by using a power-law profile with an exponent of 4.5. These settings were maintained for the final simulations.

Since the qualitative comparison of the temperature distribution in the burner setup deviated from the results of Ahn et al. [1] (especially in the area of the hydrogen inlet), in a further study, the high temperature zone of the diffusion flame between pilot inlet and ambient air was extended by setting a higher temperature (800 K) for the ambient air in the the vicinity of the burner geometry (up to 2.5 mm radius from the edge of the hydrogen pilot). The velocity profile thereby is based on the power-law profile with an exponent of 4.5. This study is termed as “Thick. diff.”. The resulting expanded pilot flame showed negligible impact on the jet behavior in terms of flame spread, flame breakup point, axial temperature, and species distribution.

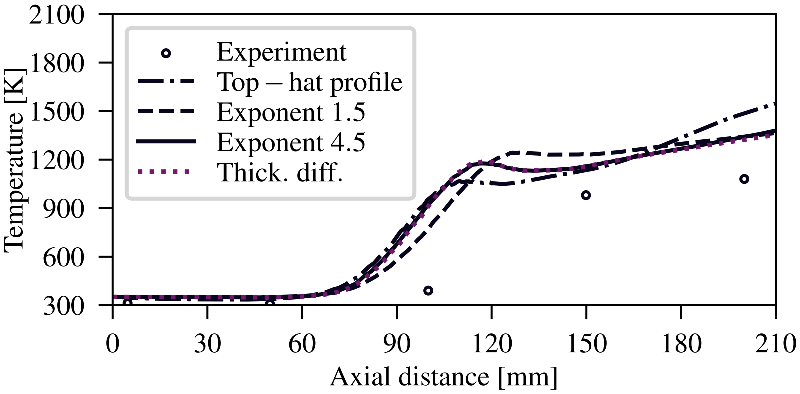

Figure 7.1: Time-averaged axial temperature profiles along the centerline of the burner. Four different test cases are shown: 1) top-hat velocity profile, 2) power-law exponent 1.5 for velocity profile, 3) power-law exponent 4.5 for velocity profile (final setting) and 4) thickened diffusion flame at the inlet (Thick. diff.).

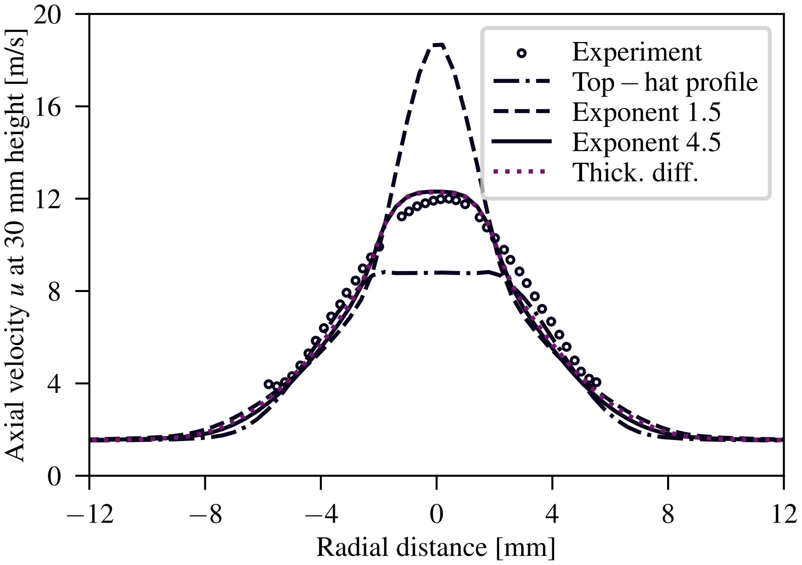

Figure 7.2: Time-averaged axial velocity profiles at 30 mm height above the burner of the four test cases mentioned above.

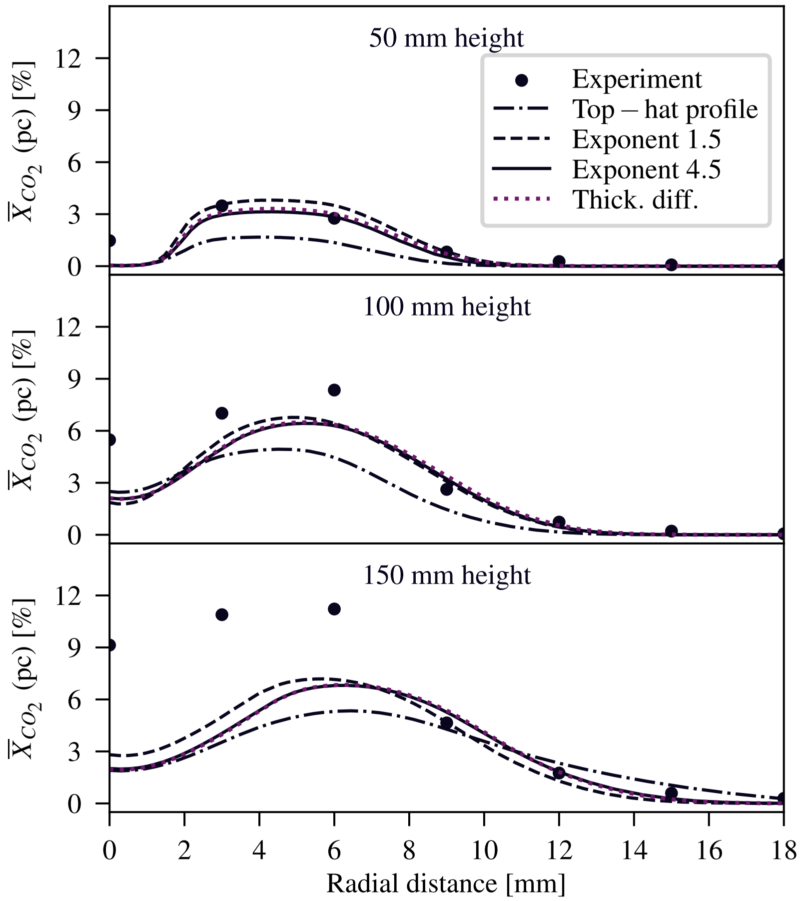

Figure 7.3: Time-averaged probe-corrected (pc) mole fraction of CO_2 at different heights of the four test cases mentioned above.

7.2 Supplemental material to section 5.2

7.2.1 Reaction path analysis

The oxidation path of a stoichiometric mixture of NH_3 and air at 1800 K using three different kinetic mechanisms (*C120*, *C129*, and *CNH*$_3$) is shown in Figs. 7.4-7.6. The numbers beside each arrow show the strength of each path (and the corresponding reaction) in kmol/m^3/s. Note that the paths with contributions below 5 % in a relative sense compared to the maximum flux in the $NH_3 \rightarrow NH_2$ path have been removed from the diagram.

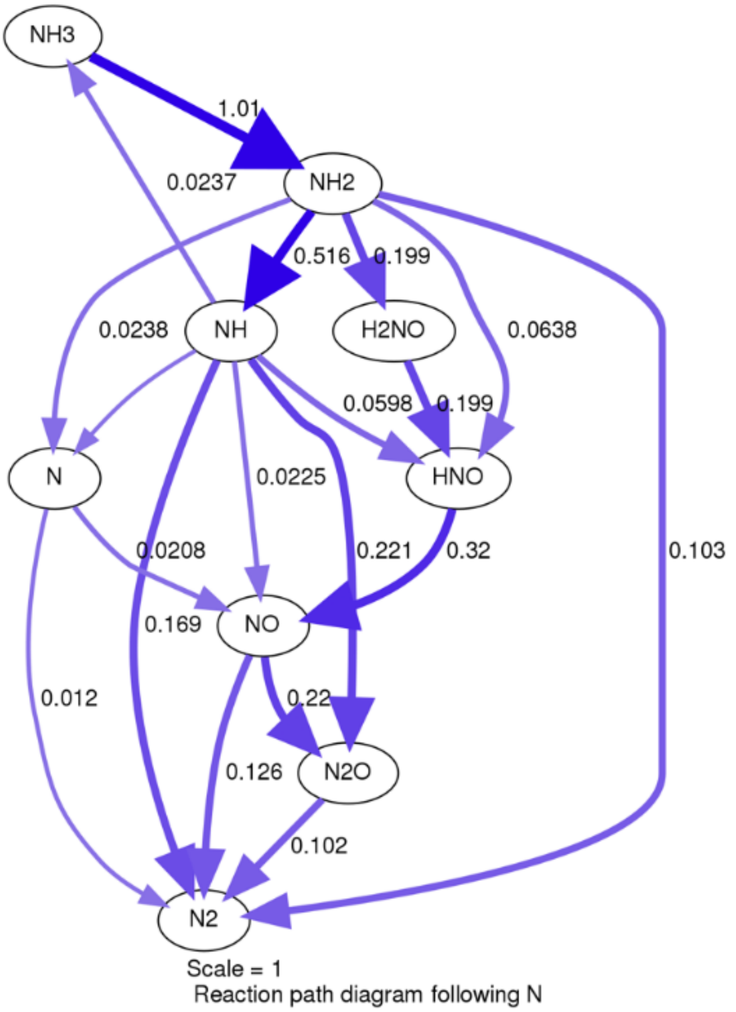

Figure 7.4: Oxidation paths of a stoichiometric mixture of NH_3 and air at 1800 K of mech. *C120*.

Comparing *CNH*$_3$ and *C129*, it can be seen that the paths are quite similar, indicating that the new mechanism (*C129*) can successfully represent the NH_3 oxidation paths observed in the detailed *CNH*$_3$ mechanism. Specifically, starting from NH_2 (the main product of dissociation of NH_3), we see that in both cases the dissociated NH_2 converts to NH and N_2H_2 by similar rates. The remaining paths belong to H_2NO, HNO, NNH, H_2NN, N_2H_3, N_2, and N, which are quite similar among the two mechanisms. NH and N_2H_2 then contribute to N_2 and NO productions. Specifically, $NH_2 \rightarrow N_2H_2 \rightarrow NNH \rightarrow N_2$ is more active in the reduction of fuel-N and NO to N_2, while $NH_2 \rightarrow NH \rightarrow N \rightarrow NO$ is responsible for NO production. The other main path of NO production is $NH_2 \rightarrow H_2NO \rightarrow HNO \rightarrow NO$. The fluxes of N within these main paths are quite similar when using both mechanisms, *CNH*$_3$ and *C129*.

On the other hand, mechanism *C120* shows a different pathway in NO reduction, which is

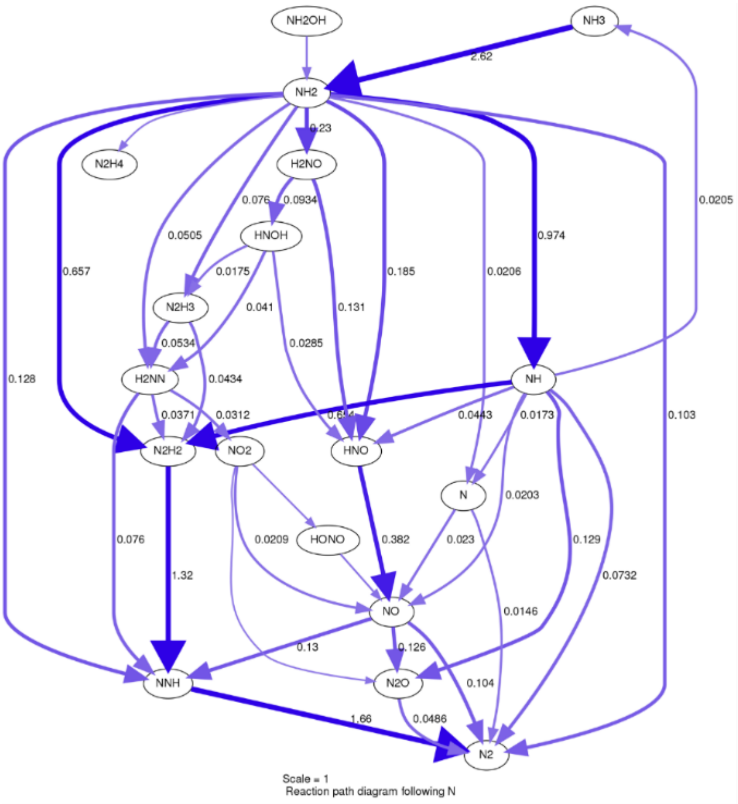

Figure 7.5: Oxidation paths of a stoichiometric mixture of NH_3 and air at 1800 K of mech. *C129*.

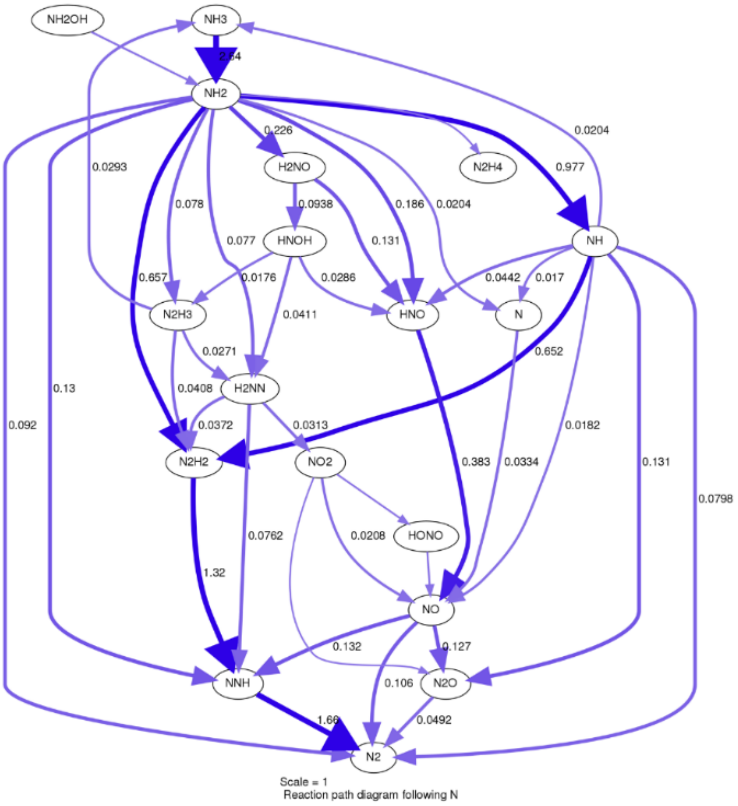

Figure 7.6: Oxidation paths of a stoichiometric mixture of NH_3 and air at 1800 K of mech. *CNH_3*.

due to the absence of some intermediate species such as N_2H_2 and NNH, which were removed during the reduction of the mechanism. The difference of the mechanisms reveals itself in NO reduction. The sum of fluxes of N_2 production is $\approx 0.512\,\mathrm{kmol/m^3/s}$ in *C120*, while in *C129* it is four times larger ($\approx 2\,\mathrm{kmol/m^3/s}$). Interestingly, the difference mainly comes from the $NH_2 \rightarrow N_2H_2 \rightarrow NNH \rightarrow N_2$ path ($\approx 1.66\,\mathrm{kmol/m^3/s}$), which is missing in *C120*. This explains the slightly higher prediction of NO with mechanism *C120* in Figs. 5.11-5.13 of the manuscript.

In conclusion, the new mechanism (*C129*) can better predict the reduction of NO.

7.2.2 Influence of radiative heat transfer on cases C and CA using mechanism C129

Figure 7.7 shows the axial mean temperature along the centerline when using mechanism *C129* for cases C and CA with and without consideration of radiative heat transfer. Simulations with consideration of radiative heat transfer are dotted, simulations without radiative heat transfer are shown with solid lines. Radiative heat transfer is considered using the discrete ordinate method (DOM) [30, 168] with a S8 quadrature grey weighted sum of grey gases (GWSGG) model, using the model parameters from Kangwanpongpan et al. [66]. Cases with particle injection were chosen here since the radiation influence is expected to be greater than without particle injection. The pure ammonia case A was not considered due to the low influence of radiative heat transfer on cases C and CA and due to the high computational costs. As can be seen in Fig. 7.7, the impact of radiation on the predicted temperature can be considered negligible, which equally applies to the radial profiles (not shown).

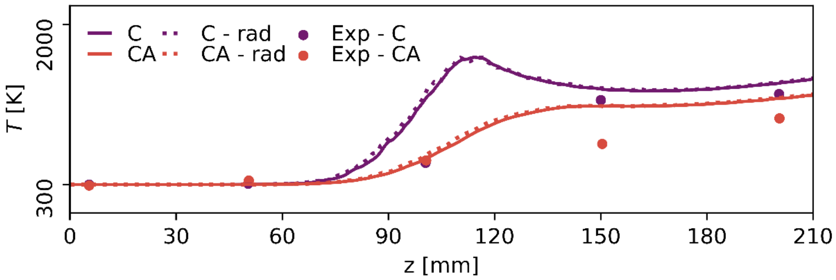

Figure 7.7: Axial mean temperature along the centerline using mechanism *C129* for cases C and CA with and without radiative heat transfer.

DOI: 10.17185/duepublico/81596
URN: urn:nbn:de:hbz:465-20240301-095557-3